

# Seismic response of historical masonry buildings and aggregates - large-scale experimental testing and macro-element modelling

Présentée le 9 décembre 2022

Faculté de l'environnement naturel, architectural et construit  
Laboratoire du génie parasismique et dynamique des structures  
Programme doctoral en génie civil et environnement

pour l'obtention du grade de Docteur ès Sciences

par

## Igor TOMIC

Acceptée sur proposition du jury

Prof. A. Vassilopoulos, président du jury  
Prof. K. Beyer, directrice de thèse  
Prof. S. Lagomarsino, rapporteur  
Prof. G. Vasconcelos, rapporteuse  
Prof. B. Stojadinovic, rapporteur

# Acknowledgements

In the first place, I want to thank Prof Katrin Beyer for the supervision that was nothing short of perfect. She has my true admiration for her knowledge, professionalism, and a creative way of thinking and resolving problems. Always on the spot with an advice, resolving obstacles and pointing in the right direction, she made this PhD much smoother than it might have been. From constructively pushing when necessary to lowering the pressure on other occasions when needed, it was a real textbook example of supervision. To conclude, I can only wish that one day when I am a professor myself I would be able to supervise PhD students half as well as was the supervision I had from Prof Beyer.

Second source of inspiration came from Dr Francesco Vanin, who I admire (aside of his brilliant macroelement), for the genuine passion, knowledge, and curiosity on the earthquake engineering and historical masonry. And of course, on very knowledgeable and rational view on the football and football tactics. I learned a lot from him, and I can assure you that if you work in the area of earthquake engineering – you will yet hear a lot about him.

Every perfect mechanism (and EESD is of course not perfect, but very close to that) has some key wheels, which if you would remove – everything would fall apart. This is definitely a role of Yvonne Buehl, who I have to thank for support throughout the years. Most importantly, all the support was always with the smile, no matter how annoying our problems/administrative issues might have been. That is really genuine care for people.

I wish to thank the PhD jury, in the alphabetical order – Prof Lagomarsino, Prof Stojadinović, and Prof Vasconcelos for the efforts they took in evaluating this thesis. Not only it was a privilege to present my work to such a group of international experts, but I truly appreciate their efforts in reading the thesis, and writing very complete evaluations and suggestions which contributed to the quality of the thesis.

Important part of this thesis was made as a part of SERA AIMS projects, so I owe sincere thanks to all the project partners – Prof Penna, Prof Guerrini, Dr Senaldi, Prof DeJong, Prof Malomo, Prof Butenweg, Prof Correia, and Prof Candeias. Their experience, knowledge, and advices were key for successfully performing such a large project.

I was lucky to always have great office-mates, from those in the past: Shenghan, Enio, Arash, to the ones in the present: Haris with whom I share passion for endless historical/philosophical debates, with which we bother the very patient Qianqing.

I also consider myself very lucky that during these four years the border between colleagues

## Acknowledgements

---

and friends was very loose. I want to thank without a particular order: Mahmoud with whom I shared the talent for making bad decisions; Amir to whom I probably still owe several burgers; Paolo and Giuseppe that I meet around the word all the time; running companions Michele and Aaron; Ivana with whom I always shared a passion for historical buildings; Mathias whose help with thesis I greatly appreciate; Maradona Ernesto; wise Savvas, the artistic soul Andrea; my favorite master student Samuel; a very deep person Nastaran; Danilo; Bastian, Bryan; Pierino; Ketson; Hnat; Georgios; Alireza; Maria Pia; and Armin.

I have to thank also other EPFL members: Selin, the best cook in the corridor, and three unique personalities – Lucas, William, and Stelios, with whom I shared many great moments and adventures. Speaking of which, it is hard to not thank the friends from The Explorers Club – Marcelo and Daniel for introducing me to this great group of people. The two Croatians I met in Lausanne, Ivan and Pavo, definitely played a positive role in my life in Lausanne.

Special thanks have to be given to Toni, meeting whom would be a reason enough to consider moving to Switzerland as worth it. In the four years, we shared many “ups”, and very few “downs”. From intellectual discussions and February lake swims, to less intellectual things, but listing all of them would require a book of its own.

I wish to thank Catherine for the French translation, and more importantly, for re-adding a sparkle of magic in my life when least expected.

Even if the reason why we met is all but a happy one, thanks to the 2020 Croatia earthquakes I consider myself really happy to have met, first of all – very good friends – and then secondary incredibly dedicated experts who held everything on their back – Josip, Mario, Marta, Marija, Petra, Maja, Jakov, Ante, Romano. Time spent together in Zagreb and Lausanne (even if most dangerous for my PhD, especially when they would start to tell Croatian jokes) was an example of combining useful with pleasant, and hopefully a start of large projects.

At the same time I must not forget the support I always had from the professor back in my home university in Split – Prof Željana Nikolić, Dr Mijo Nikolić, and Prof Boris Trogrlić.

I have to thank all the friends that came to visit me in a very expensive Switzerland, some even a few times - Dominik, Marča, Joke, Željana, Radanović, Taraš, Jurić, Peović, Teo, Ines, Jurašin, Jole, Laus, Dinko, Alejandro, Kostas, Robert, Cristofer. I should not forget Jakov, the main strategist/advisor on working style and strategies, even if I ignored his advices on deleting all social networks for better concentration.

For the very end I left the most important. The ones who are the true co-owners of this thesis – my family sorted by age: Boris, Srđana, Ivan, and Mira. They were an incredible support during the last four years, as during my whole life. At least equal thanks are due to my grandparents – Srećko and Mira, teachers by profession, who dedicated later part of their lives to raising my siblings and me. They are probably the main ones to blame for me receiving the PhD title. I am also very thankful to my other grandparents – Josip and Jermina for all the love and support. If I forgot someone, you will hopefully understand that I am writing all of this while running a bit late as usual...

*Lausanne, December 2022*

*Igor Tomić*

# Preface

The seismic response of historical masonry buildings is difficult to predict due to multiple uncertainties related to material properties, structural details, existing damage, and previous interventions and alterations. Furthermore, in city centres, these buildings are often not free standing but form aggregates of several buildings. Predicting the seismic response of buildings that are part of aggregates is complicated by the interactions between adjacent units. This includes, for example, opening of the joints and pounding.

Researchers and practitioners alike usually resort to modelling the units of an aggregate either as isolated or as fully connected. This is mainly caused by the lack of experimental data and the lack of systematic studies on how the modelling assumptions with regard to the unit-to-unit interface influence the seismic response of buildings within aggregates.

Igor Tomić's PhD thesis enhances the understanding of masonry aggregates and provides publicly available experimental data and numerical tools for predicting the seismic response of unreinforced masonry buildings and aggregates. The work extends beyond the aggregates, by looking into general uncertainties and the importance of modelling connections between structural elements, providing a contribution to the field of earthquake engineering of historical masonry buildings.

Igor performed the only second shake table test worldwide on a large-scale aggregate, which was at the same time the first to apply bidirectional excitation and the first to capture significant pounding between the units. Before the shake table test, Igor organised a blind prediction competition, in which twelve groups from academia and industry participated. This blind prediction competitions is the first to address a building developing both in-plane and out-of-plane damage mechanisms, the first to use bi-directional excitation, and the first on a masonry aggregate. The scatter between the predictions highlights the importance of Igor's work. It also helped us to gain a better understanding of important modelling choices and material parameter selection. In order to improve the simulation of the aggregate behaviour, Igor implemented a new material model into OpenSEES, which is able to simulate the interaction between the units when these are modelled using the equivalent frame approach. Igor made all experimental data openly available and the research groups that performed post-dictions of the shake table test have already used this data set, which shows that it is well documented and easy to use.



Igor's numerical modelling work addressed modelling uncertainties for historical masonry buildings. He shows that certain modelling assumptions might lead to a safe conclusion with regard to the peak ground acceleration for which a certain limit state is reached, but such assumptions might also predict a wrong damage mechanism. This can be dangerous as retrofit interventions might target incorrect mechanisms. As part of this work, it emerged that modelling assumptions with regard to the floor-to-wall connections have a significant impact on the predicted failure mode as they often determine whether the predicted failure mode is an out-of-plane or an in-plane failure mode. In the last part of this thesis, Igor looks more in detail into this particular connection. He shows that for masonry buildings where the floor beams are simply supported on the walls, modelling this connection as rigid – which was the state-of-the-art - can constitute an unrealistic modelling assumption which overestimates the box-behaviour. He also shows through analysis that retrofitting this connection can be often a rather effective, non-invasive, and economical first intervention.

The shake table test on the masonry aggregate was part of the SERA-AIMS project, which was led by our research group and co-led by Prof. Andrea Penna (University of Pavia, Italy), Prof. C. Butenweg (RWTH Aachen, Germany) and Prof. M. DeJong (University of California Berkeley, United States). The test was carried out at the Laboratório Nacional de Engenharia Civil, under the leadership of Dr Antonio Correia. The test was financed through the European Union's Horizon 2020 research and innovation programme under grant agreement No 730900. I would like to thank all project partners for their active engagement. I would also like to thank the thesis committee for their helpful and insightful comments and the discussion. Members of the thesis committee were: Prof Sergio Lagomarsino (University of Genoa, Italy), Prof Božidar Stojadinović (ETH Zurich, Switzerland), and Prof Graça Vasconcelos (University of Minho, Guimaraes).

*Prof. Dr. Katrin Beyer*

*Earthquake Engineering and Structural Dynamics Laboratory, EPFL*

*Ecublens, December 2022*



# Abstract

The seismic analysis of existing unreinforced masonry buildings is a challenging task, troubled by different sources of material and modelling uncertainties. The historical heritage value of a building can further complicate the assessment and design of retrofit interventions as any kind of intervention needs to respect limits imposed from the conservational perspective. At the same time earthquakes worldwide keep causing unacceptable losses and damages, reminding us about the sensitivity of this building typology to the seismic loading.

Across historical city centres of Europe, masonry buildings are often part of building aggregates, which developed when the layout of the city or village was densified. In these aggregates, adjacent buildings can share structural walls to support floors and roofs. Meanwhile, the masonry walls of the façades of adjacent buildings are often connected by dry joints since adjacent buildings were constructed at different times. Observations after, for example, the Central Italy and Croatia earthquakes showed that the joints between the building units were often the first elements to be damaged. It is hypothesised that, due to the lacking interlock, the joints opened up leading to pounding between the building units and a complicated interaction at floor and roof beam supports. The analysis of such building aggregates is very challenging and modelling guidelines are missing. Advances in the development of analysis methods have been impeded by the lack of experimental data on the seismic response of such aggregates. This leads to such buildings often modelled as separated or fully connected.

The first part of this thesis is concentrated on enhancing the understanding of the seismic behaviour of such aggregates. By testing a large-scale unreinforced stone masonry aggregate, consisting of two units, the necessary experimental data was generated and confirmed the hypotheses about significant interaction at the interface between the units. It was the second experimental campaign on a masonry aggregate in the literature, and the first to apply bidirectional loading, have no interlocking at the interface and capture the relative displacements in both the longitudinal and transversal directions. A blind prediction competition accompanying the experimental campaign was organized with participants coming from both the industry and academia. This was among the only very few (to our knowledge three) blind prediction competitions on the seismic behaviour of unreinforced masonry buildings (i) the first to address a building developing in-plane and out-of-plane failure modes, (ii) the first that used bi-directional shaking as input and (iii) the first on a masonry aggregate.

Modelling approaches among the blind prediction participants were well distributed with regard to the level of detail and modelling assumptions. The scatter between the predictions was very large, although all the participants were given detailed information on the material properties including the results of cyclic shear-compression tests. It can therefore be assumed that the scatter can be largely attributed to the modelling uncertainties. We participated with an equivalent frame model in the blind prediction competition. To model the interaction between units of an aggregate using the equivalent frame approach, a new material model was developed and implemented in OpenSEES, coupling normal and shear behaviour, and allowing us to model interaction in terms of separation, pounding, and shear - first such material model within the equivalent frame approach.

Recent advances in macroelement modelling using the equivalent frame approach have enabled to simultaneously model both the in-plane and out-of-plane behaviour. It opened new research questions with regard to the uncertainties affecting the fragility of buildings and the type of damage mechanisms and their location. It showed that nonlinear connections between structural elements play a more important role for out-of-plane behaviour than in the case of in-plane analysis only. Floor-to-wall connections have been shown to play an important role and their retrofitting, paired with subsequent stiffening of floor diaphragms, can be an effective means of intervention, which is often compatible with requirements by conservation scientists.

**Keywords:** historical masonry, masonry aggregates, seismic performance, shake table test, blind prediction competition, equivalent frame models, uncertainty analysis, flexible diaphragms

# Résumé

L'analyse sismique des bâtiments existants en maçonnerie non renforcée est une tâche difficile, troublée par différentes sources d'incertitudes liées aux matériaux et à la modélisation. La valeur du patrimoine historique d'un bâtiment peut compliquer davantage l'évaluation et la conception des interventions de modernisation, car tout type d'intervention doit respecter les limites imposées vis-à-vis de leur conservation. En même temps, les tremblements de terre dans le monde entier continuent à causer des pertes et des dommages inacceptables, ce qui nous rappelle la sensibilité de cette typologie de bâtiment à la charge sismique.

Dans les centres-villes historiques d'Europe, les bâtiments en maçonnerie font souvent partie d'groupements de bâtiments, qui se sont développés lorsque le plan de la ville ou du village a été densifié. Dans ces groupements, les bâtiments adjacents peuvent partager des murs structurels pour soutenir les planchers et les toits. Parallèlement, les murs de maçonnerie des façades des bâtiments adjacents sont souvent reliés par des joints secs puisque les bâtiments adjacents ont été construits à des époques différentes. Par exemple, les observations faites après les tremblements de terre en Italie centrale et en Croatie ont montré que les joints entre les unités de construction étaient souvent les premiers éléments à être endommagés. Nous supposons qu'en raison du manque de verrouillage, les joints se sont ouverts, ce qui a entraîné un martèlement entre les unités de construction et une interaction complexe au niveau des appuis des poutres de plancher et de toit. L'analyse de tels groupements de construction est très difficile et les directives de modélisation sont manquantes. Les progrès dans le développement des méthodes d'analyse ont été entravés par le manque de données expérimentales sur la réponse sismique de ces groupements. De ce fait, ces bâtiments sont souvent modélisés comme étant séparés ou entièrement connectés.

La première partie de cette thèse est concentrée sur l'amélioration de la compréhension du comportement sismique de tels groupements. En testant un groupement de maçonnerie en pierre non renforcé à grande échelle, composé de deux unités, les données expérimentales nécessaires ont été générées et ont confirmé les hypothèses sur une interaction significative à l'interface des unités. Il s'agissait de la deuxième campagne expérimentale sur un groupement de maçonnerie dans la littérature, et la première à appliquer une charge bidirectionnelle, sans avoir d'emboîtement à l'interface et à capturer l'interaction à l'interface des deux directions longitudinale et transversale. Un concours de prédiction en aveugle accompagnant la

campagne expérimentale a été organisée avec des participants issus de l'industrie et du monde universitaire. Il s'agissait de l'un des très rares concours de prédiction en aveugle (trois à notre connaissance) sur le comportement sismique des bâtiments en maçonnerie non renforcée et (i) le premier à porter sur un bâtiment développant des modes de défaillance dans le plan et hors du plan, (ii) le premier à utiliser des secousses bidirectionnelles comme entrée et (iii) le premier sur un regroupement de maçonnerie. Les approches de modélisation parmi les participants aux prédictions en aveugle étaient bien réparties en ce qui concerne le niveau de détail et les hypothèses de modélisation. La dispersion entre les prédictions était flagrante, même si tous les participants avaient reçu des informations détaillées sur les propriétés des matériaux, y compris les résultats des essais cycliques de cisaillement-compression. Nous supposons ainsi, que la dispersion peut être largement attribuée aux incertitudes de la modélisation. Nous avons participé au concours de prédiction en aveugle avec un modèle de cadre équivalent. Pour modéliser l'interaction entre les unités d'un regroupement en utilisant l'approche du cadre équivalent, un nouveau modèle de matériau a été développé et implémenté dans OpenSEES, couplant le comportement normal et de cisaillement, et nous permettant de modéliser l'interaction en termes de séparation, de martèlement et de cisaillement - premier modèle de matériau de ce type dans l'approche du cadre équivalent.

Les progrès récents dans la modélisation des macroéléments utilisant l'approche du cadre équivalent ont permis de modéliser simultanément le comportement dans le plan et hors du plan. Cela a ouvert de nouvelles questions de recherche en ce qui concerne les incertitudes affectant la fragilité des bâtiments et le type de mécanismes de dommages et leur localisation. Elle a montré que les connexions non linéaires entre les éléments structurels jouent un rôle plus important pour le comportement hors du plan que dans le cas d'une analyse dans le plan uniquement. Il a été démontré que les connexions sol-mur jouent un rôle important et que leur mise à niveau, associée à un raidissement ultérieur des diaphragmes de plancher, peut être un moyen d'intervention efficace, souvent compatible avec les exigences des scientifiques de la conservation.

**Mots clés :** maçonnerie historique, regroupements de maçonnerie, performance sismique, essai sur table vibrante, concours de prédiction en aveugle, modèles de cadres équivalents, analyse d'incertitude, diaphragmes flexibles

# Contents

## Acknowledgements

<b>Preface</b>	<b>ii</b>
----------------	-----------

<b>Abstract (English/Français)</b>	<b>v</b>
------------------------------------	----------

<b>List of figures</b>	<b>xiii</b>
------------------------	-------------

<b>List of tables</b>	<b>xxi</b>
-----------------------	------------

<b>1 Introduction</b>	<b>1</b>
-----------------------	----------

1.1 Background and problem statement . . . . .	1
1.2 Objectives and scope of the study . . . . .	4
1.3 Arrangement of the thesis . . . . .	6

<b>2 Shake table testing of a half-scale stone masonry aggregate</b>	<b>9</b>
--	----------

2.1 Introduction . . . . .	10
2.2 Specimen description . . . . .	13
2.2.1 Masonry properties . . . . .	15
2.2.2 Interface between the units . . . . .	18
2.2.3 Floor structures . . . . .	18
2.2.4 Strengthening . . . . .	19
2.2.5 Masses . . . . .	19
2.3 Seismic input and loading sequence . . . . .	20
2.4 Instrumentation . . . . .	23
2.5 Results . . . . .	24
2.5.1 Damage mechanisms and crack maps . . . . .	25
2.5.2 Interface behaviour . . . . .	31
2.5.3 In-plane responses of facades . . . . .	33
2.5.4 Force-displacement hysteretic response . . . . .	36
2.6 Conclusions . . . . .	40
2.7 Data availability . . . . .	41
2.8 Acknowledgments . . . . .	41
2.9 Funding . . . . .	41

<b>3</b>	<b>Shake table testing of a stone masonry building aggregate: Overview of blind prediction study</b>	<b>43</b>
3.1	Introduction . . . . .	44
3.1.1	Review of past blind prediction competitions and software benchmarks	45
3.2	Case study information shared with the participants . . . . .	49
3.2.1	Geometry and material properties . . . . .	50
3.2.2	Earthquake record . . . . .	53
3.3	Blind prediction submissions . . . . .	58
3.3.1	Submitted models . . . . .	58
3.3.2	Statistical evaluation of blind prediction submissions . . . . .	63
3.3.3	Qualitative description of the damage mechanisms . . . . .	74
3.4	Conclusions . . . . .	80
3.5	Data availability . . . . .	83
3.6	Funding . . . . .	83
3.7	Appendix . . . . .	83
<b>4</b>	<b>Shake table test on a historical masonry aggregate - prediction and postdiction using an equivalent frame model</b>	<b>97</b>
4.1	Introduction . . . . .	98
4.1.1	Modelling of masonry aggregates . . . . .	98
4.1.2	Modelling experimental case studies featuring masonry aggregates . . .	100
4.1.3	Large-scale assessment procedures for masonry aggregates . . . . .	101
4.1.4	Uncertainty in modelling historical masonry . . . . .	102
4.1.5	Structure of the paper . . . . .	102
4.2	Modelling approach . . . . .	103
4.2.1	Modelling of the unit-to-unit interface . . . . .	104
4.3	Equivalent frame model of the SERA-AIMS aggregate . . . . .	107
4.3.1	Material and modelling parameters . . . . .	108
4.3.2	Earthquake record . . . . .	112
4.4	Methodology . . . . .	113
4.5	Results - illustrative examples of the impact of interface modelling . . . . .	113
4.6	Discussion of IDA results . . . . .	116
4.7	Post-diction analyses . . . . .	120
4.7.1	Pre-diction with the actual accelerations recorded at the shake-table . .	121
4.7.2	Re-calibration of material properties based on wallette tests . . . . .	124
4.7.3	Post-diction with updated material properties . . . . .	126
4.7.4	Post-diction with updated material properties and secant stiffness proportional damping . . . . .	128
4.8	Conclusion . . . . .	130



## CONTENTS

---

<b>5</b>	<b>Uncertainties in the Seismic Assessment of Historical Masonry Buildings</b>	<b>133</b>
5.1	Introduction . . . . .	134
5.2	Case Studies . . . . .	136
5.2.1	Holsteiner Hof . . . . .	137
5.2.2	Lausanne Malley . . . . .	137
5.2.3	Modelling approach . . . . .	138
5.2.4	Material and modelling parameters . . . . .	139
5.2.5	Earthquake record . . . . .	141
5.3	Methodology . . . . .	142
5.3.1	Seismic Response Parameters . . . . .	143
5.3.2	Failure Criterion . . . . .	143
5.4	Results . . . . .	146
5.4.1	Holsteiner Hof . . . . .	146
5.4.2	Holsteiner Hof-Out-of-Plane Disabled and Rigid Connections . . . . .	150
5.4.3	Lausanne Malley . . . . .	154
5.4.4	Lausanne Malley-Out-of-Plane Disabled and Rigid Connections . . . . .	158
5.5	Discussion . . . . .	162
5.6	Conclusions . . . . .	167
<b>6</b>	<b>Numerical Simulation of Unreinforced Masonry Buildings with Timber Diaphragms</b>	<b>169</b>
6.1	Introduction . . . . .	170
6.2	Equivalent Frame Models for Unreinforced Masonry Buildings with Timber Slabs	173
6.2.1	A Macro-Element for Modelling the in-Plane and out-of-Plane Response of Unreinforced Masonry Piers and Spandrels . . . . .	173
6.2.2	Modelling Assumptions for Masonry Walls and Wall-to-Wall Connections	174
6.2.3	Modelling Assumptions for Timber Floors . . . . .	175
6.2.4	Modelling Assumptions for Wall-to-Diaphragm Connections . . . . .	176
6.2.5	Damping Model for Dynamic Analyses . . . . .	177
6.3	Case-Study Building . . . . .	178
6.3.1	Experimental Campaign . . . . .	178
6.3.2	Numerical Model . . . . .	180
6.3.3	Seismic Excitation . . . . .	182
6.4	Numerical Results for the Case-Study Building . . . . .	184
6.4.1	Model Validation . . . . .	184
6.4.2	Modelling Retrofitting Interventions . . . . .	186
6.4.3	Force Demand on the Wall-to-Diaphragm Connections . . . . .	190
6.5	Conclusions . . . . .	191
6.6	Data availability . . . . .	192
6.7	Acknowledgments . . . . .	192

<b>7 Conclusions and future work</b>	<b>193</b>
7.1 Conclusions . . . . .	193
7.1.1 Shake table testing of a half-scale stone masonry aggregate . . . . .	194
7.1.2 Shake table testing of a stone masonry building aggregate: Overview of blind prediction study . . . . .	195
7.1.3 Uncertainties in modelling the seismic response of historical masonry aggregates: a prediction and postdiction using equivalent frame approach	195
7.1.4 Uncertainties in the seismic assessment of historical masonry buildings	196
7.1.5 Unreinforced masonry buildings with timber diaphragms . . . . .	196
7.2 Future work . . . . .	196
<b>Bibliography</b>	<b>211</b>

# List of Figures

1.1	Examples of (a,b) out-of-plane gable wall failures and (c,d) in-plane damage to internal walls in masonry aggregate buildings in Zagreb after the Croatia 2020 earthquakes. . . . .	2
1.2	Newly developed Macroelement 3D by Vanin et al. (2020a) able to model both the in-plane and out-of-plane behaviour . . . . .	3
1.3	Masonry aggregates damaged after earthquake in the town of Visso . . . . .	4
2.1	a) Example aggregate in Basel, Switzerland; b) Half-scale masonry aggregate tested at the EUCENTRE. . . . .	11
2.2	Unit orientation and facade numbering of the half-scale stone masonry aggregate tested in this study. . . . .	14
2.3	Facade 3 of the half-scale stone masonry aggregate specimen: a) Without plaster, paint, and additional masses; b) Completed test specimen. . . . .	14
2.4	Facade 3 of the half-scale stone masonry aggregate specimen: a) Without plaster, paint, and additional masses; b) Completed test specimen. . . . .	15
2.5	Masonry typology: a-b) Masonry texture; c-d) Construction detail of a corner; e) Horizontal section; f) Detail of a lintel; g-h) Construction detail of a spandrel. . . . .	17
2.6	Interface between the units in the stone masonry aggregate specimen. . . . .	18
2.7	Beam supports at the 1st floor of Unit 2 of the masonry aggregate specimen. . . . .	18
2.8	Details of the strengthening interventions against out-of-plane wall overturning: a) Bearing plate connection on the exterior of the wall; b) Steel angles along the edge beam parallel to the wall; c) Steel angles at the beam supports. . . . .	19
2.9	Processed acceleration time histories of the Montenegro 1979 earthquake recorded at the Ulcinj-Hotel Albatros station, with the scaled time step: a) East-west component and b) North-south component. . . . .	21
2.10	Elastic response spectra of the Montenegro 1979 earthquake recorded at the Ulcinj-Hotel Albatros station for 5% damping ratio, with the scaled period: a) Acceleration and b) Displacement. . . . .	22
2.11	Comparison of response spectra for selected nominal and actual records: a) Test runs 2.1 and 2.1S in the longitudinal y -direction; b) Test run 2.2S in the transverse x-direction. . . . .	23
2.12	Layout of accelerometers. . . . .	24

2.13	Layout of LVDTs, potentiometers and optical devices (excluding LVDTs measuring beam-to-wall relative displacement). . . . .	24
2.14	Crack maps after test runs 1.1, 1.2 and 1.3. black lines mark previously detected damage; blue lines mark damage observed after run 1.1; red lines mark damage observed after run 1.3. . . . .	25
2.15	Crack maps after test run 2.1. black lines mark previously detected damage; red lines mark damage observed after the current test. . . . .	26
2.16	Illustrative deformed shape of Unit 2 for test run 2.1 . . . . .	27
2.17	Damage observed at the end of test run 2.1: a-b) External view of the aggregate; c) Flexural cracking of a 2nd floor spandrel and at the top of a 2nd storey pier of Unit 2; d) Cracking and near-detachment of the top of a 2nd storey corner of Unit 2; e) Flexural cracking of a 1st floor spandrel of Unit 2; f) Slip of a 2nd floor joist of Unit 2; g) Damage at the interface between the units; h) Horizontal crack at the 1st floor level of facade 4 of Unit 2. . . . .	28
2.18	Crack maps after run 2.1S: black lines mark previously detected damage; red lines mark damage observed after the current test. . . . .	29
2.19	Crack maps after run 2.2S: black lines mark previously detected damage; red lines mark damage observed after the current test. . . . .	30
2.20	Illustrative deformed shape of Unit 1 for run 2.2S.. . . .	31
2.21	Position of Optotrak markers on facade 3 used to calculate relative displacements at the interface between the units. . . . .	31
2.22	Openings of the interface joint: a) Peak values in longitudinal (blue) with simultaneous absolute values in transverse (red) directions; b) Peak absolute values in transverse (red) with simultaneous values in longitudinal (blue) directions. . .	32
2.23	Markers used to calculate the in-plane facade elongations. . . . .	34
2.24	Time history of the longitudinal elongation of facade 3 for Units 1 and 2: a) Run 2.1; b) Run 2.1S. . . . .	35
2.25	Time history of the transverse elongation of facade 1 of Unit 1. . . . .	36
2.26	Markers used to calculate global drift ratios: red for Unit 1, blue for Unit 2. . . .	37
2.27	Hysteretic responses in both directions for run 1.3. . . . .	38
2.28	Hysteretic responses in the y-direction for run 2.1. . . . .	39
2.29	Hysteretic responses in the y-direction for run 2.1S. . . . .	39
2.30	Hysteretic responses in the x-direction for run 2.2S. . . . .	39
3.1	Damage to masonry aggregates in Central Italy after the 2016 earthquake. . . .	45
3.2	Case study of the stone masonry aggregate experimental campaign in Tomić et al. (2022a). 3D view, floor plan with beam orientation and facade layout of the two units. . . . .	50
3.2	Case study of the stone masonry aggregate experimental campaign in Tomić et al. (2022a). 3D view, floor plan with beam orientation and facade layout of the two units. . . . .	51

## LIST OF FIGURES

---

3.3	Masonry typology: detail of a corner of Unit 1 of the SERA AIMS aggregate in Tomić et al. (2022a). . . . .	52
3.4	Detail of the interface between the units of the SERA AIMS aggregate in Tomić et al. (2022a). . . . .	53
3.5	Processed acceleration time histories of the Montenegro 1979 earthquake (Albatros station), with the scaled time step for: a) E-W direction; b) N-S direction (Luzi et al., 2016). . . . .	54
3.6	Acceleration response spectra of the Montenegro 1979 earthquake (Albatros station) for a 5% damping ratio with the scaled time step (Luzi et al., 2016). . . . .	54
3.7	Comparison of response spectra for nominal and effective records of Runs 1.1 – 1.3 in the SERA AIMS shake-table test in Tomić et al. (2022a). . . . .	55
3.8	Comparison of response spectra for selected nominal and effective records in the SERA AIMS shake-table test in Tomić et al. (2022a). . . . .	57
3.9	Models submitted to the SERA AIMS blind prediction competition. . . . .	58
3.10	Compared quantities for the blind prediction submissions. Displacements relative to the ground (Rd1-6) and interface opening (Id1-4). . . . .	63
3.11	Statistical representation of the results of the blind prediction submissions in terms of peak roof displacements, interface openings and peak base-shear forces for Runs 1.3, 2.3, 3.3 and 4.3. Blind prediction Run 1.3 is compared with experimental Run 1.3. . . . .	64
3.11	Statistical representation of the results of the blind prediction submissions in terms of peak roof displacements, interface openings and peak base-shear forces for Runs 1.3, 2.3, 3.3 and 4.3. Blind prediction Run 1.3 is compared with experimental Run 1.3. . . . .	65
3.12	Reported Rd2, Rd3, Id3, Id4, BSx, and BSy values for Runs 3.1 and 3.2 from the blind prediction submissions grouped according to the modelling approach, compared with the values from the corresponding experimental runs. The reported CoV value is related to all submissions. . . . .	67
3.13	Reported Rd2, Rd3, Id3, Id4, BSx, and BSy values for Runs 3.1 and 3.2 from the blind prediction submissions grouped according to unit-to-unit connection type, compared with the values from the corresponding experimental runs. The reported CoV value is related to all submissions. . . . .	68
3.13	Reported Rd2, Rd3, Id3, Id4, BSx, and BSy values for Runs 3.1 and 3.2 from the blind prediction submissions grouped according to unit-to-unit connection type, compared with the values from the corresponding experimental runs. The reported CoV value is related to all submissions. . . . .	69
3.14	Reported Rd2, Rd3, Id3, Id4, BSx, and BSy values for Runs 3.1 and 3.2 from the blind prediction submissions grouped according to floor type, compared with the values from the corresponding experimental runs. The reported CoV value is related to all submissions. . . . .	70

3.15	Reported Rd2, Rd3, Id3, Id4, BSx, and BSy values for Runs 3.1 and 3.2 from the blind prediction submissions grouped according to floor-to-wall connection type, compared with the values from the corresponding experimental runs. The reported CoV value is related to all submissions. . . . .	71
3.16	Reported Rd2, Rd3, Id3, Id4, BSx, and BSy values for Runs 3.1 and 3.2 from the blind prediction submissions grouped according to wall-to-wall connection type, compared with the values from the corresponding experimental runs. The reported CoV value is related to all submissions. . . . .	72
3.17	Reported Rd2, Rd3, Id3, Id4, BSx, and BSy values for Runs 3.1 and 3.2 from the blind prediction submissions grouped according to Rayleigh damping ratio, compared with the values from the corresponding experimental runs. The reported CoV value is related to all submissions. . . . .	73
3.18	Illustrative description of damage mechanisms. It should be noted that in-plane damage mechanisms were always illustrated as flexural mechanisms. Actual observed behaviour in the experiment was always flexural, so if a participant reported in-plane shear damage, it was counted as incorrect prediction. . . . .	74
4.1	Definition of the local and basic system of the macroelement for modelling the in-plane and out-of-plane response (Vanin et al., 2020a). . . . .	104
4.2	CohesionFriction3D monotonic behaviour for: a) shear displacement applied in y-direction; b) shear displacement applied in the y-z plane at 45 degrees to the y and z axes direction. . . . .	106
4.3	CohesionFriction3D cyclic behaviour with: a) shear displacement applied in y-direction; b) shear displacement applied in the y-z plane at 45 degrees to the y and z axes direction. . . . .	106
4.4	Illustration of the CohesionFriction3D model for unit-to-unit connections. . . . .	107
4.5	Case study: Floor plan layout of the two units and 3D view of the test unit with the positions of the interfaces. . . . .	108
4.6	Processed acceleration time histories of the Montenegro 1979 earthquake (Albatros station), with the scaled time step in the: a) E-W direction; b) N-S direction (Luzi et al., 2016). . . . .	112
4.7	Modal shapes of the first vibration mode of the four models. . . . .	114
4.8	Hysteretic responses of the four models in y-direction subjected to Montenegro Albatros record with PGA of 0.84 g. . . . .	115
4.9	Failure mechanisms for the four models: a) nD interfaces model; b) 1D interfaces model; c) Separate units model; d) Fully connected units model. . . . .	116
4.10	Comparison of seismic fragility curves for four aggregate modelling approaches. . . . .	117
4.11	Examples of out-of-plane and in-plane failure (nD non-linear interfaces model). . . . .	119
4.12	Compared quantities for the blind prediction submissions. Displacements relative to the ground (Rd1–6) and interface opening (Id1–4). . . . .	121
4.13	Illustrations of principal damage mechanisms observed during the SERA-AIMS experimental campaign (Tomić et al., 2022a). . . . .	122

## LIST OF FIGURES

---

4.14	Maximum recorded flexural drifts for the post-diction analysis with the original model. . . . .	122
4.15	Comparing the original post-diction model with experimental results. . . . .	123
4.16	Maximum recorded flexural drifts for the post-diction analysis performed using the model with parameter set 143 and classical Rayleigh initial stiffness and mass proportional damping. . . . .	126
4.17	Comparing the stochastic response of 21 post-diction models updated with material parameters calibrated according to wallettes experimental results. . .	127
4.18	Damage mechanism for model parameter set 143. . . . .	128
4.19	Comparing the stochastic response of 21 post-diction models updated with secant damping and material parameters calibrated according to wallettes experimental results. . . . .	129
5.1	Example of masonry buildings damaged in recent earthquakes in Italy. . . . .	134
5.2	Definition of the local and basic system of the macroelement for modelling the in-plane and out-of-plane response (Vanin et al., 2020a). . . . .	136
5.3	Holsteiner Hof. (left) Main façade. (right) Numerical model with the coordinate system. . . . .	137
5.4	Lausanne Malley. (left) Main façade. (right) Numerical model with the coordinate system. . . . .	138
5.5	Processed acceleration time-histories of the Montenegro 1979 earthquake. Albatros station records: (up) east-west direction. (down) north-south direction Luzi et al. (2016). . . . .	141
5.6	Acceleration response spectra of the Montenegro 1979 earthquake. Albatros station response spectra: (up) east-west direction. (down) north-south direction Luzi et al. (2016). . . . .	142
5.7	Pier lateral strength and stiffness loss after reaching a collapse drift value. (left) Flexural. (right) Shear. . . . .	144
5.8	Building failure criterion chart describing the procedure to classify the building model as collapsed. OOP, out-of-plane failure; IP, in-plane failure. . . . .	145
5.9	IDA curves for the Holsteiner Hof model for various seismic demand parameters: (a) Total base shear in x-direction. (b) Total base shear in y-direction. (c) Average roof displacement in x-direction. (d) Average roof displacement in y-direction. . . . .	147
5.10	Holsteiner Hof model Spearman correlation matrix for PGA 0.21 g. . . . .	148
5.11	Holsteiner Hof model: (a) Distribution of modal periods. (b) Fragility curve. (c) Correlations between the PGA at failure and input parameters. . . . .	149
5.12	Holsteiner Hof model failure statistics: (a) Type of failure. (b) In-plane type of failure. (c) Failure location. . . . .	150
5.13	Holsteiner Hof model (with out-of-plane disabled and rigid connections) IDA curves displaying the maximum values of seismic demand parameters: (a) Total base shear in x-direction. (b) Total base shear in y-direction. (c) Average roof displacement in x-direction. (d) Average roof displacement in y-direction. . . . .	151

5.14 Holsteiner Hof model (with out-of-plane disabled and rigid connections) Spearman correlation matrix for PGA 0.21 g. . . . .	152
5.15 Holsteiner Hof model with out-of-plane disabled and rigid connections: (a) Distribution of modal periods. (b) Fragility curve. (c) Correlations between PGA at failure and input parameters. . . . .	153
5.16 Holsteiner Hof model (with out-of-plane disabled and rigid connections) failure statistics: (a) In-plane type of failure. (b) Failure location. . . . .	154
5.17 Lausanne Malley model IDA curves for maximum values of seismic demand parameters: (a) Total base shear in x-direction. (b) Total base shear in y-direction. (c) Average roof displacement in x-direction. (d) Average roof displacement in y-direction. . . . .	155
5.18 Lausanne Malley model Spearman correlation matrix for PGA 0.105 g. . . . .	156
5.19 Lausanne Malley model (a) Distribution of modal periods. (b) Fragility curve. (c) Correlations between PGA at failure and input parameters. . . . .	157
5.20 Lausanne Malley model failure statistics: (a) Type of failure. (b) In-plane type of failure. (c) Failure location. . . . .	158
5.21 Lausanne Malley model (with out-of-plane disabled and rigid connections) IDA curves displaying the maximum values of seismic demand parameters: (a) Total base shear in x-direction. (b) Total base shear in y-direction. (c) Average roof displacement in x-direction. (d) Average roof displacement in y-direction. . . . .	159
5.22 Lausanne Malley model (with out-of-plane disabled and rigid connections) Spearman correlation matrix for PGA 0.105 g. . . . .	160
5.23 Lausanne Malley model with out-of-plane disabled and rigid connections: (a) Distribution of modal periods. (b) Fragility curve. (c) Correlations between PGA at failure and input parameters. . . . .	161
5.24 Lausanne Malley model (with out-of-plane disabled and rigid connections) failure statistics: (a) In-plane type of failure. (b) Failure location. . . . .	162
5.25 Holsteiner Hof comparison of IDA curves for models with: (i) out-of-plane enabled and non-linear connections, and (ii) out-of-plane disabled and rigid connections, displaying the maximum values of seismic demand parameters: (a) Total base shear in x-direction. (b) Total base shear in y-direction. (c) Average roof displacement in x-direction. (d) Average roof displacement in y-direction. . . . .	163
5.26 Comparison of Holsteiner Hof fragility curves for models with: (i) out-of-plane enabled and non-linear connections, and (ii) out-of-plane disabled and rigid connections. . . . .	164
5.27 Lausanne Malley comparison of IDA curves models with: (i) out-of-plane enabled and non-linear connections, and (ii) out-of-plane disabled and rigid connections, displaying the maximum values of seismic demand parameters: (a) Total base shear in x-direction. (b) Total base shear in y-direction. (c) Average roof displacement in x-direction. (d) Average roof displacement in y-direction. . . . .	166



## LIST OF FIGURES

---

5.28 Comparison of Lausanne Malley fragility curves for models with: (i) out-of-plane enabled and non-linear connections, and (ii) out-of-plane disabled and rigid connections. . . . .	167
6.1 Examples of out-of-plane damage patterns from L'Aquila 2009 earthquake: (a) Out-of-plane mechanism in long walls. (b) Global overturning of external walls. (c) Overturning due to the lack of anchorage between walls and horizontal diaphragms. (d) Corner out-of-plane mechanism Ortega et al. (2018). (Sources: Dr. Javier Ortega, Prof. Hugo Rodrigues) . . . . .	172
6.2 Macro-element by Vanin et al. (2020a): deformation modes. . . . .	174
6.3 Equivalent frame model of wall-to-wall interface Vanin et al. (2020b) . . . . .	175
6.4 Equivalent frame model of wall-to-diaphragm connection Vanin et al. (2020b). . . . .	177
6.5 Drawings of Pavia Building 1 with the positions of accelerometers: (a) West wall. (b) East wall. (c) North wall. (d) South wall Magenes et al. (2010). . . . .	179
6.6 Building 1 details: (a) masonry wall. (b,c) timber floor. (d,e) timber roof Magenes et al. (2010), Guido Magenes et al. (2014), Senaldi et al. (2014), and Andrea Penna et al. (2016). . . . .	180
6.7 OpenSEES model of Pavia Building 1.: (a) View from the northwest corner. (b) View from the northeast corner. . . . .	181
6.8 . . . . .	183
6.9 Processed acceleration time-histories of the Montenegro 1979 earthquake at the Albatros station: (a) east-west direction. (b) north-south direction Luzi et al. (2016). . . . .	183
6.10 Acceleration response spectra of the Montenegro 1979 earthquake at the Albatros station for 5% damping ratio Luzi et al. (2016) . . . . .	183
6.11 Comparison of experimental and numerical maximum displacements at each run. . . . .	185
6.12 Out-of-plane behaviour (magnification factor $\times 10$ ): (a) North facade-out-of-plane displacement involving the 2nd storey piers and the gable. (b) South facade-out-of-plane displacement involving only the gable. . . . .	186
6.13 IDA curves for the four configurations in terms of PGA vs. the absolute maximum values of average 2nd storey displacement: (a) in the x-direction (b) in the y-direction. . . . .	187
6.14 Deformed shapes and maximum element drifts in flexure and shear (magnification factor $\times 10$ ): (a) Unretrofitted. (b) Diaphragms retrofitted. (c) Connections retrofitted. (d) Both retrofitted. . . . .	189



## List of Tables

2.1	Mortar and masonry mechanical properties of the University of Pavia's (Guerrini et al. 2017; Senaldi et al. 2018) and the SERA-AIMS test specimens. . . . .	16
2.2	Mass breakdown for the masonry aggregate specimen. . . . .	20
2.3	Planned testing sequence. . . . .	22
2.4	Actual testing sequence. . . . .	22
2.5	Maximum, minimum, and residual relative displacements at the interface of the two units. . . . .	33
2.6	Maximum global drift-ratio values for both units in both directions. . . . .	38
3.1	Comparison of blind prediction studies on the seismic response of unreinforced masonry buildings. . . . .	48
3.2	Timeline for the blind prediction competition associated with the SERA AIMS stone masonry aggregate experimental campaign in Tomić et al. (2022a). . . . .	50
3.3	Specimen masses of the units of the SERA AIMS stone masonry aggregate experimental campaign in Tomić et al. (2022a). . . . .	51
3.4	Estimates of the mortar, stone and masonry properties that were distributed to the blind prediction participants before the tests. These values correspond to the properties obtained in the EUCENTRE tests (Guerrini et al., 2017; Senaldi et al., 2018; Senaldi et al., 2019a). . . . .	52
3.5	Nominal SERA AIMS shake-table testing sequence. . . . .	55
3.6	Actual applied testing sequence of the SERA AIMS shake-table test in Tomić et al. (2022a). . . . .	57
3.7	List of experimental results compared with blind predictions by participants to account for differences between nominal and effective shake-table accelerations. . . . .	57
3.8	Modelling assumptions for blind submissions to the SERA AIMS project based on Discrete - Finite Element Models (DEM-FEM). . . . .	59
3.9	Modelling assumptions for blind submissions to the SERA AIMS project based on Finite Element Models (FEM). . . . .	61
3.10	Modelling assumptions for the blind submissions to the SERA AIMS project based on Equivalent Frame Models (EFM). . . . .	62
3.11	Modelling assumptions for the blind submissions to the SERA AIMS based on analytical approach and limit analysis. . . . .	63

3.12 CoV values for predictions grouped using the same model class for Runs 3.1 and 3.2 . . . . .	66
3.13 Damage mechanisms reported by the SERA AIMS blind prediction participants. IP = in-plane mechanism; OOP = out-of-plane mechanism. Correctly predicted mechanisms are indicated with a green circle, incorrectly predicted mechanisms with a red circle and a failure to indicate a correct mechanism with a red x. . . .	75
3.14 Damage mechanisms reported by the SERA AIMS blind prediction participants divided according to modelling approach. IP = in-plane mechanism; OOP = out-of-plane mechanism. Correctly predicted damage mechanisms are marked by filled green circles, and incorrectly predicted mechanisms are marked by filled red circles. . . . .	76
3.15 Damage mechanisms reported by the SERA AIMS blind prediction participants divided according to unit-to-unit connection type. IP = in-plane mechanism; OOP = out-of-plane mechanism. Correctly predicted damage mechanisms are marked by filled green circles, and incorrectly predicted mechanisms are marked by filled red circles. . . . .	77
3.16 Damage mechanisms reported by the SERA AIMS blind prediction participants divided according to floor type. IP = in-plane mechanism; OOP = out-of-plane mechanism. Correctly predicted damage mechanisms are marked by filled green circles, and incorrectly predicted mechanisms are marked by filled red circles. .	78
3.17 Damage mechanisms reported by the SERA AIMS blind prediction participants divided according to floor-to-wall connection type. IP = in-plane mechanism; OOP = out-of-plane mechanism. Correctly predicted damage mechanisms are marked by filled green circles, and incorrectly predicted mechanisms are marked by filled red circles. . . . .	79
3.18 Damage mechanisms reported by the SERA AIMS Blind prediction participants divided with regards to wall-to-wall connection type. IP = in-plane mechanism; OOP = out-of-plane mechanism. Correctly predicted damage mechanisms are marked by filled green circles, and incorrectly predicted mechanisms are marked by filled red circles. . . . .	80
3.19 Submission DEM 1 to SERA AIMS blind prediction competition. Characteristics of the model are taken from the submission form. . . . .	84
3.20 Submission DEM 2 to SERA AIMS blind prediction competition. Characteristics of the model are taken from the submission form. . . . .	84
3.21 Submission DEM 3 to SERA AIMS blind prediction competition. Characteristics of the model are taken from the submission form. . . . .	85
3.22 Submission FEM 1 to SERA AIMS blind prediction competition. Characteristics of the model are taken from the submission form. . . . .	85
3.23 Submission FEM 2 to SERA AIMS blind prediction competition. Characteristics of the model are taken from the submission form. . . . .	86
3.24 Submission FEM 3 to SERA AIMS blind prediction competition. Characteristics of the model are taken from the submission form. . . . .	86

## LIST OF TABLES

---

3.25 Submission FEM 4,5 to SERA AIMS blind prediction competition. Characteristics of the model are taken from the submission form. . . . .	87
3.26 Submission FEM 5 to SERA AIMS blind prediction competition. Characteristics of the model are taken from the submission form. . . . .	87
3.27 Submission EFM 1 to SERA AIMS blind prediction competition. Characteristics of the model are taken from the submission form. . . . .	88
3.28 Submission EFM 2 to SERA AIMS blind prediction competition. Characteristics of the model are taken from the submission form. . . . .	88
3.29 Submission HAC 1 to SERA AIMS blind prediction competition. Characteristics of the model are taken from the submission form. . . . .	89
3.30 Submission LIM 1 to SERA AIMS blind prediction competition. Characteristics of the model are taken from the submission form. . . . .	89
3.31 Submission DEM 1 to SERA AIMS blind prediction competition. Image reporting the damage in the model and damage mechanisms reported by a participant (column 1), and a qualitative comparison with the experimental results (column 2). . . . .	90
3.32 Submission DEM 2 to SERA AIMS blind prediction competition. Image reporting the damage in the model and damage mechanisms reported by a participant (column 1), and a qualitative comparison with the experimental results (column 2). . . . .	90
3.33 Submission DEM 3 to SERA AIMS blind prediction competition. Image reporting the damage in the model and damage mechanisms reported by a participant (column 1), and a qualitative comparison with the experimental results (column 2). . . . .	91
3.34 Submission FEM 1 to SERA AIMS blind prediction competition. Image reporting the damage in the model and damage mechanisms reported by a participant (column 1), and a qualitative comparison with the experimental results (column 2). . . . .	91
3.35 Submission FEM 2 to SERA AIMS blind prediction competition. Image reporting the damage in the model and damage mechanisms reported by a participant (column 1), and a qualitative comparison with the experimental results (column 2). . . . .	92
3.36 Submission FEM 3 to SERA AIMS blind prediction competition. Image reporting the damage in the model and damage mechanisms reported by a participant (column 1), and a qualitative comparison with the experimental results (column 2). . . . .	92
3.37 Submission FEM 4 to SERA AIMS blind prediction competition. Image reporting the damage in the model and damage mechanisms reported by a participant (column 1), and a qualitative comparison with the experimental results (column 2). . . . .	93

3.38 Submission FEM 5 to SERA AIMS blind prediction competition. Image reporting the damage in the model and damage mechanisms reported by a participant (column 1), and a qualitative comparison with the experimental results (column 2). . . . .	93
3.39 Submission FEM 6 to SERA AIMS blind prediction competition. Image reporting the damage in the model and damage mechanisms reported by a participant (column 1), and a qualitative comparison with the experimental results (column 2). . . . .	94
3.40 Submission EFM 1 to SERA AIMS blind prediction competition. Image reporting the damage in the model and damage mechanisms reported by a participant (column 1), and a qualitative comparison with the experimental results (column 2). . . . .	94
3.41 Submission EFM 2 to SERA AIMS blind prediction competition. Image reporting the damage in the model and damage mechanisms reported by a participant (column 1), and a qualitative comparison with the experimental results (column 2). . . . .	95
3.42 Submission HAC 1 to SERA AIMS blind prediction competition. Image reporting the damage in the model and damage mechanisms reported by a participant (column 1), and a qualitative comparison with the experimental results (column 2). . . . .	95
3.43 Submission LIM 1 to SERA AIMS blind prediction competition. Image reporting the damage in the model and damage mechanisms reported by a participant (column 1), and a qualitative comparison with the experimental results (column 2). . . . .	96
4.1 Four different classes of models. . . . .	109
4.2 Distributions of material and modelling parameters. The mean values of parameters with lognormal distribution feature an equivalent normal mean value inside the colon. . . . .	111
4.3 Assumed correlation coefficients between sets of input parameters. . . . .	112
4.4 Modal periods of the four models, depending on the interface model. . . . .	114
4.5 Nominal SERA AIMS shake-table testing sequence. . . . .	120
4.6 Actual applied testing sequence of the SERA AIMS shake-table test in Tomić et al. (2022a). . . . .	121
4.7 Distribution of material and modelling parameters. . . . .	124
4.8 Best stiffness matches for each wallette and overall. The left side shows the material parameter set number, and the right side shows the difference in secant stiffness between the experimental and numerical stiffnesses. . . . .	125
4.9 Chosen material parameter sets. . . . .	125
5.1 Assumed distributions of material and modelling parameters. . . . .	140
5.2 Correlation coefficients between input parameters . . . . .	140

## LIST OF TABLES

---

5.3	List of seismic response parameters for which the maximum absolute values are observed. . . . .	143
5.4	Lausanne Malley: Failure location divided by units, floors and directions. . . . .	145
6.1	Pavia Building 1: Material parameters assumed for masonry elements (Andrea Penna et al., 2016). . . . .	181
6.2	Pavia Building 1: Material parameters of diaphragms and the wall-to-diaphragm connections. . . . .	182
6.3	Building 1: Summary of shake-table runs Magenes et al. (2010). . . . .	182
6.4	Maximum tensile force demands on the anchors of the first storey, second storey, and gable of the model with connections retrofitted for the PGA of 0.63 g. . . . .	190





# 1 Introduction

## 1.1 Background and problem statement

With the passage of time, many historical masonry structures have shown to be vulnerable to seismic actions. These structures represent a heterogeneous category featuring different materials, construction details, existing damages, and previous interventions. Generally, masonry is a composite material characterized by various geometrical configurations and low tensile strength Heyman (1966). Due to very different properties in terms of stiffness, strength and ductility between the masonry units and the mortar, the response is governed by the interaction between the constituents. Early work by Mann et al. (1982), Turnšek and Cacovic (1971), Turnšek (1980) contributed to a deeper understanding of mechanics behind failure modes in masonry elements. Decades later, machine learning algorithms are used for earthquake loss assessment, such as in Stojadinović et al. (2022), but accurate prediction of the seismic response of an individual masonry building remains a significant challenge. Such analyses are the basis for designing retrofit measures, which in the case of heritage structures do not only need to satisfy safety conditions but the interventions must follow principles of minimal intervention, reversibility, authenticity (ICOMOS and Mission, 1994). Research in this field is necessary to better understand masonry behaviour and evaluate seismic risks and possible interventions (Lagomarsino and Serena Cattari, 2015). Events like the 2020 Zagreb earthquake (Atalić et al., 2021), whose effects are shown in Figure 1.1, (un)fortunately remind us that we are far from having closed this topic, and that city centers of Europe and the World are filled with unreinforced masonry buildings and aggregates that are not designed for seismic loads. On the one hand, we need new experimental campaigns to generate data needed to verify and calibrate models and mechanical calculations (Vasconcelos, 2005). On the other hand, improved models are required to predict the performance of historical masonry structures in order to assess the seismic vulnerability and plan effective retrofitting interventions.



Figure 1.1: Examples of (a,b) out-of-plane gable wall failures and (c,d) in-plane damage to internal walls in masonry aggregate buildings in Zagreb after the Croatia 2020 earthquakes.

One of the most widely used modelling approaches for unreinforced masonry buildings is the “equivalent frame approach”, where the facades are split into piers, spandrels and rigid nodes (Quagliarini et al., 2017). Both within the research community and among practitioners, one of the most widely used software is Tremuri with its beam element and macroelement for modelling unreinforced historical masonry. (Lagomarsino et al., 2013; Andrea Penna et al., 2014a). Recently, inspired by Tremuri in-plane model, a new macroelement (shown in Figure 1.2) has been developed at EESD at EPFL by Vanin et al. (2020a) and implemented into OpenSees open-source framework (McKenna et al., 2000). The macroelement is formulated as a one-dimensional element defined by three nodes in three-dimensional space. It consists of three non-linear sections accounting for axial deformation and the non-linear interface for shear response in the central section, where all the shear deformations are lumped. The in-plane shear and flexural response is formulated similar to the macro-element in Tremuri (with small extensions by including 3D fibre sections and various drift capacities laws), whereas the important novelty is the extension to the out-of-plane behaviour. By including a third flexural section at midspan of the element, the macro-element can capture simple one-way bending out-of-plane failure modes. The element is based on a P-delta formulation through second-order Taylor-series expansion of the compatibility equations. Therefore, when combined with interface elements for the wall-to-wall and floor-to-wall connections, it eliminates the need for

separate analysis in order to verify the out-of-plane stability of unreinforced masonry buildings Vanin et al. (2020b). At the same time, these new modelling capacities have generated new research questions. First, because we can switch on and off the out-of-plane option in the macro-element, we can assess the effect of considering or neglecting out-of-plane failures when computing fragility curves of historical unreinforced masonry buildings, which are today often based on the assumption that in-plane mechanisms govern the response (Stefania Degli Abbatì et al., 2022; Siano et al., 2018; Andrea Penna et al., 2016). Second, because out-of-plane mechanisms in historical masonry buildings mostly develop when floor-to-wall and/or wall-to-wall connections have limited strength, it raises the question on how to model such connections.

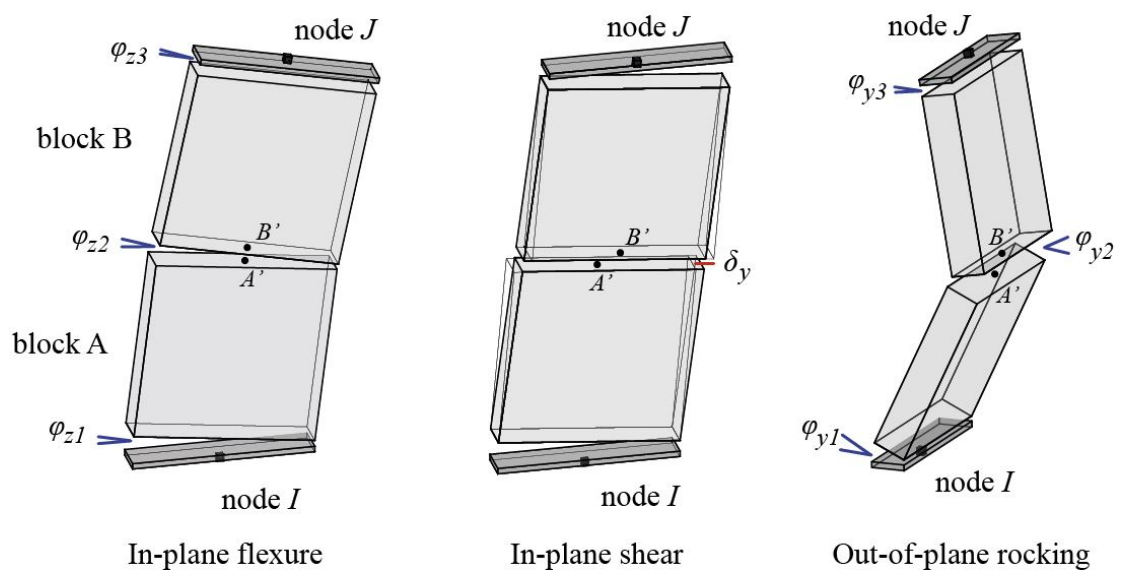


Figure 1.2: Newly developed Macroelement 3D by Vanin et al. (2020a) able to model both the in-plane and out-of-plane behaviour

Recent post-earthquake assessments show that city centers featuring building aggregates are often damaged in earthquakes with clear signs of separation and pounding between the units (Atalić et al., 2021). The historical city centres throughout Europe are often characterized by masonry building aggregates, developed over long spans of time due to economical, practical and safety reasons in the past. Due to the same reasons, they have usually developed without consistent planning or engineering – resulting in various heights, floor levels, materials, stiffnesses, and distributions of openings (Da Porto et al., 2013; Carocci, 2012). In order to save space and resources, units can share a structural wall, with the facades of adjacent buildings often connected by dry joints. As shown by the recent earthquakes in Italy and Croatia, the opening of the joint can lead to very complex behaviour and interaction of the units. An example of damage to aggregates after the earthquakes in North Italy in 2016 is shown in Figure 1.3. However, progress in this area has been impeded by the lack of experimental data, with only one such experimental campaign performed by Senaldi et al. (2019a) and Guerrini

et al. (2019). This is understandable considering the costs and organizational complexity surrounding large test campaigns featuring more than a single building. Due to the lack of experimental data, engineers and scientists alike resort to simplifying the aggregate behaviour by modelling units either as separate, fully connected, or by accounting for aggregate behaviour by one-dimensional linear springs (Senaldi et al., 2010; Antonio Formisano et al., 2015; Antonio Formisano, 2017; Antonio Formisano and Massimilla, 2018; Maio et al., 2015; Malcata et al., 2020). It is sometimes argued that these modelling assumptions lead to conservative approximations in terms of peak ground acceleration required for reaching a certain limit state, but neglecting the interaction between buildings could lead to incorrect predictions of the prevalent damage mechanisms.



Figure 1.3: Masonry aggregates damaged after earthquake in the town of Visso

To summarize, there are several topics and questions that have to be addressed with regard to the seismic response of masonry aggregates in general and their modelling by means of equivalent frame models in particular:

- How does the interaction between units of an aggregate affect the seismic behaviour of units and of an aggregate as a whole?
- Are the present practices of modelling units of an aggregate as fully separated or fully connected sufficiently safe?
- To which extent are material and modelling uncertainties affecting the predicted seismic response of masonry aggregates? On the modelling uncertainty side, how do simplifying assumptions with regard to floor-to-floor, wall-to-wall and unit-to-unit connection as well as neglecting out-of-plane failure mechanisms affect the predicted fragility curves of a building, and the type and location of the damage mechanism?

## 1.2 Objectives and scope of the study

This dissertation aims to enhance the understanding of seismic behaviour of historical masonry buildings, with particular attention paid to masonry aggregates. Due to the previously defined lack of experimental data on the seismic behaviour of masonry aggregates, the first

step is to perform such an experimental campaign and generate data that can be used for the validation and calibration of numerical models. Such a large and complex experimental campaign needs to be meticulously planned, with a-priori numerical analyses run in OpenSees software to finalize the test unit design which satisfies objectives placed upon it, while adhering to the limits imposed by the shake-table capacity. The experimental data should be processed and documented in such a way that it can be shared openly to serve the entire research community. Not to limit the findings to the equivalent frame approach, a blind prediction competition should follow such experimental campaign with participants both from industry and academia. By doing so, I aim to understand what are the uncertainties specific for each modelling assumption, and which are common for all of them. Finally, when it comes to the aggregates, there is space for improvement when it comes to modelling the interaction between units. Therefore, I aim to develop a new 3D material model that will take into account the full interaction at the interface - separation, pounding, and friction, and implement it into OpenSEES.

When it comes to unreinforced masonry buildings in general, a recent new development by Vanin et al. (2020a), building upon the work of Lagomarsino et al. (2013) and Andrea Penna et al. (2014a) has opened up the possibility of predicting not only in-plane but also out-of-plane failure modes using equivalent frame models. This is a new opportunity but at the same time naturally leads to new research questions. I aim at investigating how modelling assumptions with regard to the connections affect the simulation results. I focus in particular on the impact of modelling assumptions with regard to floor-to-wall connections on the building behaviour. This topic is especially relevant for the engineering community, as the retrofitting of connections is often one of the cheapest and least intrusive methods of intervention.

At the same time, it raises questions on uncertainties affecting seismic analyses. The goal is to understand which material and modelling assumptions affect the seismic performance the most. The seismic response refers here not only to the PGA for which a certain limit state is reached but also the damage mechanism that is predicted to form. The potential sensitivity of the predicted damage mechanism to material and modelling uncertainties is especially relevant if the goal of the study is to design a retrofitting intervention.

To summarize, the main objectives of this PhD thesis are:

- To perform a large-scale experimental campaign on an unreinforced masonry aggregate. This comprises test unit design, test planning and preparation, execution, data post-processing, interpretation, and documentation such that the data can be shared publicly.
- To organize a blind prediction competition, featuring participants both from industry and academia to better understand modelling uncertainties that are affecting the simulations of the seismic behaviour of masonry aggregates.
- To develop and implement into OpenSEES a new material model for modelling the interaction between units of an aggregate, taking into account separation, pounding,

and friction.

- To understand the influence of material and modelling uncertainties when modelling historical masonry buildings using equivalent frame models that can capture both in-plane and out-of-plane failure modes. The influence is analysed both on the seismic fragility and the type and location of the damage mechanism.
- To further enhance the understanding of the impact of modelling floor-to-wall connections and their strengthening on the seismic behaviour of buildings - their fragility and formation of damage mechanisms.

### 1.3 Arrangement of the thesis

This work is a compilation of five peer-reviewed or under peer-review papers that were slightly modified. Below is the summary how each chapter addresses the objectives of the study:

- Chapter 2: This chapter presents the experimental campaign on a half-scale stone masonry aggregate. The material properties, masonry typology, construction details and loading sequence are described in detail. The response of the aggregate is described in terms of crack maps and damage mechanisms, force-displacement curves, and special attention is paid to the interface behaviour. The key objective was fulfilled with the signs of pounding, separation, and shear deformation at the interface observed during higher intensity runs, together with the formation of a soft storey mechanism at the upper storey of the higher unit. The mechanism involved an out-of-plane response of the shared wall, with a horizontal crack at the height of the interaction. These findings contribute to a better understanding of the seismic behaviour of masonry aggregates.
- Chapter 3: In this chapter, a blind prediction accompanying the experimental campaign from Chapter 2 is presented. The blind prediction was organized with participants from academia and industry to test modelling approaches and assumptions to learn more about the extent that modelling uncertainty has on modelling masonry aggregates. All participants were provided with the full set of material and geometrical data, construction details, and original seismic input and asked to predict the seismic response in terms of the formed damage mechanisms, roof displacements, interface openings, and base-shear forces. The modelling approaches were well distributed across all levels of complexity, and so were the different modelling assumptions. The results provided a surprisingly large scatter which is further elaborated in the chapter.
- Chapter 4: This chapter features our own prediction and postdiction of the experimental campaign from Chapter 2. The analyses are extended with the uncertainty quantification unrelated to the blind-prediction competition that studies the influence of material and modelling uncertainties both on the fragility of the aggregate and on the damage mechanism type and location. This chapter also presents a newly developed material model which is a step forward for modelling the interaction between units of an aggregate using the equivalent frame approach.

- Chapter 5: This chapter deals with material and modelling uncertainties in the seismic assessment of historical masonry buildings in a more broad sense. The fragility of buildings is analyzed, together with the failure mechanisms and locations. To highlight the influence of the explicit out-of-plane modelling, the fragilities of buildings taking this property into account and not are compared. Special attention is paid to modelling nonlinear connections between structural elements. Even if their properties were not so crucial during in-plane only analyses, in the out-of-plane analyses they prove essential.
- Chapter 6: Having established the importance of non-linear connections, this chapter deals in particular with the floor-to-wall connections. It has been understood for a while that flexible timber diaphragms play a role in seismic behaviour, but connections themselves are still often modelled as rigid. To analyze the effects here we model a case study building in an unretrofitted configuration, with retrofitted diaphragms, retrofitted connections, and both retrofitted. We show that strengthening the diaphragm alone is ineffective when the friction capacity of the wall-to-diaphragm connection is exceeded. This also means that modelling an unstrengthened wall-to-diaphragm connection as having infinite stiffness and strength leads to unrealistic box-type behaviour. This is particularly important if the equivalent frame model should capture both global in-plane and local out-of-plane failure modes.





## 2 Shake table testing of a half-scale stone masonry aggregate

This chapter is a pre-print version of the paper: Tomić I, Penna, A, DeJong, M, Butenweg C, Correia AA, Candeias PX, Senaldi I, Guerrini G, Malomo D, Beyer K (2022a) Shake table testing of a half-scale stone masonry building. Submitted to Bulletin of Earthquake Engineering

The formatting and numbering of equations, tables and figures have been adapted to this document. The contributions of the first author are: test unit design, test preparation, test execution, post-processing, data curation, visualization and writing.

### Abstract

Masonry aggregates have developed throughout city centres of Europe due to a centuries-long densification process that generally lacked consistent planning or engineering. Adjacent units are connected either through interlocking stones or a layer of mortar. Without interlocking stones, the connection between the units is weak, and an out of-phase response of the units can lead to separation and pounding. Modelling guidelines and code instructions are missing for modelling the interaction of such adjacent units because of scarce experimental data. Therefore, in this study an unreinforced stone masonry aggregate was tested on the bidirectional shake table with an incremental seismic protocol as a part of the SERA AIMS – Adjacent Interacting Masonry Structures project. The aggregate was constructed at half-scale with double-leaf undressed stone masonry without interlocking between the units. Floors were built with timber beams and one layer of planks, with different beam span orientation for each unit. After significant damage, one of the units was retrofitted by anchoring the timber beams to the walls to prevent out-of-plane failure and testing was continued. Significant interaction between the units was observed with specific damage mechanisms. Cracking and separation were observed at the interface in both longitudinal and transverse direction, starting at lower intensity runs and progressively increasing. Bidirectional seismic excitation affected the unit separation, with friction forces seemingly playing a role in the transverse direction. Signs of pounding at the interface were observed during higher intensity runs, together with the formation of a soft storey mechanism at the upper storey of the higher unit. The mechanism

involved an out-of-plane response of the shared wall, with a horizontal crack at the height of the interaction. These findings contribute to a better understanding of the seismic behaviour of masonry aggregates.

## 2.1 Introduction

Historical city centres throughout Europe were developed and densified over centuries in the form of building aggregates, where it is common for adjacent buildings (often referred to as structural units) to share the structural walls that are orthogonal to the streets. This densification process often took place without consistent planning or engineering, meaning that adjacent buildings can have different material properties, distribution of openings, and floor and roof heights. Facades of adjacent buildings are connected via interlocking and protruding stones or just through vertical mortar joints. Recent earthquakes in Italy showed that the opening of the joint can lead to pounding between the structural units and to complex interacting behaviour (Carocci, 2012; Da Porto et al., 2013). Therefore, the analysis of masonry building aggregates poses numerous challenges, with no clear or detailed modelling guidelines due to lack of experimental data stemming from the high cost and complexity of performing tests on large-scale aggregates.

Although multiple experimental campaigns were performed on stone masonry buildings (Miha Tomažević et al., 1991a; Magenes et al., 1995; Benedetti et al., 1998; Mazzon et al., 2010; Senaldi et al., 2014; Guido Magenes et al., 2014; Vintzileou et al., 2015), only a single experimental campaign (Senaldi et al., 2020; Guerrini et al., 2019) investigated the interaction between the adjacent buildings in an aggregate. A stone masonry aggregate was designed at the University of Pavia, Italy, to reproduce the features typical for the historical centre of Basel, Switzerland, and was tested on the EUCENTRE shake table in Pavia, Italy both in original and strengthened configurations. The aggregate was composed of two adjacent three-storey units that were weakly connected by interlocking stones. The walls were constructed from double-leaf undressed stone masonry. The floors were composed of timber beams and one layer of planks and were therefore assumed to act as flexible diaphragms in their plane. The floor beams of the adjacent units were at the same level; they were connected to each other by steel elements as part of a possible strengthening solution. The specimen was built to half-scale, and the material properties were scaled accordingly to respect the similitude laws, with detailed material characterizations performed before the test (Senaldi et al., 2018; Guerrini et al., 2017). The specimen is shown in Figure 2.1.



Figure 2.1: a) Example aggregate in Basel, Switzerland; b) Half-scale masonry aggregate tested at the EUCENTRE.

An incremental, unidirectional dynamic test was performed on the original specimen up to the near-collapse state for a peak ground acceleration (PGA) of 0.35 g, and an out-of-plane mechanism formed in both the north and south gables. Portions of the west and east facades also acted as flanges due to good interlocking in the corners. Due to the interlocking stones and connected slab beams, little separation between units was detected: the adjacent piers belonging to different units behaved as one, forming a wide central pier. However, these high-quality connections, ensured by good workmanship on a carefully constructed laboratory specimen, can be updated and extended to represent the wide range of masonry quality found in actual city centres. For instance, units can also be connected by only a vertical layer of mortar without interlocking stones, which can further weaken the aggregate interface. Additionally, floor levels can be at different heights and timber beams of adjacent units cannot be connected. Finally, bidirectional excitation can trigger a more complex response of the aggregate interface.

In the past numerical studies on masonry aggregates, the units were modelled as fully coupled (Senaldi et al., 2010; Antonio Formisano et al., 2015; Antonio Formisano, 2017; Antonio Formisano and Massimilla, 2018; Maio et al., 2015). In some cases, they were also modelled in parallel as fully separated to compare the responses (Senaldi et al., 2010; Antonio Formisano et al., 2015; Antonio Formisano and Massimilla, 2018). In other cases, a part of an aggregate was modelled separately with the rest of the aggregate accounted for through modelling of springs (Antonio Formisano and Massimilla, 2018), rod and foundation elements (Stavroulaki, 2019) or restraints (Malcata et al., 2020). For the large-scale seismic vulnerability assessment of masonry building aggregates, Antonio Formisano et al. (2015) numerically calibrated a procedure derived from the well-known existing vulnerabilities of masonry buildings (Benedetti and Petrini, 1984; Benedetti et al., 1998): this procedure integrated five parameters accounting for the aggregate conditions, which were the presence of adjacent buildings with different heights, the position of the unit in the aggregate, the number of staggered floors, the structural or typological heterogeneity among adjacent structural units, and the different percentages of

opening areas among adjacent facades. Numerical calibration and validation were performed with an equivalent-frame method (EFM) using the software 3Muri (Data, 2008) by subjecting the two case-study aggregates and single units to several pushover analyses. The units were modelled as fully connected.

Different studies reached different conclusions, i.e., Senaldi et al. (2010) concluded that the impact of aggregate behaviour in the transverse direction can be ignored, while Antonio Formisano and Massimilla (2018) came to the same conclusion for the longitudinal direction. However, in all these cases, reference analyses performed on entire masonry aggregates modelled the units of the aggregate as perfectly connected. Modelling fully coupled units leads to wide piers at the interface of the units and overestimates the interface strength and stiffness, especially if built with weak or no interlocking. Conversely, modelling fully separated units can result in either a conservative or nonconservative approximation, depending both on the position of each unit in the aggregate and on the material and geometrical properties of the neighbouring units (Senaldi et al., 2010; Antonio Formisano et al., 2015).

To assess the capability of the EFM to capture the experimental response of masonry aggregates, the University of Pavia's test was modelled by Senaldi et al. (2019b) with the software Tremuri (Lagomarsino et al., 2013), using a macro-element developed by Andrea Penna et al. (2014a). The two units were modelled as fully connected with a continuous wide pier at the interface. Numerical and experimental results were compared in terms of pushover and backbone curves, hysteretic responses, lateral displacement profiles, damage patterns and failure mechanisms. The pushover curve estimated the lateral strength well but overestimated the global stiffness of the aggregate. The dynamic analysis, instead, estimated the hysteretic response well but underestimated the displacement demand. However, the overestimation of the global stiffness was attributed more to the EFM difficulty in reproducing the out-of-plane response, rather than to a perfect connection between the units in the model. In fact, the specimen had interlocking stones across the interface, and the floor beams of adjacent units were at the same level and connected.

This same aggregate was modelled by Vanin et al. (2020a) using a newly developed macro-element (Vanin et al., 2020b) implemented in the OpenSEES software (McKenna et al., 2000). The approach accounted for both in-plane and out-of-plane behaviour and the nonlinearity of floor-to-wall and wall-to-wall connections. The two units were modelled as perfectly connected. After calibrating it based on an experimental campaign, the model satisfactorily predicted the failure mode, displacement, and distribution of drift values in the piers. However, it was highly sensitive to parameters such as damping ratio and floor-to-wall friction coefficient, especially for higher levels of seismic excitation.

The lack of advanced modelling approaches for the interface between the units might be due to the absence of experimental data on their typologies and behaviour. The need for experimental data prompted a joint research programme named SERA AIMS – Adjacent Interacting Masonry Structures, between the École Polytechnique Fédérale de Lausanne

(EPFL), Switzerland; the University of Pavia, Italy; the University of California, Berkeley, USA; the RWTH Aachen University, Germany; and the National Laboratory for Civil Engineering (LNEC), Portugal. To fill the knowledge gaps and contribute to the understanding of the behaviour of masonry building aggregates, a test unit was designed with the assistance of numerical modelling, to meet these goals:

- Induce opening of the interface between the units;
- Aim for a global behaviour sensitive to the interface behaviour (i.e., numerical results are sensitive to the modelling assumptions with regard to the interface between units);
- Modal properties differ between fully connected units (elastic interface for the modal analysis) and isolated units (separate units);
- Avoid premature out-of-plane collapse;
- Fit within the geometrical and payload limitations of the shake table.

The following sections describe the specimen geometry, material properties, construction details, masses, and strengthening interventions. The input ground motion is presented along with the loading sequence. Results are presented in terms of crack maps and damage mechanisms, interface behaviour, in-plane facade elongations, and force-displacement responses. Finally, the data are discussed with the aim of enhancing the understanding of historical masonry aggregates behaviour.

## 2.2 Specimen description

The specimen was constructed as a half-scale stone masonry aggregate consisting of two units. The orientation of the units with respect to the x-y reference system and the labels of the walls are shown in Figure 2.2. Masonry typology and material properties reproduced, as much as possible, those of the aggregate tested by the University of Pavia (Senaldi et al., 2020; Guerrini et al., 2019). The construction sequence replicated that of historical city centres such that Unit 2 was constructed before Unit 1 to ensure no interlocking between the units at any given height.

The main dimensions are shown in Figure 2.3. Unit 1 had a single storey with a height of 2.2 m, while Unit 2 had two storeys with heights of 1.65 m and 1.5 m, respectively, for a total height of 3.15 m. Unit 1 had a U-shaped three-wall layout with plan dimensions of  $2.5 \times 2.45$  m. Unit 2 was rectangular with four walls and plan dimensions of  $2.5 \times 2.5$  m. Unit 1 had a wall thickness of 30 cm, while Unit 2 had wall thicknesses of 35 cm and 25 cm for the first and second storeys, respectively. The thickness of the spandrels was decreased to 15 cm underneath the openings.

To finish the building, a layer of plaster was applied using mortar of class NHL 2.0, without fibres. The plaster thickness depended on the surface roughness and was approximately 15

mm on average. A layer of paint was applied afterwards to make cracks more visible. The specimen is shown in Figure 2.4 before and after application of plaster, paint, and additional masses of Unit 2.

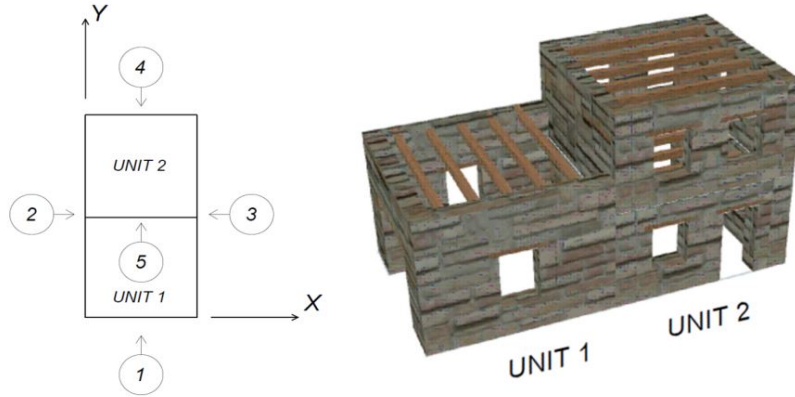


Figure 2.2: Unit orientation and facade numbering of the half-scale stone masonry aggregate tested in this study.

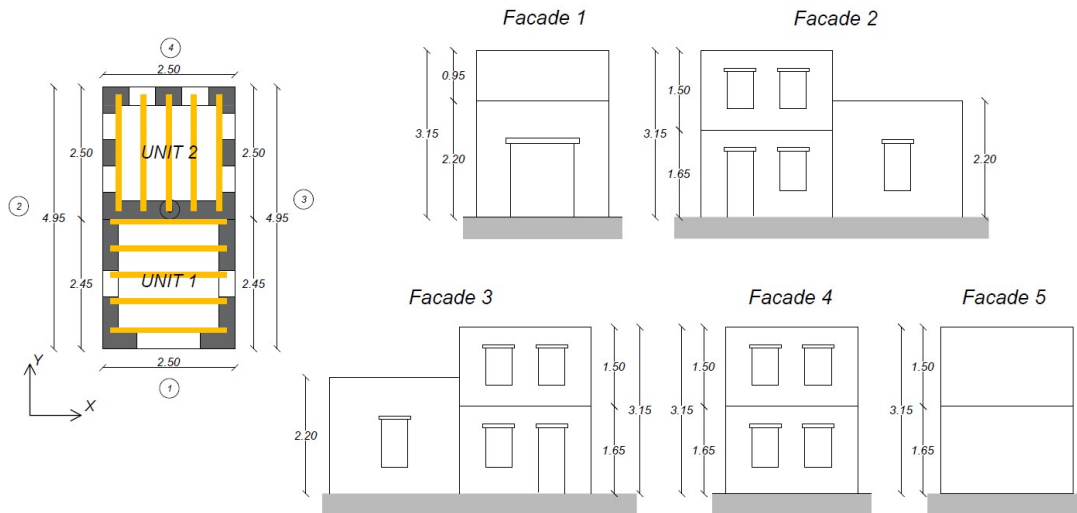


Figure 2.3: Facade 3 of the half-scale stone masonry aggregate specimen: a) Without plaster, paint, and additional masses; b) Completed test specimen.

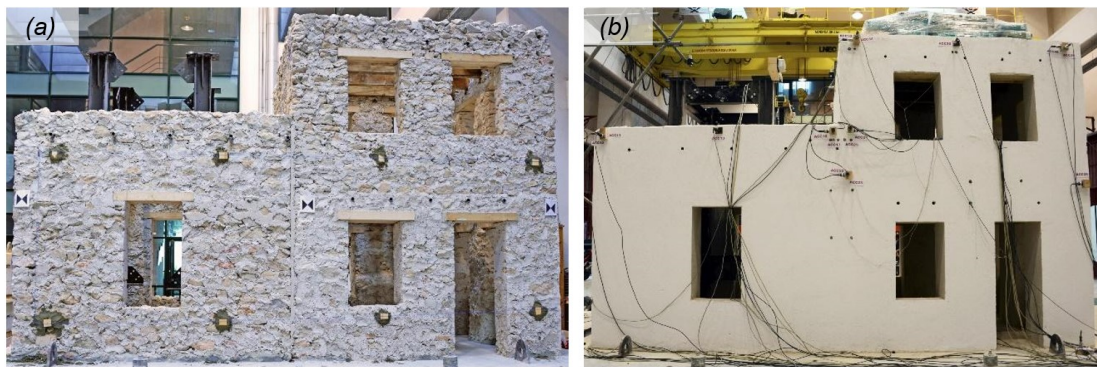


Figure 2.4: Facade 3 of the half-scale stone masonry aggregate specimen: a) Without plaster, paint, and additional masses; b) Completed test specimen.

### 2.2.1 Masonry properties

The maximum payload of the shake table limited construction of the specimen to half-scale. The specimen scale was commonly reduced in previous experimental campaigns to research the seismic response of unreinforced masonry buildings (Miha Tomažević et al., 1991a; Benedetti et al., 1998; Croci et al., 2010; Mazzon et al., 2010; Vintzileou et al., 2015; Mouzakis et al., 2018). However, when conducting a dynamic test on a scaled model, it is necessary to meet similitude relationships to obtain physically sound results (Buckingham, 1914; Krawinkler and Moncarz, 1981; Sullivan et al., 2004; Coutinho et al., 2016). Common similitude relationships, such as Cauchy's or Cauchy-Froude's, were not applicable, as the former requires scaling the gravity acceleration, which was unfeasible, and the latter requires increasing the material density, which increases the specimen weight and was also unviable. Consequently, the scale factors used by Guerrini et al. (2019) and Senaldi et al. (2020) were adopted.

Walls were constructed as double-leaf stone masonry without interlocking between the leaves, except for through stones placed at opening edges and building corners, as shown in Figure 2.5. Stone scraps mixed with mortar filled the voids between the leaves, which amounted to about 10% of the volume. The construction material reproduced the University of Pavia's shake table test as much as possible (Senaldi et al. 2019a; Guerrini et al. 2019), to facilitate numerical model calibrations. Table 2.1 summarises the material properties of the mortar and masonry, with those of the University of Pavia's specimen (Guerrini et al., 2017; Senaldi et al., 2018). Three-point bending, and compression tests were performed on mortar specimens after curing for 28 days. To derive masonry compressive and tensile strength, three vertical and three diagonal compression tests were performed on masonry wallettes, 17 months after their construction and nine months after the shake table test. The shake table test was carried out 8 months after completion of the half-scale aggregate. The delay in material and shake-table testing was due to the pandemic.

Due to differences in stone quarries, it was impossible to exactly replicate the stone type and

shape that had been used for the test in Pavia. Therefore, the specimen was constructed with more irregular stones than those used in Pavia, which increased the irregularity of the masonry texture. The stones ranged in size from 10 to 25 cm and were arranged in approximately horizontal courses. The mortar was a commercial hydraulic lime mix, with EPS spheres added in 2:3 volumetric ratio. The EPS spheres were used to half the stiffness and strength of the masonry material (Crocì et al., 2010; Zheng et al., 2016) thus meeting the adopted similitude law (Senaldi et al., 2020; Guerrini et al., 2019).

Table 2.1: Mortar and masonry mechanical properties of the University of Pavia's (Guerrini et al. 2017; Senaldi et al. 2018) and the SERA-AIMS test specimens.

Value	Univ. of Pavia	SERA-AIMS
Mortar compressive strength $f_c$		
Average [MPa]	1.75	1.28
Coefficient of variation	0.28	0.284
Mortar flexural strength $f_{ct}$		
Average [MPa]	0.60	0.66
Coefficient of variation	0.23	0.200
Masonry compressive strength $f_m$		
Average [MPa]	1.30	1.37
Coefficient of variation	0.026	0.18
Masonry tensile strength $f_t$		
Average [MPa]	0.17	0.21
Coefficient of variation	0.073	0.05
Masonry cohesion $c$		
Average [MPa]	0.23	0.29
Coefficient of variation	0.073	0.05





Figure 2.5: Masonry typology: a-b) Masonry texture; c-d) Construction detail of a corner; e) Horizontal section; f) Detail of a lintel; g-h) Construction detail of a spandrel.



### 2.2.2 Interface between the units

The two structural units constituting the aggregate were connected by mortar alone without interlocking stones. Unit 2 was constructed first as the older unit of the aggregate. The contact surface of Unit 2 was smoothed with a layer of mortar before constructing the adjacent facades of Unit 1, which ensured no interlock between protruding stones between the units. This detail was chosen to facilitate separation during the test and to create a clearly defined boundary condition between the two units. Figure 2.6 shows the interface between the units.



Figure 2.6: Interface between the units in the stone masonry aggregate specimen.

### 2.2.3 Floor structures

Floors were composed of wooden beams with a cross-section of  $8 \times 16$  cm that were simply supported on the masonry walls (Figure 2.7). The beam support length was 20 cm for the 1st storey of Unit 2, and 15 cm for both Unit 1 and the 2nd storey of Unit 2. Unit 1 beams spanned in the transverse direction (x-direction). Unit 2 beams spanned in the longitudinal direction (y-direction; the coordinate system is shown in Figure 2.2). A single layer of 2-cm-thick planks was placed perpendicularly to the beams and connected by two nails at each intersection. PVC tubes were placed in the walls at the end of each beam and along each edge-beam, to be used in a later phase of the test to install precaution against out-of-plane collapse of the walls.

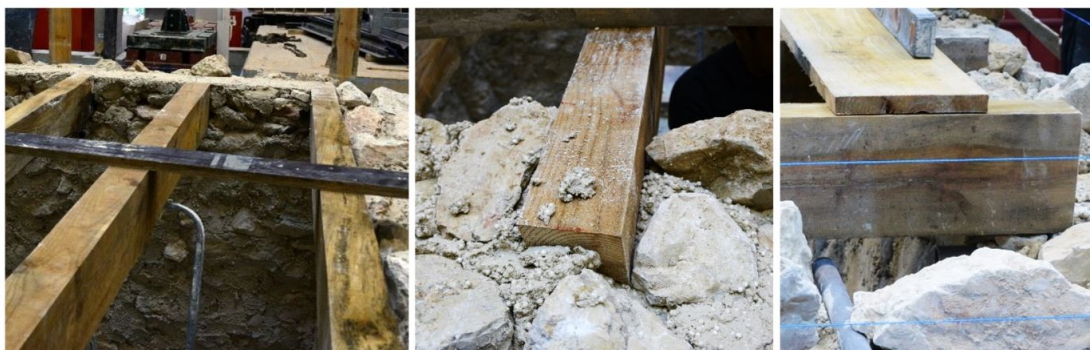


Figure 2.7: Beam supports at the 1st floor of Unit 2 of the masonry aggregate specimen.

### 2.2.4 Strengthening

PVC tubes were placed in the walls of both units, under each beam support and along beams running parallel next to walls, to allow locally strengthening of the structure. Strengthening included steel angles fastened to the beams and steel bearing plates on the wall outer surfaces, connected through the walls by threaded rods inserted within the PVC tubes. The rods were manually post-tensioned. The details of the intervention are shown in Figure 2.8. These improved connections between beams and walls can contrast out-of-plane mechanisms and ensure a box-type behaviour of the building. Strengthening measures were installed after Run 2.1, during which the onset of out-of-plane wall overturning was observed on Unit 2, as shown later in Table 2.4.

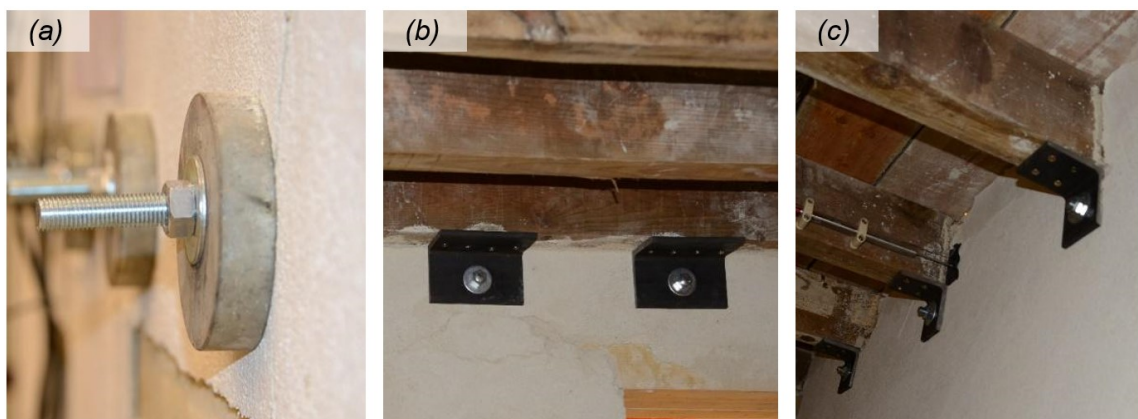


Figure 2.8: Details of the strengthening interventions against out-of-plane wall overturning: a) Bearing plate connection on the exterior of the wall; b) Steel angles along the edge beam parallel to the wall; c) Steel angles at the beam supports.

### 2.2.5 Masses

The total mass of Unit 1 was 7,434 kg. The structural mass of Unit 2 was 13,272 kg; additional 1,500 kg from steel plates and concrete bags were evenly distributed on each floor of Unit 2, bringing its total mass to 16,272 kg. This increased the differences in modal properties between the units without exceeding the payload limits of the shake table. The stiff steel-concrete foundation added 18,000 kg to the total mass of the aggregate, as shown in Table 2.2.

Table 2.2: Mass breakdown for the masonry aggregate specimen.

Component	Mass [kg]
Walls of Unit 1	7,270
Floors of Unit 1	164
<b>Total Unit 1</b>	<b>7,434</b>
Walls of Unit 2	12,937
Floors of Unit 2	335
Additional masses of Unit 2	3,000
<b>Total Unit 2</b>	<b>16,272</b>
Steel-concrete foundation	18,000
<b>TOTAL</b>	<b>41,706</b>

### 2.3 Seismic input and loading sequence

The aggregate specimen was tested under one- and two-component excitations, using the horizontal records of the 1979 Montenegro earthquake from the Ulcinj-Hotel Albatros station (Luzi et al., 2016). These ground motions are plotted in Figure 2.9 as time series and in Figure 2.10 as elastic response spectra, with time and periods scaled according to the similitude law (Senaldi et al., 2020; Guerrini et al., 2019). The east-west component was applied in the longitudinal direction (positive y-direction), and the north-south component in the transverse direction (negative x-direction).

For a structure the size of the AIMS specimen, the shake table capacity was 0.875 g in the longitudinal and 0.62 g in the transverse direction. Four incremental steps were initially planned for the input motions, to reach peak ground accelerations (PGA) of 25%, 50%, 75% and 100% of the shake table capacity in the longitudinal direction, maintaining the original acceleration ratio between the two components. Each step consisted of three stages, i.e., an initial unidirectional test in the longitudinal direction, then a unidirectional test in the transverse direction, and finally a bidirectional test, as shown in Table 2.3. The actual testing sequence comprised ten overall runs, as shown in Table 2.4. To improve the calibration of the shake table, three runs at 12.5% of the table capacity were added at the beginning. Widespread damaged after Run 7 (2.1) required strengthening Unit 2 before resuming. The sequence was interrupted at step 2, with PGA nominally equal to 50% of the table capacity. Intermediate dynamic identification tests were carried out to track the modal properties of the units.

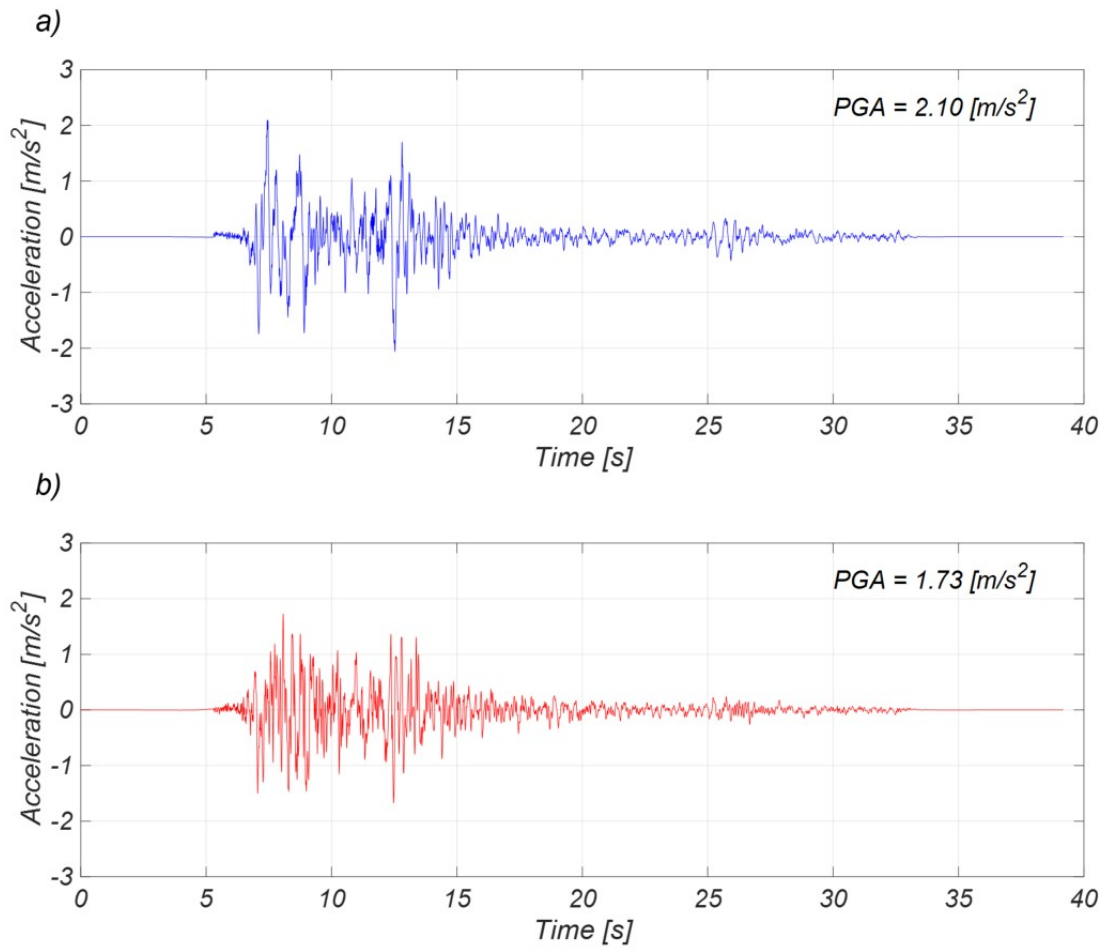


Figure 2.9: Processed acceleration time histories of the Montenegro 1979 earthquake recorded at the Ulcinj-Hotel Albatros station, with the scaled time step: a) East-west component and b) North-south component.

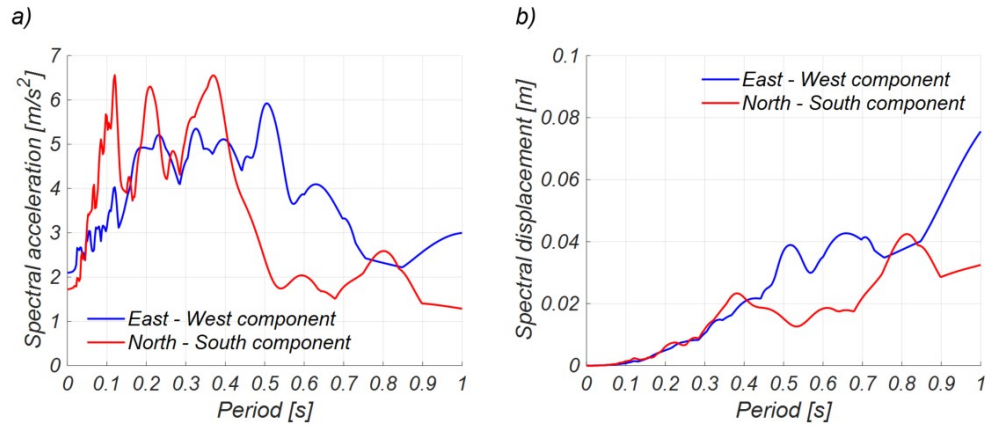


Figure 2.10: Elastic response spectra of the Montenegro 1979 earthquake recorded at the Ulcinj-Hotel Albatros station for 5% damping ratio, with the scaled period: a) Acceleration and b) Displacement.

Table 2.3: Planned testing sequence.

Run ID	Direction	Level of shaking (w.r.t. longitudinal table capacity)	Nominal PGA (direction) [g]
1.1	Longitudinal	25%	0.219 (y)
1.2	Transverse	25%	0.156 (x)
1.3	Bidirectional	25%	0.219 (y); 0.156 (x)
2.1	Longitudinal	50%	0.438 (y)
2.2	Transverse	50%	0.313 (x)
2.3	Bidirectional	50%	0.438 (y); 0.313 (x)
3.1	Longitudinal	75%	0.656 (y)
3.2	Transverse	75%	0.469 (x)
3.3	Bidirectional	75%	0.656 (y); 0.469 (x)
4.1	Longitudinal	100%	0.875 (y)
4.2	Transverse	100%	0.625 (x)
4.3	Bidirectional	100%	0.875 (y); 0.469 (x)

Table 2.4: Actual testing sequence.

Run ID	Direction	Level of shaking (w.r.t. longitudinal table capacity)	Nominal PGA (direction) [g]	Actual PGA (direction) [g]
<b>Unstrengthened specimen</b>				
0.1	Longitudinal	12.5%	0.110	0.113 (y)
0.2	Transverse	12.5%	0.078	0.075 (x)
0.3	Bidirectional	12.5%	0.110 (y); 0.078 (x)	0.114 (y); 0.072 (x)
1.1	Longitudinal	25%	0.219	0.170 (y)
1.2	Transverse	25%	0.156	0.178 (x)
1.3	Bidirectional	25%	0.219 (y); 0.156 (x)	0.208 (y); 0.174 (x)
2.1	Longitudinal	50%	0.438	0.593 (y)
<b>Strengthened specimen</b>				
2.1S	Longitudinal	50%	0.438	0.615 (y)
1.2S	Transverse	25%	0.156	0.258 (x)
2.2S	Transverse	50%	0.313	0.425 (x)



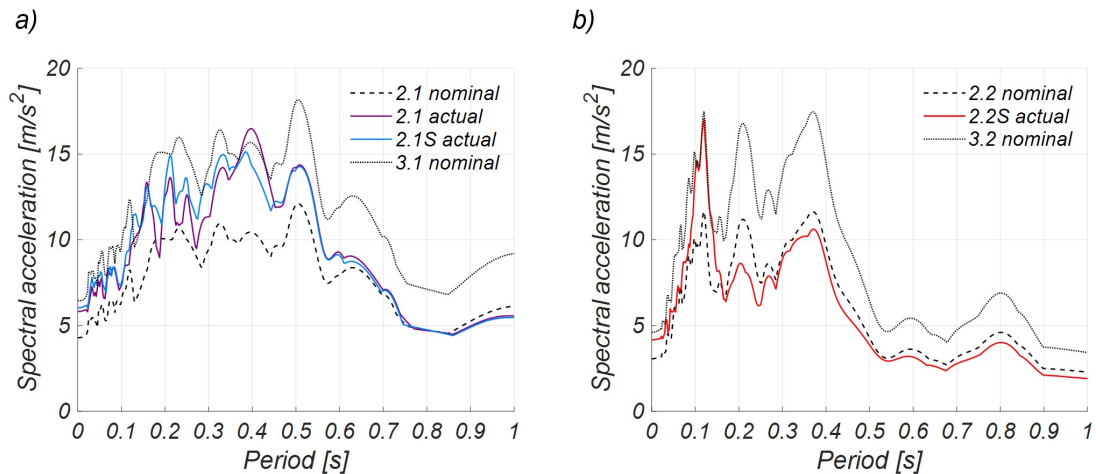


Figure 2.11: Comparison of response spectra for selected nominal and actual records: a) Test runs 2.1 and 2.1S in the longitudinal y -direction; b) Test run 2.2S in the transverse x-direction.

For Run 2.1 and Run 2.1S in y-direction, the target PGA was 0.438 g, but 35% and 40% greater PGAs were applied (0.593 g and 0.615 g). The overshoot in spectral acceleration spanned across the entire period range up to 0.8 s; as a result, for an estimated fundamental period  $T = 0.13$  s, the actual spectrum of Run 2.1 resembled that of nominal Run 3.1 at 75% of the shake table capacity. Actual Run 2.2S in x-direction was also affected by a 35% overshoot in terms of PGA, but the issue was limited to periods shorter than 0.2 s where the response spectrum approached that of nominal Run 2.3. Response spectra for nominal and actual records are compared on Figure 2.11.

## 2.4 Instrumentation

Forty accelerometers recorded the accelerations of the foundation and the in- and out-of-plane accelerations of the masonry walls. The relative displacement of points were monitored with linear variable displacement transducers (LVDTs) and potentiometers; LVDTs were also used to record the relative displacement between wooden beams and masonry walls. Optotrak LED, Krypton, and Hamamatsu optical measurement systems were used to monitor absolute displacements of chosen points; the absolute displacement measures were used to compute the interface opening between the units. The layout of accelerometers is shown in Figure 2.12. The layout of displacement measurements is shown in Figure 2.13.

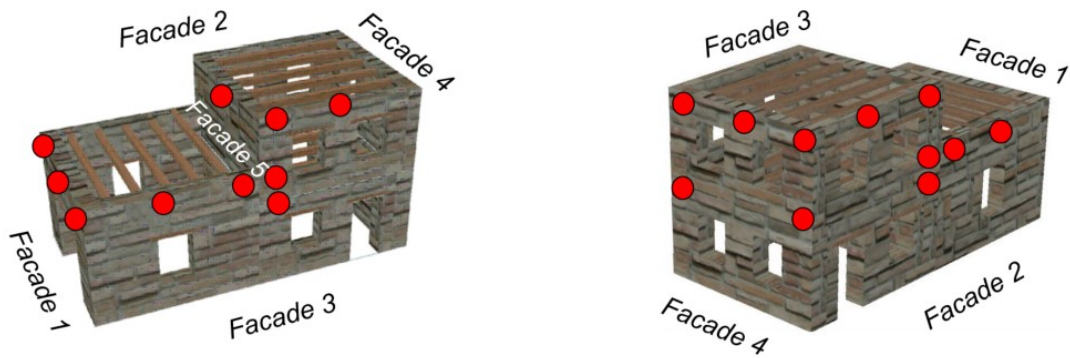


Figure 2.12: Layout of accelerometers.

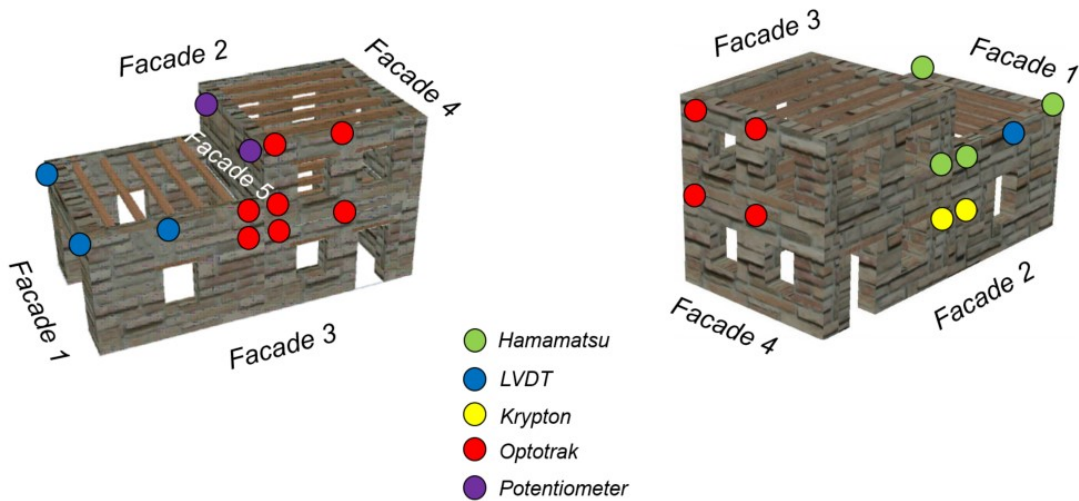


Figure 2.13: Layout of LVDTs, potentiometers and optical devices (excluding LVDTs measuring beam-to-wall relative displacement).

## 2.5 Results

Test results are first evaluated in terms of crack maps and descriptions of underlying damage mechanisms, interpreting the global behaviour of the aggregate. Then, the interface behaviour is studied in terms of opening in the longitudinal and transversal direction. Moreover, in-plane elongations of spandrels are studied to interpret the extent of flexural rocking mechanisms of the facades. Finally, force-displacement responses of both units are shown to describe the hysteretic behaviour.



### 2.5.1 Damage mechanisms and crack maps

The structural damage sustained by the units was surveyed at the end of every test run. Runs 0.1, 0.2, and 0.3 were performed at 12.5% of the shake table capacity for shake-table calibration purposes, and no damage was detected in any part of the aggregate or at the interface. After the following runs, cracks were mapped on the exterior and interior of each facade to obtain the damage pattern evolution. New cracks observed at the end of each run are marked in colour on the figures, while old cracks in black.

Runs 1.1, 1.2, and 1.3 were performed at 25% of the shake table capacity. The crack maps for these runs are shown in Figure 2.14. Blue lines represent damage after run 1.1 (longitudinal run) and red lines represent damage after run 1.3 (bidirectional run). Damage was only detected at the interface between the two units. Optotrak markers placed on both units next to the interface captured the longitudinal and transverse opening of the joint. The maximum opening during run 1.1 was 0.9 mm and 0.2 mm in the longitudinal and transverse directions, respectively. During run 1.3 it was 1.5 mm and 2.7 mm in the same directions, respectively. Signs of minor sliding of the beams above the spandrels at the 2nd storey of Unit 2 were detected after Run 1.3. LVDT data showed that the maximum sliding as well as the residual displacement were 0.1 mm.

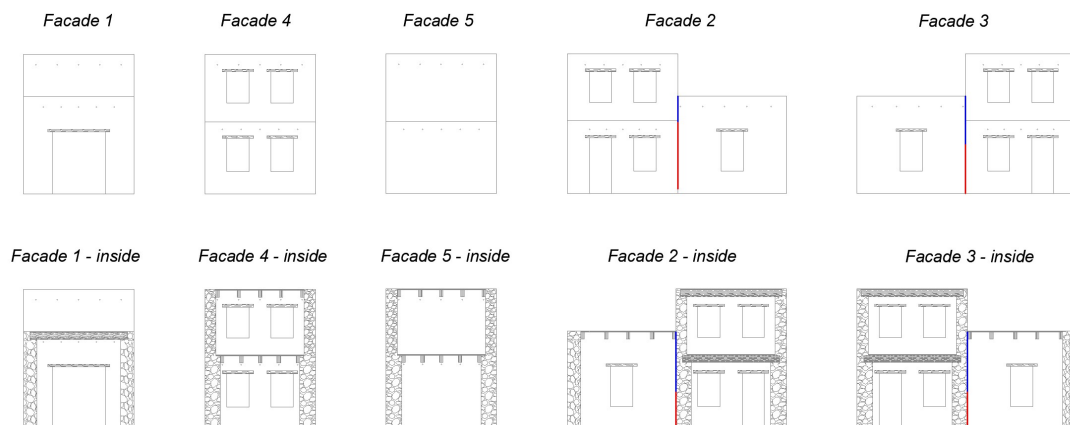


Figure 2.14: Crack maps after test runs 1.1, 1.2 and 1.3. black lines mark previously detected damage; blue lines mark damage observed after run 1.1; red lines mark damage observed after run 1.3.

Run 2.1, which approached nominal run 3.1 for short period oscillators (Figure 2.11), resulted in extensive damage to Unit 2, as shown in the crack maps of Figure 2.15 and on the illustrative mechanism of Figure 2.16. Cracks on the external and internal sides of the walls were predominantly aligned across the thickness of the walls. An in-plane flexural-rocking mechanism fully formed in both facades 2 and 3 at the upper storey of Unit 2. Spandrels and piers suffered extensive flexural cracking, with maximum residual width of 5.0 mm and 1.4 mm, respectively, at the 2nd storey, and of 1.9 mm and 1.2 mm, respectively, at the 1st storey.

Out-of-plane cracks were visible at the 1st floor level of facade 4 with residual width up to 0.6 mm, with extensive cracking of the top spandrels of the same facade. Two out-of-plane horizontal cracks were detected on the partition wall (facade 5), at its bottom and at the level of Unit 1 roof. The cracks at the 1st floor level of Unit 2 on facade 4 and the roof level of Unit 1 on facade 5 confirm the interaction with the adjacent unit in the formation of the damage mechanism. Out-of-plane and in-plane cracks were continuous around corners; in fact, thanks to the interlock between orthogonal walls, the end piers of longitudinal facades acted as webs in the out-of-plane overturning mechanism of the transverse walls (Figure 2.16).

Signs of sliding of the 2nd floor beams of Unit 2 and residual displacement were also detected. LVDT data showed that the maximum sliding was 4.4 mm and 8.8 mm at the supports of the instrumented beam on facades 4 and 5, respectively, while the residual displacement were 4.3 mm and 8.0 mm, respectively.

Significant interaction, separation and pounding occurred at the interface between the structural units. The maximum recorded openings of the joint were 20.7 mm and 0.6 mm in the longitudinal and transverse directions, respectively. Unit 1 was nearly undamaged, apart from a few hairline cracks that spread horizontally from the interface between units. The damage on facades, interface, and beam supports after run 2.1 are shown in Figure 2.17.

Unit 2 was retrofitted due to the widespread damage caused by run 2.1, to prevent out-of-plane collapse especially of facade 4. The strengthening was performed by nailing steel angles to the timber beams, installing threaded rods in the PVC tubes, and fastening them to the steel angles and to steel plates located outside of the walls. Unit 1 instead did not require any strengthening.

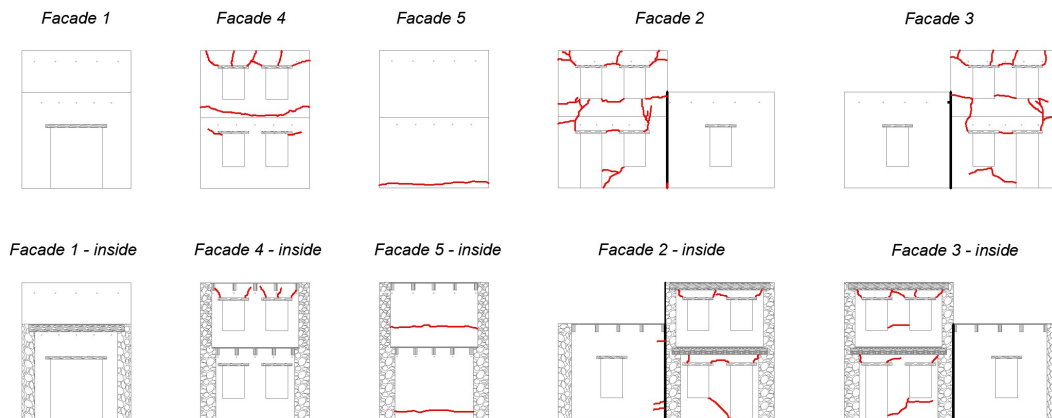


Figure 2.15: Crack maps after test run 2.1. black lines mark previously detected damage; red lines mark damage observed after the current test.

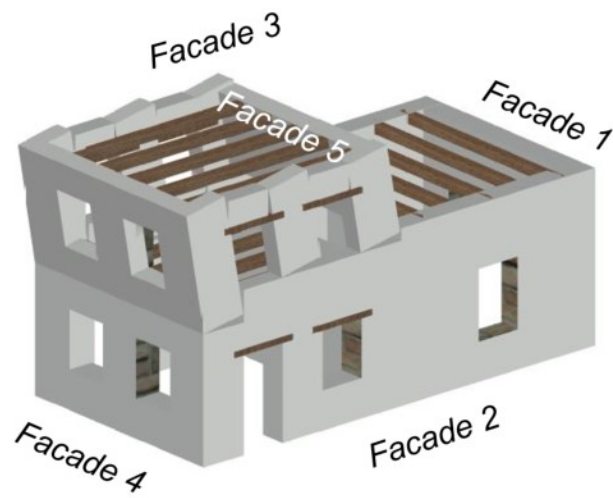


Figure 2.16: Illustrative deformed shape of Unit 2 for test run 2.1



Figure 2.17: Damage observed at the end of test run 2.1: a-b) External view of the aggregate; c) Flexural cracking of a 2nd floor spandrel and at the top of a 2nd storey pier of Unit 2; d) Cracking and near-detachment of the top of a 2nd storey corner of Unit 2; e) Flexural cracking of a 1st floor spandrel of Unit 2; f) Slip of a 2nd floor joist of Unit 2; g) Damage at the interface between the units; h) Horizontal crack at the 1st floor level of facade 4 of Unit 2.

To understand the effect of the strengthening intervention, run 2.1 was repeated in this configuration as run 2.1S. The crack maps for this run are shown in Figure 2.18. Strengthening

prevented out-of-plane failures. After connecting the beams of Unit 2 to the walls, no additional displacement of the beams at their support was expected. However, further sliding was confirmed by the LVDT readings. In fact, the residual displacement of the beams of the 2nd storey of Unit 2 increased to 6.7 mm and 8.6 mm for facades 4 and 5, respectively. This sliding was attributed to the deformation of the masonry, which was already significantly cracked before retrofitting the beam supports.

As cracks in the masonry were not repaired, run 2.1S further amplified the damage mechanism, increasing the width of existing cracks and forming new cracks. Existing cracks at the 2nd storey of Unit 2 increased to a residual width larger than 5.0 mm. A new vertical crack formed inside the partition wall (facade 5) at the centre of the 2nd story, indicating out-of-plane bending. Facade 4 experienced extensive damage at the 1st floor level, with formation of new cracks, widening of old ones, and detachment of portions of plaster. The top corners of the 2nd storey of Unit 2 were severely damaged and almost detached. The 1st storey piers of Unit 2 adjacent to Unit 1 also formed flexural cracks with residual width up to 0.7 mm. Due to interlocking between orthogonal walls, the end piers of the longitudinal facades were still acting as webs in the out-of-plane overturning mechanism of the transverse walls.

Like in the previous run, separation and pounding occurred at the interface between the two units. The maximum recorded openings of the joint were 21.2 mm and 2.0 mm in the longitudinal and transverse directions, respectively.

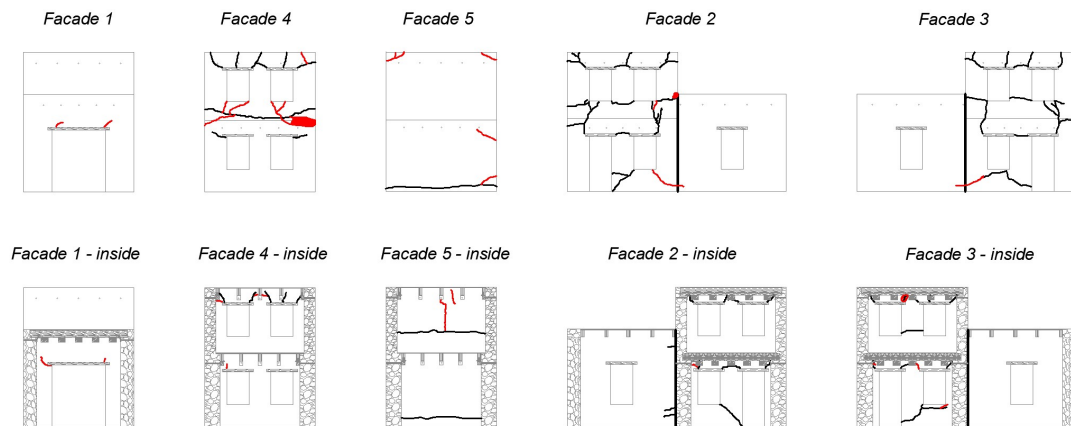


Figure 2.18: Crack maps after run 2.1S: black lines mark previously detected damage; red lines mark damage observed after the current test.

The following run 1.2S was a repetition of run 1.2 (25% of the shake table capacity), to assess the remaining capacity of the specimen in the transverse direction. However, the run produced no further damage to the specimen.

Finally, the specimen was subjected to run 2.2 in the transverse direction, which approached nominal run 3.2 for short period structures, as shown in Figure 2.11. The crack maps for this

run are shown in Figure 2.19. No new cracks or amplification of previous damage was detected in Unit 2. However, in-plane flexural cracking of the spandrels and piers of facade 1 was observed, as Unit 1 developed the damage mechanism illustrated on Figure 2.20. The residual crack width was up to 3.0 mm and 1.0 mm for spandrels and piers of facade1, respectively.

Thin out-of-plane horizontal cracks were observed at the pier bases of facades 2 and 3 in Unit 1. The cracks were continuous around the corners of the building, meaning that the end piers of the transverse facades acted as flanges in the out-of-plane overturning mechanism of the longitudinal walls, thanks to the interlock between orthogonal walls. The maximum residual width of these cracks was 1.0 mm and 0.4 mm for facades 2 and 3, respectively. Indications of beam sliding at the supports were observed and confirmed via LVDT measurements, which showed residual displacements of 1.0 mm and 3.3 mm on facade 2 and facade 3, respectively.

With the failure mechanism now activated in Unit 1, and with Unit 2 suffering widespread damage from the previous runs, the test was concluded to prevent the specimen from collapsing on the shake table.

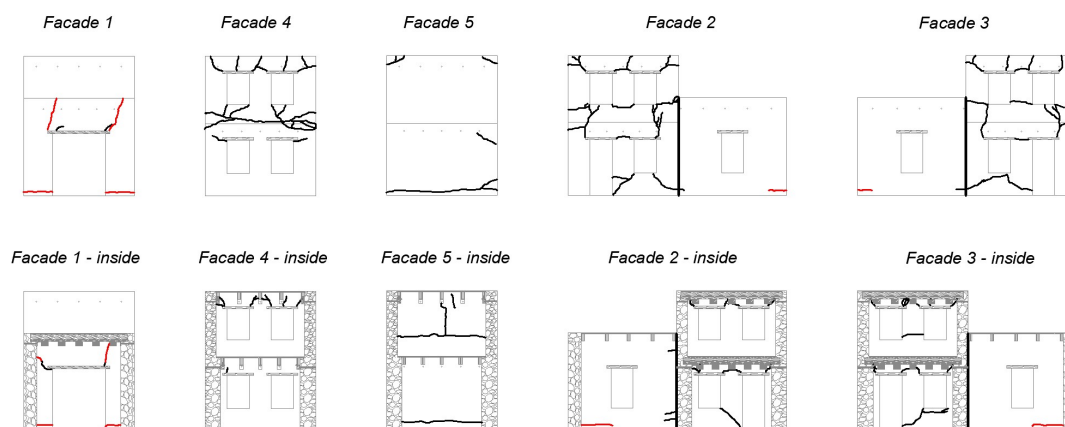


Figure 2.19: Crack maps after run 2.2S: black lines mark previously detected damage; red lines mark damage observed after the current test.



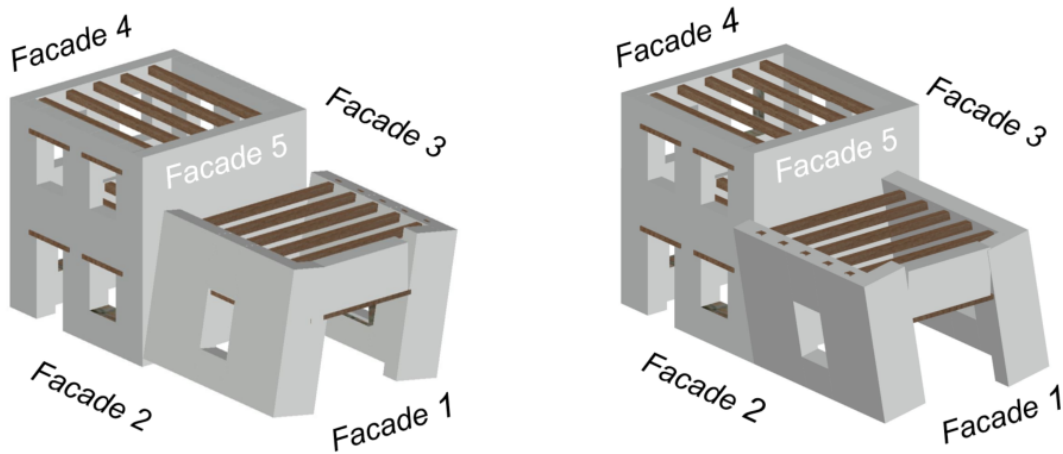


Figure 2.20: Illustrative deformed shape of Unit 1 for run 2.2S..

### 2.5.2 Interface behaviour

The behaviour of the interface between the units of the aggregate was captured using the Optotrak optical device and LED markers, as described in Section 4. The precision of the Optotrak device is under a millimetre, and the recording frequency was set to 200 Hz, which was considered sufficient to capture the effects of dynamic motion. Two markers were placed close to the top of the interface on facade 3, 10 cm away from the dry-joint on each side, as illustrated on Figure 2.21.

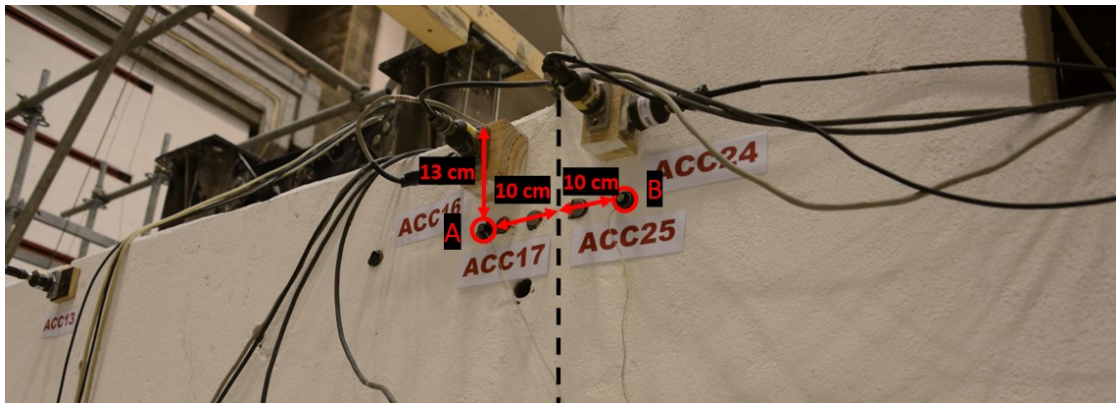


Figure 2.21: Position of Optotrak markers on facade 3 used to calculate relative displacements at the interface between the units.

The longitudinal ( $U_y$ ) and transverse ( $U_x$ ) openings of the interface joint between the units on facade 3 were calculated from the recordings of markers A and B, using Equations 2.1 and 2.2 in the global coordinate system, as defined in Figure 2.2:

$$U_y = \Delta_y^B - \Delta_y^A \quad (2.1)$$

$$U_x = \Delta_x^B - \Delta_x^A \quad (2.2)$$

where  $\Delta_y^i$  and  $\Delta_x^i$  stand for the  $i$ -th marker displacement in the global  $y$ - or  $x$ -direction, respectively. Consequently, a positive sign of the transverse opening implies that the marker on Unit 2 moves more in the global positive  $x$ -direction than the one on Unit 1. A positive value of the longitudinal opening implies separation, and a negative value implies pounding between the units.

Figure 2.22 shows the peak values of interface joint opening in the longitudinal and transverse directions as well as the simultaneous opening of the interface in the other direction. For each maximum absolute value of the transverse opening, the longitudinal opening had always a positive value. This means the units were separated at that instant and there was no frictional force opposing the transverse relative displacement. Bidirectional loading (run 1.3) led to significantly larger maximum absolute transverse displacement than unidirectional loading in the transverse direction (run 1.2).

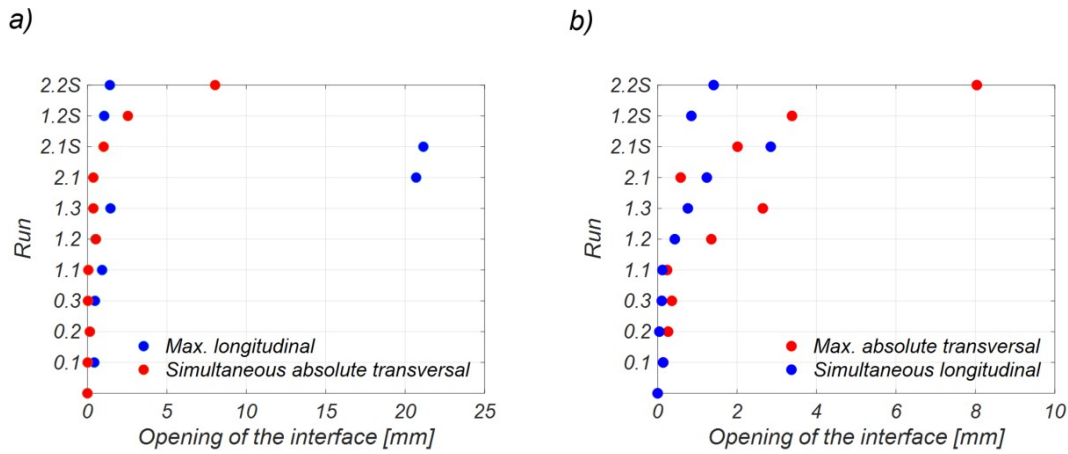


Figure 2.22: Openings of the interface joint: a) Peak values in longitudinal (blue) with simultaneous absolute values in transverse (red) directions; b) Peak absolute values in transverse (red) with simultaneous values in longitudinal (blue) directions.

The maximum values of relative and residual displacements at the interface for each run are shown in Table 2.5. During the bidirectional run 1.3, the maximum longitudinal opening increased up to 1.45 mm, while the maximum positive and negative transverse opening reached 2.33 mm and 2.65 mm, respectively. This indicates the out-of-plane vibration of facades 2 and 3 of Unit 1, which was later confirmed by crack maps and illustrated in Figure 2.20. During the



same run, the negative longitudinal displacement of -0.58 mm at the interface showed that the units were already experiencing pounding.

The longitudinal opening of the interface joint became especially pronounced during run 2.1, when it reached 20.7 mm. During the same run, the largest negative displacement of -1.85 mm indicated significant pounding at the interface. The residual longitudinal displacement after run 2.1 was -0.46 mm, i.e., with the units in contact with each other. Run 2.1 with the strengthened specimen produced similar longitudinal displacement, with the maximum and minimum being 21.2 mm and -1.87 mm, respectively. The residual longitudinal displacement reached 0.31 mm, with the units now separated.

The largest transverse displacement at the interface was observed during run 2.2S with the maximum absolute value of 8.04 mm. After the same run, the residual transverse displacement was -0.94 mm, which was the largest residual value observed on the interface in either direction.

Table 2.5: Maximum, minimum, and residual relative displacements at the interface of the two units.

	Run ID	Longitudinal			Transversal		
		Max [mm]	Min [mm]	Residual [mm]	Max [mm]	Min [mm]	Residual [mm]
Unstrengthened	0.1	0.43	-0.09	0.02	0.12	-0.14	0.04
	0.2	0.15	-0.05	0.02	0.26	-0.26	-0.01
	0.3	0.47	-0.09	0.03	0.36	-0.22	0.02
	1.1	0.92	-0.20	0.1	0.14	-0.24	-0.03
	1.2	0.51	-0.06	0.16	0.87	-1.35	-0.08
	1.3	1.45	-0.58	0.21	2.33	-2.65	-0.13
	2.1	20.69	-1.85	-0.46	0.56	-0.58	-0.07
Strengthened	2.1S	21.15	-1.87	0.31	2.01	-0.41	0.39
	1.2S	1.05	-0.02	0.13	3.28	-3.38	0.14
	2.2S	1.41	-0.02	0.22	5.40	-8.04	-0.94

### 2.5.3 In-plane responses of facades

The three-dimensional optical LED acquisition systems enabled monitoring of the in-plane response of the longitudinal facades. As previously described, a clear flexural-rocking mechanism developed in Unit 2 with extensive cracking of the spandrels and piers. The in-plane horizontal elongation of the facades was calculated as a difference in displacements of the Optotrak markers at two corners of facade 3 for Unit 2. For Unit 1, the elongations were calculated as a difference in displacements of the Optotrak and Hamamatsu markers at the

two corners of facades 1 and 2. Figure 2.23 shows the displacements used to calculate the facade elongations according to Equations 2.3 through 2.6:

$$U_y^1 = \Delta^2 8_y - \Delta_y^4 \quad (2.3)$$

$$U_x^1 = \Delta_x^5 - \Delta_x^2 \quad (2.4)$$

$$U_y^2 1 = \Delta^5 4_y - \Delta^6 0_y \quad (2.5)$$

$$U_y^2 2 = \Delta^5 7_y - \Delta^6 0_y \quad (2.6)$$

where  $U_y^1$  is the longitudinal facade elongation of Unit 1;  $U_y^2 1$  and  $U_y^2 2$  the longitudinal facade elongations of Unit 2 at the 1st and 2nd floor, respectively; and  $U_x^1$  the transverse facade elongation of Unit 1.  $\Delta_y^i$  and  $\Delta_x^i$  are the  $i$ -th marker displacement in the global  $y$ - or  $x$ -direction, respectively.

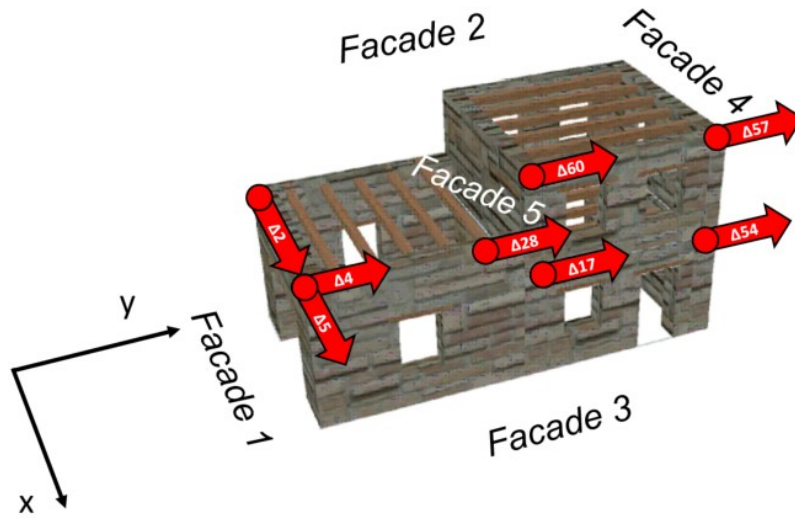


Figure 2.23: Markers used to calculate the in-plane facade elongations.

Figure 2.24(a) presents the recorded time histories of longitudinal elongations for both units in run 2.1, with a PGA of 0.593 g. There were no residual elongations prior to this run in both units. In Unit 2 the elongation was greater at the 2nd storey, compatibly with the out-of-plane tendency of facade 4, that involved the end piers of the longitudinal facade as webs. This resulted in a residual elongation of approximately 26.0 mm. Residual elongations of the 1st

storey of Unit 1 and Unit 2 were approximately 0.3 mm and 5.0 mm, respectively.

Figure 2.24(b) presents the recorded time histories of the longitudinal elongations for both units from run 2.1S, with a PGA of 0.615 g. The floor-to-wall connections of Unit 2 were retrofitted prior to this run, thus limiting the cumulation of residual deformations. Like the previous run, the elongation was greater at the 2nd storey of Unit 2, but the residual value increased by only 7.4 mm to a total of approximately 33.4 mm. Residual elongations of the 1st storey of Unit 1 and Unit 2 were approximately -0.74 mm and 7.4 mm, respectively, with increments of -1.04 mm and 2.4 mm.

For the last two transverse runs (run 1.2S and run 2.2S), the time-histories of the elongation of facade 1 is shown in Figure 2.25. Residual values were approximately 1.4 mm and 4.7 mm for run 1.2S and run 2.2S, respectively. This confirms the observed behaviour of Unit 1, with the formation of the first cracks and the development of the transverse flexural-rocking mechanism during run 2.2S.

The LVDT data at the beam supports indicated progressive slippage, caused by the cumulative elongation of the longitudinal facades first, followed by that of the transverse ones.

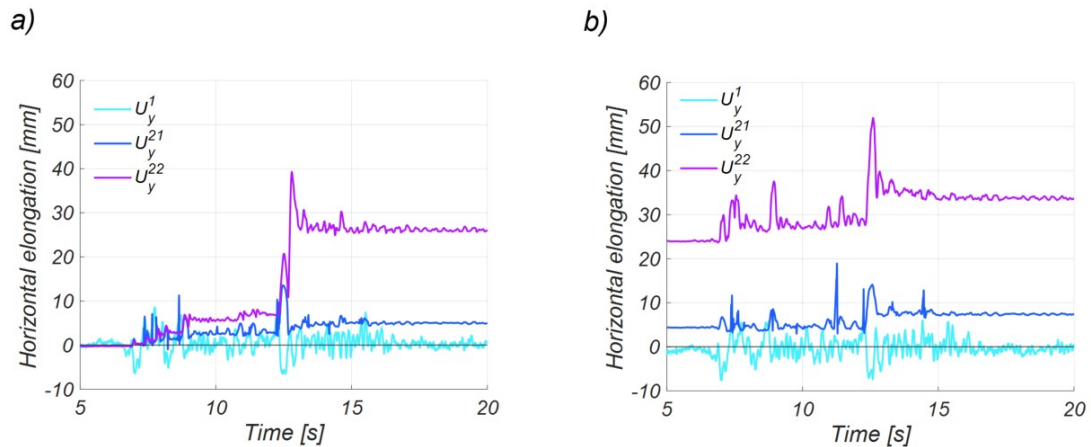


Figure 2.24: Time history of the longitudinal elongation of facade 3 for Units 1 and 2: a) Run 2.1; b) Run 2.1S.

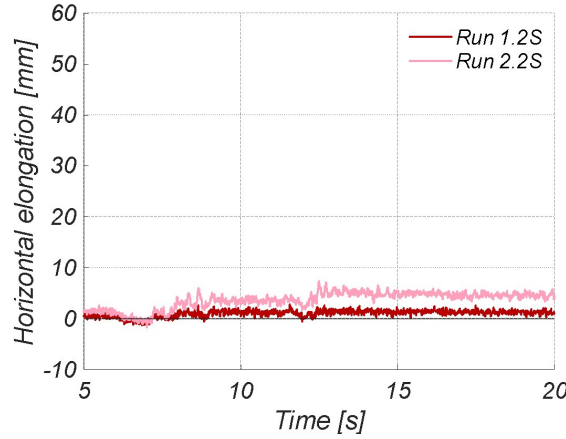


Figure 2.25: Time history of the transverse elongation of facade 1 of Unit 1.

#### 2.5.4 Force-displacement hysteretic response

Hysteretic curves were plotted for the entire structure in terms of base-shear coefficient (BSC) versus global drift ratio. Base-shear values were calculated by assigning tributary masses to each accelerometer in both directions. Tributary masses were multiplied by the recorded and filtered accelerations. The base shear ( $V_B$ ) and the BSC were defined considering the full mass of the specimen; the mass of the lower half of the 1st storey walls was assumed to move rigidly with the table, and was multiplied with the shake table accelerations. Accordingly,  $V_B$  and BSC are given by Equation 2.7:

$$BSC = \frac{V_B}{g \cdot m_{TOT}} = \frac{\sum_{i=1}^n (a_i \cdot m_i) + a_{st} \cdot m_{st}}{g \cdot (\sum_{i=1}^n m_i + m_{st})} \quad (2.7)$$

where  $a_i$  is the acceleration recorded by the  $i$ -th accelerometer and  $m_i$  is the tributary mass assigned to it;  $a_{st}$  is the shake table acceleration and  $m_{st}$  is the mass of the lower half of the 1st storey walls.

The global drift ratio ( $\tilde{\theta}_{j,AVG}$ ) represents the average displacement at the top of a unit divided by the total height of a unit, as given by Equation 2.8:

$$\tilde{\theta}_{j,AVG} = \frac{\sum_{i=1}^n \Delta_i}{n \cdot h_j} \quad (2.8)$$

where  $j$  identifies the structural unit (either 1 or 2),  $h_j$  is the total height of the unit (3.15 m for Unit 2 or 2.20 m for Unit 1),  $\Delta_i$  is the displacement of the  $i$ -th marker or potentiometer at

the top of a unit, and  $n$  is the total number of markers at the unit's top. Figure 2.26 shows the markers that were used to calculate the global drift ratios for the two structural units.

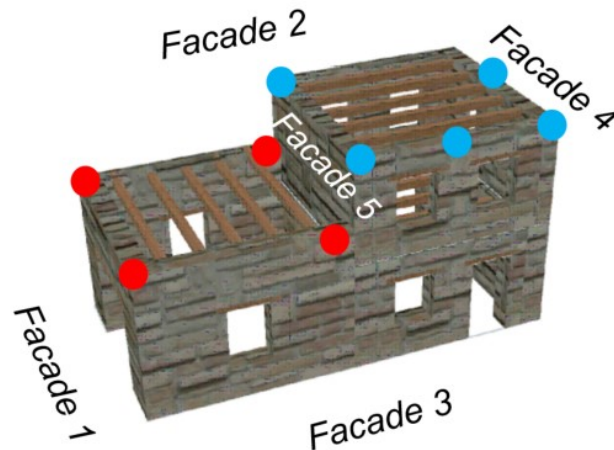


Figure 2.26: Markers used to calculate global drift ratios: red for Unit 1, blue for Unit 2.

The hysteretic response for run 1.3, the strongest bidirectional run, is shown in Figure 2.27. The response of both units in both directions was mostly elastic. The only damage detected at the units after this run was cracking and separation at the interface.

Figure 2.28 shows the hysteretic response for run 2.1 in the longitudinal  $y$ -direction. The formation of a soft-storey mechanism in the upper storey of Unit 2 resulted in anelastic hysteretic response, reaching global drift-ratio values greater than 1.5%. Figure 2.29 illustrates the behaviour for run 2.1S, where accumulated damage increased the global drift ratio of Unit 2 to values above 3%, even if retrofitted.

For the higher seismic intensity (run 2.1 and run 2.1S), the 1st storey drift ratio in the  $y$ -direction was significantly lower than the global drift ratio due to the soft-storey flexural mechanism forming in the 2nd storey of Unit 2. This behaviour was possibly emphasized by the interaction with a lower, stiffer and stronger structural unit, that did not show large drift values either. The effects of pounding between the two units are visible as sudden spikes in the hysteretic loops.

Finally, the hysteretic response during the strongest transverse  $x$ -direction run is shown in Figure 2.30. It confirms the onset of a rocking mechanism in Unit 1, with slight loss of strength in large-amplitude cycles of increasing displacement demand.

Table 2.6 summarizes the maximum global drift-ratio values per run for both units in both directions.

Table 2.6: Maximum global drift-ratio values for both units in both directions.

Run ID	Unit 1		Unit 2	
	Transverse drift-ratio [%]	Longitudinal drift-ratio [%]	Transverse drift-ratio [%]	Longitudinal drift-ratio [%]
0.1	0.04	0.06	0.03	0.07
0.2	0.05	0.03	0.04	0.02
0.3	0.05	0.06	0.06	0.07
1.1	0.04	0.08	0.05	0.12
1.2	0.07	0.05	0.07	0.03
1.3	0.14	0.10	0.12	0.12
2.1	0.09	0.24	0.16	1.67
2.1S	0.10	0.22	0.29	3.20
1.2S	0.16	0.06	0.21	0.27
2.2S	0.42	0.06	0.41	0.32

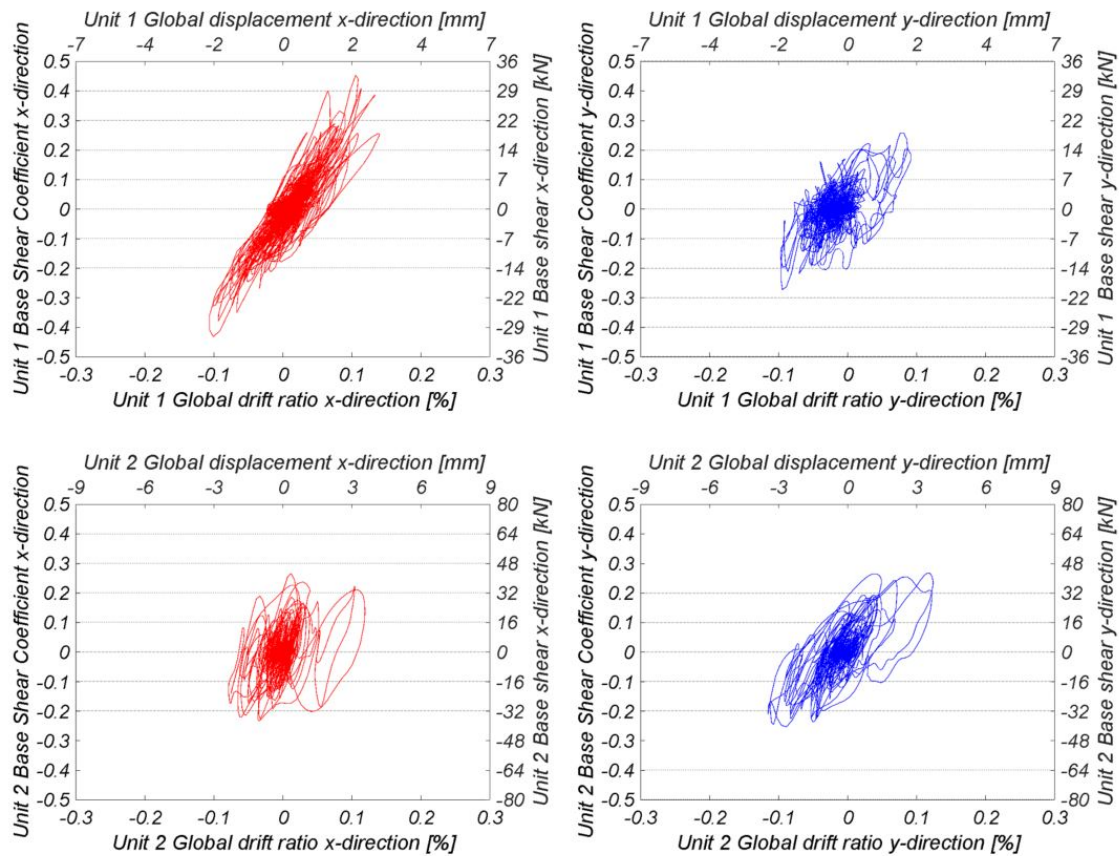


Figure 2.27: Hysteretic responses in both directions for run 1.3.



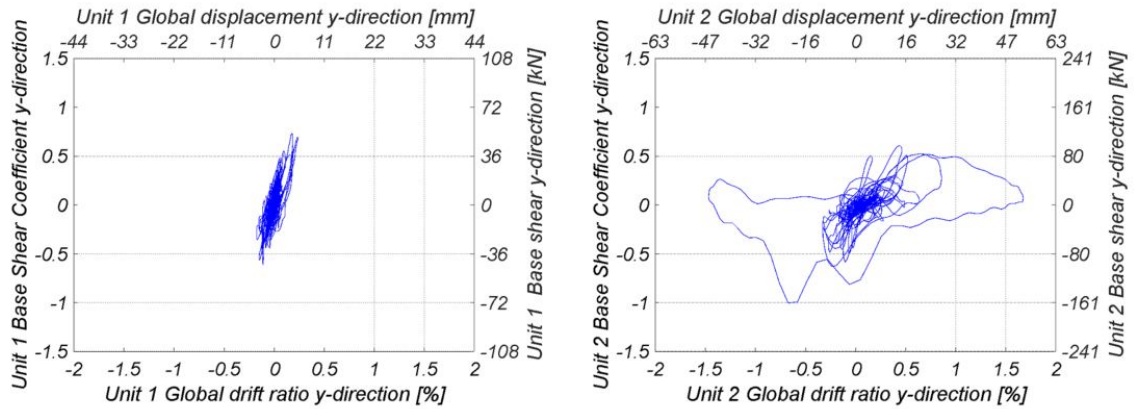


Figure 2.28: Hysteretic responses in the y-direction for run 2.1.

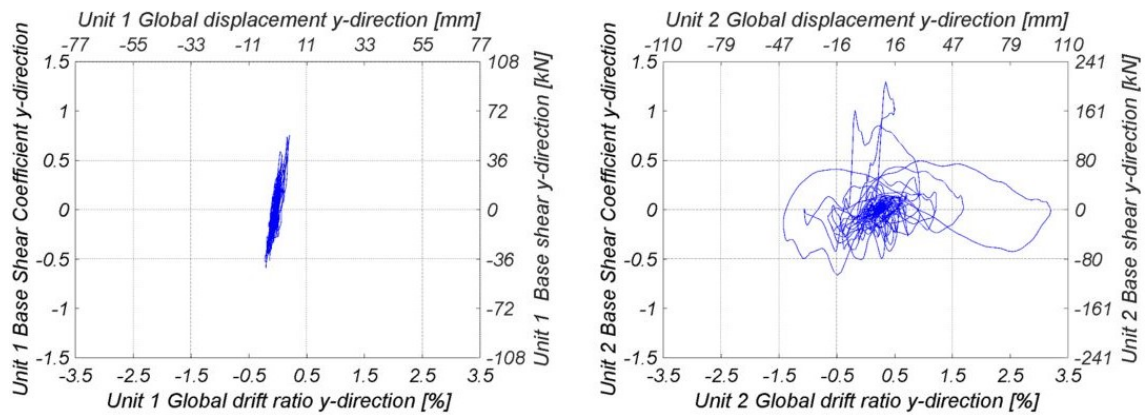


Figure 2.29: Hysteretic responses in the y-direction for run 2.1S.

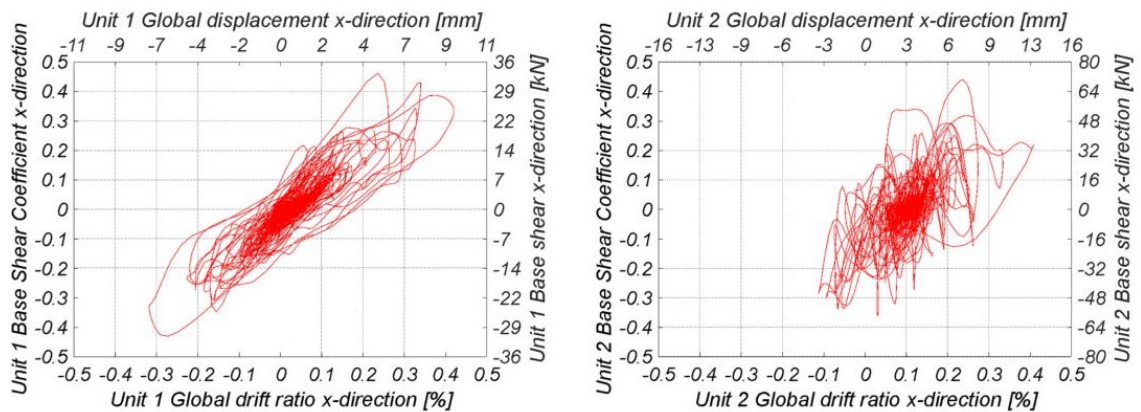


Figure 2.30: Hysteretic responses in the x-direction for run 2.2S.

## 2.6 Conclusions

This paper presented the half-scale bidirectional shake table test of a two-units stone masonry building aggregate. The specimen was built of undressed double-leaf stone masonry with poor interlocking to replicate a typical historical construction. A two-storey unit was constructed first, and mortar was applied at the interface with the adjacent unit to prevent any interlock between stones. Finally, the adjacent one-storey unit was completed. Timber beams and a layer of planks formed the floors, resulting in flexible diaphragms.

The project had two main goals: (i) investigating experimentally the role of the interface on the aggregate behaviour, (ii) producing high-quality data for the validation of numerical models. The loading sequence consisted of orthogonal unidirectional and simultaneous bidirectional shake table runs of increasing intensity. The building prototype experienced its first visible damage in the form of a vertical crack at the interface between the units for a PGA of 0.170 g in the longitudinal direction.

Extensive damage on the two-storey unit was reached during the unidirectional longitudinal run with PGA of 0.593 g. Interaction with the adjacent shortest unit forced the development of a soft-storey mechanism at the 2nd storey of the tallest unit, while the 1st storey and the shortest unit did not undergo large drift ratios. Both piers and spandrels suffered extensive flexural cracking in the longitudinal facades at the 2nd story, with permanent horizontal elongations of the spandrels. The mechanism included significant out-of-plane displacements and cracking on the transverse facades. Cracks were continuous and connected across orthogonal walls because, due to interlocking between orthogonal walls, the end piers of the longitudinal facades acted as webs in the out-of-plane overturning mechanism of the transverse walls.

To protect against out-of-plane collapse after the full activation of the 2nd storey mechanism, the tallest unit was strengthened by improving beam-to-wall connections, and testing was resumed by repeating the longitudinal run at the same intensity. Existing damage mechanisms progressed, but out-of-plane collapse was effectively prevented. When applying the input motion in the transverse direction, the shortest unit exhibited out-of-plane vibrations of the longitudinal walls, especially close to the edges not connected to the transverse wall. This mechanism might become particularly relevant in the absence of interlock between the structural units.

The interface behaviour was one of the main focuses of this test campaign. Optical markers, installed adjacent to the interface, recorded relative displacements of the joint in both longitudinal and transverse directions. In the longitudinal direction, the specimen exhibited both pounding and separation. In the transverse direction, the largest absolute relative displacements always occurred at instants when the units were longitudinally separated. This suggests that friction forces across the interface were sufficiently large to reduce the magnitude of the relative transverse displacement when the joint was closed. This behaviour could be observed thanks to bidirectional loading.



The outcomes of the shake-table test show that the observed experimental behaviour can be replicated only by explicitly modelling the connection between the units, including both normal and frictional characteristic of the contact interface. Moreover, the complexities emerged in the dynamic responses of each structural unit and of the contact interface make further three-dimensional shake table tests necessary to better understand the seismic behaviour of aggregates, to calibrate numerical models, and to define practical strategies to account for the interaction.

## 2.7 Data availability

Raw experimental data, files used to process raw data, processed data, and files used to produce the figures presented in this paper can be accessed through the repository DOI:10.5281/zenodo.6546434

## 2.8 Acknowledgments

The authors would like to thank the technicians of the LNEC laboratory in Lisbon whose dedicated work allowed the project run smoothly and across all the obstacles: Artur Santos, Susana Almeida, Aurélio Bernardo, and Anabela Martins. We owe our thanks to master students whose efforts helped the project: Cecilia Noto and Samuel Cosme. Finally, want to stress the contribution of post-doctoral researcher Filipe Luis Ribeiro to the successful outcome of the project.

## 2.9 Funding

The project leading to this paper has received funding from the European Union's Horizon 2020 research and innovation programme under grant agreement No 730900.



### **3 Shake table testing of a stone masonry building aggregate: Overview of blind prediction study**

This chapter is a pre-print version of the paper: Tomić I, Penna, A, DeJong, M, Butenweg C, Correia AA, Candeias PX, Senaldi I, Guerrini G, Malomo D, Beyer K, et al (2022b) Shake-table testing of a stone masonry building aggregate: Overview of blind prediction study. Submitted to Bulletin of Earthquake Engineering

The formatting and numbering of equations, tables and figures have been adapted to this document. The contributions of the first author are: organization of the blind prediction competition, analysis of data, data curation, visualization and writing.

#### **Abstract**

City centres of Europe are often composed of unreinforced masonry structural aggregates, whose seismic response is challenging to predict. To advance the state of the art on the seismic response of these aggregates, the Adjacent Interacting Masonry Structures (AIMS) project from The Seismology and Earthquake Engineering Research Infrastructure Alliance for Europe (SERA) provides shake-table test data of a two-unit, double-leaf stone masonry aggregate subjected to two horizontal components of dynamic excitation. A blind prediction was organized with participants from academia and industry to test modelling approaches and assumptions and to learn about the extent of uncertainty in modelling for such masonry aggregates. The participants were provided with the full set of material and geometrical data, construction details and original seismic input and asked to predict prior to the test the expected seismic response in terms of damage mechanisms, base-shear forces, and roof displacements. The modelling approaches used differ significantly in the level of detail and the modelling assumptions. This paper provides an overview of the adopted modelling approaches and their subsequent predictions. It further discusses the range of assumptions made when modelling masonry walls, floors and connections, and aims at discovering how the common

solutions regarding modelling masonry in general, and masonry aggregates in particular, affect the results. The results are evaluated both in terms of damage mechanisms, base shear forces, displacements and interface openings in both directions, and then compared with the experimental results. The modelling approaches featuring Discrete Element Method (DEM) led to the best predictions in terms of displacements, while a submission using rigid block limit analysis led to the best prediction in terms of damage mechanisms. Large coefficients of variation of predicted displacements and general underestimation of displacements in comparison with experimental results, except for DEM models, highlight the need for further consensus building on suitable modelling assumptions for such masonry aggregates.

### 3.1 Introduction

Historical stone masonry structures are very vulnerable to earthquakes, and effective risk mitigation strategies require the development of suitable assessment procedures. However, the seismic performance assessments of masonry buildings are often hindered by a lack of information regarding the structure, materials and structural details. As an added complexity, interventions can increase the heterogeneity of the construction material and structural details, as these also degrade during the building's lifespan (P. B. Lourenço, 2002; Lagomarsino and Serena Cattari, 2015). Additionally, the properties of the connections between the structural elements, such as the wall-to-wall and floor-to-wall interfaces, are often unknown (Ortega et al., 2018; Solarino et al., 2019; Almeida et al., 2020; Vanin et al., 2020b; Tomić et al., 2021). At the same time, it is often not feasible to test the properties of the materials and components, either due to high costs or the limits imposed by the cultural value of the building (Borri and Corradi, 2019).

The seismic response of historical masonry is further complicated for buildings that are part of aggregates, which are common in European city centres due to the centuries-long process of densification (Carocci, 2012; Da Porto et al., 2013; Mazzoni et al., 2018). In these aggregates, neighbouring units often share a structural wall, with the connection ensured either through interlocking stones or by a layer of mortar. These aggregates usually developed over centuries and without consistent planning or engineering, resulting in adjacent buildings that often have different material properties, floor and roof heights, and are poorly connected. Figure 1 shows an example from Central Italy where the 2016 earthquakes damaged buildings and their connection joints in an aggregate built to densify the block by 'borrowing' walls from the adjacent buildings.



Figure 3.1: Damage to masonry aggregates in Central Italy after the 2016 earthquake.

To simulate the behaviour of masonry and help predict seismic responses, various modelling techniques and approaches have been adopted, each with differing levels of complexity and computational burden (Roca et al., 2010; P. B. Lourenço, 2013). The key pre-requisite of every model is to adequately describe the geometry, morphology, connections and boundary conditions. In addition to the challenges in accurately determining these properties, another challenge stems from the lack of clear and detailed modelling guidelines and codes for representing the interaction between adjacent building units. In the following, we review the literature on benchmark studies and existing blind prediction competitions focused on modelling unreinforced masonry (URM).

### 3.1.1 Review of past blind prediction competitions and software benchmarks

Modelling the seismic response of URM buildings in general and historical masonry aggregates in particular is challenging because it requires to perform nonlinear numerical simulations, which requires experience in nonlinear modelling (Andrea Penna et al., 2013; Lagomarsino et al., 2018; Serena Cattari et al., 2021; D'Altri et al., 2022). Open questions on how to account for the material and modelling uncertainties and how to calibrate numerical models of URM buildings have been raised since the very first nonlinear analyses were performed (Tomažević, 1978). Since then, multiple studies have addressed material and modelling uncertainties for URM buildings, either by organising blind prediction competitions or by directly benchmarking different software packages.

A dozen studies benchmarked modelling approaches and assumptions for URM buildings (Salonikios et al., 2003; Rui Marques and P. B. Lourenço, 2011; Giamundo et al., 2014; Betti et al., 2015; Calderoni et al., 2015; Bartoli et al., 2017; De Falco et al., 2017; Serena Cattari et al., 2018; Siano et al., 2018; Aşikoğlu et al., 2020; Malcata et al., 2020). The large number of studies here differ by case-study size, complexity, software used and modelling approaches, but highlight a large scatter in obtained results due to the many alternatives in choosing material parameters, defining a numerical model, and interpreting results. Particularly relevant for the present work is the study by Malcata et al. (2020), which focused on a building aggregate of seven

units, for which results of in-situ material tests and a detailed geometric survey were available. Two models were created; the first one was an equivalent frame method (EFM) model in 3Muri (Data, 2008) and the second one a solid finite element method (FEM) model in ABAQUS (Smith, 2009). In the 3Muri model, the entire aggregate was modelled assuming that all units of the aggregate were fully connected to each other. On the other hand, in ABAQUS only about half of the units represented in the 3Muri model were included and constraints applied to account for the missing units. The models were calibrated using frequencies obtained from ambient vibration measurements. The authors obtained some similarities in terms of damage mechanisms, but also different base shear force capacities, with the 3Muri model having less force capacity than the ABAQUS model. This difference was attributed to the difference in constitutive models adopted in each software and to the fact that the ABAQUS model contained only half of the units. In general, for complex buildings Malcata et al. (2020) recommended using EFM due to the much shorter analysis time and their finding that this modelling approach tends to lead to more conservative results.




Serena Cattari and Guido Magenes (2022) presented the study from the ReLUIS project, which sought to define a set of reference structures of increasing complexity. This research program carried out by several Italian universities tested these reference structures by means of non-linear static analyses using different software packages. Here, the focus was on the global response governed by the in-plane response of the walls and did not consider out-of-plane collapse failures. Some of the case study buildings were permanently monitored (Mauro Dolce et al., 2017), and an earthquake that hit during the project phase (Serena Cattari et al., 2019) allowed the numerical results to be verified. To account for the various scenarios, the following properties were varied: (i) masonry typology, (ii) boundary conditions in case of wallettes (fixed-fixed and cantilever) and (iii) spandrel configurations. The spandrel configurations included in that study comprised spandrels without any tensile resistant horizontal element, spandrels with horizontal steel tie rods, spandrels coupled to reinforced concrete beams, and infinitely stiff spandrels. To limit the scatter, the following assumptions were made: (i) good wall-to-wall connections, (ii) rigid diaphragms and (iii) a perfect connection between the diaphragm and walls. While other papers stemming from the ReLUIS project elaborate on the specific results obtained on each of these case studies, Serena Cattari and Guido Magenes (2022) presented an overview of the benchmark structures, their purpose, and the standardized criteria for comparison of the results.

Finally, the latest study by Parisse et al. (2021) described a benchmark exercise performed as part of the European Conference on Earthquake Engineering (Magenes et al., 2018). Two three-storey buildings were considered as case studies. The first was a stone masonry building with flexible diaphragms, and the second was a brick masonry building with rigid horizontal diaphragms. A wide range of approaches was used, with participants free to choose modelling strategies, methods of analysis and criteria for attaining limit states, which were not predefined. Here, the majority of participants submitted predictions using EFMs. The results were compared in terms of capacity curves, predicted damage mechanisms and the attainment of the damage and the near collapse limit states. The study showed good agreement for damage

patterns and collapse mechanisms, with some differences in failure modes. However, the scatter was very high in the capacity curves and peak ground accelerations (PGAs) required for attaining the limit state, including for the case study presenting similar masonry quality and details to the present study.

While benchmarking studies compare modelling strategies and assumptions of hypothetical structures and / or loading scenarios, blind prediction studies compare simulations to experimental results where the experimental test is carried out after the simulations have been performed. The blind predictions by Mendes et al. (2017) and Esposito et al. (2019) are the most relevant for the present study and discussed here. In both studies, participants were free to choose their modelling approach and type of analysis (static or dynamic, and linear or nonlinear). The study by Mendes et al. (2017) was organized for research groups and tested two structures with the similar geometric dimensions but with different masonry typologies (irregular stone masonry and solid brick masonry). The structures represented three walls (facade and side walls) of a single storey building and a gable on the facade wall. They were tested on a shake-table, focusing on the out-of-plane behaviour of the facade wall. The groups were asked to report a PGA value and the failure mode that would lead to the out-of-plane collapse of the specimen. Even though the average provided value was on the safe side, the coefficient of variation (CoV) was high, 63% for the stone structure and 39% for the brick structure, meaning that some of the participants were extremely conservative whereas others were unconservative. Moreover, only 9 out of 19 models predicted the failure mode correctly for the stone structure, and 6 out of 17 for the brick structure. The study by Esposito et al. (2019) was organized for engineering companies that were asked to simulate and predict the in-plane behaviour of the quasi-static cyclic test on a two-storey modern house, representative of Dutch URM building stock. Nine participants submitted 16 models but were asked to choose one final contribution per participant. The participants were requested to provide base-shear versus first and second floor displacements and a clear description and explanation of the failure mechanism. The FEM models overestimated the peak strength and underestimated the ultimate displacement capacity. On the opposite, the analytical-based model underestimated the peak strength, but overestimated the ultimate displacement capacity. Finally, EFM models generally underestimated the experimental capacity in terms of both force (at peak load) and displacement (at near collapse). Peak strength CoV was 51% and 42% for negative and positive loads, respectively. Displacement at near collapse CoV was 32% and 41% for negative and positive displacements, respectively. Only 4 out of 9 models predicted the failure mode correctly. Based on their submissions, the capacity/demand (C/D) ratio was calculated. EFM models resulted on average in smaller values of C/D, and FEM and analytical models resulted on average with larger values of C/D ratios than those computed from the experiment. For all submissions, C/D CoV was in between 26% and 69%, depending on the load direction and method for computing C/D ratio. The two blind prediction studies and the SERA – AIMS study presented herein are summarized in Table 3.1.

Table 3.1: Comparison of blind prediction studies on the seismic response of unreinforced masonry buildings.

Blind prediction	Mendes et al. 2017	Esposito et al. 2019	SERA - AIMS
<b>Test specimen and loading</b> 	Two specimens consisting each of three walls; uni-directional shake-table test loading one of the walls out-of-plane and two in-plane	Modern Dutch terraced house made of calcium silicate brick masonry and reinforced concrete floors; Quasi-static cyclic test 	Double-leaf stone masonry aggregate consisting of two units connected by a layer of mortar; uni- and bi-directional incremental shake-table test 
<b>Typology</b>	Specimen 1: Stone masonry; Specimen 2: Solid brick masonry	Calcium silicate brick masonry	Stone masonry
<b>Diaphragm</b>	None	Rigid	Flexible
<b>Submissions</b>	Academia: 36/36; Limit analysis: 23/36; FEM: 10/36; DEM: 3/36	Industry: 16/16 FEM: 6/16 EFM: 7/16 Analytical: 3/16	Industry: 2/13 Academia: 11/13 FEM: 6/13 EFM: 2/13 DEM: 3/13 Limit analysis: 1/13 Analytical: 1/13
<b>Failure modes</b>	Out-of-plane and in-plane	In-plane	In-plane and out-of-plane
<b>Key findings</b>	Predicted PGA at collapse on average on the safe side. For the stone structure: PGA at collapse with CoV of 63%, 9 out of 19 failure modes predicted correctly. For the brick structure: PGA at collapse with CoV of 39%, 6 out of 17 failure modes predicted correctly	The average of computed displacement C/D ratio on the unsafe side for FEM and analytical models, and on the safe side for EFM models; C/D ratio CoV from 26% to 69%, depending on the load direction and method used to calculate C/D. Peak strength CoV: 51% for negative loads, and 42% for positive loads. Near collapse displacement COV: 32% for negative displacements, and 41% for positive displacements. 4 out of 9 predicted failure mode correctly	At significant damage: CoV of reported displacements: 160%-177%; CoV of reported interface openings: 186%-268%; CoV of reported base shear: 58%-74%. DEM models only able to capture the correct order of magnitude of displacements. Limit analysis best predicted the failure mechanism. Models, except DEM, generally underestimated displacements and interface opening

With the blind prediction study presented in this paper, we intend to contribute as follows to the existing benchmarking and blind prediction studies and their findings:

- In the previous studies, participants were either free to choose the analysis method (Mendes et al., 2017; Esposito et al., 2019; Parisse et al., 2021) or pushover analyses were performed (Serena Cattari and Guido Magenes, 2022). In the present study, participants were asked to perform a time-history analysis to capture the full complexity of the URM response and aggregate out-of-phase behaviour. In total, eleven out of the thirteen participants performed nonlinear time-history analysis.
- Previous blind predictions were either focusing on in-plane (Esposito et al., 2019) or



out-of-plane behaviour (Mendes et al., 2017). The present study was designed such that in-plane and out-of-plane components were expected to play an important role in the behaviour of the two units.

- Previous studies usually narrowed the modelling choices by considering wall-to-wall and floor-to-wall connections as rigid (Serena Cattari and Guido Magenes, 2022), or floor-to-wall connections as rigid and not specifying the properties of wall-to-wall connections (Parisse et al., 2021). The present study was designed such that a nonlinear response of the unit-unit connections and the floor-to-wall connections was expected.
- Blind prediction studies on masonry aggregates were not yet conducted. When a unit was part of an aggregate, the influence of adjacent units on the response was either out of scope and not accounted for (Parisse et al., 2021) or accounted for in a simplified manner (Malcata et al., 2020). The principal objective of this study was the masonry aggregate behaviour and the aggregate behaviour was designed such that a nonlinear response of the interface was expected.
- In previous benchmark studies, modelling approaches were often limited to a few different software packages. In the present study, thirteen submissions covered a wide variety of modelling approaches using various modelling approaches: three discrete element method (DEM) models, four solid FEM models, two shell FEM models, two EFM models, one limit analysis model and one hand calculation.

The following sections first describe the timeline and information on the case study aggregate that was shared with the participants of the blind prediction competition together with the nominal and actual seismic input. Second, the categories of modelling approaches used by the participants are described and discussed. Third, the statistical evaluation of the submitted results and the qualitative description of the predicted damage mechanisms are discussed and compared with experimental results. Finally, conclusions and recommendations on modelling URM aggregates are drawn.

### 3.2 Case study information shared with the participants

The chosen case study was a half-scale prototype of a masonry building aggregate, designed for the shake-table test of the SERA AIMS project. Details about the experimental campaign can be found in Tomić et al. (2022a). Table 3.2 shows the timeline of the blind prediction competition. Participants were provided with data on mortar, stone, and masonry material properties (Table 3.4), data from quasi-static cyclic shear tests on wallettes of the same masonry typology, as well as data on the geometry, mass, construction details and testing sequence (Tomić et al., 2022a).

Table 3.2: Timeline for the blind prediction competition associated with the SERA AIMS stone masonry aggregate experimental campaign in Tomić et al. (2022a).

Date	Event
2019 September	Opened blind prediction competition and shared information on specimen geometry and mass, masonry typology, mortar, stone, and masonry material properties (Table 3.4), quasi-static wallettes tests, construction details, planned earthquake records and testing sequence
2019 December	Construction of SERA AIMS aggregate began at LNEC facilities
2020 March	Construction of SERA AIMS aggregate completed
2020 November	Blind prediction competition submissions closed
2020 November	Shake-table test performed at LNEC facilities in Lisbon
2021 August	LNEC provided the test data; compression and diagonal compression tests on masonry wallettes performed at LNEC facilities
2021 September	Opened post-diction competition: shared recorded shake-table accelerations and preliminary results of tests on mortar and wallettes in terms of maximum recorded forces
2021 November	Raw and processed test data made available on the Designsafe platform (Rathje et al., 2017) platform for the post-diction competition

### 3.2.1 Geometry and material properties

The aggregate was composed of two units. The two-storey unit (Unit 2) was built first and had a closed rectangular footprint with plan dimensions of 2.5 m  $\times$  2.5 m and a total height of 3.15 m. The one-storey unit (Unit 1) had a U-shape footprint with plan dimensions of 2.5 m  $\times$  2.45 m and a total height of 2.2 m. The wall thicknesses were 30 cm for Unit, 35 and 25 cm for Unit 2 for the first and second floor, respectively. The thickness of the spandrels beneath the openings was 15 cm. The floor plan and facades are shown in Figure 3.2.

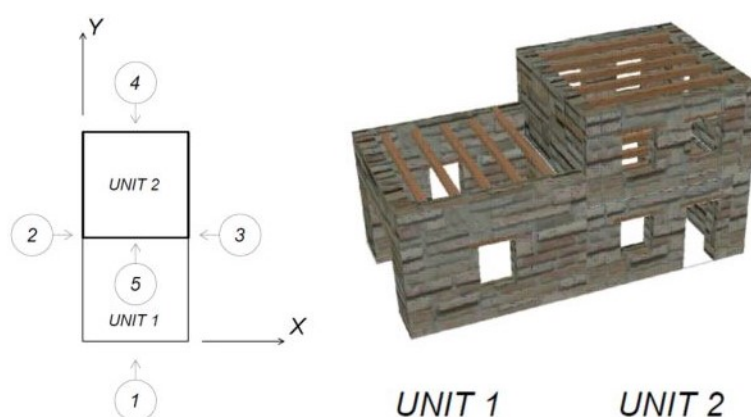


Figure 3.2: Case study of the stone masonry aggregate experimental campaign in Tomić et al. (2022a). 3D view, floor plan with beam orientation and facade layout of the two units.

Table 3.3: Specimen masses of the units of the SERA AIMS stone masonry aggregate experimental campaign in Tomić et al. (2022a).

Walls of Unit 1	7,270 kg
Floors of Unit 1	164 kg
Total Unit 1	<b>7,434 kg</b>
Walls of Unit 2	12,937 kg
Floors of Unit 2	335 kg
Additional masses of Unit 2	3,000 kg
Total Unit 2	<b>16,272 kg</b>
Steel-concrete foundation	18,000 kg
TOTAL	<b>41,706 kg</b>

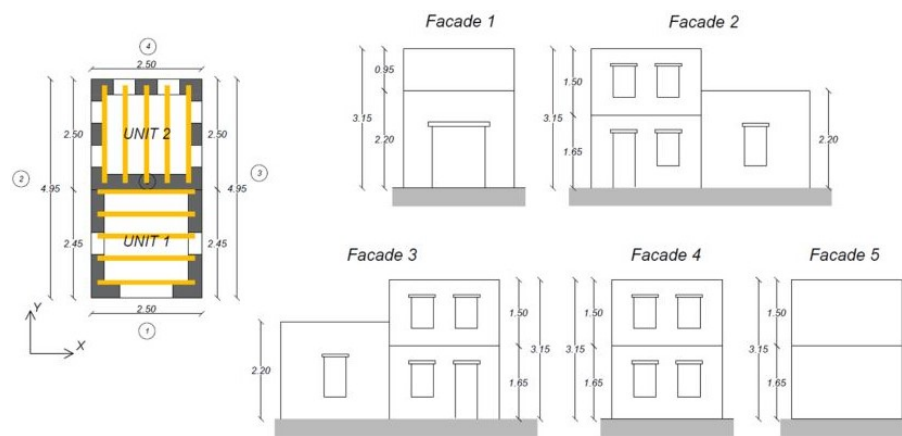


Figure 3.2 (Continued): Case study of the stone masonry aggregate experimental campaign in Tomić et al. (2022a). 3D view, floor plan with beam orientation and facade layout of the two units.

The total masses of Unit 1 and Unit 2 were 7,434 and 13,272 kg, respectively. Unit 2 had additional masses of 1500 kg evenly distributed per floor. The detailed mass distribution is displayed in Table 3.3.

The walls of the stone masonry aggregate were built from double-leaf irregular stone masonry. Commercial hydraulic lime mortar was used, with the addition of 2:3 volumetrically proportional expanded polystyrene (EPS) spheres to further reduce the strength and stiffness of the mortar. Stone chips were placed between the leaves. The interlocking between the leaves was poor, except near openings and corners. The masonry typology (shown in Figure 3.3) and materials were chosen to be as similar as possible to the ones used in a previous test at the EUCENTRE (Senaldi et al., 2019a; Guerrini et al., 2019). Material properties of the EUCENTRE test, as shown in Table 3.4, were shared with all participants of the blind prediction, together with the data from quasi-static cyclic shear tests on wallettes of the same typology.

Table 3.4: Estimates of the mortar, stone and masonry properties that were distributed to the blind prediction participants before the tests. These values correspond to the properties obtained in the EUCENTRE tests (Guerrini et al., 2017; Senaldi et al., 2018; Senaldi et al., 2019a).

Mortar properties	Average	CoV [%]
Compressive strength, $f_m$ [MPa]	1.75	28
Tensile strength, $f_{m,t}$ [MPa]	0.60	23
Young's modulus, $E_m$ [MPa]	243	35
Stone properties	Average	CoV [%]
Credaro Berrettino stone compressive strength, $f_b$ [MPa]	144	-
Credaro Berrettino stone tensile strength, $f_{bt}$ [MPa]	19	-
Masonry properties	Average	CoV [%]
Density, $\rho$ [kg/m <sup>3</sup> ]	1980	5
Compressive strength, $f$ [MPa]	1.30	2.6
Tensile strength, $f_t$ [MPa]	0.17	7.3
Cohesion, $f_{v0}$ [MPa]	0.233	7.3
Poisson's modulus, $\nu$ [-]	0.14	56
Young's modulus in compression, $E$ [MPa]	3462	12
Shear modulus, $G$ [MPa]	1524 <sup>†</sup>	17
Shear modulus, $G$ [MPa]	1898 <sup>‡</sup>	58

<sup>†</sup>from vertical compression tests

<sup>‡</sup>from diagonal compression tests



Figure 3.3: Masonry typology: detail of a corner of Unit 1 of the SERA AIMS aggregate in Tomić et al. (2022a).

The walls of Unit 2 were constructed first, representing the ‘older’ unit of the aggregate. Afterwards, a layer of mortar was applied to the interface (shown in Figure 3.4) to ensure that there was no interlocking between the units, simulating a weak connection between the two units. The timber floors were simply supported on the masonry walls and were oriented differently for the two units, with the Unit 1 beams spanning in the x-direction and the Unit 2 beams spanning in the y-direction. One layer of 2-cm-thick planks was nailed to the beams by two nails at each intersection. PVC tubes were placed in the walls under the beams and alongside beams running adjacent to walls to leave the possibility of connecting the walls to the beams to prevent any out-of-plane failure during the test.



Figure 3.4: Detail of the interface between the units of the SERA AIMS aggregate in Tomić et al. (2022a).

### 3.2.2 Earthquake record

The aggregate specimen was tested under one- and two-component excitations, using the two horizontal components of the 1979 Montenegro earthquake Albatros station records displayed in Figure 3.5. Note that the time axes of the ground motions are scaled by  $1/\sqrt{2}$  because the units were built at half scale (Tomić et al., 2022a). The response spectra are displayed in Figure 3.6. The maximum accelerations that could be applied to the specimen by the shake-table are 0.875 g in the y-direction and 0.625 g in the x-direction.

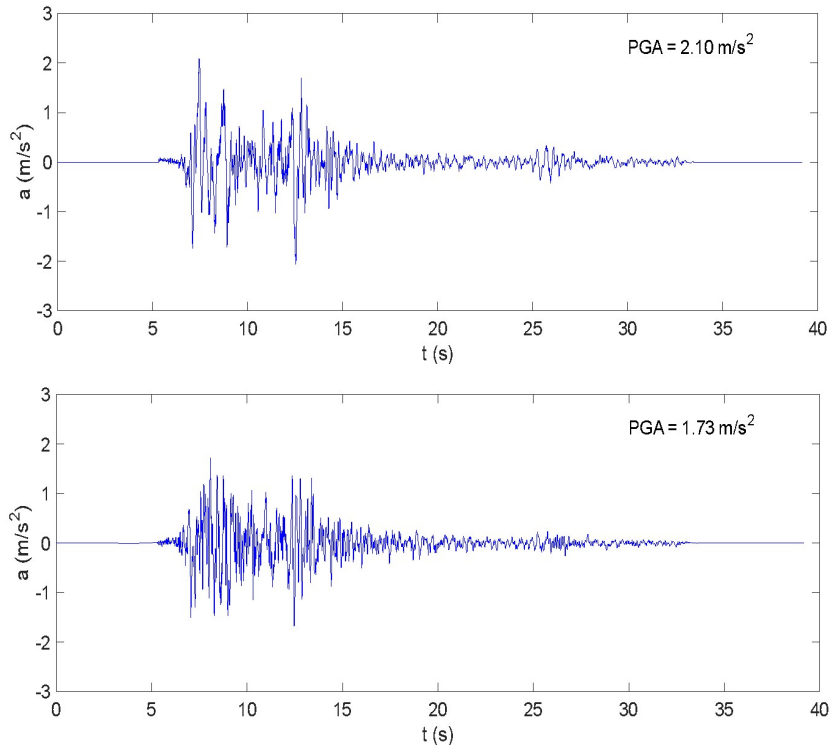


Figure 3.5: Processed acceleration time histories of the Montenegro 1979 earthquake (Albatros station), with the scaled time step for: a) E-W direction; b) N-S direction (Luzi et al., 2016).

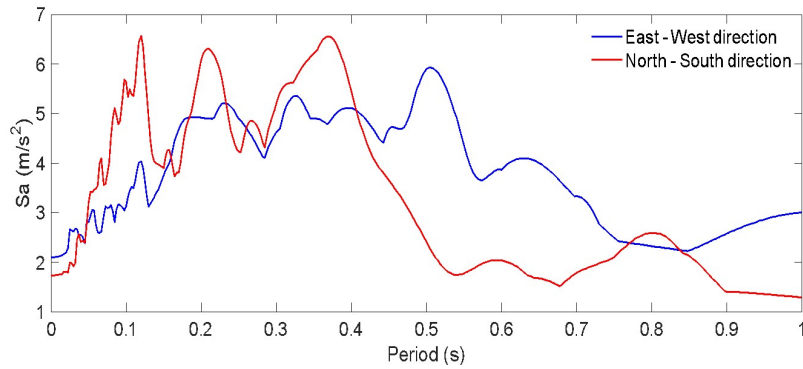


Figure 3.6: Acceleration response spectra of the Montenegro 1979 earthquake (Albatros station) for a 5% damping ratio with the scaled time step (Luzi et al., 2016).

The theoretical specified limit was planned to be reached in four steps, with the ground motion applied at 25%, 50%, 75% and 100% of such limit. Each step consisted of three stages, comprising (i) a uni-directional test in the y-direction, (ii) a uni-directional test in the x-direction and (iii) a bi-directional test in x- and y-directions, as shown in Table 3.5. However, the actual testing sequence differed from the original plan and comprised ten steps overall, as

Table 3.5: Nominal SERA AIMS shake-table testing sequence.

Run number	Run notation	Direction	Level of shaking (shake-table capacity)	Nominal PGA
1	1.1	y	25%	0.219 g
2	1.2	x	25%	0.156 g
3	1.3	Bidirectional	25%	0.219 (y)/0.156 (x) g
4	2.1	y	50%	0.438 g
5	2.2	x	50%	0.313 g
6	2.3	Bidirectional	50%	0.438 (y)/0.313 (x) g
7	3.1	y	75%	0.656 g
8	3.2	x	75%	0.469 g
9	3.3	Bidirectional	75%	0.656 (y)/0.469 (x) g
10	4.1	y	100%	0.875 g
11	4.2	x	100%	0.625 g
12	4.3	Bidirectional	100%	0.875 (y)/0.469 (x) g

shown in Table 3.6. Due to this discrepancy, Table 3.7 shows the list of experimental results compared with blind predictions by participants to account for differences between nominal and effective shake-table accelerations.

First, three additional runs at 12.5% of the shake-table capacity were added to better calibrate the table for the runs. The nominal and effective spectra for Runs 1.1 – 1.3 matched well, as shown in Figure 3.7. Note that nominal Run 1.3 was composed by nominal Runs 1.1 and 1.2 combined. Components of the bi-directional run 1.3 were very similar as when applied separately in Runs 1.1 and 1.2.

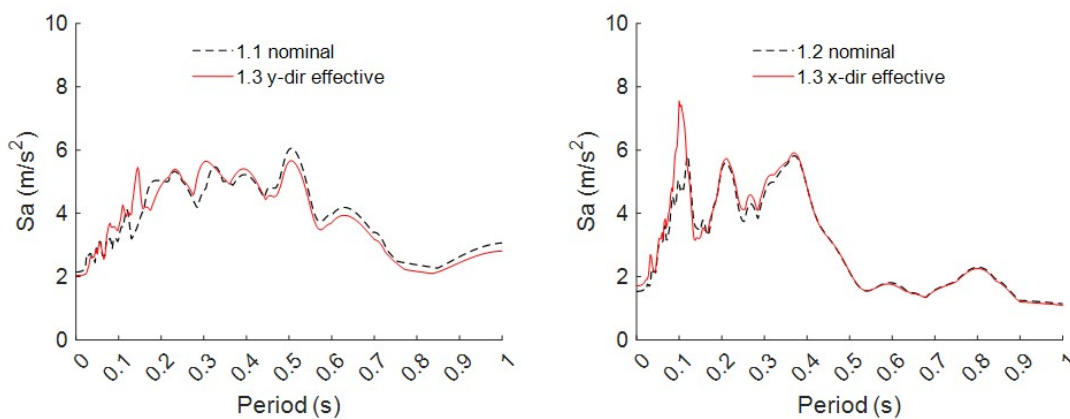


Figure 3.7: Comparison of response spectra for nominal and effective records of Runs 1.1 – 1.3 in the SERA AIMS shake-table test in Tomić et al. (2022a).

After Run 2.1, the damage was widespread, so the specimen was strengthened before continuing (Tomić et al., 2022a). For all subsequent runs, the run label ends therefore with an “S” to



highlight that the specimen was strengthened. Overall, the nominal and effective PGA and spectral shape of the runs differed, making it challenging to compare numerical and experimental displacements and base shear. Figure 3.8 shows the effectively applied acceleration spectra for Run 2.1, which was the last run before strengthening measures were installed. Run 2.1 was a uni-directional excitation in y-direction. The effectively applied spectra are computed from the recorded shake-table accelerations. Figure 3.8 also shows the nominal excitations of Runs 2.1 and 3.1. The fundamental period of the undamaged structure were approximately 0.13 s (Tomić et al., 2022a). Comparing the effective to the nominal spectra shows that for a period range between 0.1-0.15 s, the effective spectra of Run 2.1 is closer to the nominal spectra of Run 3.1 rather than 2.1. At the same time, the effective spectra of Run 2.2S is closer to the nominal spectra of Run 3.2 rather than 2.2. For this reason, for displacements and base shear in the longitudinal direction we will compare in the next section the blind predictions of Run 3.1, keeping in mind, however, that the comparison is somewhat ambiguous due to differences in nominal and effective spectre and therefore rather comparing an order of magnitude of the variable. For excitation in the transversal direction, we will compare the predicted responses for Run 3.2 to experimental results of Run 2.2S. Again, the objective is to compare the predicted responses of the participants, while the experimental comparison is only to compare an order of the magnitude. However, it needs to be kept in mind that at Run 2.2S the structure was already retrofitted and heavily damaged because Run 2.1 corresponded rather to Run 3.1. In addition to comparing predicted and observed values for displacements and base shears we compare predicted and actual damage mechanisms.



Table 3.6: Actual applied testing sequence of the SERA AIMS shake-table test in Tomić et al. (2022a).

Run number	Run notation	Direction	Level of shaking (shake-table capacity)	Nominal PGA	Effective PGA
1	0.1	$y$	12.5%	0.110 g	0.113 g
2	0.2	$x$	12.5%	0.078 g	0.075 g
3	0.3	Bidirectional	12.5%	0.110 g (y) 0.078 g (x)	0.114 g (y) 0.072 g (x)
4	1.1	$y$	25%	0.219 g	0.170 g
5	1.2	$x$	25%	0.156 g	0.178 g
6	1.3	Bidirectional	25%	0.219 g (y) 0.156 g (x)	0.208 g (y) 0.174 g (x)
7	2.1	$y$	50%	0.438 g	0.593 g
<b>Specimen strengthened</b>					
8	2.1S	$y$	50%	0.438 g	0.615 g
9	1.2S	$x$	25%	0.156 g	0.258 g
10	2.2S	$x$	50%	0.313 g	0.425 g

Table 3.7: List of experimental results compared with blind predictions by participants to account for differences between nominal and effective shake-table accelerations.

Experimental result for run	Blind prediction for run	Quantities compared
1.3	1.3	BSx, BSy, Rd1, Rd2, Rd3, Rd4, Rd5, Rd6, Id1, Id2, Id3, Id4
2.1	3.1	BSy, Rd2, Id3
2.2S	3.2	BSx, Rd3, Id4

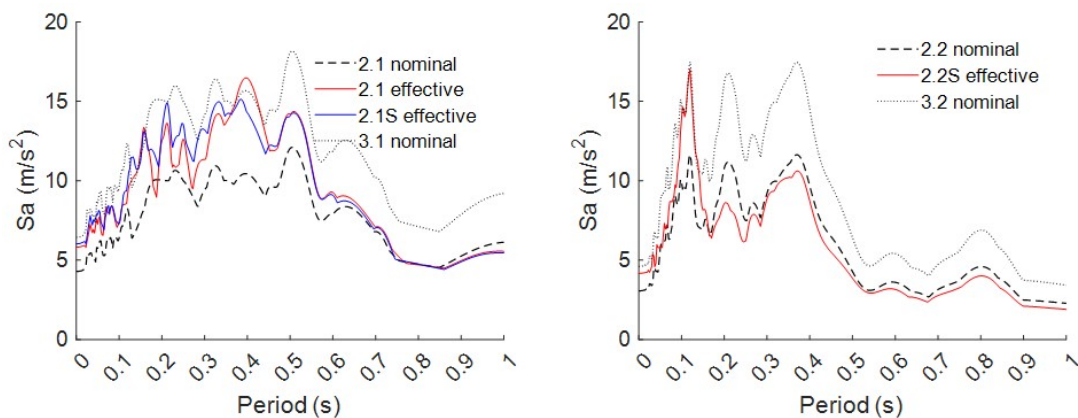


Figure 3.8: Comparison of response spectra for selected nominal and effective records in the SERA AIMS shake-table test in Tomić et al. (2022a).

### 3.3 Blind prediction submissions

To derive conclusions about the influence of modelling uncertainties on the response of the models, this section first presents the submitted models by describing the modelling approach and assumptions with regard to floors, floor-to-wall connections, wall-to-wall connections, unit-to-unit connections and damping. Second, we present a statistical representation of the reported results in terms of roof displacements, interface openings and base-shear forces. To derive conclusions on the general trend that modelling approaches or assumptions exert on the results in terms of roof displacements, interface openings and base-shear forces, statistical plots are used to compare the overall values with the values from the models using some of the previously described modelling assumptions, and with the experimental results. Third, we compare the damage mechanisms reported by the participants with the actual observed mechanisms.

#### 3.3.1 Submitted models

In total, 12 groups with 10 coming from academia and two from industry submitted a total of 13 models. Here, submissions are split by modelling approach and presented using tables to show modelling assumptions considered essential for the further processing of the results. Each of the important modelling choices is described in more detail. Figure 3.9 shows all the submitted models.

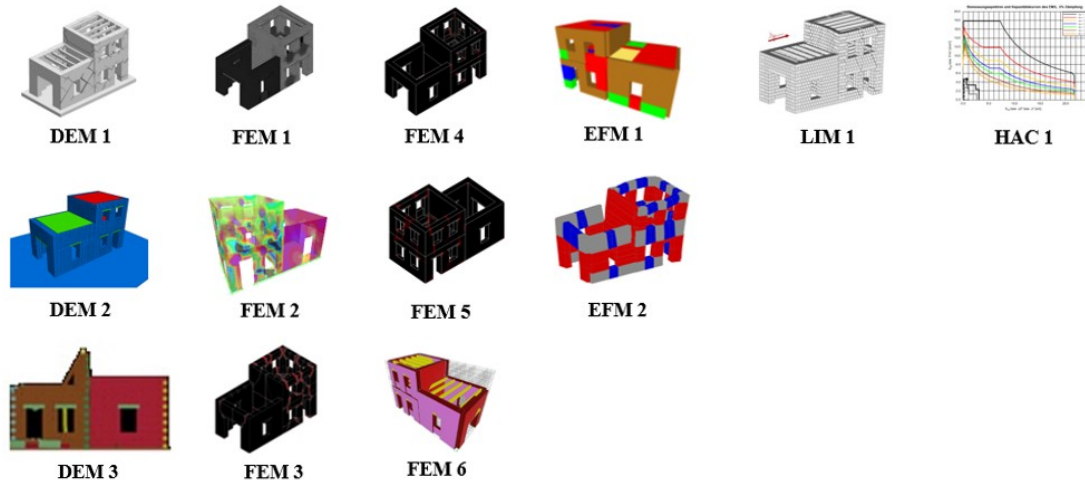


Figure 3.9: Models submitted to the SERA AIMS blind prediction competition.

Three participating groups submitted models using DEM or Finite-Discrete element method (FEM-DEM) using 3DEC (Itasca, 2013) and LS-DYNA (Jo, 2006) software, which modelled the material as an assemblage of either rigid (DEM) or deformable (FEM-DEM) discrete elements with discontinuities at their boundaries. For the sake of simplicity, the nomenclature “DEM” will be used for indicating all three submissions hereinafter. The DEM 1 was developed

according to the Macro-Distinct Element Model (M-DEM), a new hybrid FEM-DEM macro-element approach (Malomo and DeJong, 2021) where each URM member is idealized an assembly of deformable FE macro-blocks connected through zero-thickness nonlinear spring layers. Two submissions (DEM 2, DEM 3) used the simplified micro-modelling technique that does not explicitly model mortar, but instead lumps mortar properties at interfaces (P. J. B. B. Lourenço, 1997), modelling each unit separately, albeit according to an equivalent masonry pattern. All the three DEM submissions modelled explicitly the two units. DEM 1 modelled floors using deformable 3D joists and link elements accounting for the in-plane stiffness of the diaphragms. DEM 2 modelled the floor slabs and beams as rigid blocks. DEM 3 modelled beams as 3D elastic elements, while the planks were not modelled. Here, the participant elaborated that, considering that the floor is very flexible, the planks were not modelled to avoid elements with small dimensions considering that the smallest finite element governs the time step in an explicit analysis, which increases the computational time (AlShawa et al., 2017). All three participants explicitly modelled floor-to-wall connections with the same interface that was used to model the connections between the blocks. DEM 2 used the same parameters for the connections between blocks and floor-to-wall and unit-to-unit connections, whereas DEM 3 used a lower tensile strength for the latter two connections. DEM 1 used the same parameters for floor-to-wall connections and connections between blocks, while the unit-to-unit connection was modelled with zero cohesion and tensile strength (compression-shear). Damping varied both in terms of whether it was mass proportional (DEM 1, DEM 2) or stiffness proportional (DEM 3) and with regards to the critical damping ratio. DEM 2 progressively lowered the damping ratio to compensate for an increase in the mass-proportional damping as damage appeared and period of the structure elongated. Table 3.8 summarizes modelling assumptions for the DEM submissions.

Table 3.8: Modelling assumptions for blind submissions to the SERA AIMS project based on Discrete - Finite Element Models (DEM-FEM).

Submission	Walls	Floors	Connections			Damping
			Wall-to-wall	Floor-to-wall	Unit-to-unit	
DEM 1	Finite-Discrete elements	Elastic beams and link elements for diaphragms	Nonli near	Nonli near	Compression -shear	Mass proportional; 4% critical damping ratio
DEM 2	Discrete elements	Rigid beams and floor slabs	Nonli near	Nonli near	Compression -shear	Mass proportional; critical damping ratio progressively reduced between runs; initially between 2% and 2.5%
DEM 3	Finite-discrete elements	Elastic beams only	Nonli near	Nonli near	Compression -shear	Stiffness proportional; 5% critical damping ratio

With six submissions, shell and solid FEM models were the most popular approach. In these models, masonry is represented as a homogenous continuous material, discretized into a mesh of finite elements of various sizes, and the nonlinear behaviour is described by material laws. Modelling choices concern the choice of element type and size, the meshing algorithm,

the integration scheme, etc. Four of these submissions featured solid FEM models, of which two used DIANA (DIANA, 2017) and two OpenSEES (McKenna et al., 2000). Two submissions feature shell FEM models using Computers and Structures (2011). FEM 1 and FEM 3 used the total strain-based crack constitutive model for masonry, with exponential and parabolic behaviour in tension and compression, respectively (P. J. B. B. Lourenço, 1997). A rotating crack orientation was selected following the coaxial stress-strain approach, where stress-strain relations were evaluated in the principal directions of the strain vector. FEM 4 and FEM 5, the same model with and without floors, used a material model for masonry based on Faria et al. (1998). FEM 2 modelled the masonry as elastic/perfectly plastic in compression. In tension, masonry was modelled as linear elastic up to a cracking strain. For larger strains, a damage material law was assumed. FEM 6 did not provide additional information on the masonry material model. The submissions differed from each other with regard to assumptions for modelling floors and floor-to-wall connections. FEM 3 and FEM 5 did not model floors, ignoring their effect and replacing them with tributary masses. On the other extreme, FEM 2 modelled floors as a rigid diaphragm by applying a diaphragm constraint in their chosen software. FEM 1 modelled floors using a linear elastic orthotropic shell membrane with equivalent properties accounting for both the beams and planks, and nonlinear elastic floor-to-wall connections with normal stiffness tending to zero after exceeding a certain threshold value. FEM 4 modelled timber beams as elastic trusses, choosing a beam material that was elastic isotropic, while the planks were neglected and not modelled. The floor-to-wall connection was modelled by elastic/perfectly plastic behaviour, with material collapse after a peak displacement level. The material model accounts for pinching and cyclic degradation. The hysteretic rules were calibrated based on floor-to-wall pull-out experiments (Moreira, 2015). FEM 6 also modelled only elastic beams, but with rigid floor-to-wall connections and without transferring the bending moments. The models differed also with regards to modelling the unit-to-unit interface. Only one participant modelled the units as separated (FEM 3). Two participants modelled the interaction only in compression (FEM 2, FEM 6), with the latter also modelling a gap/separation of 3 mm. Three participants (FEM 1, FEM 4, FEM 5) modelled the connection between units as a nonlinear 3D surface accounting for both the Mode I and Mode II failure at the interface (compression-shear) (Walter et al., 2005). All submissions included mass and stiffness proportional Rayleigh damping, with critical damping ratios often set to 3% (FEM 3, FEM 4, FEM 5) and 5% (FEM 2, FEM 6). An outlier was FEM 1 with a damping ratio of 10% to balance the underestimation of dissipated energy at the material level, as reported by the participant. Table 3.9 summarizes modelling assumptions for FEM.

Table 3.9: Modelling assumptions for blind submissions to the SERA AIMS project based on Finite Element Models (FEM).

Participant	Walls	Floors	Connections			Damping
			Wall-to-wall	Floor-to-wall	Unit-to-unit	
FEM 1	Solid FEM	Linear elastic orthotropic shell elements	Rigid	Nonlinear elastic	Compression-shear	Mass and stiffness proportional; 10% critical damping ratio
FEM 2	Shell FEM	Rigid; diaphragm constraint applied	Rigid	Rigid	Compression-only	Mass and stiffness proportional; 5% critical damping ratio
FEM 3	Solid FEM	Not modelled	Rigid	No floors	No connection	Mass and stiffness proportional; 3% critical damping ratio
FEM 4	Solid FEM	Timber beams modelled as elastic trusses	Rigid	Nonlinear	Compression-shear	Mass and stiffness proportional; 3% critical damping ratio
FEM 5	Solid FEM	Not modelled	Rigid	No floors	Compression-shear	Mass and stiffness proportional; 3% critical damping ratio
FEM 6	Shell FEM	Elastic beams only	Rigid	Rigid	Compression-only	Mass and stiffness proportional; 5% critical damping ratio

Though the use of EFM dominated in previous studies, only two participants submitted EFM predictions for this study, which were done using in-house and OpenSEES (McKenna et al., 2000) software. In these models, the structure was discretized into piers, spandrels and rigid nodes on the structural element level (Bracchi et al., 2015; Quagliarini et al., 2017). EFM 1 modelled the piers and spandrels with beams using the concentrated plasticity approach. The out-of-plane (OOP) mechanism was accounted for using a series of representative pin-ended column elements that were geometrically defined to reflect the expected one-way out-of-plane mechanism and wall section, with an appropriate tributary mass and stiffness. The capacity of the column was independent of the in-plane wall actions (similarly the in-plane capacities were treated as independent of the out-of-plane response). However, to impose the correct displacements, the out-of-plane column was slaved to the relevant floor levels. The capacity of the out-of-plane wall elements was defined a priori using a nonlinear kinematic approach, with out-of-plane collapse assumed to occur when mid-height displacements exceeded the wall thickness. Where parapet behaviour occurred, the out-of-plane displacement limit was taken as the wall thickness. Floors were modelled as nonlinear plane stress finite elements. The floor model assumed that the elements maintained their strength after yielding, but the stiffness was reduced as a function of the maximum deformation. The floor-to-wall and wall-to-wall connections were modelled as rigid, and the unit-to-unit connection was modelled with gap elements that could transfer only compression forces but no shear or tension forces. The compression stiffness of the gap element was calibrated based on: (i) the shear depth of the adjacent Unit 1 and Unit 2 piers, (ii) the pier wall thickness and (iii) the given masonry Young's modulus value. Mass and initial stiffness proportional damping was used with a 3% critical damping ratio. EFM 2 used a newly developed macro-element (Vanin et al., 2020a) to simultaneously model in-plane and out-of-plane behaviour. Floors were modelled as linear

orthotropic shell membranes, with nonlinear sliding floor-to-wall connections. Nonlinear interfaces were also used for wall-to-wall and unit-to-unit connections. Mass and initial stiffness damping was used together with a 1% critical damping ratio to avoid overdamping of the out-of-plane behaviour. Table 3.10 summarizes the modelling assumptions for EFM.

Table 3.10: Modelling assumptions for the blind submissions to the SERA AIMS project based on Equivalent Frame Models (EFM).

Participant	Walls	Floors	Connections			Damping
			Wall-to-wall	Floor-to-wall	Unit-to-unit	
EFM 1	Piers and spandrels modelled using beams with concentrated plasticity	Nonlinear plane stress finite elements	Rigid	Rigid	Compression-only	Mass and initial stiffness proportional; 3% critical damping ratio
EFM 2	Piers and spandrels modelled as macro-elements	Linear elastic orthotropic shell	Nonlinear	Nonlinear	Compression-shear	Mass and initial stiffness proportional; 1% critical damping ratio

Finally, one participant submitted a prediction using a simple design code-based spreadsheet calculation (also referred to as hand-calculation, HAC, or analytical approach), and one participant submitted a prediction through a limit analysis (LIM) approach using the LiABlock 3D software (Cascini et al., 2018). HAC 1 used the capacity spectrum method, performing a pushover analysis with Acceleration Displacement Response Spectrum (ADRS) (Freeman, 1998). Only the ground floors were modelled, meaning that failures and nonlinearities were concentrated at the ground floor in this approach, with extrapolated roof displacements. The effective stiffness was reduced according to SIA 269/8 (Wenk, 2014), the shear capacity was calculated according to SIA 266 (Pfyl-Lang et al., 2009), and the drift capacity was chosen according to Vanin et al. (2017b). There were no connections between walls or units, neglecting the rotation, and floors were replaced with tributary masses.

LIM 1 predicted the aggregate response using rigid block limit analysis by mathematical programming. The structure was idealized into a three-dimensional assemblage of rigid blocks interacting via no-tension frictional interfaces, with zero cohesion and infinite compressive strength. The sliding failure was governed by a Coulomb friction criterion with zero cohesion. The beams were modelled as rigid with unilateral floor-to-wall connections, which matched what was done for the rest of the interfaces. The unit-to-unit connection used the same interfaces, but the interaction at the head joints was only considered for this connection. Table 3.11 summarizes the modelling assumptions for the approaches based on spreadsheet analysis method and limit analysis.

Table 3.11: Modelling assumptions for the blind submissions to the SERA AIMS based on analytical approach and limit analysis.

Participant	Walls	Floors	Connections			Damping
			Wall-to-wall	Floor-to-wall	Unit-to-unit	
HAC 1	Hand calculation	Not modelled	No connection	No floors	No connection	Damping ratio of nonlinear ADRS spectra = 5%
LIM 1	Rigid blocks	Rigid beams	Nonlinear	Nonlinear	Compression-shear	None

### 3.3.2 Statistical evaluation of blind prediction submissions

Here we present the submitted maximum absolute values of the recorded relative displacements of the units in relation to the ground (Rd1-6), interface openings (Id1-4) and total base-shear forces (BSx, BSy) using statistical methods for each step. The displacements and interface openings are shown in Figure 3.10. Then, the values of Rd2, Rd3, Id3, Id4, BSx, and BSy for Run 3.1 and 3.2 predicted by each participant are grouped by a modelling approach or assumption. These values are then compared with statistical representation (using boxplots) of all submissions and with the values from the comparable experimental runs. Roof displacement, interface opening, and the base shear are considered both in the longitudinal and in the transversal directions. The values reported by each participant are classified according to the following five properties of a model: (i) model class, (ii) unit-to-unit connection, (iii) floor model, (iv) floor-to-wall connection and (v) wall-to-wall connection.

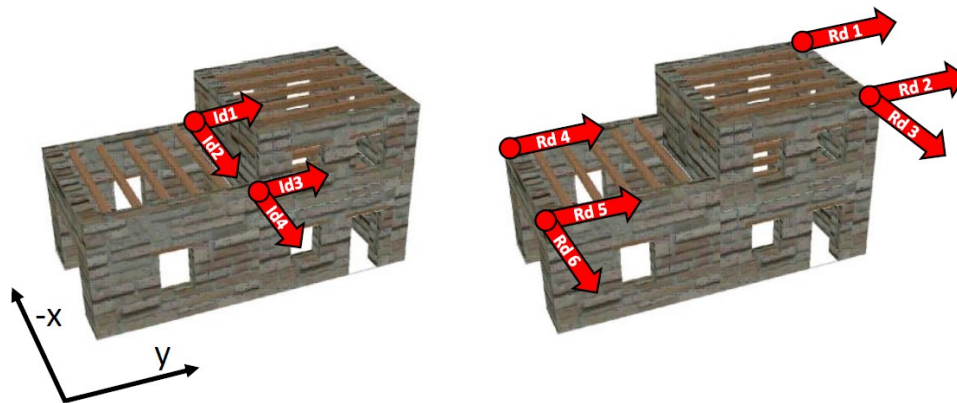


Figure 3.10: Compared quantities for the blind prediction submissions. Displacements relative to the ground (Rd1-6) and interface opening (Id1-4).

First, Figure 3.11 shows the scatter of maximum values through the test steps, compared with the values from the corresponding experimental runs. The red mark indicates the median, and the box edges indicate the 25th and 75th percentile, respectively. The whiskers extend to the most extreme data points not considered outliers. The outliers are plotted separately

using the '+' symbol. Already for Step 1.3, the results tend to scatter significantly, and this scatter increases through the runs. The scatter is more significant for roof displacements and interface openings than for base-shear forces.

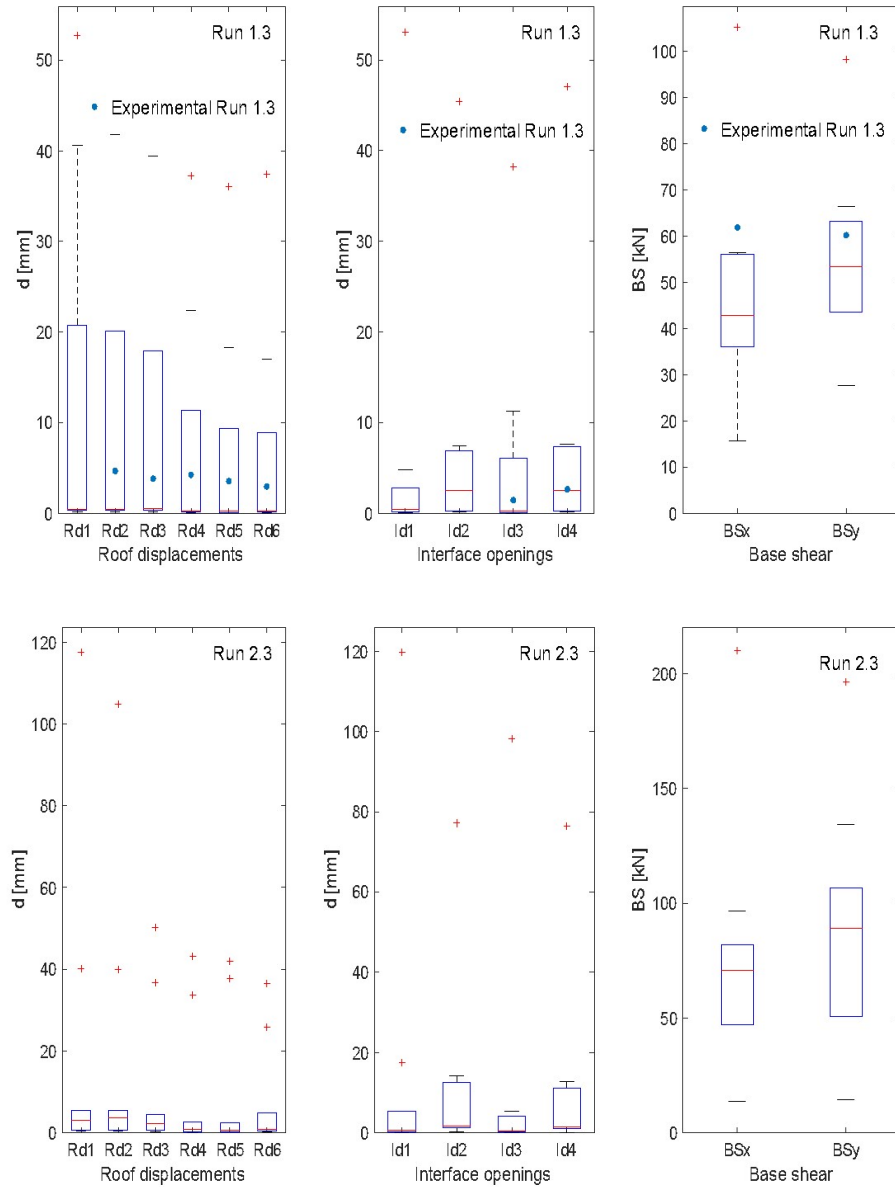


Figure 3.11: Statistical representation of the results of the blind prediction submissions in terms of peak roof displacements, interface openings and peak base-shear forces for Runs 1.3, 2.3, 3.3 and 4.3. Blind prediction Run 1.3 is compared with experimental Run 1.3.



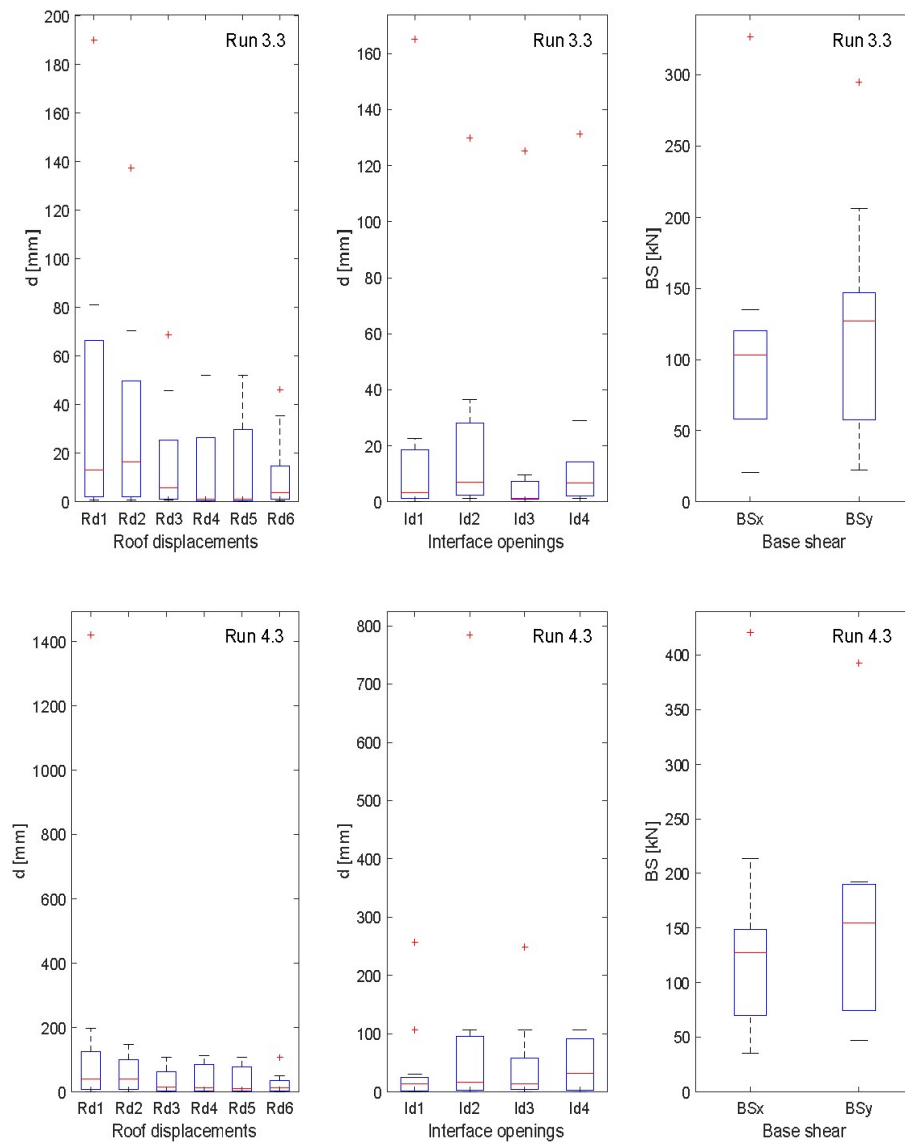


Figure 3.11 (Continued): Statistical representation of the results of the blind prediction submissions in terms of peak roof displacements, interface openings and peak base-shear forces for Runs 1.3, 2.3, 3.3 and 4.3. Blind prediction Run 1.3 is compared with experimental Run 1.3.

Figure 3.12 shows the reported values of Rd2, Rd3, Id3, Id4, BSx, and BSy grouped according to the model class, compared with the values from the corresponding experimental runs. On average, the DEM models predict larger displacements and interface openings and lower base shear forces than the rest of the models, partially due to an outlier. All shown DEM results are outside the 25th to 75th percentile range of the predicted values but are in fact the only models to correctly capture the order of magnitude of the experimentally measured displacements.

Conversely, the shell and solid FEM models show the lowest displacements and interface openings and the highest base shear forces on average, indicating that the stiffness of the aggregate was probably overestimated. Also, it should be kept in mind that in continuous FEM models it is not possible to simulate the separation of masonry portions, therefore the displacements are limited. The majority of the shell FEM models are also either close to or outside the 25th to 75th percentile range of predicted values, but on the opposite side as the DEM models. On average, the EFM models seem to be closer to the median values, but median values were not close to the experimental values. We also calculated the CoV values for predictions using the same model class for Runs 3.1 and 3.2, for model classes with more than one submission (EFM, shell FEM, solid FEM, DEM). However, Table 3.12 shows that CoV values did not show any clear trend and varied largely between predicted quantities. Only on the average the CoV values of the solid FEM model were lower than those of other model classes. However, these four solid FEM models were submitted by members of the same research group. CoV values computed for all submissions together were large with a CoV of 160%-268% for displacement quantities and a CoV of 58%-74% for base shears at near collapse. The largest CoV values were obtained for the interface openings, highlighting that the interaction between the units of an aggregate is very difficult to predict. These values are higher than those of previous blind prediction studies. Mendes et al. (2017) reported a CoV of 39%-63% for the predicted PGA at collapse and Esposito et al. (2019) a CoV of 51% for the predicted peak strength and 41% for the predicted displacement at near collapse. The values of the SERA-AIMS study might be higher because the analysed structure is significantly more complex than the specimens tested in Mendes et al. (2017) and Esposito et al. (2019) (Table 3.1).

Table 3.12: CoV values for predictions grouped using the same model class for Runs 3.1 and 3.2

	<b>DEM</b>	<b>Shell FEM</b>	<b>Solid FEM</b>	<b>EFM</b>
<b>Rd2</b>	80.8%	16.3%	49.9%	17.9%
<b>Rd3</b>	63.1%	71.1%	10.0%	81.2%
<b>Id3</b>	127.7%	133.0%	57.2%	53.2%
<b>Id4</b>	123.6%	27.6%	106.9%	127.5%
<b>BSx</b>	91.2%	67.1%	4.8%	16.3%
<b>BSy</b>	105.7%	49.3%	5.7%	8.5%
<b>Mean</b>	98.7%	60.7%	39.1%	50.8%

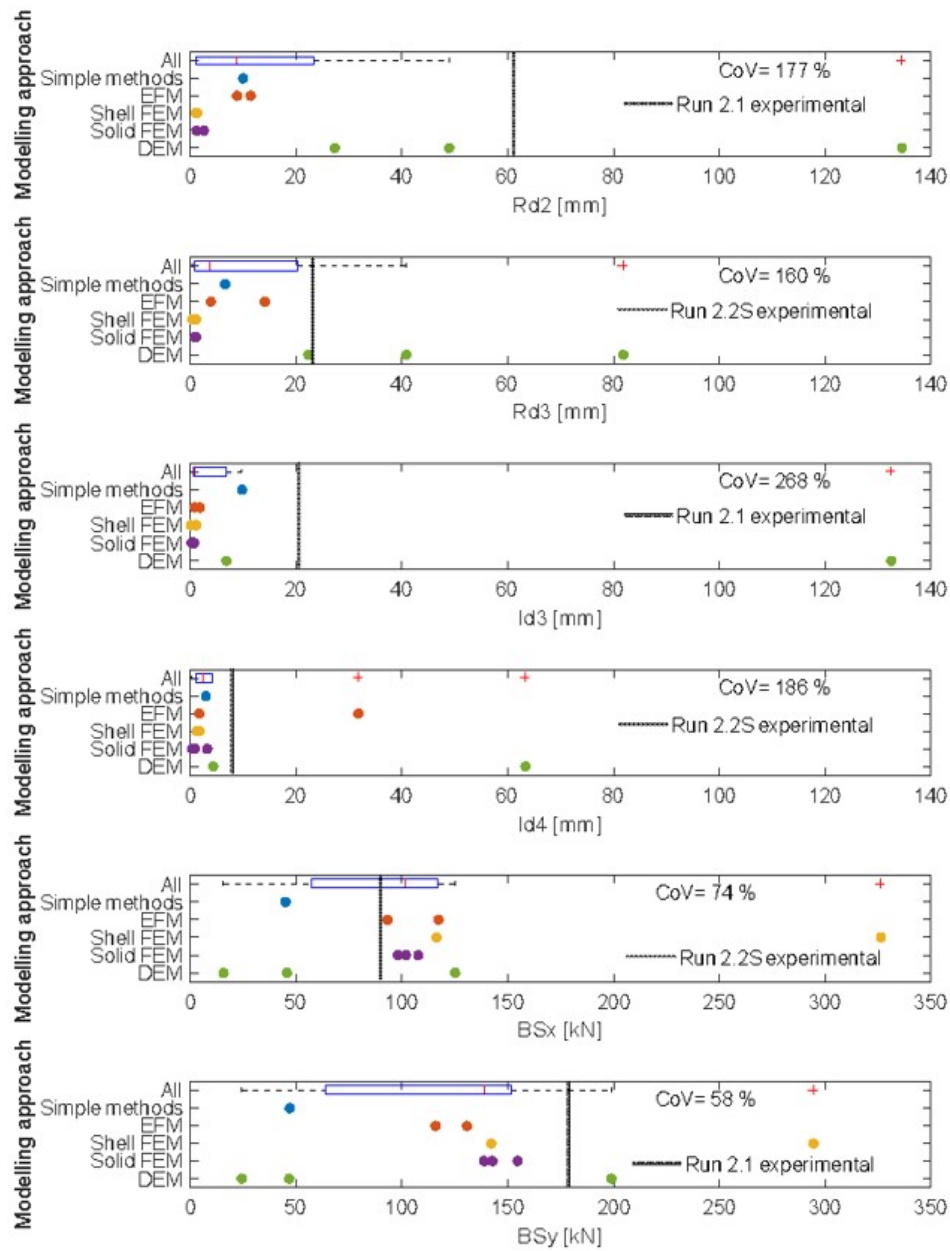


Figure 3.12: Reported Rd2, Rd3, Id3, Id4, BSx, and BSy values for Runs 3.1 and 3.2 from the blind prediction submissions grouped according to the modelling approach, compared with the values from the corresponding experimental runs. The reported CoV value is related to all submissions.

Figure 3.13 shows the reported values of Rd2, Rd3, Id3, Id4, BSx, and BSy grouped by the unit-to-unit connection type, compared with the values from the corresponding experimental runs. Models were separated in three groups. The models in the first group considered the units as completely separate, with no interaction. The models in the second group accounted for Mode 1 (interaction in compression) only, ignoring interaction in the transversal direction. The

models in the third group included both Mode 1 and Mode 2 interaction (interaction in shear) by the transfer of compression and shear forces, where the maximum shear force is a function of the compression force. Some of these models also included tensile strength, which was small and therefore ignored in defining the model categories. Models with a compression-shear unit-to-unit interface show on average larger roof displacements and interface openings and lower base-shear forces than models with a compression-only interface, which is unexpected. It would be expected that models with no interaction or compression-only interaction would on average produce larger transversal openings of the interface (Id4), but this was not the case probably because of the generally stiff behaviour of these models. It is worth noting that just two models did not model the interaction between the two units, and they also differed in modelling approach (hand calculation method versus solid FEM model).

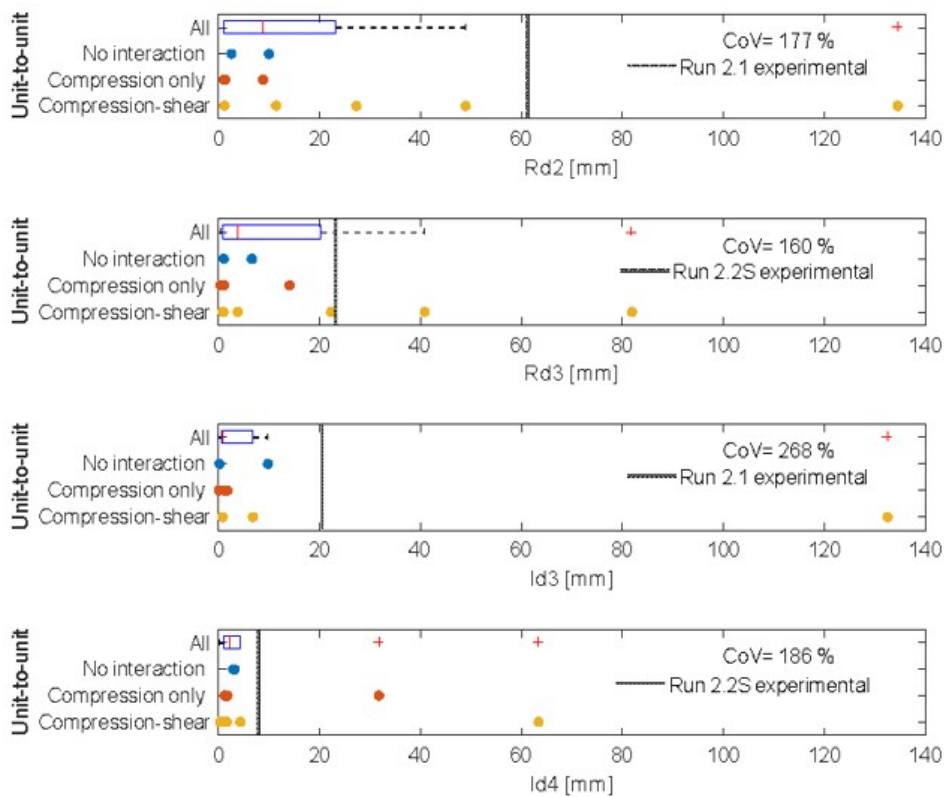


Figure 3.13: Reported Rd2, Rd3, Id3, Id4, BSx, and BSy values for Runs 3.1 and 3.2 from the blind prediction submissions grouped according to unit-to-unit connection type, compared with the values from the corresponding experimental runs. The reported CoV value is related to all submissions.

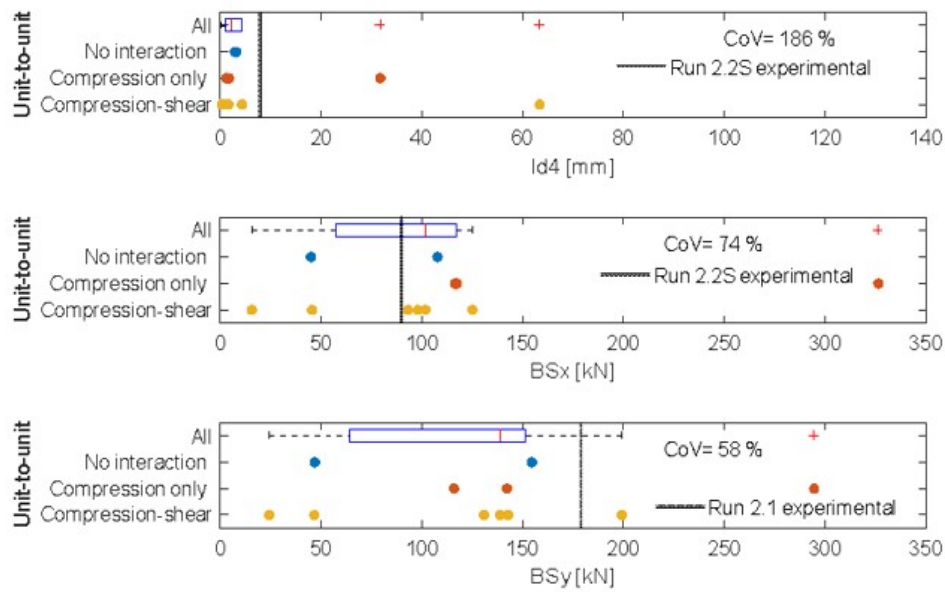


Figure 3.13 (Continued): Reported  $Rd_2$ ,  $Rd_3$ ,  $Id_3$ ,  $Id_4$ ,  $BS_x$ , and  $BS_y$  values for Runs 3.1 and 3.2 from the blind prediction submissions grouped according to unit-to-unit connection type, compared with the values from the corresponding experimental runs. The reported CoV value is related to all submissions.

Figure 3.14 shows the reported values of  $Rd_2$ ,  $Rd_3$ ,  $Id_3$ ,  $Id_4$ ,  $BS_x$ , and  $BS_y$  grouped by floor type, compared with the values from the corresponding experimental runs. The model featuring rigid floors shows the lowest roof displacements and interface openings—close to the 25th percentile, with a base-shear force close to the 75th percentile of the predicted values. However, there is just one model featuring this property. The models with no floors average lower displacements and similar interface openings and base-shear forces compared to the models featuring flexible floor diaphragms. This is surprising as we would have expected that models with no floors lead to larger displacements than models that include the diaphragm. However, the effect of the diaphragm might have been minor because the structure was symmetric in the  $x$ -direction. Finally, comparing models featuring only beams with those featuring the entire diaphragm (therefore including the shear stiffness of the floor) presents inconclusive results due to exceptionally high scatter within the group of teams that modelled only the beams.

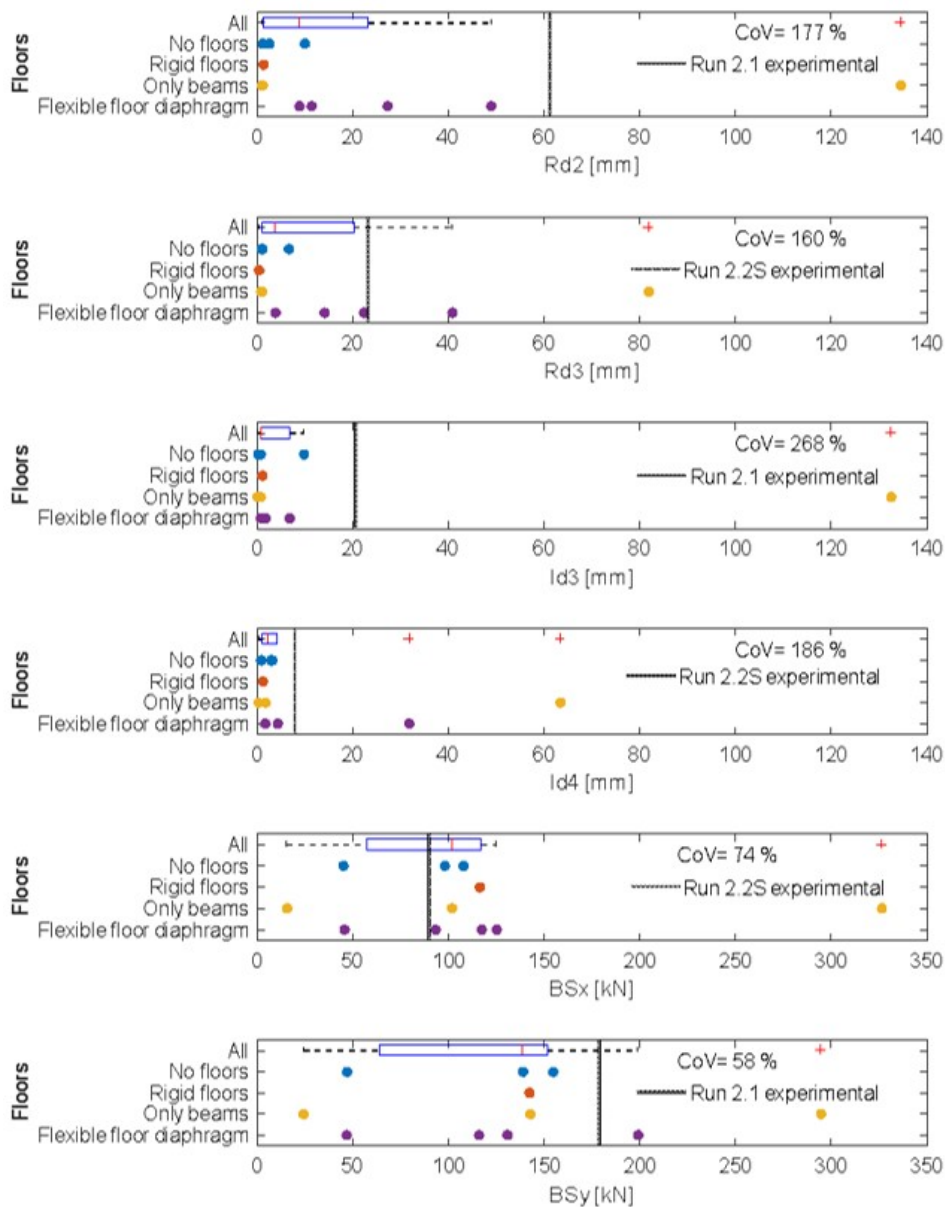


Figure 3.14: Reported Rd2, Rd3, Id3, Id4, BSx, and BSy values for Runs 3.1 and 3.2 from the blind prediction submissions grouped according to floor type, compared with the values from the corresponding experimental runs. The reported CoV value is related to all submissions.

Figure 3.15 shows the reported values of Rd2, Rd3, Id3, Id4, BSx, and BSy grouped by the floor-to-wall connection type, compared with the values from the corresponding experimental runs. The models featuring rigid floor-to-wall connections show lower roof displacements and interface openings (close to 25th percentile on average) as well as higher base-shear forces (on average larger than 75th percentile). The opposite applies for the models with nonlinear floor-to-wall connections. There are no values reported for the models with elastic floor-to-wall connections, as they only reported the results starting at Run 4.1 (100% shake-table capacity).

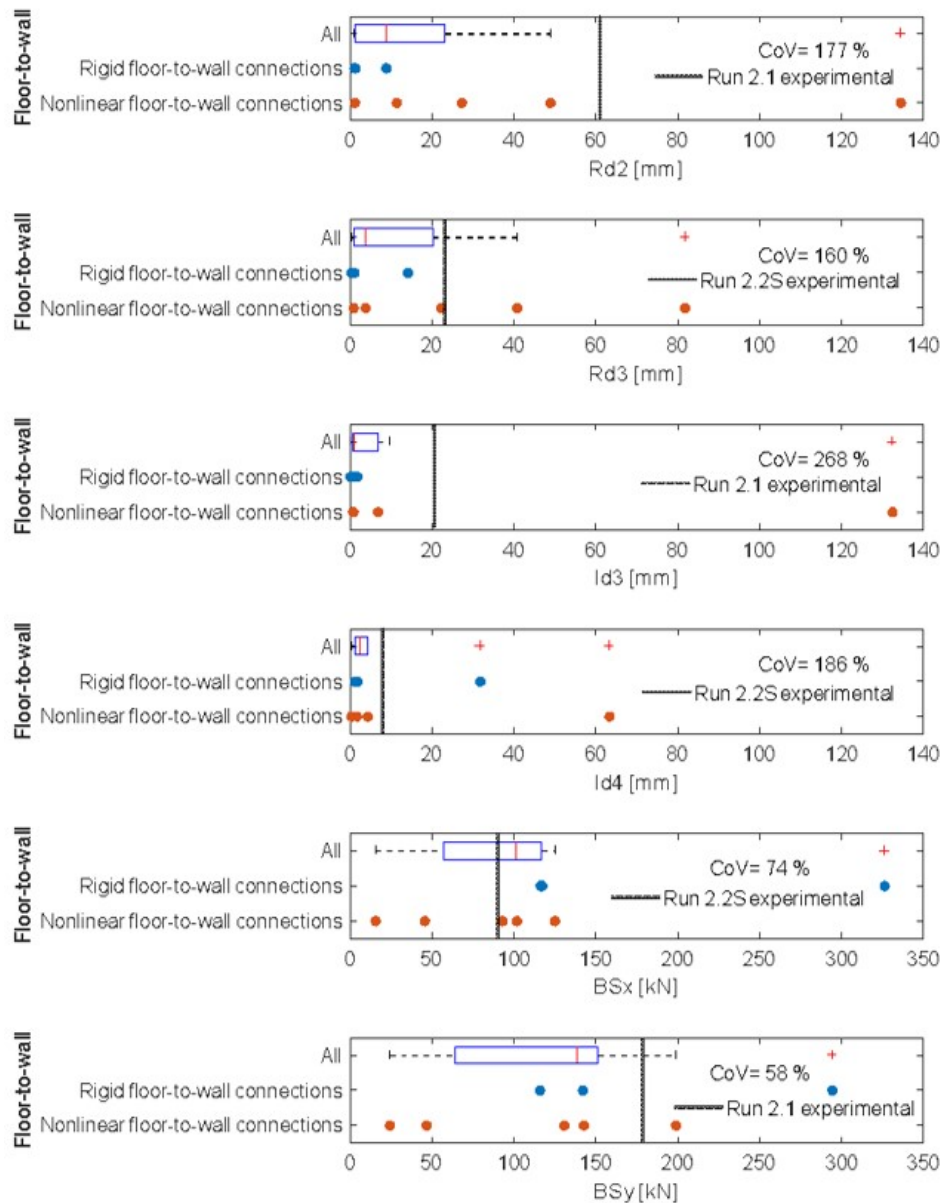


Figure 3.15: Reported  $Rd2$ ,  $Rd3$ ,  $Id3$ ,  $Id4$ ,  $BSx$ , and  $BSy$  values for Runs 3.1 and 3.2 from the blind prediction submissions grouped according to floor-to-wall connection type, compared with the values from the corresponding experimental runs. The reported CoV value is related to all submissions.

Figure 3.16 shows the reported values of  $Rd2$ ,  $Rd3$ ,  $Id3$ ,  $Id4$ ,  $BSx$ , and  $BSy$  grouped by the wall-to-wall connection type, compared with the values from the corresponding experimental runs. The models featuring nonlinear wall-to-wall connections show on average larger roof displacements and interface openings and lower base-shear forces than those with rigid wall-to-wall connections. However, in case of interface openings and base shear, this behaviour largely stems from an outlier with nonlinear wall-to-wall connections for interface openings,



and an outlier with rigid wall-to-wall connections for base shear. Without outliers, the two groups of models would on average yield similar results in these two categories.

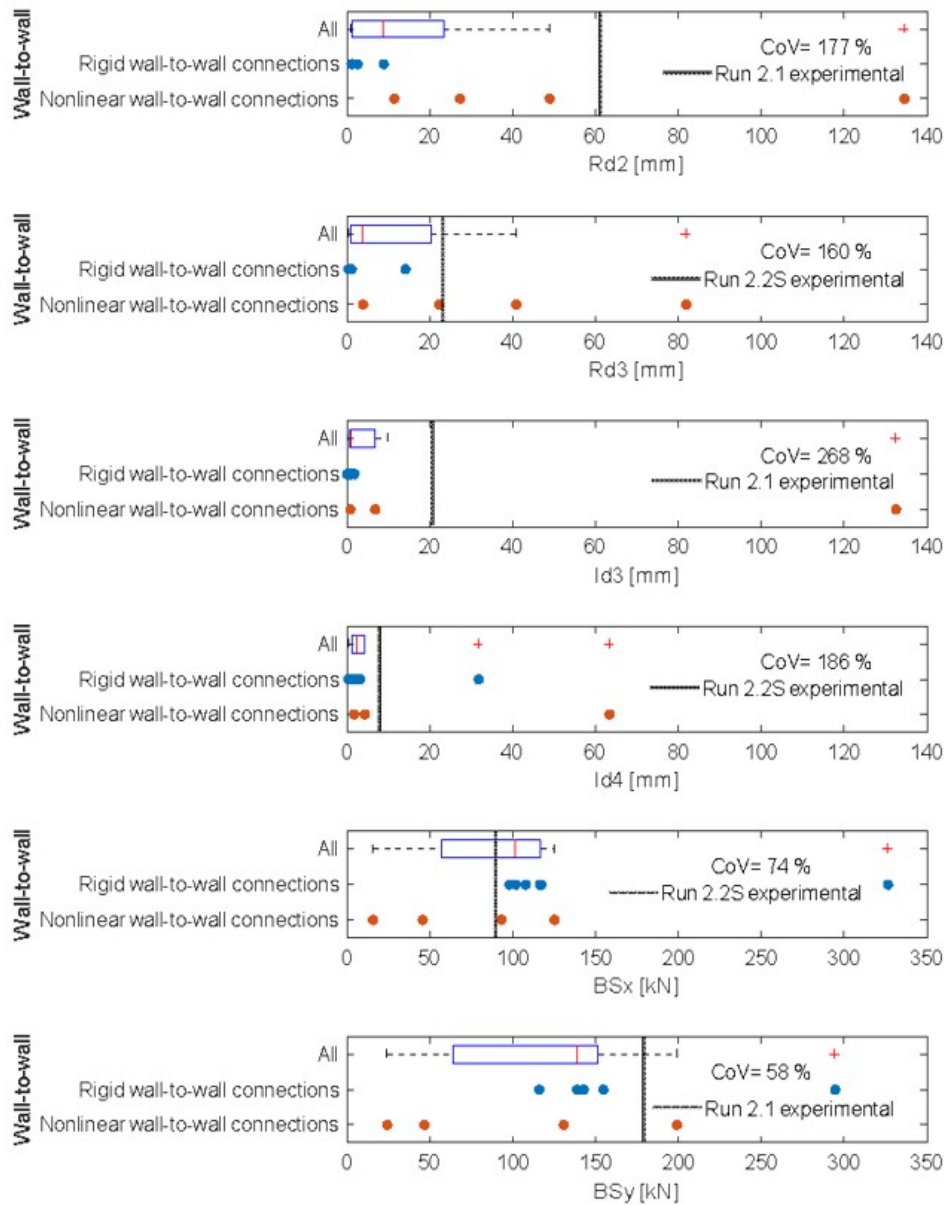


Figure 3.16: Reported Rd2, Rd3, Id3, Id4, BSx, and BSy values for Runs 3.1 and 3.2 from the blind prediction submissions grouped according to wall-to-wall connection type, compared with the values from the corresponding experimental runs. The reported CoV value is related to all submissions.

Figure 3.17 shows the reported values of Rd2, Rd3, Id3, Id4, BSx, and BSy grouped by the Rayleigh damping ratio, compared with the values from the corresponding experimental runs. The models do not show any correlation between the reported values and damping



ratio. However, the model with 10% damping ratio predicted almost no damage even at 100% acceleration values, and therefore has reported values starting with Run 4.1.

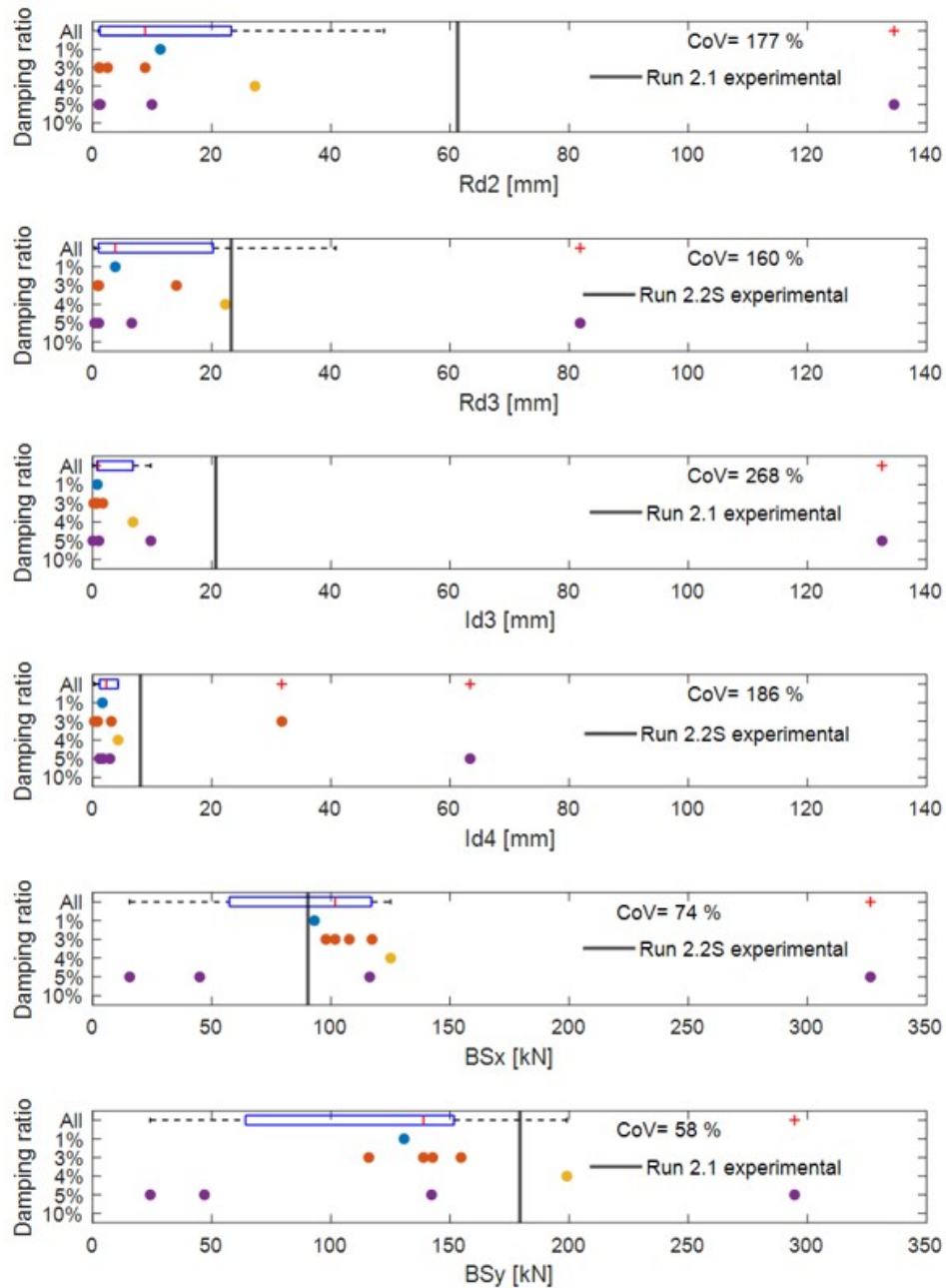


Figure 3.17: Reported Rd2, Rd3, Id3, Id4, BSx, and BSy values for Runs 3.1 and 3.2 from the blind prediction submissions grouped according to Rayleigh damping ratio, compared with the values from the corresponding experimental runs. The reported CoV value is related to all submissions.

3.3.3 Qualitative description of the damage mechanisms

A qualitative evaluation was performed that compared the predicted damage mechanisms with the one observed in the experimental campaign. We analysed the damage mechanisms reported after Step 3 (75% shake-table capacity), as they were the closest match to the actual Runs 2.1 and 2.2S in terms of response spectrum and PGA. Figure 3.18 shows the illustrative possible damage mechanisms. Therefore, Tables 3.31 - 3.43 in the appendix show the following rows for each participant: (i) image reporting the damage in the model (if applicable); (ii) short resume of predicted damage mechanisms reported by participant; (iii) qualitative comparison of the reported damage mechanisms to those observed in the experimental campaign.

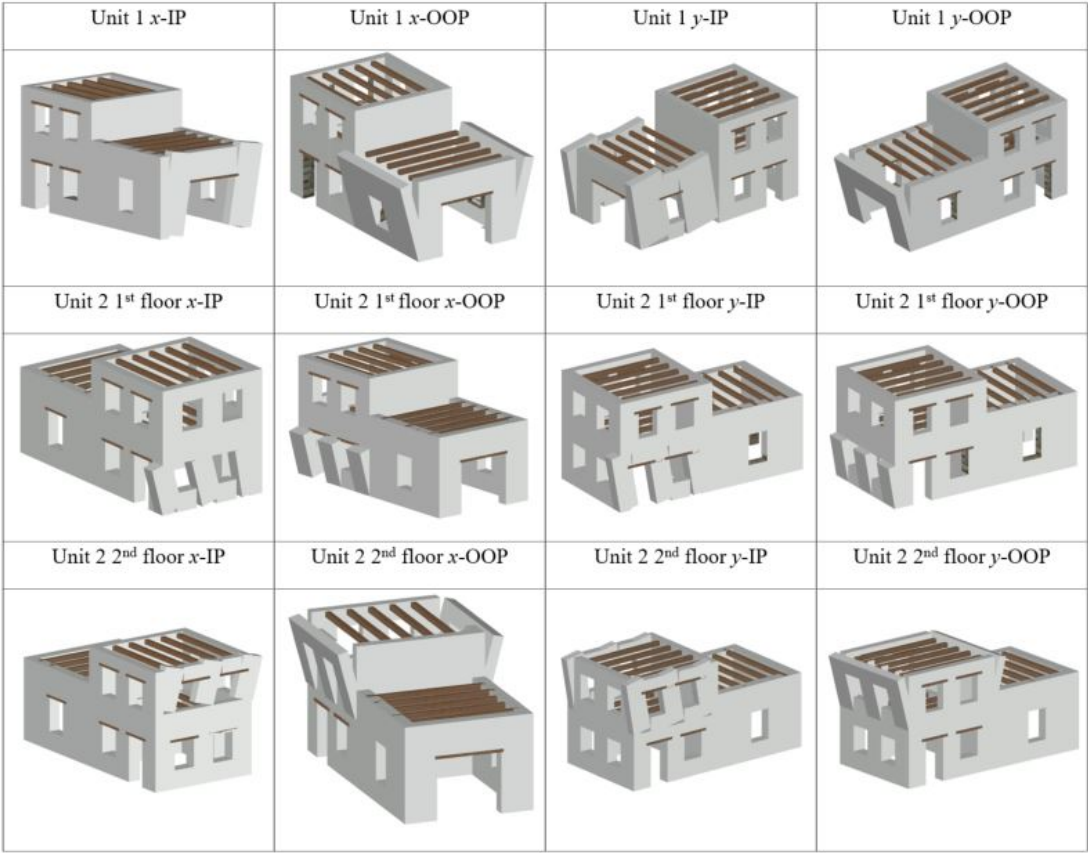


Figure 3.18: Illustrative description of damage mechanisms. It should be noted that in-plane damage mechanisms were always illustrated as flexural mechanisms. Actual observed behaviour in the experiment was always flexural, so if a participant reported in-plane shear damage, it was counted as incorrect prediction.

Table 3.13 reviews the types of damage mechanisms reported by the participants split by unit, storey, direction and failure mode in terms of in-plane (IP) and out-of-plane (OOP) mechanism. Correctly predicted mechanisms are indicated by a green circle, and incorrectly predicted mechanisms are indicated by a red circle. Failure to indicate a correct mechanism is

marked by a red x. Finally, correct predictions, false positive, and false negative predictions are summarised at the bottom rows. Not many participants correctly predicted in-plane and out-of-plane mechanisms in the x-direction of Unit 1, though a majority correctly predicted both in-plane and out-of-plane mechanisms in the y-direction of Unit 2 for both storeys. This response was the principal mechanism of the tested aggregate, so this prediction was key to correctly capturing the experimental behaviour. A common mistake was a prediction of in-plane damage in the x-direction of Unit 2 for both storeys, which was not observed in the tests.

Unit and storey	Direction and failure mode	D E M 1	D E M 2	D E M 3	F E M 1	F E M 2	F E M 3	F E M 4	F E M 5	F E M 6	E F M 1	E F M 2	H A C 1	L I M 1
Unit 1	x-IP	x	x	x	x	●	●	x	●	x	x	●	●	●
Unit 1	y-IP	●								●			●	
Unit 1	x-OOP	x	x	x	x	●	x	x	x	x	●	●	x	●
Unit 1	y-OOP		●											
Unit 2 1 <sup>st</sup> floor	x-IP	●	●			●	●	●		●	●		●	
Unit 2 1 <sup>st</sup> floor	y-IP	●	●	●	x	x	●	x	x	●	●	●	●	●
Unit 2 1 <sup>st</sup> floor	x-OOP													
Unit 2 1 <sup>st</sup> floor	y-OOP	●	●	x	x	x	●	●	x	x	●	●	x	●
Unit 2 2 <sup>nd</sup> floor	x-IP	●	●			●	●		●		●	●		
Unit 2 2 <sup>nd</sup> floor	y-IP	●	●	●	x	x	●	●	●	x	●	●	x	●
Unit 2 2 <sup>nd</sup> floor	x-OOP													
Unit 2 2 <sup>nd</sup> floor	y-OOP	●	●	●	x	x	●	x	x	x	●	●	x	●
True positive		4	4	3	0	2	5	2	2	1	5	6	2	6
False positive		3	3	0	0	2	2	1	1	2	2	1	2	0
False negative		2	2	3	6	4	1	4	4	5	1	0	4	0

Table 3.13: Damage mechanisms reported by the SERA AIMS blind prediction participants. IP = in-plane mechanism; OOP = out-of-plane mechanism. Correctly predicted mechanisms are indicated with a green circle, incorrectly predicted mechanisms with a red circle and a failure to indicate a correct mechanism with a red x.

Table 3.14 reviews the reported damage mechanisms according to the modelling approach, with the number of submissions in each category indicated in parentheses after the name. Correctly predicted damage mechanisms are marked by green circles, and incorrectly predicted mechanisms are marked by red circles. For each row and column, the total number of circles represents the total number of submissions of this category, and filled circles show those that

reported a particular damage mechanism. DEM models seemed to miss the mechanisms in the x-direction of Unit 1, while they mostly correctly predict mechanisms in the y-direction of Unit 2. It is important to highlight that the latter mechanisms were the principal ones. EFM models generally performed well, with some incorrectly predicted mechanisms, such as an in-plane mechanism in the x-direction of Unit 2. The best prediction in terms of activated damage mechanisms came from the limit analysis submission, which correctly predicted all the mechanisms, emerging as a clear winner from this comparison.

Table 3.14: Damage mechanisms reported by the SERA AIMS blind prediction participants divided according to modelling approach. IP = in-plane mechanism; OOP = out-of-plane mechanism. Correctly predicted damage mechanisms are marked by filled green circles, and incorrectly predicted mechanisms are marked by filled red circles.

Unit and storey	Direction and failure mode	Simple methods (1)	Limit analysis (1)	EFM (2)	Shell FEM (2)	Solid FEM (4)	DEM (3)
Unit 1	x-IP	●	●	●○	●○	●●○○	○○○
Unit 1	y-IP	●	○	○○	●○	○○○○	●○○
Unit 1	x-OOP	○	●	●●	●○	○○○○	○○○
Unit 1	y-OOP	○	○	○○	○○	○○○○	●○○
Unit 2 1 <sup>st</sup> storey	x-IP	●	○	●○	●●	●●○○	●●○
Unit 2 1 <sup>st</sup> storey	y-IP	●	●	●●	●○	●○○○	●●●
Unit 2 1 <sup>st</sup> storey	x-OOP	○	○	○○	○○	○○○○	○○○
Unit 2 1 <sup>st</sup> storey	y-OOP	○	●	●●	○○	●●○○	●●○
Unit 2 2 <sup>nd</sup> storey	x-IP	○	○	●●	●○	●●○○	●●○
Unit 2 2 <sup>nd</sup> storey	y-IP	○	●	●●	○○	●●○○	●●●
Unit 2 2 <sup>nd</sup> storey	x-OOP	○	○	○○	○○	○○○○	○○○
Unit 2 2 <sup>nd</sup> storey	y-OOP	○	●	●●	○○	●○○○	●●●
True positive		2	6	11	3	9	11
False positive		2	0	3	4	4	6
False negative		4	0	1	9	15	7

Table 3.15 reviews the reported damage mechanisms according to the unit-to-unit connection type. Models with no interaction between the units and with a compression-only unit-to-unit interface seem to predict more incorrect in-plane mechanisms in the x-direction in Unit 2. At the same time, models with a compression-shear unit-to-unit interface seem to predict damage more correctly in the y-direction of Unit 2, especially for out-of-plane failure modes.

Table 3.15: Damage mechanisms reported by the SERA AIMS blind prediction participants divided according to unit-to-unit connection type. IP = in-plane mechanism; OOP = out-of-plane mechanism. Correctly predicted damage mechanisms are marked by filled green circles, and incorrectly predicted mechanisms are marked by filled red circles.

Unit and storey	Direction and failure mode	No interaction between the units (2)	Compression-only unit-to-unit interface (3)	Compression-shear unit-to-unit interface (8)
Unit 1	x-IP	●●	●○○	●●●○○○○○
Unit 1	y-IP	●○	●○○	●○○○○○○○
Unit 1	x-OOP	○○	●●○	●●○○○○○○
Unit 1	y-OOP	○○	○○○	●○○○○○○○
Unit 2 1 <sup>st</sup> storey	x-IP	●●	●●●	●●●○○○○○
Unit 2 1 <sup>st</sup> storey	y-IP	●●	●●○	●●●●○○○○
Unit 2 1 <sup>st</sup> storey	x-OOP	○○	○○○	○○○○○○○○
Unit 2 1 <sup>st</sup> storey	y-OOP	●○	●○○	●●●●○○○○
Unit 2 2 <sup>nd</sup> storey	x-IP	●○	●●○	●●●●○○○○
Unit 2 2 <sup>nd</sup> storey	y-IP	●○	●○○	●●●●●○○○
Unit 2 2 <sup>nd</sup> storey	x-OOP	○○	○○○	○○○○○○○○
Unit 2 2 <sup>nd</sup> storey	y-OOP	●○	●○○	●●●●○○○○
True positive		7	8	27
False positive		4	6	9
False negative		5	10	21

Table 3.16 reviews the reported damage mechanisms according to the floor type. Contrary to what might be expected, models with no floors predicted less out-of-plane mechanisms. Models with flexible floor diaphragms seemed to incorrectly predict an in-plane mechanism in the x-direction of Unit 2. With regards to the other mechanisms, the results are inconclusive, partially due to the large variation in total number of submissions leading to a low number of models per category.

Table 3.16: Damage mechanisms reported by the SERA AIMS blind prediction participants divided according to floor type. IP = in-plane mechanism; OOP = out-of-plane mechanism. Correctly predicted damage mechanisms are marked by filled green circles, and incorrectly predicted mechanisms are marked by filled red circles.

Unit and storey	Direction and failure mode	No floors (3)	Rigid floors (1)	Only beams (4)	Flexible floor diaphragms (5)
Unit 1	x-IP	●●●	●	●○○○	●○○○○
Unit 1	y-IP	●○○	○	●○○○	●○○○○
Unit 1	x-OOP	○○○	●	●○○○	●●○○○
Unit 1	y-OOP	○○○	○	○○○○	●○○○○
Unit 2 1 <sup>st</sup> storey	x-IP	●●○	●	●●○○	●●●○○
Unit 2 1 <sup>st</sup> storey	y-IP	●●○	○	●●○○	●●●○○
Unit 2 1 <sup>st</sup> storey	x-OOP	○○○	○	○○○○	○○○○○
Unit 2 1 <sup>st</sup> storey	y-OOP	●○○	○	●●○○	●●●○○
Unit 2 2 <sup>nd</sup> storey	x-IP	●●○	●	○○○○	●●●○○
Unit 2 2 <sup>nd</sup> storey	y-IP	●●○	○	●●○○	●●●○○
Unit 2 2 <sup>nd</sup> storey	x-OOP	○○○	○	○○○○	○○○○○
Unit 2 2 <sup>nd</sup> storey	y-OOP	●○○	○	●●○○	●●●○○
True positive		9	2	12	19
False positive		5	2	3	9
False negative		9	4	12	11

Table 3.17 reviews the reported damage mechanisms according to the floor-to-wall connection type. Models with a nonlinear floor-to-wall connection better predict both the in-plane and out-of-plane damage mechanism in both storeys of Unit 2 in the y-direction. This effect is especially pronounced for the out-of-plane damage mechanisms.



Table 3.17: Damage mechanisms reported by the SERA AIMS blind prediction participants divided according to floor-to-wall connection type. IP = in-plane mechanism; OOP = out-of-plane mechanism. Correctly predicted damage mechanisms are marked by filled green circles, and incorrectly predicted mechanisms are marked by filled red circles.

Unit and storey	Direction and failure mode	Rigid floor-to-wall connection (3)	Elastic floor-to-wall connection (1)	Nonlinear floor-to-wall connection (6)
Unit 1	x-IP	●○○	○	●●○○○○
Unit 1	y-IP	●○○	○	●○○○○○
Unit 1	x-OOP	●●○	○	●●○○○○
Unit 1	y-OOP	○○○	○	●○○○○○
Unit 2 1 <sup>st</sup> storey	x-IP	●●●	○	●●●○○○
Unit 2 1 <sup>st</sup> storey	y-IP	●●○	○	●●●●○○
Unit 2 1 <sup>st</sup> storey	x-OOP	○○○	○	○○○○○○
Unit 2 1 <sup>st</sup> storey	y-OOP	●○○	○	●●●●○○
Unit 2 2 <sup>nd</sup> storey	x-IP	●●●	○	●●●○○○
Unit 2 2 <sup>nd</sup> storey	y-IP	●○○	○	●●●●●●
Unit 2 2 <sup>nd</sup> storey	x-OOP	○○○	○	○○○○○○
Unit 2 2 <sup>nd</sup> storey	y-OOP	●○○	○	●●●●○○
True positive		8	0	25
False positive		6	0	8
False negative		10	6	11

Table 3.18 reviews the reported damage mechanisms according to the wall-to-wall connection type. Models with rigid wall-to-wall connections more accurately predicted the in-plane mechanism in the x-direction of Unit 1. At the same time, they incorrectly predicted an in-plane mechanism in the x-direction of the 1<sup>st</sup> storey of Unit 2. Models with nonlinear wall-to-wall connections better predicted both in-plane and out-of-plane damage mechanisms of both storeys of Unit 2 in the y-direction. Models with nonlinear wall-to-wall connections comprise the three DEM models, an EFM model and a limit analysis model.

Table 3.18: Damage mechanisms reported by the SERA AIMS Blind prediction participants divided with regards to wall-to-wall connection type. IP = in-plane mechanism; OOP = out-of-plane mechanism. Correctly predicted damage mechanisms are marked by filled green circles, and incorrectly predicted mechanisms are marked by filled red circles.

Unit and storey	Direction and failure mode	Rigid wall-to-wall connections (7)	Nonlinear wall-to-wall connections (5)
Unit 1	x-IP	●●●●●○○	●●○○○
Unit 1	y-IP	●●○○○○○	●○○○○
Unit 1	x-OOP	●○○○○○○	●●○○○
Unit 1	y-OOP	○○○○○○○	●○○○○
Unit 2 1 <sup>st</sup> storey	x-IP	●●●●●○○	●●○○○
Unit 2 1 <sup>st</sup> storey	y-IP	●●●●●○○	●●●●●
Unit 2 1 <sup>st</sup> storey	x-OOP	○○○○○○○	○○○○○
Unit 2 1 <sup>st</sup> storey	y-OOP	●●○○○○○	●●●●○
Unit 2 2 <sup>nd</sup> storey	x-IP	●●●●●○○	●●●●○
Unit 2 2 <sup>nd</sup> storey	y-IP	●●●●●○○	●●●●●
Unit 2 2 <sup>nd</sup> storey	x-OOP	○○○○○○○	○○○○○
Unit 2 2 <sup>nd</sup> storey	y-OOP	●○○○○○○	●●●●●
True positive		14	23
False positive		10	7
False negative		28	7

### 3.4 Conclusions

This paper presents the results of a blind prediction competition organized as a part of a shake-table test within the SERA AIMS project. All available data on the unreinforced stone masonry aggregate—material, geometry, construction details, seismic input and testing sequence were shared with all the participants before the tests. The participants were asked to submit their predictions of the damage mechanisms, roof displacements, interface openings and base-shear forces for four levels of shaking. In total, 12 participants from academia and industry submitted a total of 13 models, which were well distributed with regards to modelling approaches, including discrete element models, shell and solid finite element models, equivalent frame models, a limit analysis model, and a code-based hand-calculation approach. The paper summarises the modelling approaches and describes the main modelling assumptions adopted, particularly with regard to the floor models and the unit-to-unit, floor-to-wall and



wall-to wall connections.

Material properties shared with the participants were assumed based on the specimen tested in Pavia, a previous experimental campaign on an aggregate of similar typology. In addition, results of in-plane quasi-static cyclic shear tests on walls from the Basel project were shared. In the SERA AIMS project, standard material tests were carried out after the shake-table test and these material properties matched well the ones from the Basel project. Hence, we conclude that discrepancies between the predictions and experimental results are not caused by differences between assumed and actual material properties.

While the assumed and actual material properties agreed well, the actual seismic input differed from the assumed one. Comparing the effective and nominal shake-table accelerations in terms of acceleration response spectra we found that, for the range close to the fundamental periods, the demand imposed in Run 2.1 corresponded closely to the nominal demand planned for Run 3.1. For this reason, the predictions for Run 3.1 were compared to the experimental results of Run 2.1, which was the last run before strengthening measures were applied. Run 2.1 and 3.1 are tests in the longitudinal direction only. For loading in the transverse direction the predictions of Run 3.2 were compared to the experimental results of Run 2.2S, following the same argumentation as for the longitudinal direction. In Run 2.2S the test specimen was already strengthened. A comparison between and experimental results is therefore affected by the following factors: (i) discrepancies between the nominal and effective testing sequence, (ii) discrepancies between the nominal and effective shake-table accelerations, (iii) for the transverse direction, discrepancy in the model (experiment: strengthened, prediction: unstrengthened).

To account for the discrepancy between planned and effective shake-table accelerations we compared submitted predictions and experimental results as follows: (i) a quantitative statistical comparison of the submitted values and a qualitative benchmarking of the submitted values against the experimental results, and (ii) a qualitative comparison of the reported damage mechanisms with the ones observed in the experiment. In the following, we summarise the main findings of the paper.

- **Modelling uncertainty:** Although uncertainties with regard to the material level and the structural element level were reduced to a minimum by providing information on the material properties and pier element response, the modelling uncertainties were very high with a CoV of 160%-268% for displacement quantities and a CoV of 58%-74% for base shears at the significant damage level. These CoVs are larger than those obtained in other blind prediction studies on unreinforced masonry buildings. Study by Mendes et al. (2017) reported CoV of 39%-63% for predicted PGA at collapse, while study by Esposito et al. (2019) reported CoV of 51% for predicted peak strength and 41% for predicted displacement at near collapse. In both cases, they call for further blind prediction competitions and further test data of complex structures to calibrate and validate numerical models. The higher CoV values in SERA AIMS are attributed to a

significantly more complex structure that included interaction between the two units. Furthermore, not only global (top displacements, base shears) but also local response quantities (interface opening) were predicted and the largest CoV values were obtained for these local response quantities.

- **Model class:** The four model classes with more than one submission were the following: discrete element models, solid finite element models, shell finite element models, and equivalent frame models. The CoV values did not show a clear trend between groups of models, except that the lowest CoV was found within the solid FE models. This result might be related to all four solid FE model submissions originating from the same research group using different modelling hypotheses and two different softwares. However, there were only few submissions per model class and therefore the statistical basis for this conclusion is weak.
- **Prediction of peak displacements, base shear forces and failure modes:** The DEM modelling approaches led to the best prediction in terms of displacement demands. A submission using limit analysis emerged as a winner in the prediction of the damage mechanisms, but at the same time, significantly underestimated the PGA for the initiation of the mechanisms. The FE model submissions (shell element models, solid element models and equivalent frame models) underestimated the displacement demands, most likely because these models tended to be too stiff.
- **Modelling of interface behaviour between units:** Only the hand-calculation submission and one solid FE model neglected the interaction between the units, while all others accounted for the interaction between the units either assuming that the interface between units can transfer only compression forces or assuming that the interface between units can transfer compression and shear forces and the maximum shear force is a function of the compression force. Although it would be expected that the models with compression-only interfaces and no connection between the units would lead to larger transverse displacements than shear-compression interface, this was not the case. However, this is attributed to the rather stiff behaviour of the models featuring compression-only interfaces and no connection between the units.
- **Modelling of timber floors and floor-to-wall connections:** Participants modelled the timber floor either modelling just the beams, or introducing elastic diaphragms, or using rigid diaphragms. As the structure was symmetric along the longitudinal axes, the choice of the diaphragm stiffness played probably a lesser role than in other studies. However, models that included rigid diaphragms predicted shear instead of flexural cracking in the spandrels because the axial elongation of the spandrels was restrained, while in the experiment the spandrels developed flexural cracks. The assumptions with regard to the floor-to-wall connections influenced the out-of-plane mechanism, with some of the models featuring rigid-wall connections predicting out-of-plane mechanisms with centre of rotation between the stories, whereas experimental overturning mechanisms involved a relative displacement between wall and timber beams. We

therefore conclude that adopting the modelling assumption of nonlinear floor-to-wall connections is important for capturing the in-plane and out-of-plane failure modes correctly.

- Damping: Although no clear trend in the results was observed with regards to chosen damping ratios, the model that applied the highest value (10%) predicted the very light damage at shake-table capacity, and no damage at acceleration values substantially affecting the physical model

This study showed that several modelling parameters influence the response of masonry aggregates, leading to large values of CoV in reported displacement results although the uncertainties at the material level and the structural element level were small. It is concerning that the majority of the models underestimated the order of magnitude of displacements. This highlights the need for further work addressing modelling uncertainties of unreinforced masonry structures, in particular for complex typologies such as masonry aggregates.

### 3.5 Data availability

Submissions by participants, files used to process them and files used to produce the figures presented in this paper can be accessed through the repository DOI: [10.5281/zenodo.6546440](https://doi.org/10.5281/zenodo.6546440)

### 3.6 Funding

The project leading to this paper has received funding from the European Union's Horizon 2020 research and innovation programme under grant agreement No 730900.

### 3.7 Appendix

A summary of the submissions to the SERA AIMS blind prediction competition is presented here, in the set of Tables 3.19- 3.43.

Table 3.19: Submission DEM 1 to SERA AIMS blind prediction competition. Characteristics of the model are taken from the submission form.

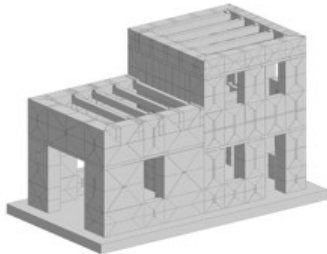
DEM 1	
	
Software	3DEC
Modelling approach	M-DEM (New Finite-Discrete macro-element approach)
Floors	Joists modelled as 3D linear elastic elements; joists connected through link elements accounting for the in-plane stiffness of the diaphragms
Floor-to-wall connection	Nonlinear springs with mortar properties; embedment explicitly modelled
Wall-to-wall connection	Nonlinear interface springs
Unit-to-unit connection	Zero-thickness nonlinear frictional spring (zero cohesion and zero tensile strength)
Damping	Mass proportional; 4% critical damping ratio

Table 3.20: Submission DEM 2 to SERA AIMS blind prediction competition. Characteristics of the model are taken from the submission form.

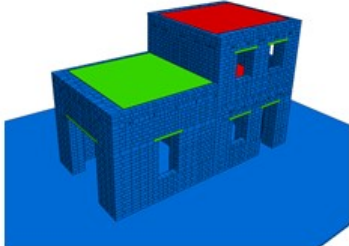
DEM 2	
	
Software	3DEC
Modelling approach	DEM
Floors	Floor slab and beams modelled independently as rigid blocks connected with nonlinear interfaces
Floor-to-wall connection	Nonlinear frictional interface, including a low tensile strength and cohesion; same as for the mortar in the rest of the model
Wall-to-wall connection	Nonlinear frictional interface, including a low tensile strength and cohesion; same as for the mortar in the rest of the model
Unit-to-unit connection	Nonlinear frictional interface, including a low tensile strength and cohesion; same as for the mortar in the rest of the model
Damping	Rayleigh mass proportional; values updated between runs (between 2 and 6%)

Table 3.21: Submission DEM 3 to SERA AIMS blind prediction competition. Characteristics of the model are taken from the submission form.

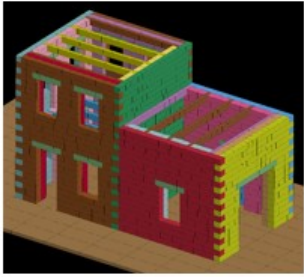
DEM 3	
	
Software	LS-DYNA
Modelling approach	DEM
Floors	Only beams modelled
Floor-to-wall connection	Nonlinear frictional interface, including a low tensile strength and cohesion; similar to the interface between blocks in the rest of the model, except with an even lower tensile strength
Wall-to-wall connection	Same as between blocks, with the interlocking present
Unit-to-unit connection	Nonlinear frictional interface, including a low tensile strength and cohesion; same as the interface between floor and wall
Damping	Stiffness proportional; 5% critical damping ratio

Table 3.22: Submission FEM 1 to SERA AIMS blind prediction competition. Characteristics of the model are taken from the submission form.

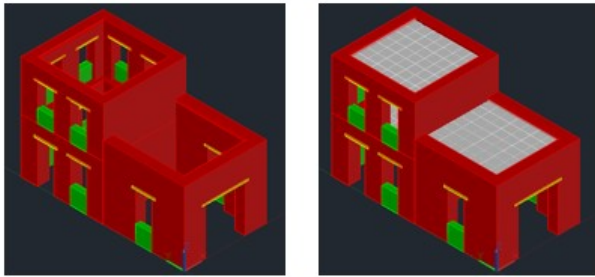
FEM 1	
	
Software	DIANA
Modelling approach	Solid FEM
Floors	One model without floors and one with orthotropic shell floor elements
Floor-to-wall connection	Distributed line interface with a nonlinear elastic material model
Wall-to-wall connection	Perfect connection between solid elements
Unit-to-unit connection	Nonlinear frictional interface, including a low tensile strength and cohesion
Damping	Rayleigh mass and stiffness proportional; 10% critical damping ratio

Table 3.23: Submission FEM 2 to SERA AIMS blind prediction competition. Characteristics of the model are taken from the submission form.

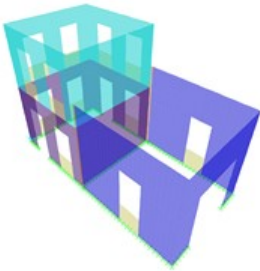
FEM 2	
	
Software	SAP2000
Modelling approach	Nonlinear shell FEM
Floors	Not modelled; diaphragm constraint applied
Floor-to-wall connection	Not modelled; diaphragm constraint applied
Wall-to-wall connection	Perfect connection between shell elements
Unit-to-unit connection	Compression-only elastic springs
Damping	Rayleigh mass and stiffness proportional; 5% critical damping ratio

Table 3.24: Submission FEM 3 to SERA AIMS blind prediction competition. Characteristics of the model are taken from the submission form.

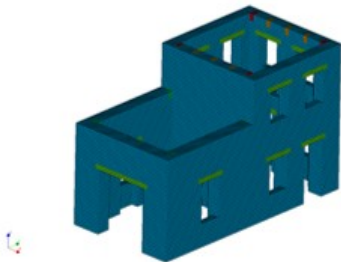
FEM 3	
	
Software	DIANA
Modelling approach	Solid FEM
Floors	Not modelled
Floor-to-wall connection	Floors not modelled
Wall-to-wall connection	Connection between solid elements modelled as a continuum
Unit-to-unit connection	Modelled as separate (no-connection tool in DIANA)
Damping	Mass and stiffness proportional; 3% critical damping ratio

Table 3.25: Submission FEM 4,5 to SERA AIMS blind prediction competition. Characteristics of the model are taken from the submission form.

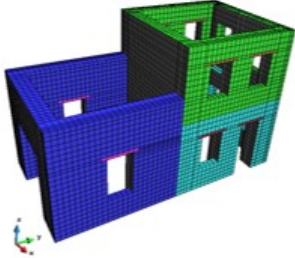
FEM 4,5	
	
Software	OpenSEES
Modelling approach	Solid FEM
Floors	Only beams modelled as simple trusses (FEM 4); floors not modelled (FEM 5)
Floor-to-wall connection	Hysteretic elastic/perfectly plastic material model with limit displacement, accounting for the stiffness degradation (FEM 4); floors not modelled (FEM 5)
Wall-to-wall connection	Connection between solid elements modelled as a continuum
Unit-to-unit connection	Frictional and simulated pounding using simplified Hertz impact theory
Damping	Mass and stiffness proportional; 3% critical damping ratio

Table 3.26: Submission FEM 5 to SERA AIMS blind prediction competition. Characteristics of the model are taken from the submission form.

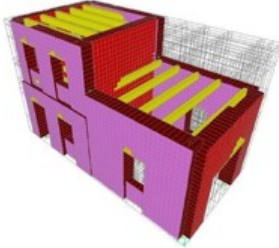
FEM 6	
	
Software	SAP2000
Modelling approach	Nonlinear shell FEM
Floors	Only beams modelled
Floor-to-wall connection	Rigid translational connection
Wall-to-wall connection	Connection between shell elements modelled as a continuum
Unit-to-unit connection	Compression-only; nonlinear link-GAP elements
Damping	Mass and stiffness proportional; 5% critical damping ratio

Table 3.27: Submission EFM 1 to SERA AIMS blind prediction competition. Characteristics of the model are taken from the submission form.

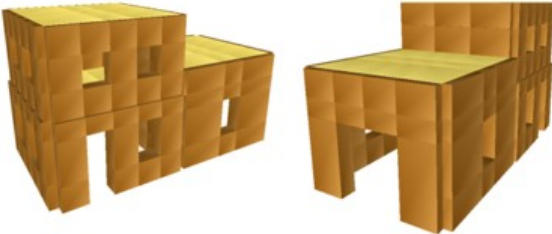
EFM 1	
	
Software	ANSR
Modelling approach	Equivalent Frame
Floors	Elastic plane stress finite elements, with stiffness appropriate for the actual floor; included stiffness reduction as a function of a maximum deformation
Floor-to-wall connection	Rigid
Wall-to-wall connection	Rigid
Unit-to-unit connection	Elastic compression-only gap elements
Damping	Mass and initial stiffness proportional; 3% critical damping ratio

Table 3.28: Submission EFM 2 to SERA AIMS blind prediction competition. Characteristics of the model are taken from the submission form.

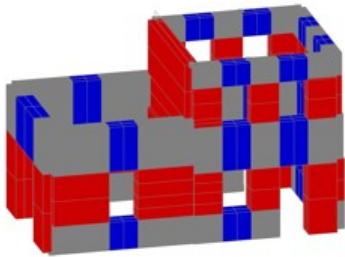
EFM 2	
	
Software	OpenSEES
Modelling approach	Equivalent frame
Floors	Elastic orthotropic membrane
Floor-to-wall connection	Nonlinear frictional connection
Wall-to-wall connection	Nonlinear; finite tensile strength with exponential softening and linear elastic in compression
Unit-to-unit connection	Nonlinear <del>rd</del> material model; frictional with a finite tensile strength and cohesion with exponential softening and linear elastic behaviour in compressions
Damping	Mass and initial stiffness proportional; 1% critical damping ratio



Table 3.29: Submission HAC 1 to SERA AIMS blind prediction competition. Characteristics of the model are taken from the submission form.

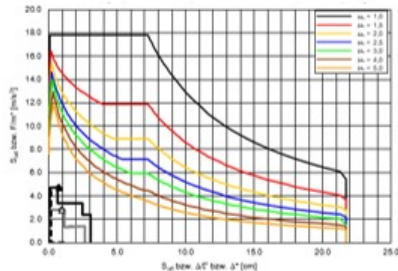
HAC 1	
	
Software	Hand calculation
Modelling approach	Response spectrum and static pushover analysis
Floors	Not modelled; floor masses attributed to the model according to the beam orientation
Floor-to-wall connection	Not modelled
Wall-to-wall connection	No connection; walls modelled separately
Unit-to-unit connection	No connection; units modelled separately
Damping	Static analysis; Damping ratio of nonlinear ADRS spectra = 5%

Table 3.30: Submission LIM 1 to SERA AIMS blind prediction competition. Characteristics of the model are taken from the submission form.

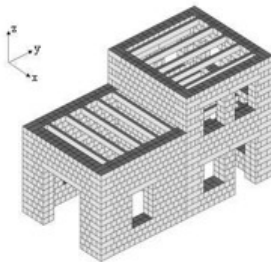
LIM 1	
	
Software	LiABlock_3D
Modelling approach	Rigid block limit analysis by mathematical programming
Floors	Only beams modelled
Floor-to-wall connection	No-tension frictional interfaces, with zero cohesion and infinite compressive strength; same as was done in the rest of the model;
Wall-to-wall connection	Same as between the blocks, with interlocking
Unit-to-unit connection	No-tension frictional interfaces, with zero cohesion and infinite compressive strength, same as was done in the rest of the model; the interaction at the head joints was activated only for the unit-to-unit interface
Damping	Not a dynamic analysis

Table 3.31: Submission DEM 1 to SERA AIMS blind prediction competition. Image reporting the damage in the model and damage mechanisms reported by a participant (column 1), and a qualitative comparison with the experimental results (column 2).

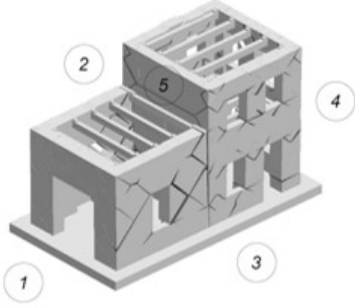
Submission DEM 1	Comparison to experimental results
 <ul style="list-style-type: none"> <li>• Out-of-plane cracks on Facade 1 and 5</li> <li>• In-plane rocking damage on Facades 2 and 3, Unit 2</li> <li>• Diagonal shear damage on squat piers of Unit 1</li> <li>• Toe-crushing failure at the base of the ground floor piers of Unit 2</li> <li>• Flexural damage in the spandrels and at the base/top of the piers of Facade 4</li> </ul>	<ul style="list-style-type: none"> <li>• Well-predicted rocking mechanisms in Facades 2 and 3 of Unit 2, as well as out-of-plane motion of Façade 5.</li> <li>• Out-of-plane motion of Facade 1 was not recorded in the experiment.</li> <li>• Cracking of Facade 4 occurred due to the out-of-plane motion, but not due to the in-plane damage as predicted here. Also, shear damage in squat piers and toe crushing were not detected in the experiment.</li> </ul>

Table 3.32: Submission DEM 2 to SERA AIMS blind prediction competition. Image reporting the damage in the model and damage mechanisms reported by a participant (column 1), and a qualitative comparison with the experimental results (column 2).


Submission DEM 2	Comparison to experimental results
<p style="text-align: center;"><b>Facade 3</b></p>  <ul style="list-style-type: none"> <li>• Unrealistic sliding of Unit 1</li> <li>• Heavy floor of Unit 2 causing horizontal cracks at Facades 4 and 5</li> <li>• Out-of-plane behaviour in Facade 4, followed by a flange effect with cracked spandrels at the ground floor of Facades 2 and 3</li> <li>• Out-of-plane behaviour of a parapet in Unit 1</li> <li>• Rocking of the upper storey of Facades 2 and 3 of Unit 2</li> <li>• Shear cracking of the spandrels of Facade 4</li> </ul>	<ul style="list-style-type: none"> <li>• Even if the unrealistic sliding of Unit 1 caused problems and unrealistic damages that the participant was aware of, it correctly predicted the out-of-plane behaviour of Facade 4 that involved the flange effect of Facades 2 and 3 the general rocking mechanisms of the latter facades.</li> <li>• However, the out-of-plane motion of Unit 1 as well as the position of the horizontal crack in Facade 5 and shear cracking in the spandrels were not accurately predicted.</li> </ul>

Table 3.33: Submission DEM 3 to SERA AIMS blind prediction competition. Image reporting the damage in the model and damage mechanisms reported by a participant (column 1), and a qualitative comparison with the experimental results (column 2).


Submission DEM 3	Comparison to experimental results
<p style="text-align: center;"><b>Facade 2</b></p>  <ul style="list-style-type: none"> <li>• Separation at the interface and large flexural displacements of Unit 2</li> <li>• Flexural deformations concentrated in the upper storey of Unit 2, leading to flexural failure of the middle pier for the Run 3.3 (75% shake-table capacity)</li> <li>• Unit 1 shows only minor damage</li> </ul>	<ul style="list-style-type: none"> <li>• <i>Very well predicted flexural rocking mechanism of the upper stories of Facades 2 and 3 of Unit 2. The level of damage satisfactorily matches that of the actual test. However, the asymmetrical response of Facades 2 and 3 might due to an underestimation of the shear stiffness of the diaphragms, as only the beams were modelled.</i></li> </ul>

Table 3.34: Submission FEM 1 to SERA AIMS blind prediction competition. Image reporting the damage in the model and damage mechanisms reported by a participant (column 1), and a qualitative comparison with the experimental results (column 2).

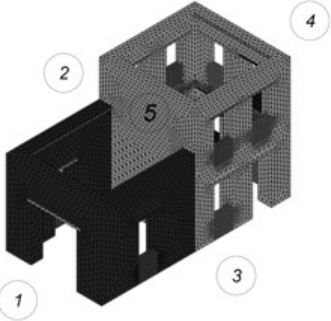
Submission FEM 1	Comparison to experimental results
 <ul style="list-style-type: none"> <li>• Initiation of damage only in the run with 100% shake-table capacity</li> <li>• Potential rocking mechanism in Facade 1</li> <li>• Initiation of the flexural mechanism in the spandrels and piers of Facades 2 and 3 of Unit 2</li> <li>• Flexural cracks in spandrels of Facade 4</li> <li>• Out-of-plane cracks in the Facade 5</li> <li>• Residual crack at the interface between units</li> </ul>	<ul style="list-style-type: none"> <li>• <i>Damping value set to rather high 10% to compensate for the secant unloading of the applied material model. This value was probably too high, leading to the initiation of the damage mechanisms only for a very high PGA. However, the mechanisms do resemble those activated for lower PGA levels.</i></li> </ul>

Table 3.35: Submission FEM 2 to SERA AIMS blind prediction competition. Image reporting the damage in the model and damage mechanisms reported by a participant (column 1), and a qualitative comparison with the experimental results (column 2).

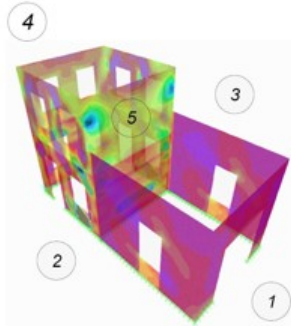
Submission FEM 2	Comparison to experimental results
 <ul style="list-style-type: none"> <li>• Rocking of all the piers of Unit 1 in the <math>x</math>-direction, both in-plane and out-of-plane</li> <li>• Shear cracking in the spandrels of the upper storey of Facades 2 and 3 of Unit 2</li> <li>• Shear cracking in the spandrels of Facade 4</li> <li>• Flexural rocking in the piers of Facade 4</li> </ul>	<ul style="list-style-type: none"> <li>• The rocking of Unit 1 in the <math>x</math>-direction was correctly predicted, both in-plane and out-of-plane, while the upper storey flexural mechanism of Unit 2 was underestimated. This, together with shear cracks in the spandrels, could be due to the rigid diaphragm modelled using the 'diaphragm restraint' in the software. The in-plane cracking of Facade 4 was not correctly predicted.</li> </ul>

Table 3.36: Submission FEM 3 to SERA AIMS blind prediction competition. Image reporting the damage in the model and damage mechanisms reported by a participant (column 1), and a qualitative comparison with the experimental results (column 2).

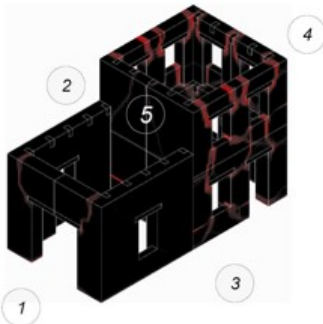
Submission FEM 3	Comparison to experimental results
 <ul style="list-style-type: none"> <li>• Only minor damage in Unit 1 in the form of flexural cracks in the spandrel of Facade 1</li> <li>• Considerable spread of damage in Unit 2</li> <li>• Flexural cracking of both the piers and spandrels of Facades 2 and 3 of Unit 2 that concentrated in the upper storey</li> <li>• Flexural in-plane and horizontal out-of-plane cracks in Facade 4</li> <li>• Some shear cracks in the spandrels between the openings in Facades 2, 3 and 4 of Unit 2</li> </ul>	<ul style="list-style-type: none"> <li>• Very well replicated damage mechanisms in Facades 2, 3 and 4 of Unit 2—out-of-plane mechanism in Facade 4 with a flange effect and flexural cracking of Facades 2 and 3. Only minor damage in Unit 1—the extent and location were exactly as in the experimental campaign. The only faults in the prediction were the incorrect out-of-plane mechanism and cracks of Facade 5 and in-plane damage in Facade 4, including the shear cracks in the spandrels—their origin is difficult to interpret as the diaphragm was not modelled.</li> </ul>



Table 3.37: Submission FEM 4 to SERA AIMS blind prediction competition. Image reporting the damage in the model and damage mechanisms reported by a participant (column 1), and a qualitative comparison with the experimental results (column 2).

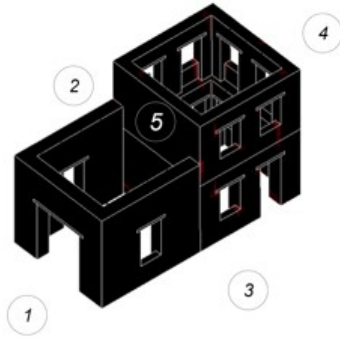
Submission FEM 4	Comparison to experimental results
 <ul style="list-style-type: none"> <li>• Minor cracks on Facade 2 of Unit 2.</li> <li>• Tensile strains starting from the corners of the openings, either vertical or horizontal</li> <li>• Minor damage at the first-floor level of Facade 4 and at the bottom of Facade 5</li> <li>• In the 100% run, potential out-of-plane failure of Unit 1 and extensive damage to Facades 2, 3 and 4 of Unit 2, including both flexural and shear cracking</li> </ul>	<ul style="list-style-type: none"> <li>• <i>The model underestimated the damage for the runs at 75% of the shake-table capacity. It correctly assumed less damage in Unit 1. Even though it correctly predicted the widespread damage of Unit 2 for 100% of the shake-table capacity, it also predicted shear cracking, while in reality, the behaviour was purely flexural.</i></li> </ul>

Table 3.38: Submission FEM 5 to SERA AIMS blind prediction competition. Image reporting the damage in the model and damage mechanisms reported by a participant (column 1), and a qualitative comparison with the experimental results (column 2).

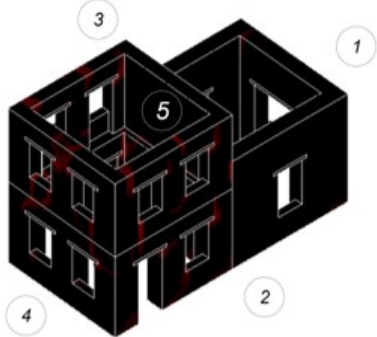
Submission FEM 5	Comparison to experimental results
 <ul style="list-style-type: none"> <li>• Minor cracks on Facade 1 of Unit 1</li> <li>• Vertical cracks in the upper storey of Facade 2 and 3 of Unit 2</li> <li>• Diagonal cracks on the second-floor level of Facade 4</li> <li>• Horizontal out-of-plane cracks at the base of Facade 5</li> </ul>	<ul style="list-style-type: none"> <li>• <i>The model underestimated the damage for the Runs at 75% of the shake-table capacity. It correctly assumed less damage in Unit 1 and correctly predicted but underestimated the flexural mechanism in the upper storey of Facades 2 and 3 as well as the out-of-plane behaviour of Facade 5. The predicted diagonal cracks in Facade 4 did not occur.</i></li> </ul>

Table 3.39: Submission FEM 6 to SERA AIMS blind prediction competition. Image reporting the damage in the model and damage mechanisms reported by a participant (column 1), and a qualitative comparison with the experimental results (column 2).

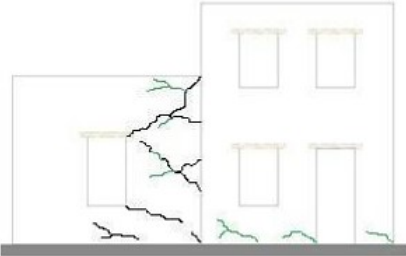
Submission FEM 6	Comparison to experimental results
<p style="text-align: center;"><b>Facade 3</b></p>  <ul style="list-style-type: none"> <li>• In-plane cracks in both Unit 1 and 2, with longer cracks in Unit 1</li> <li>• Slight in-plane cracking at the bottom of Facade 4 of Unit 2</li> <li>• The same mechanism further extended in the 100% shake-table capacity run</li> </ul>	<ul style="list-style-type: none"> <li>• The model generally underestimated the damage. The flexural mechanism was correctly detected in Facades 2 and 3 of Unit 2, but was located at ground floor. The actual damage was more widespread in the upper storey. Unit 1 showed widespread in-plane damage, while it was barely damaged in the actual experiment.</li> </ul>

Table 3.40: Submission EFM 1 to SERA AIMS blind prediction competition. Image reporting the damage in the model and damage mechanisms reported by a participant (column 1), and a qualitative comparison with the experimental results (column 2).

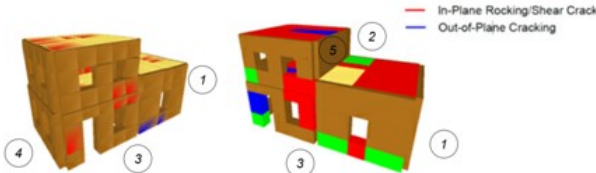
Submission EFM 1	Comparison to experimental results
 <ul style="list-style-type: none"> <li>• Potential for out-of-plane failure of Facade 2 and/or 3 of Unit 1 that would occur first with peak mid-height wall displacement exceeding half the wall thickness</li> <li>• This would be closely followed by out-of-plane failure of Facade 5 based on recorded peak displacements and then out-of-plane failure of Facade 2</li> <li>• Diaphragm yield/damage expected to first occur at 50% ground motion intensity and to become significant at 75% ground motion</li> <li>• Pier rocking in Unit 2, in both the <math>x</math>- and <math>y</math>-directions, was expected to be minor at 50% capacity and become significant at 75% capacity</li> <li>• Moderate panel shear failure in Unit 1 and significant panel shear failure in Unit 2 expected for 100% ground motion intensity</li> </ul>	<ul style="list-style-type: none"> <li>• Fixed floor-to-wall connections lead to two-fold effects: First, it led to the out-of-plane mechanism with rotation around the mid-height wall. Second, in-plane damage to the diaphragm was reported. In reality, beam sliding occurred instead, preventing diaphragm damage. Out-of-plane, even if in different walls than predicted here, happened by rotation of the pier at the bottom due to a weaker floor-to-wall connections.</li> <li>• The minor rocking at 50% that became significant at 75% in Facades 2 and 3 of Unit 2 was very well predicted.</li> </ul>

Table 3.41: Submission EFM 2 to SERA AIMS blind prediction competition. Image reporting the damage in the model and damage mechanisms reported by a participant (column 1), and a qualitative comparison with the experimental results (column 2).

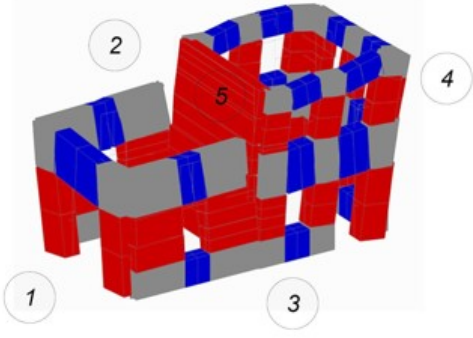
Submission EFM 2	Comparison to experimental results
 <ul style="list-style-type: none"> <li>• Flexural mechanism in the upper storey of Facades 2 and 3 of Unit 2</li> <li>• Large flexural deformations of both the spandrels and the piers</li> <li>• Out-of-plane behaviour of Facade 4, with a flange effect involving portions of Facades 2 and 3</li> <li>• Possible collapse predicted only for Run 4.1 (100% shake-table capacity)</li> <li>• Out-of-plane mechanism in Facades 2 and 3 of Unit 1</li> <li>• Unit 1 developed in-plane/out-of-plane mechanism in x-direction</li> <li>• Flexural cracking of Facade 4 in x-direction</li> </ul>	<ul style="list-style-type: none"> <li>• The model correctly predicted the soft storey mechanism of the upper storey of Facades 2 and 3 of Unit 2, together with out-of-plane mechanism of Facade 4, but it underestimated the scale of the out-of-plane displacement. The out-of-plane behaviour of Unit 1 was correctly predicted but overestimated. The predicted flexural cracking of Facade 4 did not occur.</li> </ul>

Table 3.42: Submission HAC 1 to SERA AIMS blind prediction competition. Image reporting the damage in the model and damage mechanisms reported by a participant (column 1), and a qualitative comparison with the experimental results (column 2).

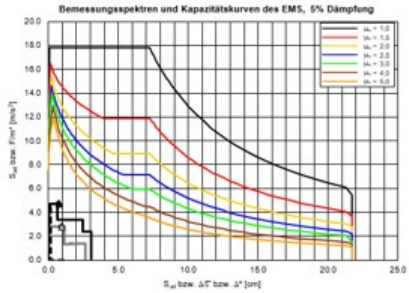
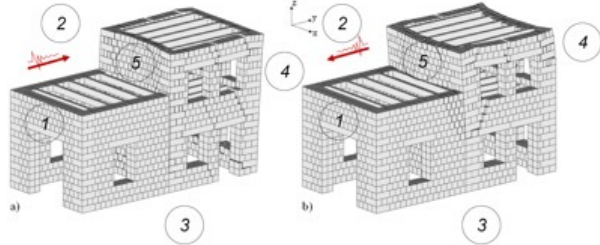
Submission HAC 1	Comparison to experimental results
 <ul style="list-style-type: none"> <li>• In-plane failure of piers of lower storey of Unit 2</li> <li>• No further information on the exact damage mechanism</li> </ul>	<ul style="list-style-type: none"> <li>• This simple modelling approach ignores the soft storey mechanism of the upper facade as well as the interaction between the out-of-plane facade and flange effect of the in-plane facade. This leads to a significant oversimplification, especially for aggregates with multiple interactions. Although the critical failure modes are not considered, the results correctly show that the failure would be located in the Unit 2.</li> </ul>

Table 3.43: Submission LIM 1 to SERA AIMS blind prediction competition Image reporting the damage in the model and damage mechanisms reported by a participant (column 1), and a qualitative comparison with the experimental results (column 2).

Submission LIM 1	Comparison to experimental results
 <ul style="list-style-type: none"> <li>• For a force in the (a) positive or (b) negative direction: both failure modes are overturning mechanisms involving the front walls and a portion of the sidewalls of Unit 2</li> <li>• The values of the collapse load multipliers obtained from the numerical simulation are equal to 0.21 and 0.22 for the positive and negative y-directions, respectively</li> <li>• The value of the PGAs corresponding to the damage limit state load multipliers are 0.24 g and 0.27 g for the positive and negative y-directions, respectively</li> <li>• Applying a load in the x-direction leads to the combined in-plane and out-of-plane failure of Unit 1</li> </ul>	<ul style="list-style-type: none"> <li>• The failure mechanisms are very well predicted. The one in the positive y-direction almost exactly matches the one occurring in Run 2.1—out-of-plane overturning of Facade 4 and a flange effect involving a portion of Facades 2 and 3. The flexural cracking in the spandrels and piers of Facades 2 and 3 was very well simulated. The damage mechanism in the x-direction replicates the experimental one very well. However, the damage limit state load multiplier is conservative, more closely resembling Run 1.3 that did not produce any damage except at the interface between units. When life-safety limit state was considered through behaviour factor <math>q=2</math>, the prediction is more close to test values.</li> </ul>



## **4 Shake table test on a historical masonry aggregate - prediction and postdiction using an equivalent frame model**

This chapter is a pre-print version of the paper: Tomić I, Beyer K (2022c) Shake table test on a historical masonry aggregate - prediction and postdiction using an equivalent frame model. Submitted to Bulletin of Earthquake Engineering

The formatting and numbering of equations, tables and figures have been adapted to this document. The contributions of the first author are: developing material models in OpenSEES, generating numerical models, running analyses, interpreting results, visualization and writing.

### **Abstract**

Modelling the seismic response of historical masonry buildings is challenging due to the large number of aleatory and epistemic uncertainties. Unreinforced masonry aggregates, encountered throughout city centres of Europe, are further complicated by the interaction between structural units. This was the motivation behind the experimental campaign performed on the half-scale, double-leaf stone masonry aggregate within SERA – Adjacent Interacting Masonry Structures project. As a part of the experimental campaign, blind prediction competition was organized - providing the participants with all the available data on the materials, geometry, construction details and seismic input. After the test, actual seismic input, and all the recorded and processed data on accelerations, base-shear, and displacements was shared to perform the postdiction simulations. Due to discrepancy between nominal and applied accelerations, instead of a single prediction, the paper presents broader stochastic incremental dynamic analyses aiming at answering the questions whether common assumptions for aggregate

modelling that assume the units either as fully coupled or completely separated can correctly simulate the behaviour of aggregates, and whether safe results can be adequately predicted by these approaches. In this work, we use a new material for modelling the interface between units and analyse it using OpenSEES. The buildings were modelled as equivalent frames using a newly developed macroelement, which represented both in-plane and out-of-plane failure modes. To assess how various modelling assumptions predict seismic vulnerability and engineering demand parameters, a probabilistic approach was applied, and incremental dynamic analyses (IDA) were carried out. Our results demonstrate the importance of explicitly modelling the non-linear connection between the units as well as the use of probabilistic approaches when evaluating the aggregate response. Although modelling simplifications and conservative deterministic approaches might appear conservative in terms of predicted failure peak ground acceleration (PGA), we find that these simplified approaches overlook the likely damage and failure modes. Post-diction analyses further confirm the importance of the probabilistic approach, while stressing the importance of calibrating material parameters according to equivalent quasi-static cyclic tests and using the appropriate damping model.

### **4.1 Introduction**

This paper deals with a blind prediction of the experimental campaign on an unreinforced masonry aggregate performed by Tomić et al. (2022a). Experimental campaign was a part of a joint research project between École Polytechnique Fédérale de Lausanne (EPFL), Switzerland, University of Pavia, Italy, University of California, Berkeley, USA, RWTH Aachen University, Germany and National Laboratory for Civil Engineering, Portugal, named SERA AIMS – Adjacent Interacting Masonry Structures. As a part of this project, a shake table test was performed on a half-scale stone masonry building aggregate at the LNEC laboratory in Lisbon, Portugal. The shake-table test was accompanied by a blind prediction competition (Tomić et al. 2022b). Each group was provided with a complete set of construction drawings, material properties, testing sequence and the list of measurements to be reported. This paper deals with the prediction submitted by the EPFL team, extended with a broader stochastic analysis, and the research on the influence of assumptions with regards to the unit-to-unit interface on the seismic behaviour of the aggregate. Even if this typology is widespread across the city centers worldwide, the lack of experimental data hindered the advances in modelling approaches. Nevertheless, several authors addressed this issue, as described in the following chapters.

#### **4.1.1 Modelling of masonry aggregates**

Recently, unreinforced masonry buildings have been extensively modelled with different approaches, but the literature on existing models of unreinforced masonry aggregates is still rather limited. In one example, Senaldi et al. (2010) modelled an unreinforced masonry aggregate by an equivalent frame approach, using the non-linear macroelement implemented in Tremuri software (Lagomarsino et al., 2013; Andrea Penna et al., 2014a). The study investigated

therefore only the in-plane and not the out-of-plane response of the masonry buildings. The aim was to assess the vulnerability of a single structural unit and its behaviour within an aggregate, as well as to investigate the effects of flexible floors and the length of row conglomerations on the seismic response. Aggregate structural units were modelled as fully connected; hence the longitudinal walls were modelled as continuous. In parallel, each unit was modelled as a single unit, and each transverse wall was modelled as a single wall with tributary masses. All the models were subject to the same ground excitation in the non-linear dynamic analyses. It was observed that the displacement response of the three models in the transversal direction was nearly equal. This was attributed to the flexible floor diaphragms, which were modelled as an orthotropic membrane with the shear modulus having  $G = 10 \text{ MPa}$ . However, single structural unit models overestimated the displacement demand in the longitudinal direction. At the same time, single unit models failed to capture the torsional behaviour of the end units of an aggregate. Therefore, modelling the single units as isolated buildings led either to conservative or unconservative results, depending on the position of the unit in the aggregate.

Formisano et al. (2013) and Antonio Formisano (2017) established a simple methodology to foresee static non-linear behaviour of building compounds, based on the provisions of the Italian Guidelines on Cultural Heritage (Circular 2009) and calibrated it using the results from two modelling approaches. Two masonry aggregates, with two and six units, were analysed. First, equivalent floor stiffness was evaluated using the SAP2000 software (Computers and Structures, 2011), then the equivalent frame model was set up using beam elements in both the SAP2000 and 3MURI software (Data, 2008). The units were modelled as fully connected with continuous wide piers. Pushover curves were generated and compared to pushover curves obtained using the Italian Guidelines, where contributions of each unit were summed to provide the global aggregate response. For both cases, aggregate shear strength in the x and y direction derived from the Guidelines underestimated the strength obtained by pushover curves on the full aggregate model by approximately half. The reason for this underestimation was found in the in-plane shear strength formulation in the Guidelines, and a correction factor was proposed for the Guidelines formulation.

Antonio Formisano and Massimilla (2018) later developed a procedure to determine the seismic response of structural units of an aggregate through a simplified modelling approach. Buildings were modelled with the equivalent frame approach in the SAP2000 software. Units were modelled as fully connected. First, the non-linear pushover analyses were performed on the whole aggregate to evaluate the seismic behaviour of both head and intermediate structural units. Next, isolated units were modelled with elastoplastic link elements, with their strength and stiffness calibrated according to the structural analysis of the whole aggregate. Elastoplastic links for isolated units were applied in the transversal direction, because the longitudinal response of the isolated unit did not differ from the response of a unit within the aggregate. The formulation was developed to determine the properties of the springs based on the main geometrical dimensions – plan layout and inter-storey height. Stavroulaki (2019) developed a procedure for simulating the interaction between aggregate units by rod elements or elastic supports that modelled the support of an adjacent structure. Elastic supports were

modelled as elastic non-linear frictionless foundation elements. FEM models were created in the Marc software (Marc, 2008) using 3D solid finite elements and considering the material as homogenous, modelled by elastoplastic theory with yield surface written in terms of the first and the second deviatoric stress invariants. Modelling entire aggregates assumed continuous mesh without specific interface modelling. The calibration of the interface elements was compared with the dynamic characteristics of the complex to which the isolated unit belonged. This approach can be extended to cases where it is possible to perform a modal identification procedure.

Recently, an important contribution from Angiolilli et al. (2021) explored the influence of the four different possible types of connection between the units of an aggregate. The four types of connections were: (i) isolated buildings (no connection), (ii) adjacent buildings (compression only connection), (iii) connected buildings (compression and shear connection), and (iv) joined buildings (fully connected units). The study found the influence of modelling the connection between the units on the seismic fragility of the aggregate, as well as on the predominant failure mode.

### **4.1.2 Modelling experimental case studies featuring masonry aggregates**

Following an EFM approach, Senaldi et al. (2020) modelled the experimental response of the masonry aggregate tested in Pavia (Senaldi et al., 2019a; Guerrini et al., 2019). The model was calibrated according to the wallettes tests (Senaldi et al., 2018) for material characterisation, and further elements were implemented to account for the out-of-plane stiffness through a combination of equivalent frames and membranes. Two units were again modelled as fully connected and formed a continuous wide pier at the interface. Numerical and experimental results were compared in terms of pushover and backbone curves, hysteretic responses, lateral displacement profiles, damage patterns, and failure mechanisms. The pushover curve estimated the force capacity well, but overestimated the global stiffness of the aggregate. The dynamic analysis estimated the hysteretic response very well, but because the global stiffness was overestimated, the displacement demand was underestimated. However, the overestimation of the global stiffness was attributed to an overestimation of the out-of-plane stiffness, rather than to a perfect connection between the units in the model. This was because the specimen had interlocking stones between the units, and the floor beams of adjacent units were at the same level and connected. These two properties proved effective in connecting the units and preventing the separation at the interface for the unidirectional dynamic excitation, as observed by Senaldi et al. (2019a) and Guerrini et al. (2019).

This same aggregate was modelled by Vanin et al. (2020b) using a newly developed macro-element (Vanin et al. 2020a) implemented in the OpenSEES software (McKenna et al. 2000). The approach accounted for both in-plane and out-of-plane behaviour and the nonlinearity of floor-to-wall and wall-to-wall connections. The two units were modelled as perfectly connected. After calibrating it based on an experimental campaign, the model satisfactorily

predicted the failure mode, displacement, and distribution of drift values in the piers. However, it was highly sensitive to parameters such as damping ratio and floor-to-wall friction coefficient, especially for higher levels of seismic excitation.

### **4.1.3 Large-scale assessment procedures for masonry aggregates**

For the large-scale seismic vulnerability assessment of masonry building aggregates, Antonio Formisano et al. (2015) numerically calibrated a procedure derived from the well-known existing vulnerability form of masonry buildings (Benedetti and Petrini, 1984; D. Benedetti et al., 1998). This procedure integrated five parameters accounting for the aggregate conditions among adjacent units, which were the presence of adjacent buildings with different heights, the position of the building in the aggregate, the number of staggered floors, the structural or typological heterogeneity among adjacent structural units, and the different percentages of opening areas among adjacent façades. Numerical calibration and validation were performed with the equivalent frame approach using the 3MURI software by subjecting the two case study aggregates and single units to several pushover analyses. Units were modelled as fully connected. In contrast to the original form, negative scores were also used to consider the beneficial effects on a masonry building within an aggregate. The seismic vulnerability of buildings within aggregates (i.e. the structural unit within a compound) was reduced compared to the same building when analysed as an isolated unit. Furthermore, it was found that the most vulnerable buildings were those found between lower buildings and those positioned at either the corner or at the end of the aggregate, where, in some cases, a building's seismic vulnerability could be increased when modelled within an aggregate.

To compare the different methodologies, Maio et al. (2015) performed the seismic vulnerability assessment of old stone masonry using equivalent frame modelling in the 3MURI software, hybrid techniques (Grünthal, 1998), and vulnerability index formulations (Antonio Formisano et al., 2015). Pushover non-linear analyses were performed on the equivalent frame model of the case study in 3MURI. Units were modelled as fully connected with wide continuous piers at the interface between units. Overall, the accuracy of the pushover analyses was influenced by the input parameters, such as the mechanical and geometrical properties of the structure, which were dependant on the quality of the provided structural survey and inspection report.

Overall, studies found the influence of adjacent units important for the evaluation of the seismic behaviour of historical masonry buildings that are part of building aggregates. However, studies do not agree on which units within an aggregate are affected, in which manner, and in which direction. Nevertheless, all the studies have shown certain limitations: (i) not explicitly modelling out-of-plane behaviour, (ii) modelling wooden floors as perfectly connected to the walls, without a non-linear interface for slab-to-wall connection, (iii) performing analysis uni-directionally or with separate analysis for each direction. All the presented limitations will be addressed within this study.

### **4.1.4 Uncertainty in modelling historical masonry**

When dealing with uncertainty, the common approach is to distinguish aleatory randomness and epistemic uncertainty (Fragiadakis and Vamvatsikos, 2010; Vamvatsikos and Fragiadakis, 2010). Several authors have approached the topic of uncertainty in modelling historical masonry buildings by treating both aleatory and epistemic uncertainty using different approaches and different levels of complexity. Dolsek (2009) performed a series of Incremental Dynamic Analyses (IDA) to account for both aleatoric uncertainty in terms of different seismic records and epistemic uncertainty in terms of material and modelling properties. Properties were distributed according to Latin Hypercube Sampling (LHS). The influence of uncertainty on the seismic response parameters was presented in terms of summarized IDA curves and dispersion measures, concluding that epistemic uncertainty did not significantly influence the seismic response parameters far from collapse, though could significantly influence the collapse capacity. Rota et al. (2014) assessed epistemic uncertainties by means of identification of knowledge levels associated with confidence factors, applied as a reduction of material strength in the Italian code. A probabilistic methodology was proposed for the quantification of appropriately defined factors. Saloustros et al. (2019) performed a stochastic analysis based on Monte Carlo simulation to investigate the effect of structural members' mechanical parameters on the evaluation of seismic fragility. The case study of the Santa Maria del Mar church in Barcelona illustrated the sensitivity of the uncertainty of material properties because, depending on the input, two different collapse mechanisms were possible. Analytical seismic fragility curves were derived by considering uncertainties regarding the material properties. Vanin and Katrin Beyer (2018) considered several sources of uncertainty, including the uncertainty associated with the material properties and the in-plane displacement capacities of piers. The displacement capacity of piers was identified as a major source of uncertainty. Since Monte-Carlo simulations can often be too computationally expensive for practical use, the logic tree approach was proposed as a way to reduce the required analyses to a minimum. Here, a moment-matching technique was used to define optimal sampling points and a combination of weights to apply to the branches. As a more refined and novel approach to structural engineering and to lower the computational cost, a Point Estimate Method was tested to further reduce the number of required non-linear simulations. Both methods were applied to a historical stone masonry building modelled by the EFM approach. Methods were compared with the Monte Carlo method and showed good accuracy.

### **4.1.5 Structure of the paper**

In the following sections, first, the newly developed nD material model for simulating the behaviour of an aggregate interface is presented. Next, the case study aggregate is described, together with material and modelling properties and their respective normal and lognormal distributions used for analyses done before the shake-table campaign. The methodology for the statistical evaluation of the data is described, and four modelling approaches that were used to perform multiple incremental dynamic analyses are described and compared,

together with the observations on their seismic fragility and failure modes. Second part of the paper deals with the post-diction analyses where acceleration recorded at the shake-table was applied first to a prediction model. Next, recalibration of material properties was performed in probabilistic manner according to wallettes test. Further calibration was done by updating damping model to the secant damping and accounting for the dependency of modulus of elasticity on the axial load ratio. The paper concludes with findings on the modelling of unreinforced masonry aggregates using probabilistic approach, and the lessons learned on calibrating numerical models against experimental campaigns.

## **4.2 Modelling approach**

In this study, Equivalent Frame Model (EFM) was used, which is one of the most widely applied engineering tools for the seismic analysis of unreinforced masonry buildings. EFM is based on discretizing façades into piers, spandrels and rigid nodes using beams or macroelements (Quagliarini et al., 2017). This approach can also capture the key mechanical parameters by using the appropriate material laws, while the inherent simplicity of the model allows for multiple dynamic analysis to be performed to include the aleatoric and epistemic uncertainties of the masonry. The newly developed macroelement by Vanin et al. (2020a) builds upon Andrea Penna et al. (2014a), which precisely demonstrates the in-plane behaviour of masonry panels by extending the formulation to in-plane and out-of-plane behaviour. This approach eliminates the need for separate analyses and provides a framework for analysing the impact of in-plane and out-of-plane failure modes on collapse capacity and failure mode.

The macroelement developed by Vanin et al. (2020a) is formulated as a one-dimensional element defined by three nodes in three-dimensional space. It consists of three non-linear sections accounting for axial deformation and the non-linear interface for shear response in the central section. The out-of-plane response is coupled with the in-plane response by considering the P-delta formulation obtained through a second-order Taylor series expansion of the compatibility equations. To correctly model the out-of-plane response of a masonry building, it is not sufficient to choose a macroelement formulation for piers that captures the out-of-plane behaviour. Therefore, it is important that the building model allows for relative displacements between the floor and walls and between intersection walls (Vanin et al., 2020b). For this purpose, interface elements for wall-to-wall and wall-to-floor connections were implemented in OpenSEES (McKenna et al., 2000).

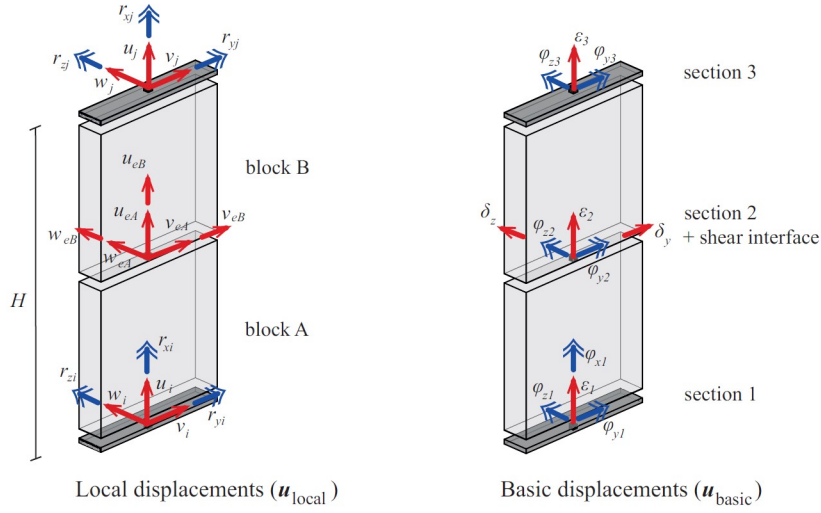


Figure 4.1: Definition of the local and basic system of the macroelement for modelling the in-plane and out-of-plane response (Vanin et al., 2020a).

#### 4.2.1 Modelling of the unit-to-unit interface

As demonstrated in the previous section, masonry aggregates are often modelled as fully coupled, fully separated, or separated with 1D non-linear connections replacing the rest of the aggregate. Modelling fully coupled units leads to wide piers at the interface of the units. However, aggregates in city centres of Europe were often built with weak interlocking at the joint or with a dry joint. In those cases, modelling units as perfectly connected overestimates the interface strength and the stiffness of the whole aggregate.

On the other hand, modelling the units as fully separated can result in either a conservative or unconservative approximation of behaviour, depending on both the position of each unit in the aggregate and the material and geometrical properties of the neighbouring units (Antonio Formisano et al., 2015). For example, the prediction might be overly conservative for the central unit but unconservative for the end unit (Senaldi et al., 2010). In fact, previous research often analysed single units and accounted for the impact of the aggregate either through elastoplastic links (Antonio Formisano and Massimilla, 2018) or through simplified procedures depending on five aggregate and unit properties (Antonio Formisano et al., 2015). However, in all these cases, reference analyses performed on whole masonry aggregates modelled the units of aggregate as perfectly connected.

In previous studies that modelled individual units and simulated the influence of the adjacent units using link elements, the interface response was modelled with zero-length elements to which 1D linear or non-linear material model was assigned (Antonio Formisano and Massimilla, 2018; Stavroulaki, 2019). This was certainly the step forward comparing to modelling the units as isolated, but still ignored the complex out-of-phase behaviour that can occur



during seismic excitations. Additionally, even if two of these zero-length elements are used per interface and represent the interaction between the two units in the normal (Mode I) and transversal (Mode II) direction of the interface, the two elements are considered independently. Therefore, any interaction between the Mode I and Mode II displacements of the interface is neglected during a bidirectional excitation. At the same time, studies that used this approach, such as the ones by Antonio Formisano and Massimilla (2018) and Stavroulaki (2019), used the full aggregate models to calibrate the link elements, but in these models the units were again perfectly connected. Therefore, the complexity of the response of the full model was not addressed. In the study presented here, the modelling of the interface was focused on the case when both units are modelled, while the new nD material model for interface simulated the interaction between adjacent walls, coupling Mode I and Mode II responses.

To model the response of the interface between two units, an nD material model named CohesionFriction3D was developed and implemented into the OpenSEES open-source software. To improve the contact model between two units, the objective was to couple the axial and the shear response of the interface. In the direction normal to the interface (x-direction of the interface), a uniaxial material model or a pre-determined axial force is assigned. The shear displacement is computed from the displacements in the y- and z-direction of the interface, which are the in-plane directions of the interface. The shear force incorporated the friction caused by the actual axial force in the contact and an exponentially degrading cohesion law. It was built upon the work by P. J. B. B. Lourenço (1997) and Vanin et al. (2017a) and extended the latter from a 2D to a 3D problem. In the first step of the material iterative cycle, the axial force acting on the interface was computed based on the uniaxial material model assigned to the axial direction; alternatively, a pre-defined axial force could be assigned. In the second step, the pre-defined or calculated axial force was used to compute a yield function for the shear stress in the local y-z plane. For this purpose, an iterative return-mapping algorithm was implemented. The degradation of cohesion was modelled through the input of the fracture energy value, and the frictional force was evaluated according to the axial force and friction coefficient. The input parameters for this interface model were: a uniaxial material model or fixed axial force, the cohesion force of the interface ( $c_i$ ), Mode II fracture energy of the interface ( $G_{f,II}$ ) and a friction coefficient of the interface ( $\mu_i$ ). Two simple monotonous examples of the interface model are shown in Figure 4.2. These numerical models assume a cohesion of 1 kN, a friction coefficient of  $\mu = 0.4$ , and a Mode II fracture energy of the interface  $G_{f,II} = 15$  Nm. In the first example (Figure 4.2) the system is subjected to a constant axial load of 1 kN and a shear displacement in the y-direction. In the second example (Figure 4.2) the system is again subjected to a constant axial load of 1 kN but this time the shear displacement is applied in the y-z plane at 45 degrees to the y and z axes. The corresponding cyclic responses for the same parameters and loading directions are shown in Figure 4.3. Illustration of CohesionFriction3D model applied to unit-to-unit connection is shown in Figure 4.4.

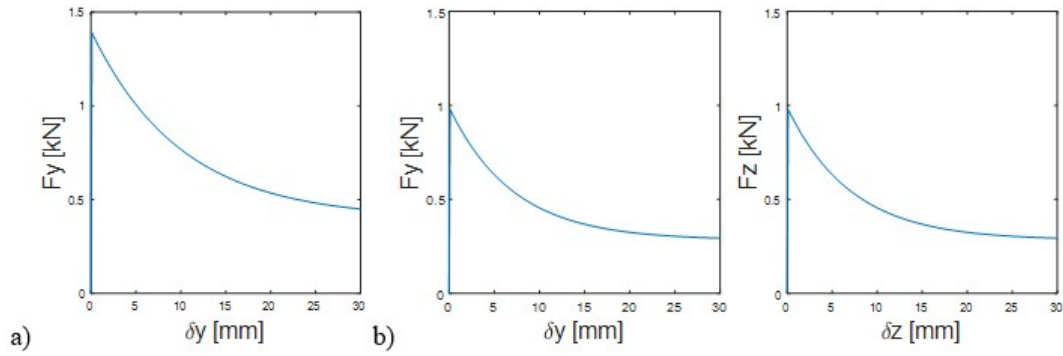


Figure 4.2: CohesionFriction3D monotonic behaviour for: a) shear displacement applied in y-direction; b) shear displacement applied in the y-z plane at 45 degrees to the y and z axes direction.

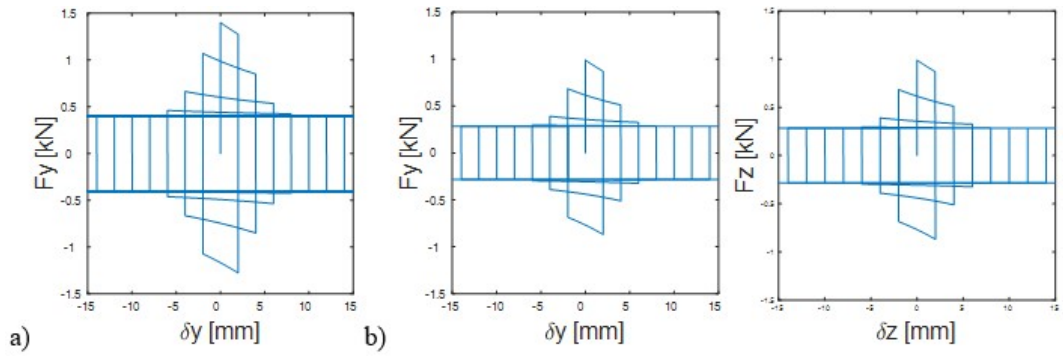


Figure 4.3: CohesionFriction3D cyclic behaviour with: a) shear displacement applied in y-direction; b) shear displacement applied in the y-z plane at 45 degrees to the y and z axes direction.

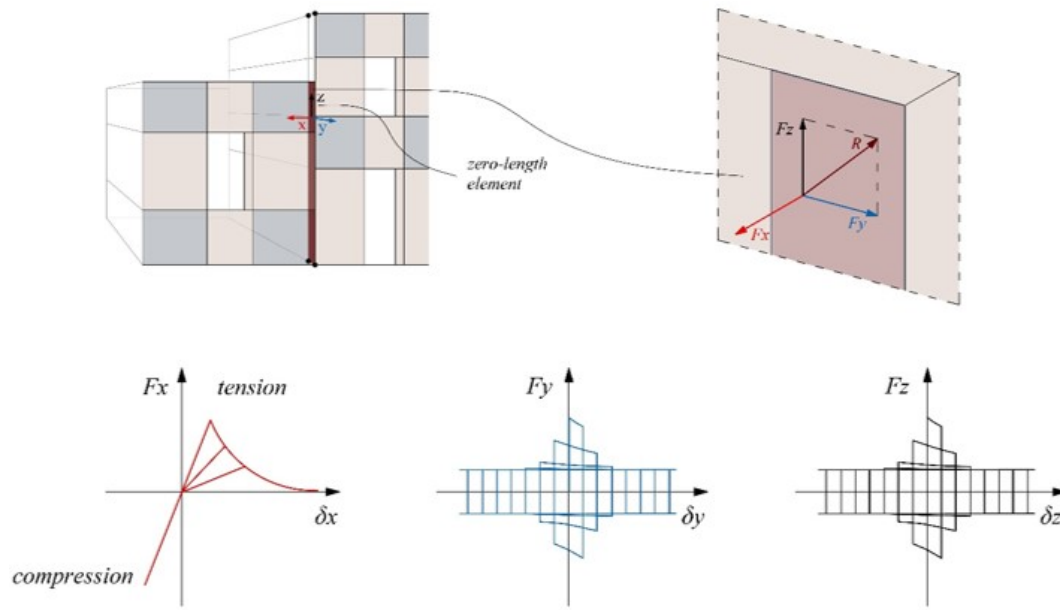


Figure 4.4: Illustration of the CohesionFriction3D model for unit-to-unit connections.

Many of the input parameters describing the interface response are difficult to estimate. Therefore, when evaluating their impact on the global behaviour of the aggregate, it is important to consider uncertainties related to these and other modelling parameters. Reference values for interface parameters and the corresponding methodology are described in the following section.

### 4.3 Equivalent frame model of the SERA-AIMS aggregate

The aggregate chosen as a case study was a half-scale prototype of a masonry building aggregate, designed for the shake table test within the scope of the SERA Adjacent Interacting Masonry Structures project (Tomić et al., 2022a). It was composed of two units. Unit 1 had a U-shape footprint with plan dimensions of  $2.5 \times 2.45 \text{ m}^2$  and a total height of 2.2 m. Unit 2 had a closed rectangular footprint with plan dimensions of  $2.5 \times 2.5 \text{ m}^2$  and a total height of 3.15 m. Unit 2 has additional masses of 1.5 tons evenly distributed per floor. Units are connected by a dry joint without interlocking stones. The wall thicknesses were 30 cm for Unit 1 and 35 and 25 cm for Unit 2 for the first and second floor, respectively. The walls were built from double-leaf irregular stone masonry. Timber floors of the two units were oriented differently, with Unit 1 beams spanning in the x-direction and Unit 2 beams spanning in the y-direction. The thickness of the spandrels underneath the openings was decreased to 15 cm.

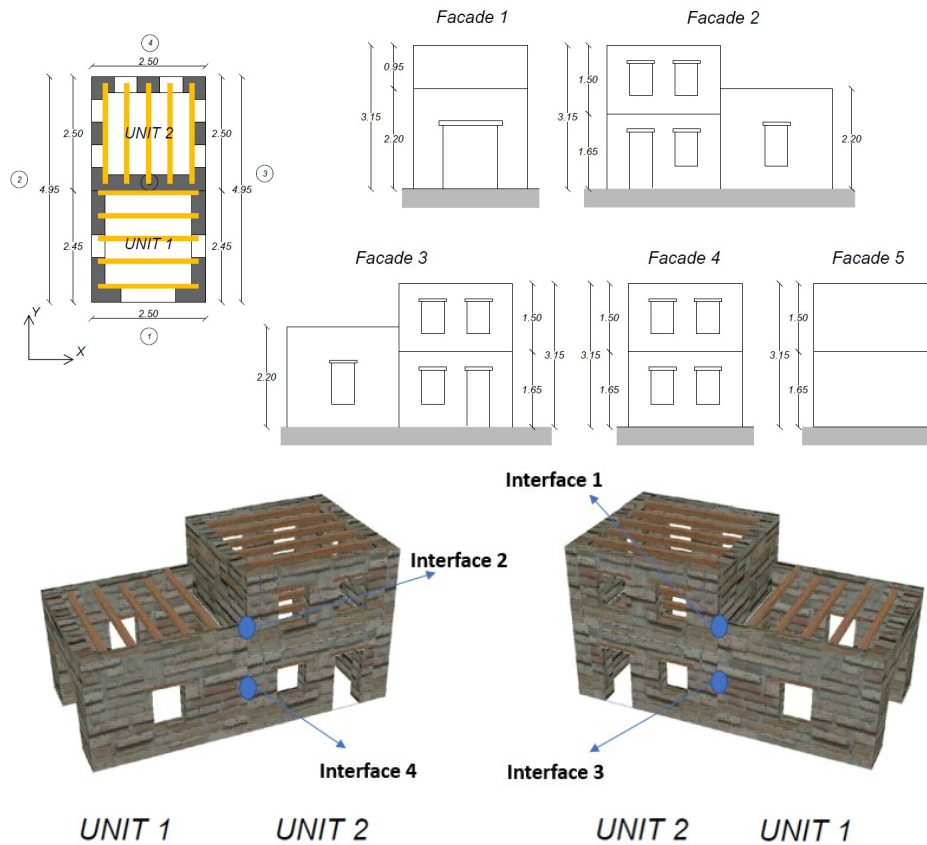


Figure 4.5: Case study: Floor plan layout of the two units and 3D view of the test unit with the positions of the interfaces.

### 4.3.1 Material and modelling parameters

The aggregate was modelled in OpenSEES using an equivalent frame approach. All masonry elements, both piers and spandrels, were modelled with the macroelement formulated in Vanin et al. (2020a). All piers and spandrels were assigned the same material properties. Nodal panels between piers and spandrels were considered as rigid. Deformable timber floors were modelled with an orthotropic elastic membrane, with a higher stiffness in the main direction of the floor, parallel to the beams and a lower stiffness in the orthogonal direction. The shear stiffness of the membrane was defined by the shear modulus. The membrane was therefore defined by the modulus of elasticity in two directions, shear modulus and thickness. Since the behaviour of the floors remained linear elastic, the connection between the floor and wall accounted for the non-linear behaviour and possible connection failure, which could result in the out-of-plane failure of a pier. This connection was modelled with a zero-length element to which a frictional model was assigned. The nodes of the floor were modelled independently of the nodes of the walls to capture the possible relative displacements. The sliding was assumed to occur when the beam moved away from the wall in the direction perpendicular to the wall,

and pounding was assumed to occur in the opposite direction. It is also possible to model the slip in the direction parallel to the wall (Vanin et al., 2020b), but, for this study, the connection in the direction parallel with the wall was assumed as linear elastic. The material was defined by the friction coefficient between the floor and walls, the modulus of elasticity and the shear modulus. Zero-length elements were also used to model the connections between orthogonal walls. The connection simulated a potential formation of a vertical crack, which could lead to the out-of-plane failure of a wall. The 1D material for the interface was defined as featuring a damage tension law with exponential softening and a linear elastic model in compression (Vanin et al., 2020b). The material was defined by the elastic modulus, the tensile strength and the Mode I fracture energy.

Four different classes of models were set up (Table 4.1). They differed only in the modelling of the interfaces between Unit 1 and Unit 2; all other modelling choices and assumptions were identical for these classes.

Table 4.1: Four different classes of models.

CASE A	Interfaces were modelled with the newly implemented nD material model.
CASE B	Interfaces were modelled with 1D material models.
CASE C	The two units were modelled as separate units. The nodes of Unit 1 and 2 at the interface were not connected.
CASE D	The two units were modelled as fully connected units. The nodes of Unit 1 and 2 at the interfaces always experienced the same absolute displacement.

Case A was the model with the newly developed nD material, as described in Section 4.2. For Case B, every degree of freedom at the interfaces was modelled by a separate 1D non-linear spring, linear elastic in compression and with limited strength and exponential softening in tension. Case C featured two units with no interaction. For Case D, the perfect connection was established through the Equivalent Degree of Freedom (EQDOF) command, which constructs a multi-point constraint between nodes.

A total of 19 material and modelling parameters were chosen to perform the uncertainty analysis. Masonry material parameters were defined as:  $E_m$  modulus of elasticity;  $G_m$ , shear modulus;  $f_{cm}$ , compressive strength;  $\mu_m$ , friction coefficient; and  $c_m$ , cohesion of masonry. Median values were chosen according to the experimental campaign performed on masonry of a similar typology by Guerrini et al. (2017) and Guerrini et al. (2019) and Senaldi et al. (2018) and Senaldi et al. (2020). Masonry material parameters were directly applied to all piers and spandrels. The floor stiffness factor ( $k_{floor}$ ) multiplied the default stiffness values of the flexible floor diaphragm, which were computed as:  $E_1 = 10$  GPa,  $E_2 = 0.5$  GPa,  $G = 10$  MPa according to Brignola et al. (2008) and Brignola et al. (2012). Wall-to-wall connection factors  $f_1$  and  $f_2$  multiply the default wall-to-wall connection strength of the first and the second

unit, respectively. Wall-to-floor friction coefficient  $\mu_{f-w}$  is directly applied to the frictional floor-wall connection with the mean value based on the work of Almeida et al. (2020). The drift capacities in flexure and shear,  $d_{c,flexure}$ , and  $d_{c,shear}$ , are the limit collapse flexural and shear drifts at which the lateral stiffness of the macroelement is set to zero, chosen according to Vanin et al. (2017b). Aggregate interface parameters were defined as:  $E_i$ , interface modulus of elasticity;  $G_i$ , interface shear modulus;  $f_{t,i}$ , tensile strength in the axial direction;  $G_{f,I,i}$  Mode I fracture energy;  $c_i$ , interface cohesion force;  $G_{f,II,i}$ , Mode II fracture energy; and  $\mu_i$ , interface friction. The aggregate interface parameters were directly applied to the interfaces between the units when applicable. The Rayleigh damping ratio was applied together with first six modal periods to calculate the damping coefficients. For each set of parameters, the modal properties were first calculated to correctly calculate their dependent damping coefficients. All the parameters were assigned normal or lognormal distributions for the LHS:

- Masonry material parameters ( $E_m, G_m, f_{cm}, \mu_m, c_m$ )
- Floor stiffness factor ( $k_{floor}$ )
- Wall-to-wall connection factors ( $f_{w1}, f_{w2}$ )
- Wall-to-floor friction coefficient ( $\mu_{w-f}$ )
- Drift capacity ( $d_{c,flexure}, d_{c,shear}$ )
- Aggregate interface parameters ( $E_i, G_i, f_{t,i}, G_{f,I,i}, c_i, G_{f,II,i}, \mu_i$ )
- Damping ( $\xi$ )

After each parameter was assigned to a normal or lognormal distribution, LHS was performed to create sets of parameters. The distributions of material and modelling properties are represented in Table 4.2. The distributions were calibrated for the present typology and case study, but for different masonry aggregate typologies, including stronger interlocking or retrofitting using modern techniques, the parameters should be updated.

Table 4.2: Distributions of material and modelling parameters. The mean values of parameters with lognormal distribution feature an equivalent normal mean value inside the colon.

Parameter	Probability distribution	Mean	Standard deviation	Reference
$E_m$	Normal	3.5 [GPa]	1.0 [GPa]	(Guerrini et al. 2017; Senaldi et al. 2018)
$G_m$	Lognormal	21.13 (1.5 [GPa])	0.5	(Guerrini et al. 2017; Senaldi et al. 2018)
$f_{cm}$	Normal	1.3 [MPa]	0.35 [MPa]	(Guerrini et al. 2017; Senaldi et al. 2018)
$\mu_m$	Lognormal	-1.39 (0.25)	0.3	(Guerrini et al. 2017; Senaldi et al. 2018)
$c_m$	Lognormal	12.36 (0.233 [MPa])	0.5	(Guerrini et al. 2017; Senaldi et al. 2018)
$k_{floor}$	Lognormal	0 (1.0)	0.5	(Brignola et al. 2008, 2012)
$f_{w1}$	Lognormal	0 (1.0)	0.3	-
$f_{w2}$	Lognormal	0 (1.0)	0.3	-
$\mu_{w-f}$	Lognormal	0 (1.0)	0.3	(Almeida et al. 2020) (Vanin et al. 2020a)
$\delta_{c, flexure}$	Lognormal	-4.57 (0.01035)	0.2	(Vanin et al. 2017b)
$\delta_{c, shear}$	Lognormal	-4.96 (0.007)	0.2	(Vanin et al. 2017b)
$E_i$	Normal	3.5 [GPa]	1.0 [GPa]	-
$G_i$	Normal	1.5 [GPa]	0.7 [GPa]	-
$f_{t,i}$	Lognormal	9.90 (20 [kN])	0.5	-
$G_{fI,i}$	Normal	100 [Nm]	30 [Nm]	-
$c_i$	Lognormal	9.90 (20 [kN])	0.5	-
$G_{fII,i}$	Normal	100 [Nm]	30 [Nm]	-
$\mu_i$	Normal	0.6	0.3	-
$\xi$	Normal	0.02	0.005	(Vanin et al. 2020b)

Additionally, correlation coefficients were imposed between certain parameters, shown in Table 4.3. A strong correlation was imposed between the modulus of elasticity, shear modulus and compressive strength, as these values are often correlated in experimental campaigns. Moderate correlation was imposed between wall-to-wall interlocking in the two units, assuming that workmanship regarding details such as interlocking was similar between units of the same aggregate. Interface parameters regarding the strength and the fracture energy for Mode I (normal) and Mode II (transversal) were selected as moderately correlated. Finally, a moderate correlation was imposed between collapse drift values in flexure and shear for masonry elements. It should be noted that the imposed correlation coefficients between the parameters are approximated, and can be disputed or evaluated separately for each case-study.

Table 4.3: Assumed correlation coefficients between sets of input parameters.

Correlated parameters	Correlation coefficient	Strength of correlation
$E_m, G_m, f_{cm}$	0.7	Strong
$f_{w1}, f_{w2}$	0.5	Moderate
$f_{t,i}, G_{fI,i}, c_i, G_{fII,i}$	0.5	Moderate
$\delta_{c, flexure}, \delta_{c, shear}$	0.5	Moderate

### 4.3.2 Earthquake record

For each set of material parameters, the incremental bi-directional time history analysis was performed. The initial acceleration was chosen as 100% of the value of the Montenegro Albatros 1979 record with a PGA of 0.21 g in the E-W direction and 0.18 g in the N-S direction, shown in Figure 4.6 (Luzi et al., 2016). This was chosen as a starting point because the initial numerical analyses showed that no failures occurred for those PGA levels. Afterwards, the acceleration was increased by 50% of the original record levels up to the point of failure.

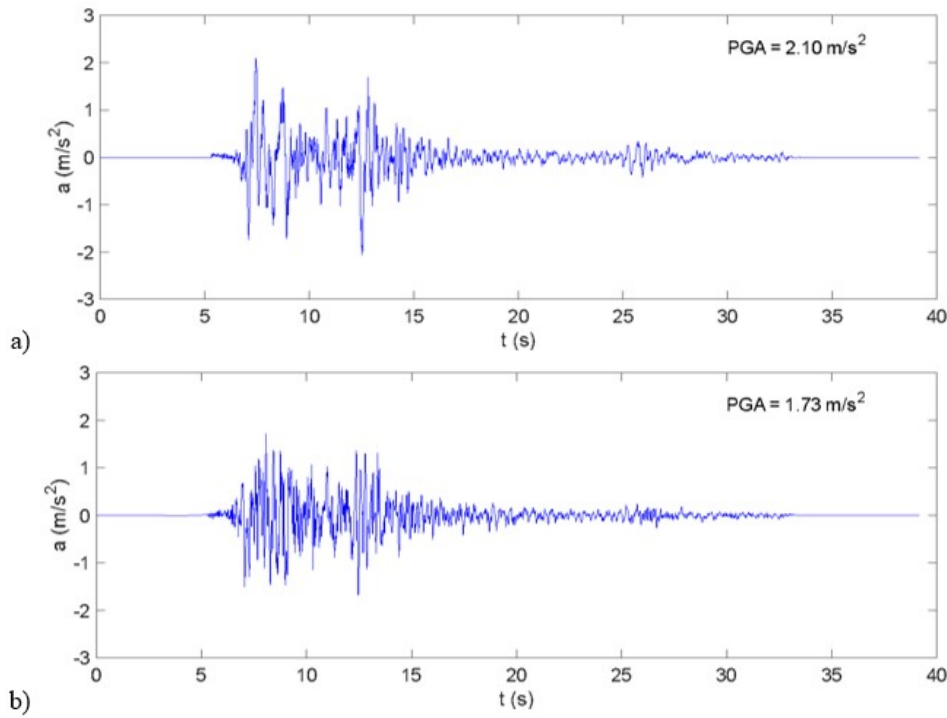


Figure 4.6: Processed acceleration time histories of the Montenegro 1979 earthquake (Albatros station), with the scaled time step in the: a) E-W direction; b) N-S direction (Luzi et al., 2016).



## **4.4 Methodology**

To account for the epistemic uncertainty of material and modelling parameters, Latin Hypercube Sampling (LHS) was performed in two steps to generate 400 sets of 19 parameters. In the first step, each parameter was assigned a normal or lognormal distribution according to the values from experimental campaigns, literature or building codes, as defined in the previous section. The generated matrix had dimensions of 19 x 400, where each column contained one set of parameters to be used for a single incremental dynamic analysis. The difference in the independent assignment of normal or lognormal distributions was that the marginal distribution of each column was adjusted so that points of the sample marginal distribution in each column were uniformly distributed on the probability scale (Stein, 1987). Additionally, correlation matrices between the parameters were assigned to avoid unrealistic sample sets, e.g. a sample with an upper bound value for the modulus of elasticity and a lower bound value for the compressive strength. Once all parameters were assigned their distributions, the correlation matrix was calculated and compared to the imposed one. The difference between the two was evaluated by the norm between the imposed and the obtained correlation matrix. This norm was the objective function that had to be minimized. According to Dolsek (2009), one way of minimizing the norm is by performing random permutations of random elements of each vector. This method is called simulated annealing (Vořechovský and Novák, 2003). After each permutation, the norm is re-evaluated and, if the norm decreased, the iteration is accepted. Otherwise, it is rejected. Sets of material and modelling parameters are then used to perform incremental dynamic analyses (Vamvatsikos and Cornell, 2002).

A method proposed by Vanin and Katrin Beyer (2018), which is a refined and novel use of a Point Estimate Method, aims to lower the computational cost by further reducing the number of required non-linear simulations. This method is valuable for more detailed analyses, i.e. non-linear dynamic analyses using shell elements or 3D solid elements, or for engineering practice. On the other hand, this different approach relies on a low computational burden of equivalent frame models in OpenSEES, where it is not necessary to keep the number of analyses low. Yet to avoid redundant analyses stemming from the classical Monte Carlo method (Metropolis and Ulam, 1949), which would not benefit the statistical output, LHS is still the best balance between accuracy and computational burden.

## **4.5 Results - illustrative examples of the impact of interface modelling**

Herein, the responses of the four models defined in Section 4.3.1 are evaluated as an illustrative example of differences in behaviour related to the aggregate interface modelling. All four models used the mean set of input parameters shown in Table 4.2 and were subjected to the Montenegro Albatros bidirectional record scaled to a PGA of 0.84 g, the value that was chosen to trigger a collapse in all the models. Modal periods of the four cases are shown in Table 4.4.

Table 4.4: Modal periods of the four models, depending on the interface model.

Mode number	nD interface	1D interface	Separate units	Fully connected units
<b>I</b>	0.060 s	0.060 s	0.061 s	0.059 s
<b>II</b>	0.048 s	0.047 s	0.060 s	0.047 s
<b>III</b>	0.046 s	0.046 s	0.059 s	0.043 s
<b>IV</b>	0.043 s	0.044 s	0.045 s	0.038 s
<b>V</b>	0.042 s	0.043 s	0.044 s	0.037 s
<b>VI</b>	0.040 s	0.038 s	0.043 s	0.035 s

We observed that the model with nD interfaces (Case A), the model with 1D interfaces (Case B), and the model with the fully connected units (Model D) showed same modal shapes, and similar modal periods. This was expected as nonlinear properties of the interface are not taken into an account in the elastic range. The only difference were a slightly lower periods in case of Model D. The separate units model (Case C) showed a lower stiffness and larger periods. Figure 4.7 shows the first modal shape for all four models. As expected, Models A, Model B, and Model D show exactly the same modal shape - transversal (x-direction) deformation of Unit 2, while the separate units model (Model C) shows transversal deformation of Unit 1, which is U-shaped when not restrained by the adjacent unit. Fig 4.8 shows the hysteretic responses of the four models for a PGA of 0.84 g, with the pier in-plane drift capacity set as infinite for illustration purposes.

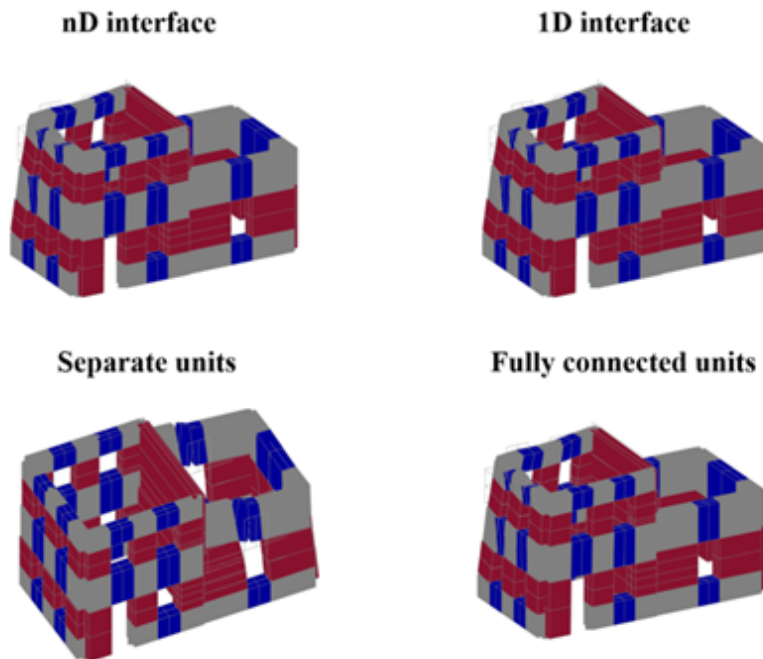


Figure 4.7: Modal shapes of the first vibration mode of the four models.

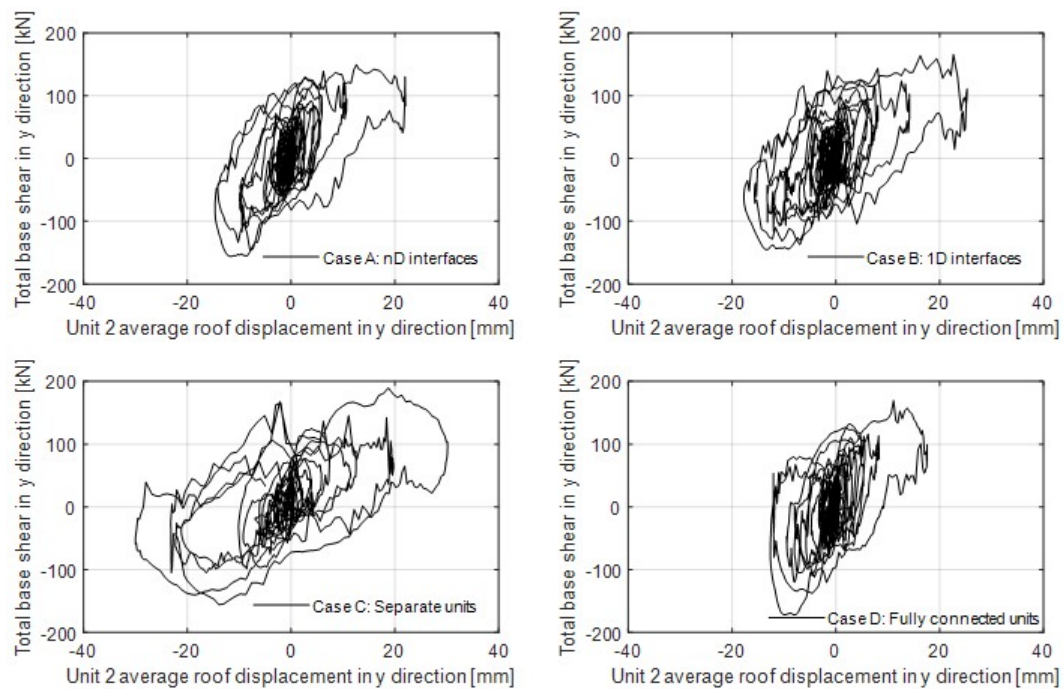


Figure 4.8: Hysteretic responses of the four models in y-direction subjected to Montenegro Albatros record with PGA of 0.84 g.

The models showed different displacement demands, with the separate unit model reaching double displacement in the negative direction compared with the model of fully connected units. This was expected, since in the negative direction Unit 2 interferes with Unit 1. In case of fully connected units, the response is very stiff in this direction, whereas for the separate units there is no restraint of any type for Unit 2. Models with nD and 1D interfaces showed larger displacement demand than the model with fully connected units in both the negative and the positive direction. At the same time, the nD and 1D interface models differed with regard to the maximum base shear in the y-direction by as much as 20%. The limit drifts were imposed as the defined mean values, and analyses were run once again to observe the failure modes with each of the four models. As previously stated, all models reached failure for a PGA of 0.84 g, and the in-plane flexural failure occurred in all cases. However, as shown in Figure 4.9, failure of the nD interface model was triggered by the failure of the upper storey piers of Unit 2. The failure of the 1D interface model was also triggered by the failure of the upper storey piers of Unit 2, but unlike the nD interface model, the failure also involved another pier in the corner, which pointed towards a possible corner mechanism. All models where forces could be transmitted across the interface of the two units (models A, B, D) lead to failure modes that involved piers of the second storey of Unit 2. When the two units were modelled as unconnected, failure occurred, however, in the first storey of Unit 2.

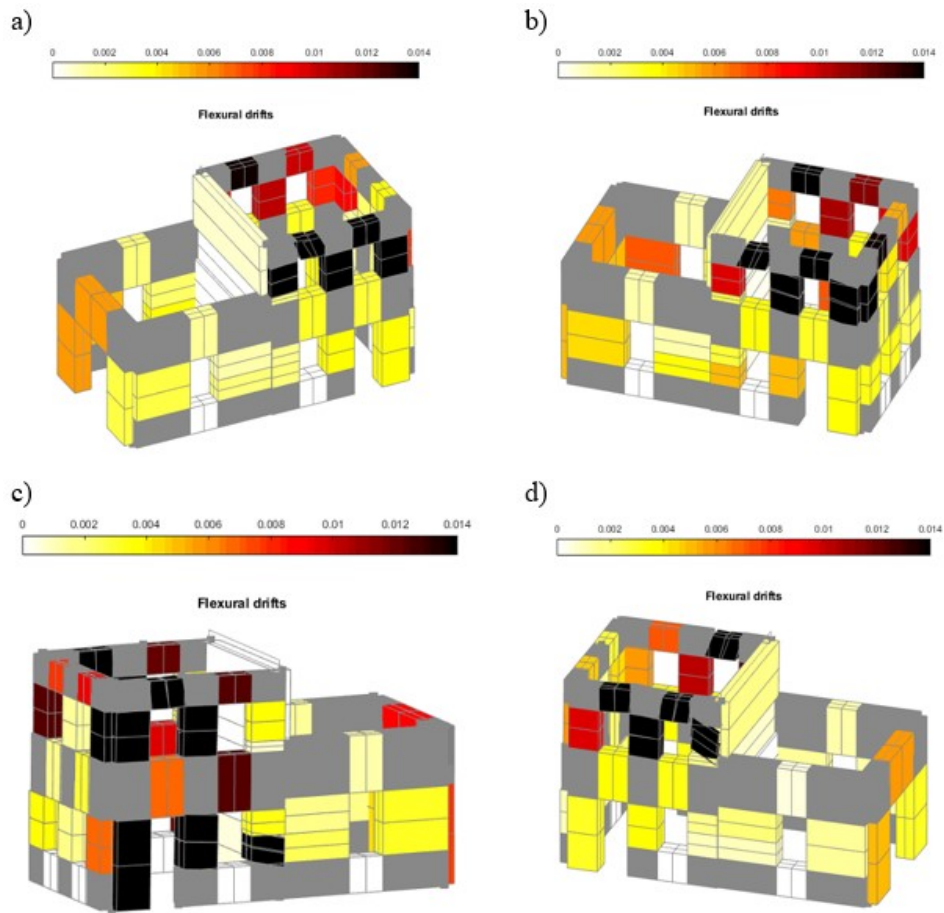


Figure 4.9: Failure mechanisms for the four models: a) nD interfaces model; b) 1D interfaces model; c) Separate units model; d) Fully connected units model.

The observed differences in modal periods, hysteretic response and mode of failure justify the need for more detailed modelling of the interface, as well as a deeper consideration of the uncertainty of modelling parameters related to the interface between the units. These results indicate that not only do differences in hysteretic responses exist, but there is also a risk of overlooking possible damage mechanisms and modes of failure. Furthermore, as shown in the next sections, these differences become even more pronounced when the uncertainty in material and modelling parameters is taken into account.

## 4.6 Discussion of IDA results

Results are discussed in terms of the differences between the four modelling approaches and in terms of the influence of uncertainty of material and modelling parameters within each modelling approach. When comparing the seismic fragility curves for all four modelling approaches (nD non-linear interfaces model, 1D interfaces model, separate units model, and fully connected units model) in Figure 4.10, all four curves have very similar shapes,

wherein the offset of initiation of failure probability depends on the modelling approach. As expected, the separate unit model appeared as the most fragile, having almost double the probability of failure at PGA 0.6 g in comparison to the nD non-linear interface model. It might seem unexpected that the fully connected units model behaved more fragile than the nD interface model, meaning that the ability of units to separate can be beneficial, even if there is a possibility of pounding. In fact, it underscores the influence of the interactions between the units on the type of damage and failure as well as its location. For the fully connected units model, we observed an increase of out-of-plane failures in the second storey of Unit 2, especially in the x-direction. At the same time, failure was localized in Unit 1 in only 3% of the cases. Additionally, in the nD non-linear interfaces model, Unit 1 accounted for 30% of the failures, and a large majority of these failures were in-plane, as seen in Figure ???. This ability of the modelling choices to significantly influence damage and failure location and type, verified through 400 different sets of parameters per modelling approach, can explain unexpected results in terms of seismic fragility curves and, at the same time, underlines the importance of using the correct modelling approach to understand the behaviour of buildings and avoid overlooking possible mechanisms. This is particularly important when retrofit interventions are designed based on the predicted failure mechanisms. Finally, these results partially contradict findings from previous studies, which considered models with fully connected units as the benchmark model to compare with other approaches. Assuming that the nD interfaces model represents best the real behaviour, modelling the units as either fully separated or fully connected could therefore be conservative, but miss a probable failure mechanism.

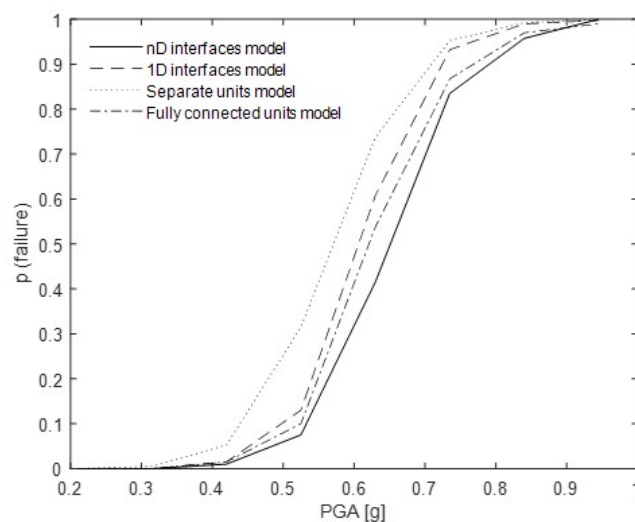


Figure 4.10: Comparison of seismic fragility curves for four aggregate modelling approaches.

All four modelling approaches showed a correlation between the modulus of elasticity, shear modulus, compressive strength, drift capacities, Rayleigh damping ratio and floor-to-wall friction with the failure PGA. The values for the linear correlation coefficients for modulus of elasticity, shear modulus, and compressive strength were similar in all four models. It should

be noted that when distributions of the modulus of elasticity, shear modulus and compressive strength were defined for LHS, a moderate correlation value was imposed between them. Similarly, the linear correlation coefficients for the limit flexure and shear drift values with the failure PGA were almost identical for all four modelling approaches. Again, it should be noted that a moderate correlation between these parameters was imposed when creating the parameter samples. The value of the Rayleigh damping ratio shows the highest linear correlation coefficient for all the modelling approaches except the fully connected units model, where floor friction takes place. This underlines the importance of the choice of the damping coefficient for non-linear time history analyses of masonry buildings and is in line with findings by Vanin et al. (2020b). Additionally, the nD interface model showed a correlation between the friction of the interface and the failure PGA. This correlation coefficient was low but still significant, and it is important to note that this effect was modelled only with the nD interface model. For Case B, the shear stiffness of the interface negatively correlated with the failure PGA, which was confirmed by the positive correlation between the shear stiffness with the seismic demand parameters for both Case A and Case B. Interestingly, all four modelling approaches showed that for the collapse capacity, the effect of the floor stiffness parameter was secondary to the friction between the floor and the wall. In fact, the floor factor correlated significantly ( $p\text{-value} < 5\%$ ) with the failure PGA only in the 1D interface model. Together with friction at the interface between the two units in the nD interface model, these results indicate the importance of connections when evaluating the collapse capacity.

When the mode of the failure was examined, the nD non-linear interfaces model showed that the units were dominated by in-plane failures. As expected, the separate unit model showed 7% out-of-plane failures, which accounted for 56% of the failures for Unit 1. This result was not surprising because when units are analysed separately, Unit 1 has a U-shaped layout, which makes it vulnerable to out-of-plane failures. However, Unit 1 also has a lower height, no additional weight, and slightly thicker walls in comparison to Unit 2, which prevented a drastic increase of out-of-plane failures. For the fully connected units model, out-of-plane failures accounted for 5% of the failures, but none of them were localized in Unit 1, consistent with the lower height and larger wall thickness of Unit 1. Furthermore, all of the out-of-plane failures were localized in the second storey of Unit 2 in the x-direction. At the same time, the failure PGA increased in comparison with the separate unit model, since the collapse of Unit 1 was prevented. In the case of the models with nD and 1D interfaces (Case A and Case B) the negative impact of Unit 1 on the out-of-plane collapse of the upper floor of Unit 2 was prevented by modelling the interface as not perfectly connected. For illustrative purposes, an example of out-of-plane and in-plane failure can be seen in Figure 4.11.

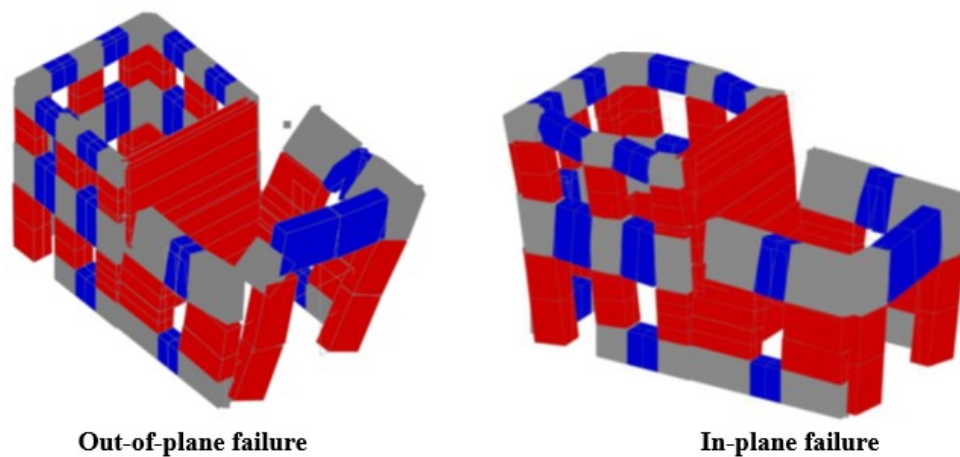


Figure 4.11: Examples of out-of-plane and in-plane failure (nD non-linear interfaces model).

In-plane failures were the dominant mode of failure, and flexural in-plane failures specifically accounted for 96–97% of the total in-plane failures for any modelling approach. Upper storey in-plane failure, primarily in the y-direction and to a lesser extent in the x-direction, accounted for all the cases of Unit 2 in-plane failure for the nD interfaces and the fully connected units models. In contrast, the failure only occurred in a few cases at the first storey of Unit 2 for the separate units model. In-plane failures of Unit 1 were always in the x-direction, which is in line with the fact that Unit 1 piers in the y-direction are rather squat. Unit 1 experienced most of the in-plane failures in the nD interfaces model, suggesting that modelling the aggregate with the fully connected units model neglected the probability of failure location in the Unit 1. For the separate units model analysis, failure localized at Unit 1 in 6% of the cases, but a large number of those failures were out-of-plane. Only by modelling the aggregate using the nD interfaces model did failure localize in 30% of the cases in Unit 1, with an in-plane failure mode in the x-direction. Our results strongly support the idea that correctly modelling the interface changes either or both the failure location and the failure mode. It seems that modelling the units with the interface: (i) prevented OOP failure of Unit 1 occurring in the separate units model, (ii) avoided the negative impact of full connection between the units on the Unit 2 upper floor. It should be noted that all four classes of models in prediction underestimated out-of-plane behaviour. As further elaborated in the next section, this was primarily due to overdamping of the out-of-plane behaviour caused by the adoption of initial-stiffness and mass proportional Rayleigh damping.

For the nD interfaces model (Case A) failure localized in Unit 1 for 30% of the cases, in comparison with only 3% of the Cases for the Fully connected units (Case D). The separate units model showed a less stiff behaviour and larger displacements. The difference between nD interfaces model (Case A) and 1D interfaces model (Case B) was significant in the opening of the interfaces in the transversal direction. Since the damage to the shear interface from relative vertical displacement is not taken into account by the 1D interfaces model (Case B), the strength of the interface in the y-direction was overestimated by the 1D interfaces model. As a result, the 1D interfaces model led to smaller interface openings than the nD interfaces



model.

## 4.7 Post-diction analyses

The blind prediction required the submission of a prediction stemming from a single model. So, aside the probabilistic approach, a model had to be chosen for the final prediction. The theoretical shake-table acceleration limit was planned to be reached in four steps, with the ground motion applied at 25%, 50%, 75% and 100% of such limit. Each step consisted of three substeps, comprising (i) a uni-directional test in the y-direction, (ii) a uni-directional test in the x-direction and (iii) a bi-directional test in x- and y-directions, as shown in Table 4.5. However, the actual testing sequence differed from the original plan and comprised ten steps overall, as shown in Table 4.6 and described in detail in Tomić et al. (2022b). Due to the difference between the nominal and applied sequences, it was necessary to rerun the analyses with the actual seismic excitation recorded at the shake table to perform a meaningful comparison of results (Tomić et al., 2022a; Tomić et al., 2022b). For the same reason, in the following only pre-diction with actual accelerations and post-diction results are reported.

Table 4.5: Nominal SERA AIMS shake-table testing sequence.

<b>Run notation</b>	<b>Direction</b>	<b>Level of shaking (shake-table capacity)</b>	<b>Nominal PGA</b>
1.1	y	25%	0.219 g
1.2	x	25%	0.156 g
1.3	Bidirectional	25%	0.219 (y)/0.156 (x) g
2.1	y	50%	0.438 g
2.2	x	50%	0.313 g
2.3	Bidirectional	50%	0.438 (y)/0.313 (x) g
3.1	y	75%	0.656 g
3.2	x	75%	0.469 g
3.3	Bidirectional	75%	0.656 (y)/0.469 (x) g
4.1	y	100%	0.875 g
4.2	x	100%	0.625 g
4.3	Bidirectional	100%	0.875 (y)/0.469 (x) g



Table 4.6: Actual applied testing sequence of the SERA AIMS shake-table test in Tomić et al. (2022a).

Run notation	Direction	Level of shaking (shake-table capacity)	Nominal PGA	Actual PGA
0.1	y	12.5%	0.110 g	0.113 g
0.2	x	12.5%	0.078 g	0.075 g
0.3	Bidirectional	12.5%	0.110 (y)/0.078 (x) g	0.114 (y)/0.072 (x) g
1.1	y	25%	0.219 g	0.170 g
1.2	x	25%	0.156 g	0.178 g
1.3	Bidirectional	25%	0.219 (y)/0.156 (x) g	0.208 (y)/0.174 (x) g
2.1	y	50%	0.438 g	0.593 g
2.1S	y	50%	0.438 g	0.615 g
1.2S	x	25%	0.156 g	0.258 g
2.2S	x	50%	0.313 g	0.425 g

#### 4.7.1 Pre-diction with the actual accelerations recorded at the shake-table

The original prediction was repeated with a model featuring mean values of material parameters from the previous sections ( $E_m$ ,  $G_m$ ,  $f_{cm}$ ,  $\mu_m$ ,  $c_m$ ) and using Rayleigh initial-stiffness and mass proportional damping with 1% critical damping ratio in combination with the actual shake-table accelerations. The compared quantities are shown in Figure 4.12.

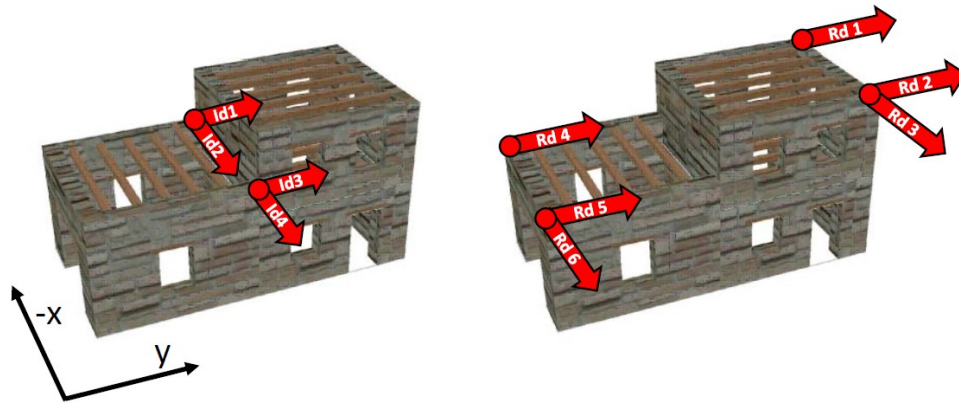


Figure 4.12: Compared quantities for the blind prediction submissions. Displacements relative to the ground (Rd1–6) and interface opening (Id1–4).

Figure 4.13 illustrates the principal damage mechanisms observed during the experimental campaign. Figure 4.14 shows the maximum recorded flexural drifts of the post-diction with the original model. This and the following group of models all correctly captured very minor shear drifts, which are therefore not displayed here or in the next figures. Comparing mechanisms,

the original model overestimated stiffness and underestimated displacements while also failing to correctly capture the localisation of the flexural deformation in the upper storey of Unit 2.

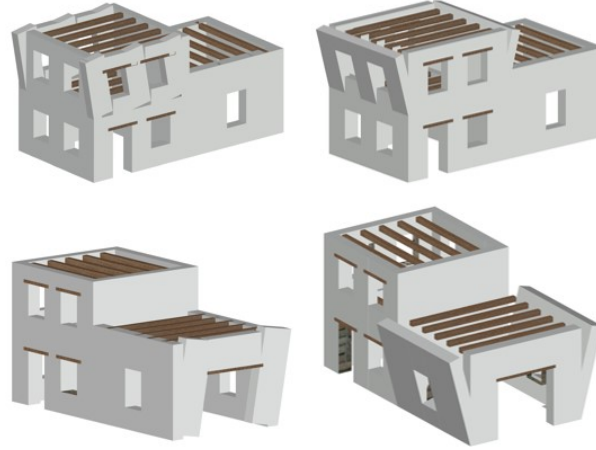


Figure 4.13: Illustrations of principal damage mechanisms observed during the SERA-AIMS experimental campaign (Tomić et al., 2022a).

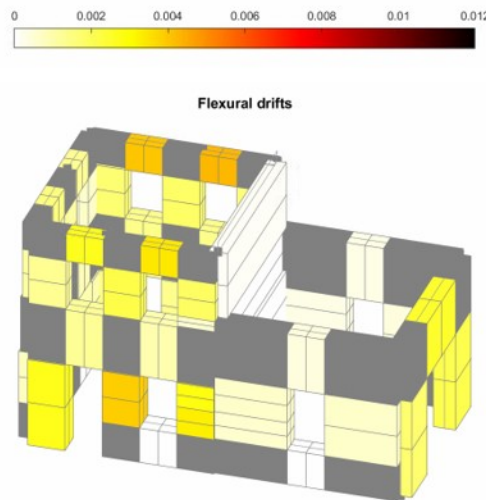


Figure 4.14: Maximum recorded flexural drifts for the post-diction analysis with the original model.

The results reported in Figure 4.15 confirm that the original model is too stiff and underestimates the displacements, especially those recorded on Unit 2. Interface openings were satisfactorily predicted in the transversal direction, but were also underestimated in the longitudinal direction. The predictions of the base shear values were better than for displacements and interface openings.

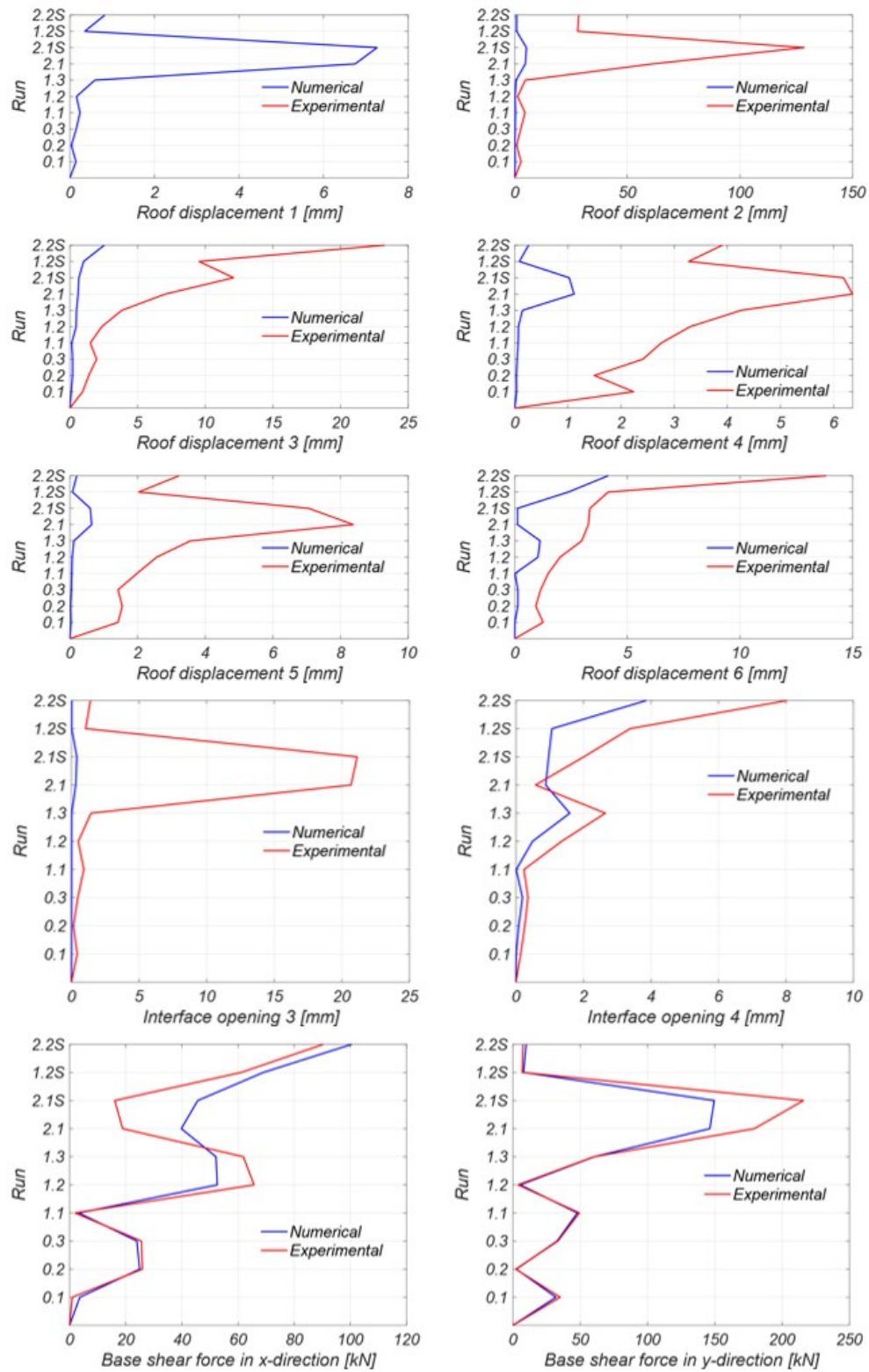


Figure 4.15: Comparing the original post-diction model with experimental results.

### 4.7.2 Re-calibration of material properties based on wallette tests

Due to poor results from the pre-diction analyses with the actual accelerations applied at the shake-table, it was necessary to step back to the calibration of the material and modelling properties. Previously, mean values for probabilistic analysis, and concrete values for the pre-diction analysis were taken from vertical compression and diagonal compression tests performed by Senaldi et al. (2018) and Guerrini et al. (2017) on a masonry of a similar typology (Tomić et al., 2022b). As this resulted in too stiff behaviour, a new calibration was performed based on the quasi-static cyclic tests on wallettes of the same typology, performed by the same authors. This time the calibration was performed based on four material parameters and one modelling parameter that affected the numerical results of the wallettes quasi-static cyclic tests. The calibration was done in following steps:

1. New 200 sets of material parameters were generated using LHS. The distributions of parameters were updated in comparison with the previous section, based on findings by Vanin et al. (2020b), which were in agreement with the observation that stiffness values should be lower.  $G$  to  $E$  ratio was fixed to 0.3 according to findings by Wilding et al. (2020). The new LHS material parameter are shown in Table 4.7.
2. Wallettes tests done by Senaldi et al. (2018) and Guerrini et al. (2017) were replicated in OpenSEES software using Macroelement3D.
3. The comparison of experimental and numerical results was based on the secant stiffness calculated between 1/3 and 2/3 of the maximal lateral force value.

Table 4.7: Distribution of material and modelling parameters.

Parameter	Probability distribution	Mean	Standard deviation
$E_m$	Normal	1.5 [GPa]	0.5 [GPa]
$G_m$	Set to $0.3E_m$ according to Wilding et al. (2020)		
$f_{cm}$	Normal	3.0 [MPa]	1.0 [MPa]
$\mu_m$	Normal	0.20	0.15
$c_m$	Normal	0.120 [MPa]	0.1
Drop drift	Normal	0.004	0.002

The five best stiffness matches for each wallette were selected based on the minimal difference between experimental and numerical secant stiffness and the overall sets were selected based on the minimal sum of stiffness differences across all four wallettes for the given material parameters set. Table 4.8 shows the top five matches for each wallette and overall, while Table 4.9 shows the 21 chosen sets of material parameters (as four occurred as a best match in more than one case) as well as the first modal period. At the time of a writing of the article,

only the first modal period was available from the experimental campaign as  $T=0.13$  s. It is indicative that the chosen material parameters set yield better approximation of the first modal period than the initial models as shown in Table 4.7.

Table 4.8: Best stiffness matches for each wallette and overall. The left side shows the material parameter set number, and the right side shows the difference in secant stiffness between the experimental and numerical stiffnesses.

CT01	CT02	CS01	CS02	Overall	CT01 [%]	CT02 [%]	CS01 [%]	CS02 [%]	Overall [%]
33	45	101	18	12	0.2	0.0	0.5	0.1	63.6
156	76	143	76	80	0.6	0.2	0.8	0.2	64.7
80	196	25	103	154	0.7	0.6	1.0	0.7	70.4
105	160	66	45	11	1.1	0.6	1.1	1.3	70.5
11	145	178	26	75	1.5	1.0	1.2	1.5	70.6

Table 4.9: Chosen material parameter sets.

Set n°	E [GPa]	G [GPa]	$f_c$ [MPa]	$\mu$	c [MPa]	T [s]
11	1.39	0.42	3.22	0.24	0.17	0.12
12	1.46	0.44	2.58	0.34	0.13	0.12
18	1.83	0.55	3.81	0.31	0.14	0.11
25	1.17	0.35	2.09	0.07	0.18	0.13
26	1.94	0.58	4.01	0.21	0.23	0.11
33	1.19	0.36	1.92	0.10	0.24	0.13
45	2.04	0.61	4.08	0.16	0.17	0.11
66	1.22	0.37	2.40	0.31	0.09	0.13
75	1.40	0.42	2.37	0.16	0.23	0.12
76	2.17	0.65	4.14	0.11	0.15	0.10
80	1.15	0.35	3.80	0.09	0.28	0.13
101	1.22	0.37	2.87	0.32	0.02	0.13
103	1.87	0.56	5.55	0.06	0.12	0.11
105	1.41	0.42	1.33	0.07	0.04	0.13
143	1.25	0.38	2.03	0.27	0.13	0.13
145	1.97	0.59	3.31	0.08	0.14	0.11
154	1.37	0.41	3.01	0.00	0.27	0.12
156	1.32	0.40	2.35	0.28	0.10	0.13
160	2.36	0.71	3.78	0.40	0.08	0.10
178	1.10	0.33	2.52	0.09	0.19	0.14
196	1.58	0.48	3.66	0.29	0.20	0.12

### 4.7.3 Post-diction with updated material properties

Post-diction analyses were first run using the 21 selected material parameter sets and classical Rayleigh initial-stiffness, mass proportional damping, and a 1% critical damping ratio. To account for uncertainties, the mean and mean  $\pm$  standard deviation curves were generated. Set 143 was selected as an exemplary representation of material parameters as it developed different mechanisms for classical and secant damping. For this set and classical initial-stiffness and mass proportional damping, the flexural deformations were still underestimated and not correctly localized in the upper storey of Unit 2 (Figure 4.16). Regardless, Figure 4.17 shows that the results did improve in comparison with the prediction model. Especially when including the standard deviation when accounting for the upper boundary, the displacements here tended to be the same order of magnitude. Still, roof displacements 1 and 2 remain underestimated.

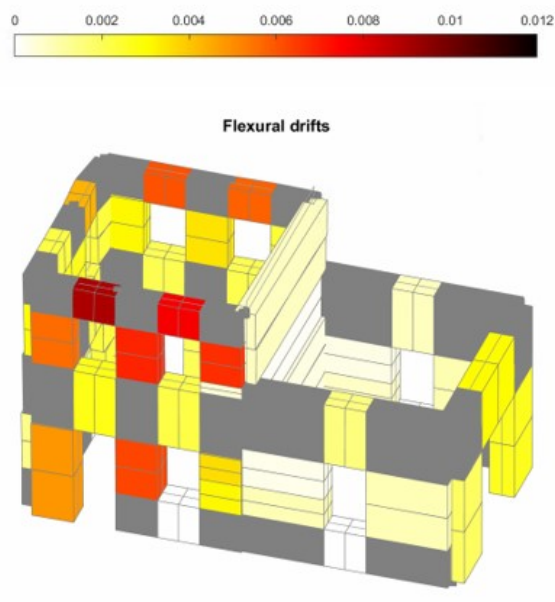


Figure 4.16: Maximum recorded flexural drifts for the post-diction analysis performed using the model with parameter set 143 and classical Rayleigh initial stiffness and mass proportional damping.



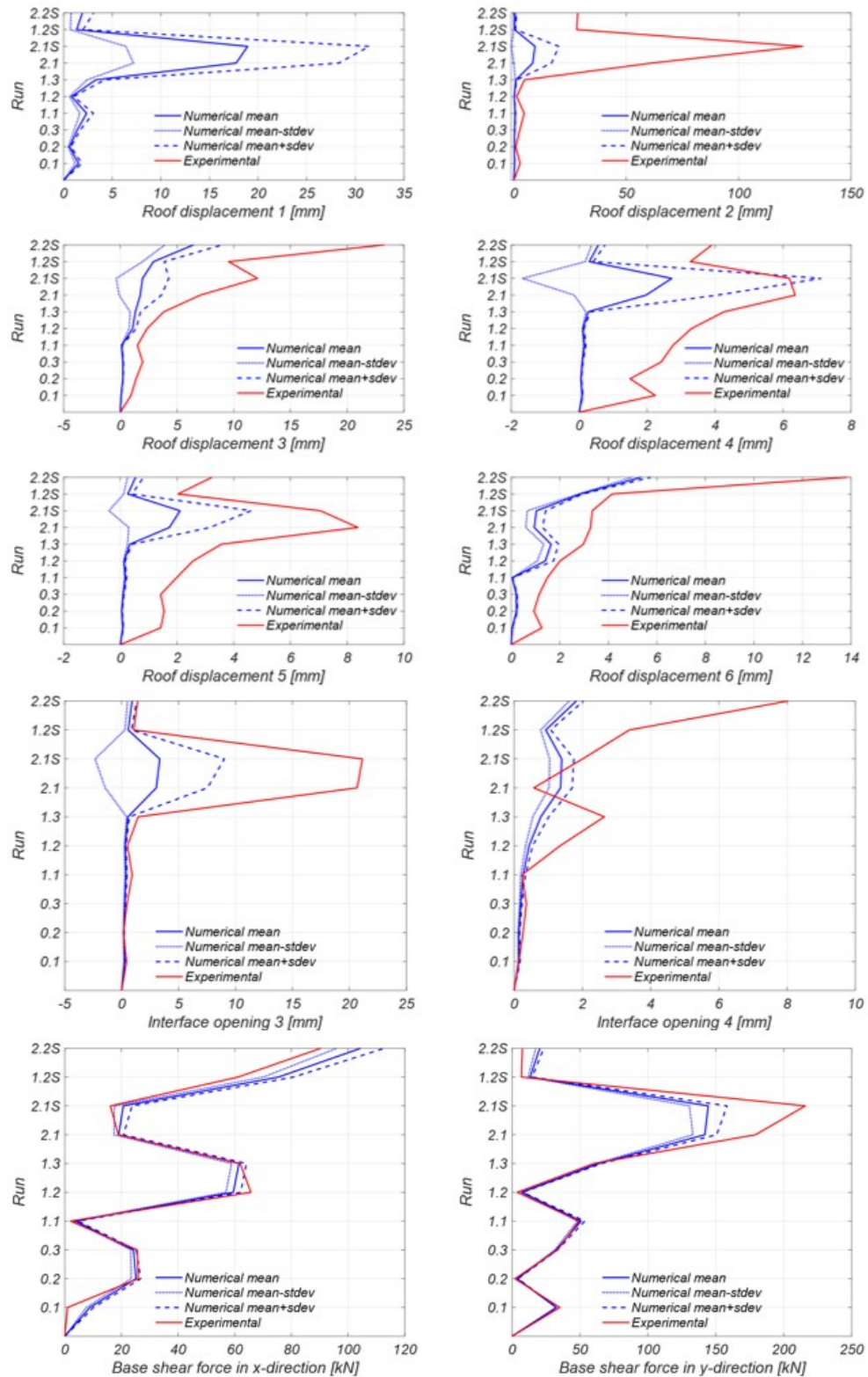


Figure 4.17: Comparing the stochastic response of 21 post-diction models updated with material parameters calibrated according to wallettes experimental results.

### 4.7.4 Post-diction with updated material properties and secant stiffness proportional damping

Post-diction analyses were run using the 21 selected material parameter sets along with a novel secant damping model (Vanin and Beyer, 2022) and a 5% critical damping ratio. To account for uncertainties, the mean and mean  $\pm$  standard deviation curves were again generated. For the exemplary parameter set 143, the flexural deformations were correctly localized in the upper storey of Unit 2 (Figure 4.18). Like in the experimental campaign (Tomić et al., 2022a), the mechanism included significant out-of-plane displacements and cracking on the transverse facades. Additionally, the mechanism was continuous and connected across orthogonal walls because the interlocking between orthogonal walls caused the end piers of the longitudinal facades to act as webs in the out-of-plane overturning mechanism of the transverse walls. The stochastic response was quite satisfactory and showed improvement compared to the case when initial-stiffness and mass proportional Rayleigh damping was used. While base shear in x-direction was overestimated, interface openings and upper storey displacements were predicted with much larger accuracy, capturing the same order of magnitude, especially when upper bound including standard deviation was accounted for.

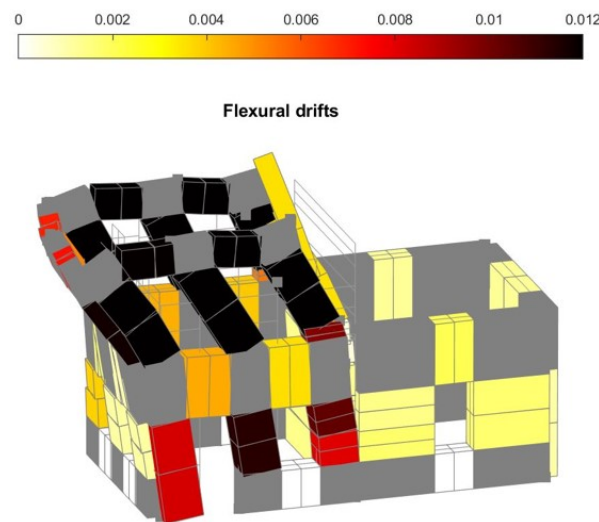


Figure 4.18: Damage mechanism for model parameter set 143.



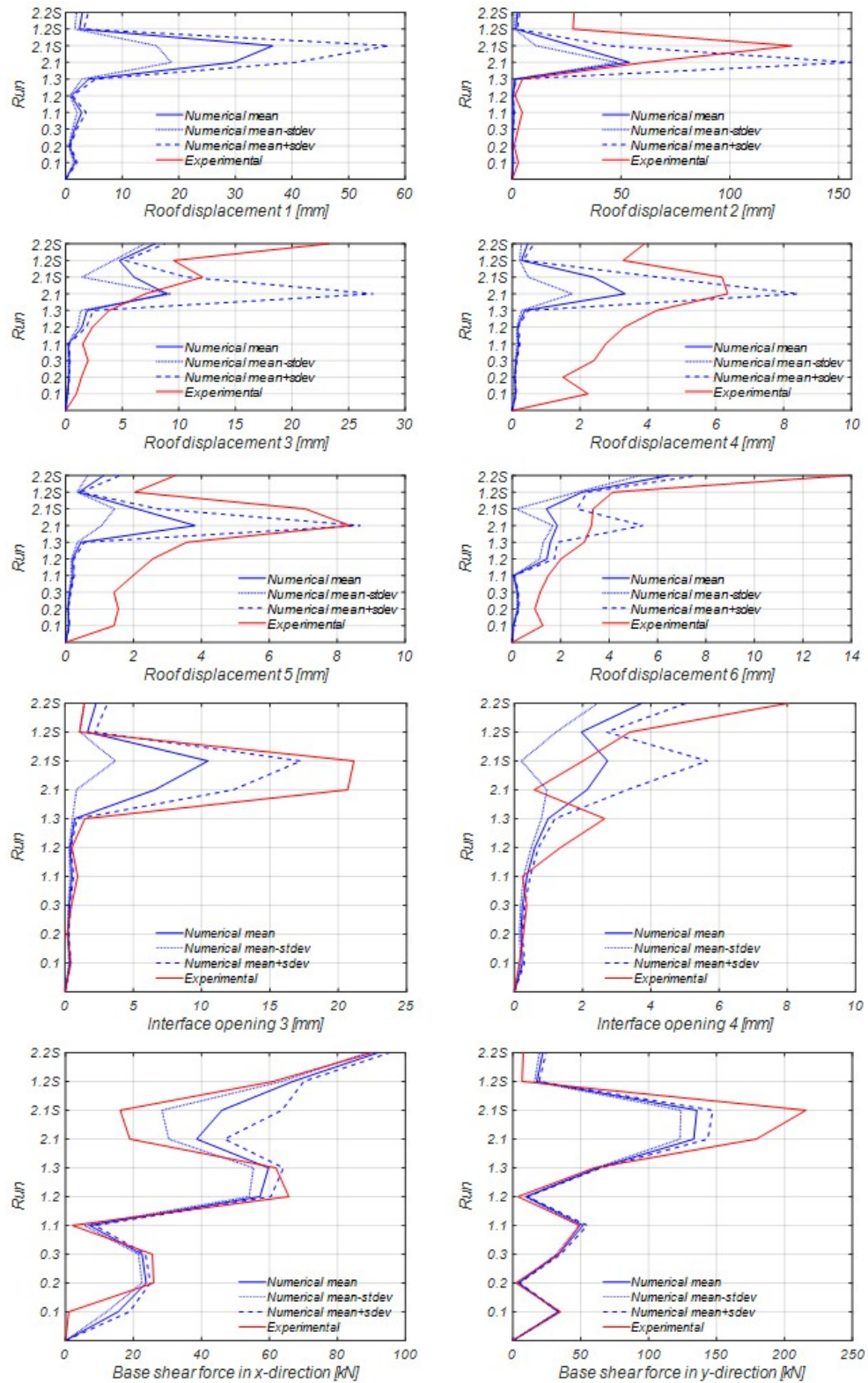


Figure 4.19: Comparing the stochastic response of 21 post-diction models updated with secant damping and material parameters calibrated according to wallettes experimental results.

Overall, post-diction models using secant damping produced significantly better estimations of model displacements as well as the dominant damage mechanisms. All models featuring classical Rayleigh initial stiffness and mass proportional damping underestimated the displacements and failed to reproduce the damage mechanism that was correctly reproduced by models featuring secant stiffness proportional damping. These classical models focused the damage in the lower storey of Unit 2 instead of in the upper storey where the soft-storey mechanism occurred in the experiment. Another important factor in post-diction model was the material properties, which were more correctly approximated when calibrated based on the wallette tests rather than on the vertical and diagonal compression tests.

### 4.8 Conclusion

The modelling of unreinforced masonry aggregates is commonly simplified by modelling the aggregate units as perfectly connected or isolated. Even if a simplified approach results in a satisfying or conservative value, there is a risk in overlooking possible damage and collapse mechanisms. Therefore, the modelling approach for masonry aggregates primarily needs to account for the interface behaviour and related modelling uncertainties that govern the complex interactions between the units.

Therefore, an n-dimensional non-linear material model for the aggregate interface was herein proposed, together with the methodology to account for epistemic uncertainties. The methodology was applied to a case study of a masonry aggregate, which was modelled by four common modelling approaches with varying connection between the units: units connected by the nD non-linear interfaces, units connected by 1D non-linear interfaces, separate units, and perfectly connected units. Our approach utilized LHS to create 400 sets of 19 material and modelling parameters, distributed according to normal and lognormal distributions, to take into account the epistemic uncertainties. Then for each model and each set of parameters, IDA were performed in OpenSEES software until failure or collapse of the aggregate was achieved using a newly developed macroelement which can capture in-plane and out-of-plane responses. The response of each modelling approach was evaluated in terms of the seismic response parameters, correlations of seismic response parameters with input parameters, seismic fragility curves, correlations of failure PGA with input parameters, and statistical distributions of failure modes and locations.

The analyses showed that the initial assumptions about the approach to modelling the interface between units can lead to differences in seismic fragility, which may be conservative in terms of failure PGA when compared to the most detailed representation through an nD interfaces model (Case A). However, the damage location (between units and within units) and the failure mode may not be adequately predicted. Therefore, a simplified modelling of masonry aggregates, either by separate units or perfectly connected units, can lead to satisfactory or conservative results but could be inaccurate with regard to damage and failure mechanisms. Modelling the interface between units of an aggregate with these simplified

assumptions therefore might be acceptable if only the PGA leading to failure is of interest. However, for designing retrofit interventions, information such as the likely failure modes and locations could be critical. The analyses have shown that these factors are very sensitive to the modelling assumptions and that the simplified models (Case C: completely separated units, Case D: fully connected units) lead to significantly different results compared with the more realistic models where the interface is modelled with a nD non-linear material law (Case A). Modelling the interface with a 1D non-linear material model (Case B) produces more realistic results than Case C or Case D but still fails to capture exactly the same response as the model that couples the interface response in all directions (Case A). All four classes of models in prediction underestimated the out-of-plane behaviour, what was attributed to the use of Rayleigh initial-stiffness and mass proportional damping that caused overdamping of the out-of-plane behaviour.

The factors that had a clear impact on the failure PGA for each modelling assumption were the standard material parameters (modulus of elasticity, shear modulus, compressive strength), the EFM modelling parameters (limit drift values, Rayleigh damping ratio) and the floor-to-wall friction coefficient. The effect of the floor-to-wall friction coefficient highlights the importance of modelling the connections in historical masonry, since correlated with the failure PGA for each modelling assumption. However, although the floor stiffness was simultaneously varied, it did not correlate significantly with the failure PGA ( $P > 0.05$ ), except in Case B. This result is in the line with the fact that if the non-linear connection is a weak point, as in most non-retrofitted buildings, variations in floor stiffness do not impact significantly the final collapse capacity. On the contrary, if the floors were perfectly connected to the walls, the failure PGA would depend on the floor stiffness factor. It is important to state that for earlier limit states, floor-wall connection might not yet reach its full capacity. Therefore, floor stiffness can be relevant for the earlier limit states, as shown with its relevance in the correlation to the seismic demand parameters. For the model with nD interfaces between the units, the coefficient of friction of the interface between the units is another parameter of a non-linear connection that correlated with the failure PGA.

As a result, we conclude that the appropriate choice of non-linear interface parameters can impact the failure PGA, and even linear or non-linear models for the interface can wrongly approximate the behaviour of a masonry aggregate if these models are overly simplified. In the case of the aggregate modelled with either separate units or perfectly connected units, an even greater error is introduced than for the model with 1D interfaces. These results highlight the importance of correctly modelling the interface between the units of an aggregate. The challenge of advanced interface models such as the nD interfaces models is the large number of input parameters that are needed. Unlike the 1D interface model, which assumes that the axial and shear response is uncoupled, coupling the responses further emphasize the need for calibrating the interface parameters or performing a probabilistic analysis to account for the uncertainties in the aggregate interface model, as well as other epistemic parameters.

Due to the discrepancies in the nominal and applied accelerations, a direct comparison of

pre-diction model with experimental results was difficult. Therefore, the comparison was performed by re-running the initial pre-diction model with the applied accelerations. For the previously selected set of material parameters and damping model the results were poorly matching the experimental ones. First, recalibration of material parameters was done according to quasi-static cyclic tests, instead of vertical compressions and diagonal compression test – leading to the improvement of the results. However, here again the discrepancies between numerical and experimental results were noted depending on which wallette geometry and axial load ratio was selected. Second, when novel secant damping model was applied the models successfully captured the out-of-plane behaviour, showing that this damping model is essential for avoiding the overdamping of the out-of-plane behaviour and wrong estimation of the damage mechanism, something that was common for all four model classes in the pre-diction. Overall, all the conclusions point to the need of adopting probabilistic approach instead of the deterministic when modelling historical masonry aggregates, due to many material and modelling parameters.

## 5 Uncertainties in the Seismic Assessment of Historical Masonry Buildings

This chapter is a post-print version of the paper: Tomić, I., Vanin, E., Beyer, K. (2021). Uncertainties in the seismic assessment of historical masonry buildings. *Applied Sciences*, 11(5), 2280.

The formatting and numbering of equations, tables and figures have been adapted to this document. The contributions of the first author are: generating numerical models, running analyses, interpreting results, visualization and writing.

### Abstract

Seismic assessments of historical masonry buildings are affected by several sources of epistemic uncertainty. These are mainly the material and the modelling parameters and the displacement capacity of the elements. Additional sources of uncertainty lie in the non-linear connections, such as wall-to-wall and floor-to-wall connections. Latin Hypercube Sampling was performed to create 400 sets of 11 material and modelling parameters. The proposed approach is applied to historic stone masonry buildings with timber floors, which are modelled by an equivalent frame approach using a newly developed macroelement accounting for both in-plane and out-of-plane failure. Each building is modelled first with out-of-plane behaviour enabled and non-linear connections, and then with out-of-plane behaviour disabled and rigid connections. For each model and set of parameters, incremental dynamic analyses are performed until building failure and seismic fragility curves derived. The key material and modelling parameters influencing the performance of the buildings are determined based on the peak ground acceleration at failure, type of failure and failure location. This study finds that the predicted PGA at failure and the failure mode and location is as sensitive to the properties of the non-linear connections as to the material and displacement capacity parameters, indicating that analyses must account for this uncertainty to accurately assess the in-plane and out-of-plane failure modes of historical masonry buildings. It also shows that modelling the out-of-plane behaviour produces a significant impact on the seismic fragility curves..

## 5.1 Introduction

Historical masonry buildings can be highly vulnerable to earthquake damage, as has unfortunately become evident in several historical city centres of Europe. An example of the damage is shown in Figure 5.1. To decrease this vulnerability, it is necessary to adopt assessment procedures that accurately reflect all the peculiarities of historical masonry. Unfortunately, correct evaluations of seismic performance are often hindered by a lack of information regarding the materials, structure and connections. To complicate this further, the heterogeneity of the construction material and structural detail often increases as buildings degrade over their life span or as a result of interventions and alternations. At the same time, the extensive testing or measuring of the properties is often not feasible due to either the high cost of experimental campaigns or limitations imposed due to the cultural value and protected status of a building. Last, but not least, connections between the structural elements, such as floor-to-wall interfaces and wall-to-wall interlocking have properties that are difficult to predict.

One approach to consider all these uncertainties is to use field data as basis for empirical vulnerability curves. This approach has been applied by Zuccaro et al. for Italian masonry buildings Zuccaro et al. (2020) and by Ruggieri et al. for masonry one-nave churches that were subjected to the Valle Scrivia Earthquake, 2003, Piemonte, Italy (Ruggieri et al., 2020). If numerical models are used for deriving the vulnerability curves, the models must adequately describe the geometry, morphology, connections and support conditions and must balance this with maintaining cost-effective computations that can be applied outside of the academic domain in seismic risk areas worldwide. To face these challenges, different modelling techniques and approaches have been developed to simulate the behaviour of masonry, and these techniques vary greatly in complexity levels and associated computational burden (P. B. Lourenço, 2002; Roca et al., 2010). No matter which model is used, the question still remains on the choice of material and modelling parameters.



Figure 5.1: Example of masonry buildings damaged in recent earthquakes in Italy.

When dealing with uncertainty, it is common to differentiate between aleatory randomness and epistemic uncertainty. Aleatory randomness is the natural randomness in the process, and the epistemic uncertainty stems from limited data and knowledge Fragiadakis and Vamvatsikos (2010) and Vamvatsikos and Fragiadakis (2010). Different approaches with different levels of complexity were applied by several authors to treat these uncertainties in modelling historical masonry buildings.

For example, many Incremental Dynamic Analyses (IDAs) were performed by Dolsek (2009) to deal with both the aleatory randomness stemming from differences in seismic records and the epistemic uncertainty stemming from material and modelling properties. Latin Hypercube Sampling (LHS) was used to distribute the material and modelling properties. The effect of uncertainty on the seismic response parameters was presented in terms of summarized IDA curves and dispersion measurements. The study concluded that epistemic uncertainty did not significantly affect the seismic response parameters in the range farther from collapse, but that the median collapse capacity was reduced when the epistemic uncertainties had been accounted for.

Rota et al. (2014) dealt with the issues of the knowledge levels and associated values of a confidence coefficient in the assessment method for existing buildings included in Eurocode 8, Part 3 European Committee for Standardization (2005). The proposed methodology assessed epistemic uncertainties using so-called variability factors, which were calibrated based on a logic-tree approach and aimed to represent the dispersion of results due to each of the uncertainties. This resulted in a global safety coefficient, applied directly to the structural capacity.

Saloustros et al. (2019) performed a stochastic analysis based on a Monte Carlo simulation to investigate the effect of material mechanical parameters on the evaluation of seismic fragility. The methodology was applied to the case study of the Santa Maria del Mar church in Barcelona and illustrated the sensitivity of the seismic analysis to the uncertainty in the material properties, as two different collapse mechanisms were possible depending on the input parameters. Finally, analytical seismic fragility curves were proposed by considering several sources of uncertainty regarding the material properties.

Vanin and Katrin Beyer (2018) instead proposed the logic tree approach as an effective method aimed at replacing the Monte Carlo simulations, which can be computationally too expensive for practical use. Optimal sampling points were defined using a moment-matching technique, and a combination of weights were applied to the branches. As a more refined and a novel approach in structural engineering, a Point Estimate Method was adopted to further reduce the number of the required non-linear simulations. A case study historical masonry building modelled by the equivalent frame model (EFM) approach was used to test both methods, which both showed good accuracy when compared with the Monte Carlo method. The in-plane displacement capacities of piers was identified as a major source of uncertainty.

This study strove to capture the key mechanical parameters of masonry on an elemental level using appropriate material laws while maintaining a simplicity that would allow for multiple dynamic analyses to be performed. This is necessary to account for the aleatory and epistemic uncertainties involved in the modelling of masonry buildings. To this scope, EFMs were used, as they fulfilled the necessary requirements and are one of the most widely applied engineering tools for the seismic analysis of unreinforced masonry buildings for both scientists and practitioners alike. For the EFM, the macro-element by Vanin et al. (2020a) was used. This

macro-element cannot only capture the in-plane behaviour of masonry elements but also their out-of-plane behaviour. This feature addressed the weakness of many EFM formulations, which require a separate analysis to account for out-of-plane behaviour, most commonly through separate limit analysis. Furthermore, this modification provided a framework to analyse the impact of mixed in-plane and out-of-plane failure modes.

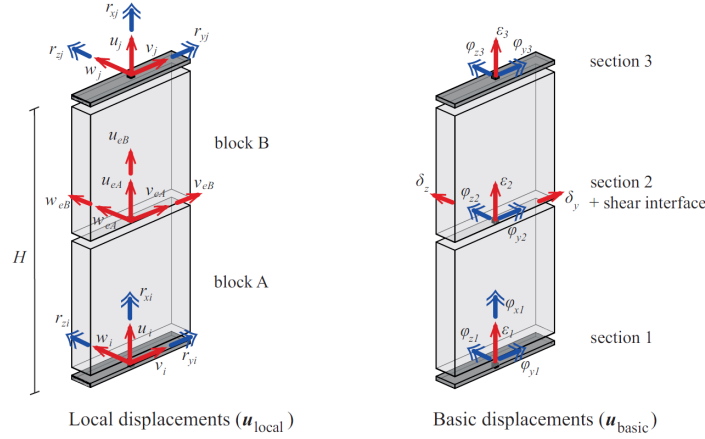


Figure 5.2: Definition of the local and basic system of the macroelement for modelling the in-plane and out-of-plane response (Vanin et al., 2020a).

In the following sections, the case study buildings and details of the modelling approach are first described. Then, material and modelling properties with their respective normal and lognormal distributions and the earthquake record used in the incremental dynamic analyses are presented and discussed. This is followed by the description of the methodology for the statistical evaluation of the data. The results for each case study building are presented and discussed. For each building two sets of analyses are performed: first, the building is modelled with the out-of-plane capability of the macroelement enabled and with non-linear wall-to-wall and floor-to-wall connections, and then without out-of-plane capability of the macroelement and rigid connections. Finally, conclusions on uncertainties in modelling unreinforced masonry buildings are drawn.

## 5.2 Case Studies

Two buildings were selected as case studies. The two typologies represent typical structures often found in city centres, which include (i) stiff monumental buildings, and (ii) tall and slender masonry buildings.



### 5.2.1 Holsteiner Hof

Holsteiner Hof, shown in Figure 5.3, is a historical stone masonry building located in the city centre of Basel. Built in 1752, it is a landmark of cultural heritage and is considered a typical representative of buildings built during the 17–19th century. The building has two storeys with a height of 4.50 m and a rectangular floor plan ( $26 \times 14 \text{ m}^2$ ). The wall thickness of both storeys is 60 cm, while the thickness of the spandrels is only 30 cm. The gables are triangular walls with a thickness of 45 cm. The floors are composed of timber beams spanning the shorter direction and one layer of planks nailed to the beams. The timber beams are simply supported on the walls and horizontal forces are transferred as friction forces. The roof system is a truss that was retrofitted with a secondary structure. Minor retrofitting interventions were performed in 1976–1979 but did not alter the structure in a significant way.

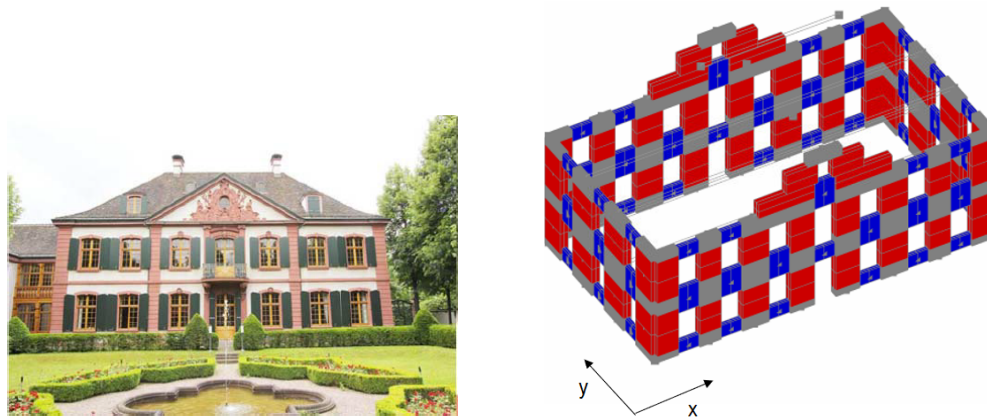


Figure 5.3: Holsteiner Hof. (left) Main façade. (right) Numerical model with the coordinate system.

### 5.2.2 Lausanne Malley

Lausanne Malley, shown in Figure 5.4, is a representative example of a tall and slender unreinforced stone masonry residential building in Lausanne. It was constructed in the second half of the 19th century with a rectangular floor plan ( $14 \times 12 \text{ m}^2$ ) and a regular layout with reinforced concrete footings under the walls. The wall thickness varies from 60 to 25 cm along with the height of the building. It has six storeys, and the storey height varies between 2.80–3.20 m. The original timber floors are composed of timber beams spanning the shorter direction and one layer of planks nailed to the beams. As for the Holsteiner Hof, the timber beams are simply supported on the walls and horizontal forces are transferred as friction forces. The roof has the original wooden truss structure. Sound-proof retrofitting has been recently performed (Michel et al., 2018), which slightly improved the seismic capacity of the structure.

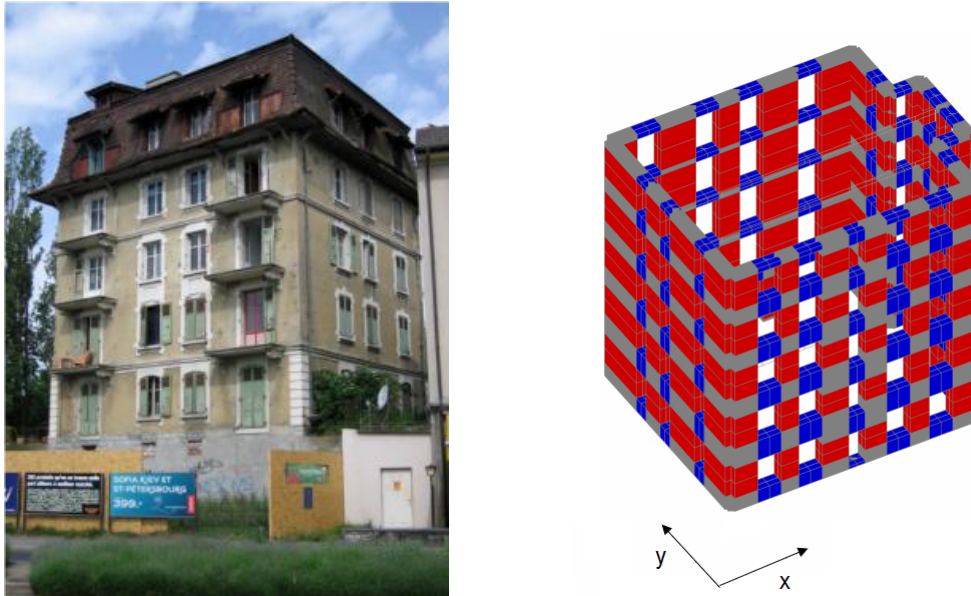


Figure 5.4: Lausanne Malley. (left) Main façade. (right) Numerical model with the coordinate system.

### 5.2.3 Modelling approach

The buildings were modelled using the equivalent frame model (EFM) approach. EFM works by discretizing façades into piers, spandrels and rigid nodes using beams or macroelements (Quagliarini et al., 2017). For this work in particular, a macroelement newly developed by Vanin et al. (2020a) was used that builds on the work of Andrea Penna et al. (2014a) to precisely model the behaviour of masonry panels in-plane. The macroelement is formulated as a one-dimensional element defined by three nodes in three-dimensional space. Three non-linear sections account for axial deformation, and the central section accounts for the non-linear shear response. The out-of-plane response is coupled with the in-plane response. Nonlinear geometrical effects are captured through a second-order Taylor series expansion of the compatibility equations, obtaining the  $P - \Delta$  formulation. To correctly simulate the out-of-plane behaviour of a masonry building, it is not sufficient to choose a macroelement formulation that captures the out-of-plane behaviour, if walls are restrained in the numerical model by rigid wall-to-wall and floor-to-wall connections. Therefore, it is crucial that the model allows for relative displacements between the nodes of the intersection walls and between the nodes of the floor and the wall (Vanin et al., 2020b). For this purpose, interface elements and material models for wall-to-wall and wall-to-floor connections were implemented in OpenSEES McKenna et al. (2000).

All piers and spandrels were assigned the same material properties, while the nodal regions between them were modelled as rigid. Timber floors were modelled as an orthotropic elastic membrane, with a higher stiffness in the direction of the beam span and a lower stiffness in

the orthogonal direction. The shear stiffness of the membrane was defined by the shear modulus, meaning the membrane was defined by the two moduli of elasticity in two orthogonal directions, as well as the shear modulus and the thickness of the diaphragm. The floors were modelled as linear elastic, but the connection between the floor and the wall was modelled to account for a nonlinear behaviour and a possible connection failure, which can result in the out-of-plane failure of a pier. The nodes of the floor were modelled separately from the nodes of the walls to allow the possible relative displacement. This connection was modelled using a zero-length element to which a frictional model was assigned. The sliding occurred in the direction perpendicular to the wall, and pounding occurred in the opposite direction. Although it is possible to model slip parallel to the wall, for this study, the connection parallel with the wall was assumed to be linear elastic. Therefore, the properties of the zero-length element were defined by the friction coefficient characterising the interface between floor beams and walls, the modulus of elasticity and the shear modulus of this connection (Vanin et al., 2020b). Another set of zero-length elements was used to model the connection between orthogonal walls. This connection simulated the potential formation of a vertical crack and separation of the orthogonal walls due to poor interlocking, which could lead to the out-of-plane failure of a wall. The one-dimensional material for the interface was defined as a damage tension law with exponential softening and a linear elastic model in compression (Vanin et al., 2020b). The material was defined by the elastic modulus, the tensile strength and the Mode I fracture energy.

#### 5.2.4 Material and modelling parameters

A total of 11 material and modelling parameters were selected to perform the uncertainty analysis. The material parameters of masonry were the following:  $E_m$ , modulus of elasticity;  $G_m$ , shear modulus;  $f_{cm}$ , compressive strength;  $\mu_m$  and  $c_m$ , friction coefficient and cohesion of masonry, respectively. No in-situ tests had been performed. For this reason, median values were chosen based on the experimental campaigns performed on masonry of a similar typology as described previously Guerrini et al. (2017), Guerrini et al. (2019), Senaldi et al. (2018), and Senaldi et al. (2020) and were applied to all piers and spandrels, i.e. any spatial variability in masonry material properties was not considered. The floor stiffness factor ( $k_{floor}$ ) multiplied the default stiffness values of the flexible floor diaphragm, which were computed as:  $E_1 = 10$  GPa,  $E_2 = 0.5$  GPa, and  $G = 10$  MPa according to previous work of Brignola et al. Brignola et al. (2008) and Brignola et al. (2012). The wall-to-wall connection factor  $f_w$  multiplied the default wall-to-wall connection strength. This default wall-to-wall connection strength was calculated according to Fontana et al. POLIMI (2010). The floor-to-wall friction coefficient  $\mu_{f-w}$  was directly applied to the frictional floor-wall connection, with the mean value based on the work of Almeida et al. Almeida et al. (2020). The drift capacities in flexure and shear,  $\delta_{c,flexure}$  and  $\delta_{c,shear}$ , are the limit collapse flexural and shear drifts at which the lateral stiffness of the macroelement is set to zero, chosen according to Vanin et al. Vanin et al. (2017b). An initial stiffness and mass proportional Rayleigh damping model was applied. The damping ratio was also a parameter that was considered uncertain. For each set of parameters,

Table 5.1: Assumed distributions of material and modelling parameters.

Parameter	Unit	Distribution	Mean	Lognormal Mean	Standard Deviation
$E_m$	Pa	Normal	$3.5 \times 10^9$	-	$1.0 \times 10^9$
$f_{cm}$	Pa	Normal	$1.3 \times 10^6$	-	$0.35 \times 10^6$
$\xi$	-	Normal	0.02	-	0.005
Parameter	Unit	Distribution	Median	Lognormal Mean	Standard Deviation
$G_m$	Pa	Lognormal	$1.5 \times 10^9$	21.13	0.5
$c_m$	Pa	Lognormal	$0.233 \times 10^6$	12.36	0.5
$\mu_m$	-	Lognormal	0.25	-1.39	0.3
$k_{floor}$	-	Lognormal	1	0	0.5
$f_w$	-	Lognormal	1	0	0.3
$\mu_{f-w}$	-	Lognormal	1	0	0.3
$\delta_{c,flexure}$	-	Lognormal	0.01035	-4.57	0.2
$\delta_{c,shear}$	-	Lognormal	0.007	-4.96	0.2

the modal properties were calculated first and then the Rayleigh damping model parameters were computed such that the damping ratios at the first and sixth mode corresponded to the damping ratio of this set of parameters. All parameters were assigned normal or lognormal distributions for the LHS, as shown in Table 5.1.

Additionally, correlation coefficients were imposed between parameters that are often correlated in experimental campaigns to avoid generating unrealistic data sets, i.e. with the lower-bound value for modulus of elasticity and the upper-bound value for the compressive strength. Imposed correlation coefficients are shown in Table 5.2. A strong correlation was imposed between the modulus of elasticity, shear modulus and compressive strength. A moderate correlation was imposed between collapse drift values in flexure and shear for masonry elements. It should be noted that the imposed correlation coefficients between the parameters were only estimated based on engineering judgment.

Table 5.2: Correlation coefficients between input parameters

Correlated parameters	Correlation coefficient	Strength of correlation
$E_m, G_m, f_{cm}$	0.7	Strong
$\Delta_{c,flexure}, \Delta_{c,shear}$	0.5	Moderate

### 5.2.5 Earthquake record

A bi-directional incremental time history analysis was performed for each set of parameters. The analyses were carried out using one ground motion record. The chosen record is the Montenegro Albatros 1979 record, with a PGA of 0.18 g in the north-south direction and 0.21 g in the east-west direction, shown in Figure 5.5 (Luzi et al., 2016). This record was selected because of its rather broad frequency content. The initial acceleration for the Holsteiner Hof was set to 100% of the recorded PGA. The north-south direction was applied in the negative direction of the  $x$ -axis and the east-west direction was applied in the positive direction of the  $y$ -axis. Response spectra are shown in Figure 5.6. The initial acceleration for the Lausanne Malley building was set to 50% of the same. These values were chosen as starting points because the initial numerical analyses showed that no failures occurred for the selected PGA levels. Afterwards, the acceleration was increased by 50% of the original record levels for the Holsteiner Hof, and by 25% of the original record for the Lausanne Malley building up to the point of failure. A smaller increment level for the Lausanne Malley building was chosen because of its greater fragility.

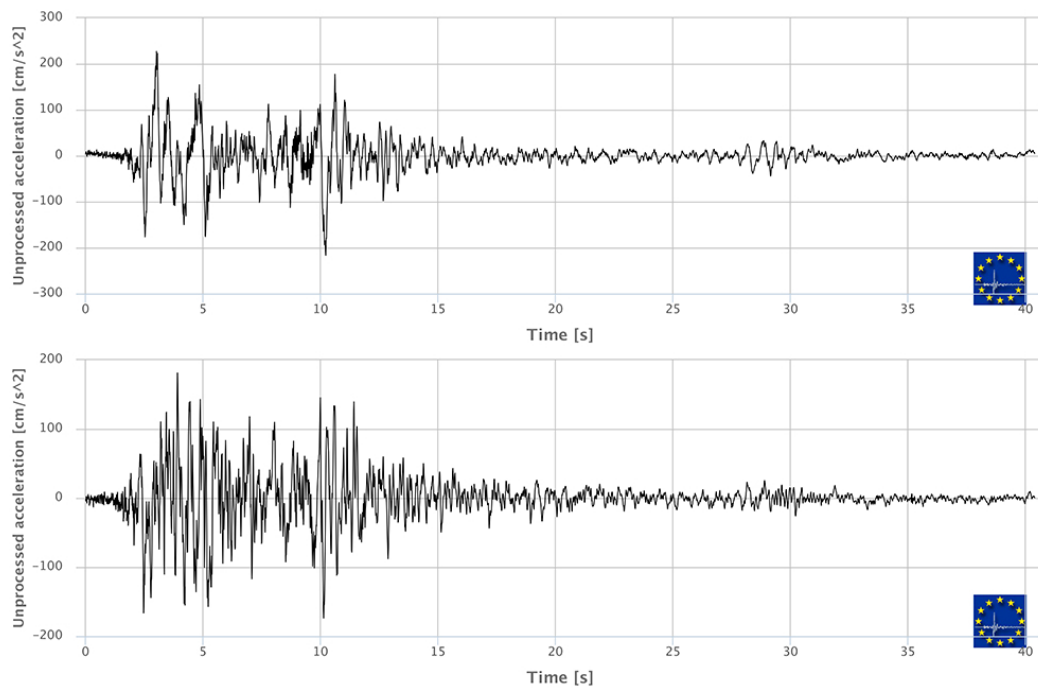


Figure 5.5: Processed acceleration time-histories of the Montenegro 1979 earthquake. Albatros station records: (up) east-west direction. (down) north-south direction Luzi et al. (2016).

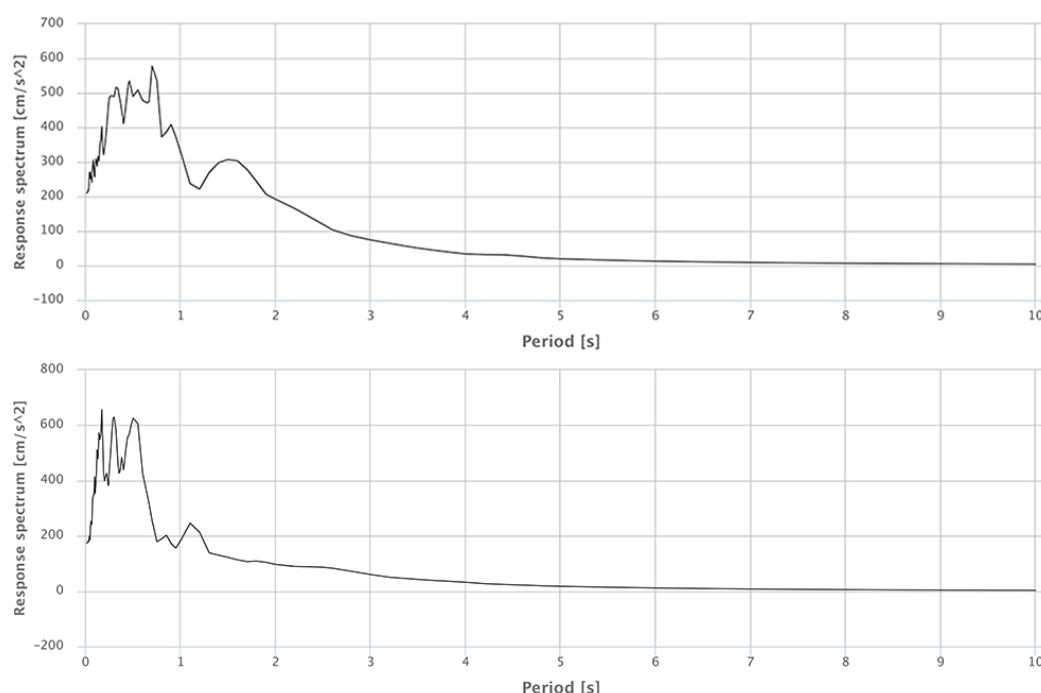


Figure 5.6: Acceleration response spectra of the Montenegro 1979 earthquake. Albatros station response spectra: (up) east-west direction. (down) north-south direction Luzi et al. (2016).

### 5.3 Methodology

Latin Hypercube Sampling (LHS) was performed to account for the epistemic uncertainty of material and modelling parameters. To do this, 400 sets of 11 parameters were generated in two steps. First, each parameter was assigned as a normal or lognormal distribution according to values from literature, buildings codes or experiments, as defined in the previous section. The generated  $11 \times 400$  matrix contained one set of parameters in each column, which was used for a single incremental dynamic analysis. The marginal distribution of each column was adjusted so that points were uniformly distributed on the probability scale (Stein, 1987). Correlation matrices were imposed between the parameters to avoid unrealistic sample sets, e.g., a sample with a lower bound value for the modulus of elasticity and an upper bound value for the compressive strength. When all parameters were generated, the actual correlation matrix was calculated and compared to the imposed one, and this difference between the two was evaluated by the objective function that was minimized, called the norm. This methodology for minimizing the norm by performing random permutations of random elements within each vector was proposed by Dolsek (2009) using a method called simulated annealing that was originally proposed by Vořechovský and Novák (2003), as an approach to find the global minimum of an objective function that might feature many local minima. The norm is re-evaluated after each permutation, and it is accepted if the norm decreased or rejected if the norm increased. Once the final set of material and modelling parameters was generated, it

Table 5.3: List of seismic response parameters for which the maximum absolute values are observed.

BSHX	Base shear in x-direction
BSHY	Base shear in y-direction
RDX	Average roof displacement in x-direction
RDY	Average roof displacement in y-direction

was used to perform incremental dynamic analyses (Vamvatsikos and Cornell, 2002).

A different approach were used in the past to reduce the computational cost by limiting the number of required non-linear analyses, i.e., a novel use of a point estimate method was proposed by Vanin et al. Vanin and Katrin Beyer (2018). This method is effective for more detailed analyses, such as discrete element models which are computationally demanding. Our approach relies on the low computational burden of running equivalent frame models in OpenSEES. Though this removes the requirement for keeping the number of analyses low, it is still better to avoid redundant analyses stemming from the application of the classical Monte Carlo method Metropolis and Ulam (1949), which does not benefit the statistical output. Therefore, for this work, LHS was used for the selection of random parameters as the best balance between computational burden and accuracy.

### 5.3.1 Seismic Response Parameters

To evaluate seismic response parameters, each of the 400 IDA curves was first plotted, together with the mean curve and the 16th and 84th percentile curves. Second, correlations between material and modelling parameters and seismic demand parameters were evaluated for the selected PGA. The PGA was selected individually for each building to balance between avoiding too many failures while still activating the dominant mechanisms. Correlations were evaluated in terms of the linear correlation coefficients between the chosen material and modelling parameters and the maximum values of seismic response parameters. Correlation coefficients were displayed for parameters that passed the P-test with probability values of less than 5%, which present strong evidence against a null-hypothesis that two variables are not correlated. In other words, it means that a  $p$ -value of less than 5% represents strong evidence of a correlation. Chosen seismic response parameters are listed in Table 5.3.

### 5.3.2 Failure Criterion

Among all the limit states, the collapse limit state is the most challenging to model because the influence of non-linear material models and modelling assumptions is large, and problems related to the numerical convergence and stability of the solution are frequent (Andrea Penna et al., 2013). For the EFMs used in this study, the equilibrium can be lost for two reasons: (i) excessive out-of-plane deformation when the  $P - \Delta$  effect causes the loss of the global



equilibrium or (ii) a series of in-plane failures until the global equilibrium cannot be reached. Alternatively, the activation of reason (ii) could lead to (i). These in-plane failures were accounted for at the element level for the macroelement developed by Vanin et al. (2020a) used in this study. More specifically, when the pier reaches either the shear or flexural drift limit, the lateral stiffness and strength are set to zero, but the pier retains the ability to transfer axial load. This is illustrated in Figure 5.7 for the flexural and shear failures in a pier reaching drift limits set as 1.2% and 0.9% for flexure and shear, respectively.

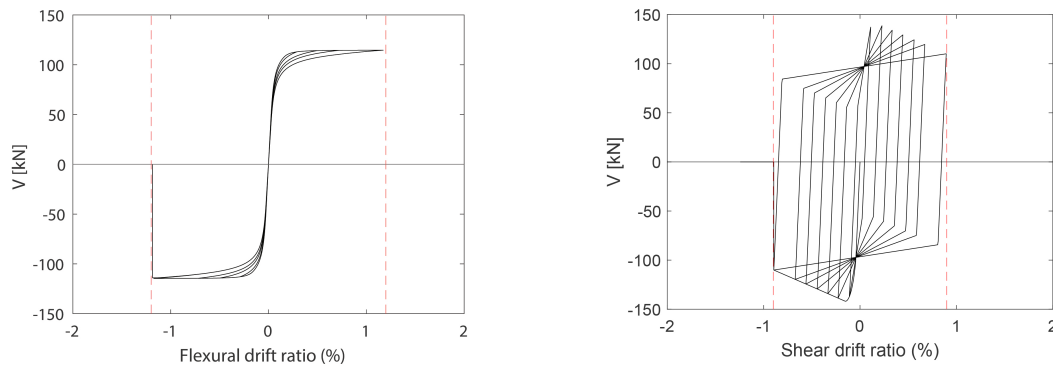


Figure 5.7: Pier lateral strength and stiffness loss after reaching a collapse drift value. (left) Flexural. (right) Shear.

In the study presented here, equilibrium loss in a particular step of an incremental dynamic analysis was considered to be a failure. Then, the failure criterion was subsequently applied to detect the cause of the loss of the global equilibrium. This applied failure criterion was inspired by one of the criteria described by Andrea Penna et al. (2013). Here, failure was defined as 50% of the piers in one direction reaching the limit drift, so the criterion was updated to consider in-plane failure when 50% of the piers in the same direction of one storey of one unit reached their drift limits. Whether it was labelled as a flexural or shear in-plane failure depended on the predominant failure mode of the piers involved. In parallel, each pier's relative out-of-plane deformation was checked. Out-of-plane rotation around the middle node of the pier was also checked, and the relative displacement between two floors was considered. This procedure was repeated for each step of the analysis that had a loss of equilibrium until one of the criteria was reached and failure of the building marked and localized, as shown in Figure 5.8. A final check was performed to ensure that one of the failure criteria was reached and to eliminate a potential erroneous numerical loss of equilibrium. If the equilibrium was lost but none of the failure criteria was reached, the particular IDA was discarded to eliminate potential erroneous numerical losses of equilibrium. However, this occurred in less than 0.5% of the cases.



Table 5.4: Lausanne Malley: Failure location divided by units, floors and directions.

F1 x-dir	1st floor in x-direction
F1 y-dir	1st floor in y-direction
F2 x-dir	2nd floor in x-direction
F2 y-dir	2nd floor in y-direction
F3 x-dir	3rd floor in x-direction
F3 y-dir	3rd floor in y-direction
F4 x-dir	4th floor in x-direction
F4 y-dir	4th floor in y-direction
F5 x-dir	5th floor in x-direction
F5 y-dir	5th floor in y-direction

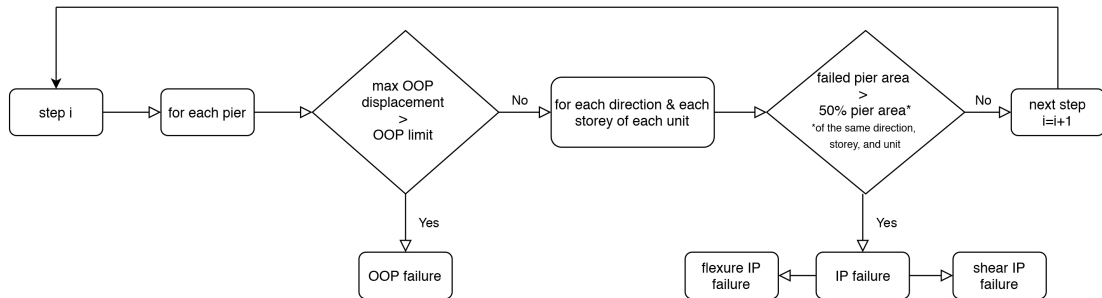


Figure 5.8: Building failure criterion chart describing the procedure to classify the building model as collapsed. OOP, out-of-plane failure; IP, in-plane failure.

The proposed methodology analysed the failure from a few different points. First, it showed the probability of failure at a certain PGA using seismic fragility curves. Then, the linear correlation coefficients were computed between the PGA at failure and the material and modelling parameters. These coefficients were then filtered using the p-value of correlation of each parameter with the PGA at failure, where only those with a p-value of less than 5% were plotted. Finally, the failure type and localization were detected for each model. Failures were divided into in-plane and out-of-plane failures, and their localization was performed according to Table 5.4, which uses Lausanne Malley building as an example. The same concept was applied to other buildings and updated according to the number of storeys. Overall, the methodology deals with three important aspects of the failure uncertainty: the impact of parameter uncertainty on the PGA collapse capacity of the building, collapse mechanism and collapse localisation.

## 5.4 Results

Herein, IDAs were performed for each of the two case-study buildings for 400 sets of material and modelling parameters. The same procedure was repeated twice for each case-study building, once including the out-of-plane capability of the macroelement and non-linear connections, and once without the out-of-plane capability of the macroelement and rigid connections. The aim of this procedure was to enhance the understanding of the impact that neglecting the out-of-plane and non-linear connections component from the equivalent frame analysis produces in terms of fragility curve. The OpenSEES models and the sets of material and modelling parameters used for the IDAs are provided in the supplementary material.

First, the seismic demand parameters were evaluated in terms of IDA curves and correlations with input parameters. Then, modal periods, seismic fragility curves and correlations of the PGA at failure with input material and modelling parameters were calculated. Finally, the statistics were evaluated regarding failure types and location.

### 5.4.1 Holsteiner Hof

Holsteiner Hof was modelled as described in Section 5.2.1. The walls were modelled using macroelements, the floors were modelled using orthotropic membrane elements, and the wall-to-wall and floor-to-wall connections were modelled using zero-length elements and non-linear material models.

#### Seismic Response Parameters

For each of the 400 sets of analyses, the IDA curves are plotted in Figure 5.9. In this figure, the chosen output variable can be seen to evolve with the PGA increment. Since the parameter values are quite scattered, the mean curve and 16th and 84th percentile curves are plotted. Higher scatter of the roof displacement was observed for the  $x$ -direction.

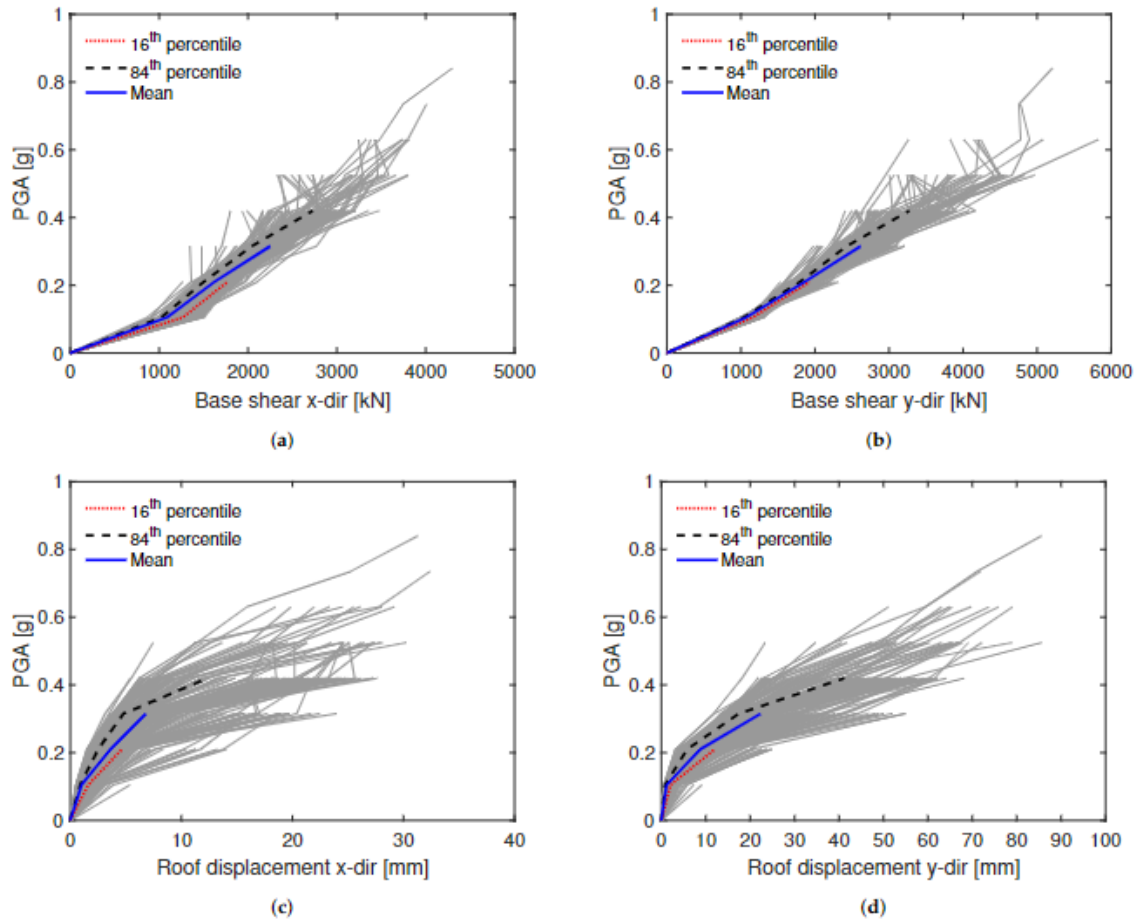


Figure 5.9: IDA curves for the Holsteiner Hof model for various seismic demand parameters: (a) Total base shear in x-direction. (b) Total base shear in y-direction. (c) Average roof displacement in x-direction. (d) Average roof displacement in y-direction.

The correlation between the base shear and roof displacement demands and the input parameters for the PGA of 0.21 g is displayed in Figure 5.10. This PGA value was chosen because it provided sufficiently large seismic demand parameters without triggering too many failures. For clarity, only the Spearman rank correlations for the parameters with a  $p$ -value of less than 5% are displayed. The strongest negative correlation was detected between the roof displacements and modulus of elasticity, shear modulus and compressive strength, followed by the Rayleigh critical damping ratio and the cohesion of masonry. The modulus of elasticity, shear modulus and compressive strength, together with the cohesion of masonry and the floor stiffness showed a positive correlation with the base shear. Since the PGA was too low to trigger element failures, in-plane drifts at collapse did not correlate with the parameters. Base shear and roof displacement demands were not correlated with the parameters of the floor-to-wall connections, suggesting that the connection capacity was not exceeded. The base shear and roof displacements were therefore dependent on the assumed floor stiffness.

### Failure Analysis

Figure 5.11 shows the results of 400 IDAs for the Holsteiner Hof model in terms of modal periods, fragility curve and the correlations between the input parameters and the predicted PGA at failure. At the start of each IDA, modal periods were determined to calculate the Rayleigh damping coefficients. The material parameters  $E_m$ ,  $G_m$  and  $f_{cm}$  correlate positively with the PGA at failure, with the strongest correlation detected for  $E_m$ . The parameters  $E_m$ ,  $G_m$  and  $f_{cm}$  were set as correlated when the LHS sample was prepared; it was therefore expected that all correlate in a similar manner with the PGA at failure. A positive correlation between the PGA at failure and drift limit values was expected for models that developed mainly in-plane failures. The shear drift at collapse had a more significant correlation with the PGA at failure than the flexural drift at collapse. Rayleigh damping ratio was expected to be correlated with the PGA at failure for any failure mode of non-linear dynamic analyses. Floor stiffness and floor-to-wall connection parameters did not correlate with the PGA at failure, even though the simulations led to an almost equal number of out-of-plane and in-plane collapses. This was because the out-of-plane failures were located in the walls spanning parallel and failing out-of-plane perpendicular to the direction in which the beams spanned, and as such were not influenced by these parameters.

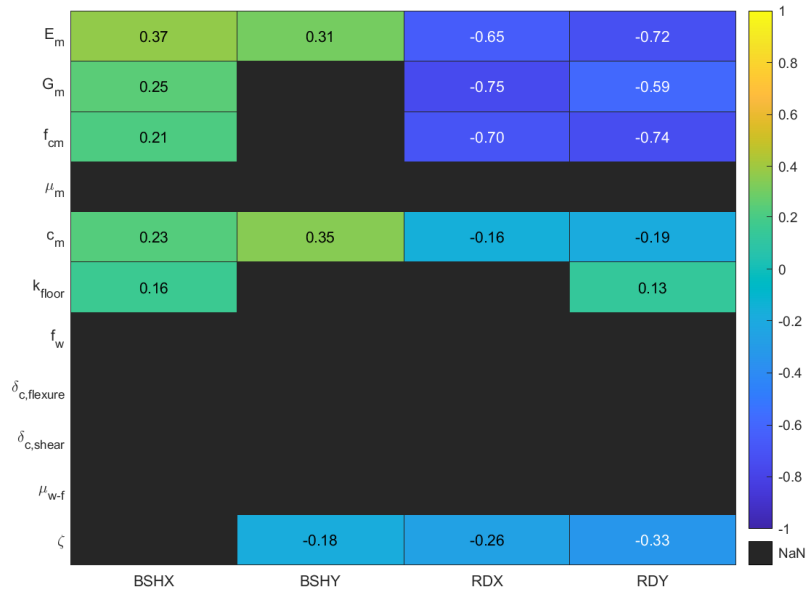


Figure 5.10: Holsteiner Hof model Spearman correlation matrix for PGA 0.21 g.

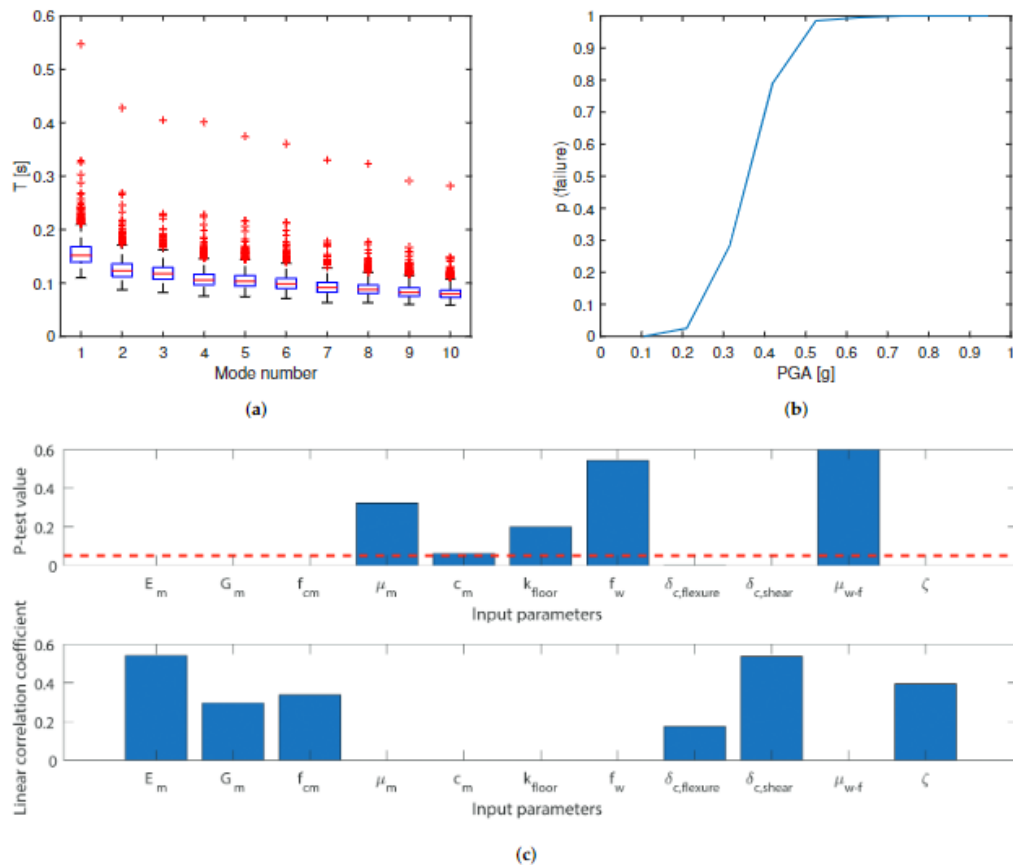


Figure 5.11: Holsteiner Hof model: (a) Distribution of modal periods. (b) Fragility curve. (c) Correlations between the PGA at failure and input parameters.

The failure PGA was not the only value impacted by the material and modelling parameters, as the portion of the building that fails was also influenced. The distribution of the types of failure can be seen in Figure 5.12. Interestingly, the number of the out-of-plane and in-plane failures was divided evenly. In-plane failures were again split between flexural and shear failures, with flexural failures accounting for a larger portion. A majority of the failures were localized in the second floor piers spanning in the  $y$ -direction for both out-of-plane and in-plane failures. Still, failure location was detected in all other parts as well.

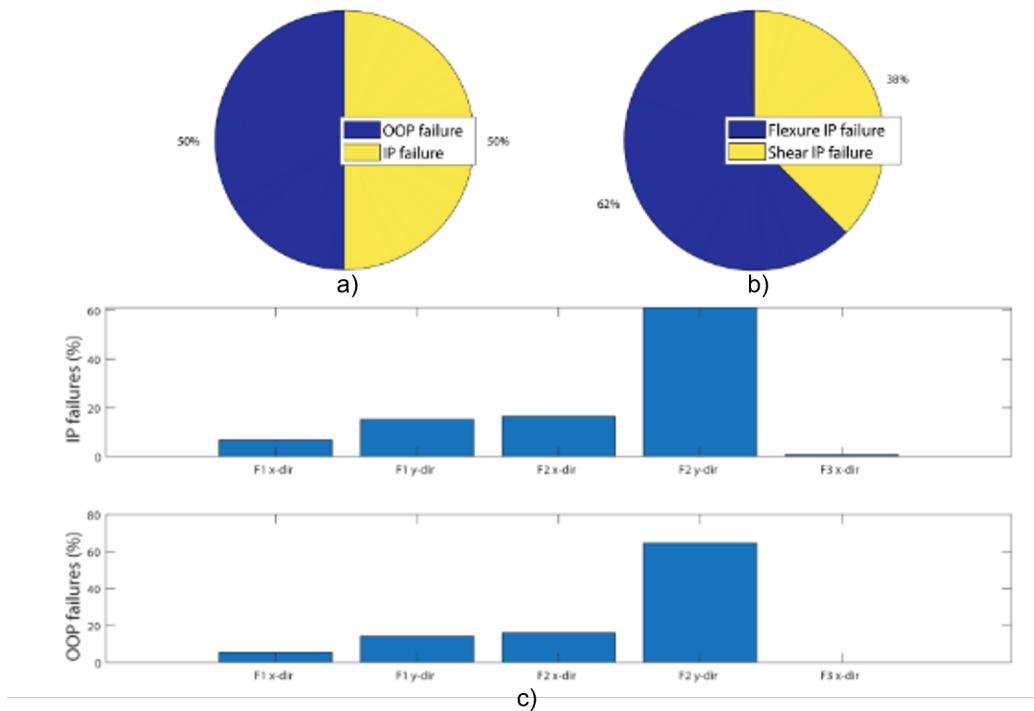


Figure 5.12: Holsteiner Hof model failure statistics: (a) Type of failure. (b) In-plane type of failure. (c) Failure location.

#### 5.4.2 Holsteiner Hof-Out-of-Plane Disabled and Rigid Connections

The Holsteiner Hof was again modelled as described in Section 5.2.1. The only difference was that the out-of-plane capability of the macro-element was disabled and connections were modelled as rigid. Therefore, both the seismic response parameters and the failure of the building were governed by the in-plane behaviour.

#### Seismic Response Parameters

For each of the 400 sets of analyses, the IDA curves are plotted in Figure 5.13. The scatter of base shear and roof displacements was similar to the model with out-of-plane enabled.

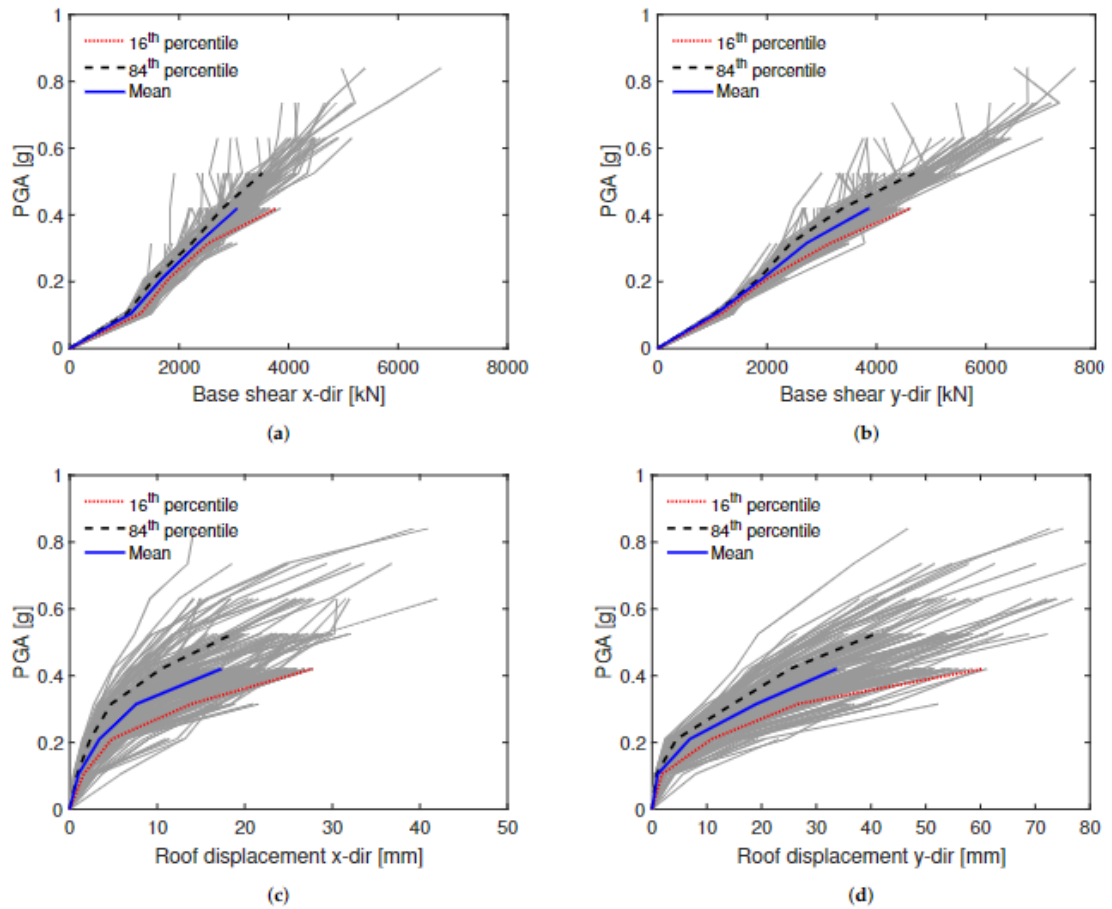


Figure 5.13: Holsteiner Hof model (with out-of-plane disabled and rigid connections) IDA curves displaying the maximum values of seismic demand parameters: (a) Total base shear in x-direction. (b) Total base shear in y-direction. (c) Average roof displacement in x-direction. (d) Average roof displacement in y-direction.

The correlation between the seismic demand parameters and the input parameters for the PGA of 0.21 g is displayed in Figure 5.14. For the selected PGA, the values were similar to the model with out-of-plane enabled, except that no influence of the floor stiffness was observed.

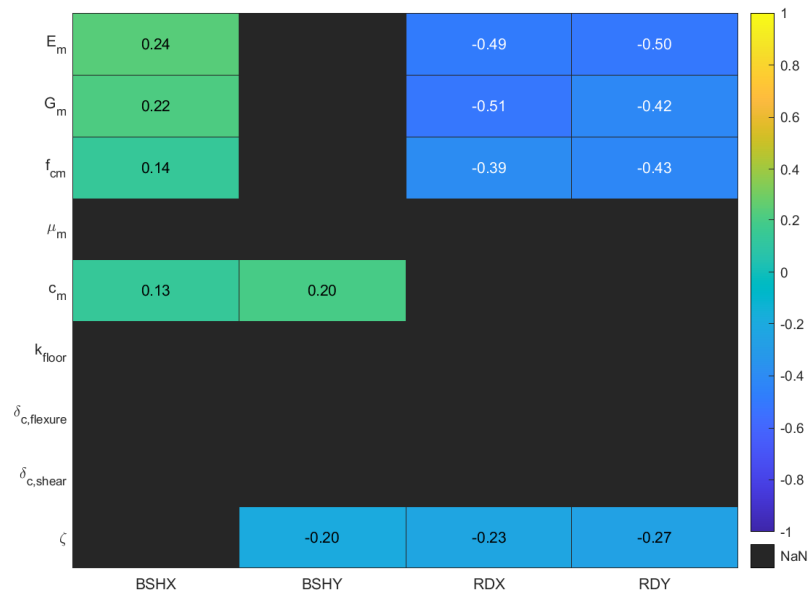


Figure 5.14: Holsteiner Hof model (with out-of-plane disabled and rigid connections) Spearman correlation matrix for PGA 0.21 g.

Failure Analysis

Figure 5.15 shows the results of 400 IDAs in terms of modal periods, fragility curve and the failure PGA correlations. Significant differences were observed at the fragility curved and discussed in the next section.



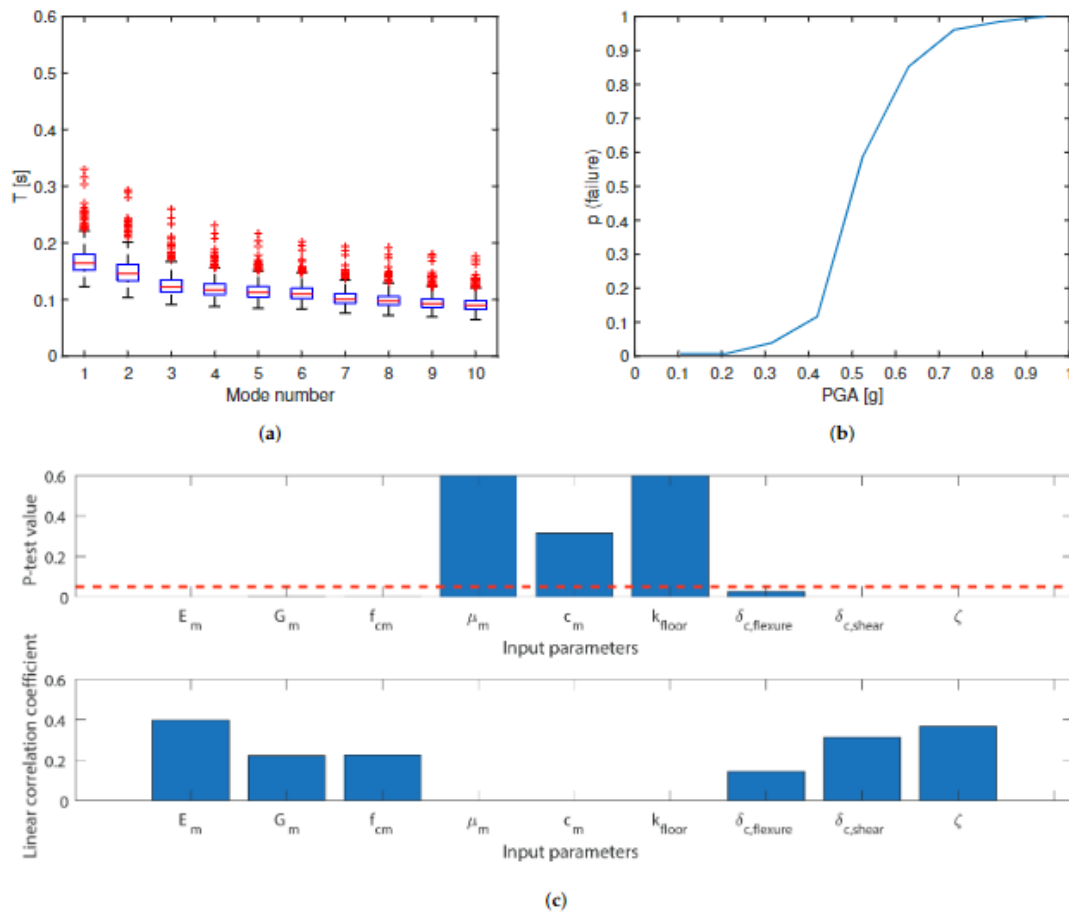


Figure 5.15: Holsteiner Hof model with out-of-plane disabled and rigid connections: (a) Distribution of modal periods. (b) Fragility curve. (c) Correlations between PGA at failure and input parameters.

The difference with the model with out-of-plane enabled was observed in the portion of the building that fails. With out-of-plane disabled, in-plane was the only mode of the failure. As shown in Figure 5.16, in-plane failures were split between flexural and shear failures, with shear failures accounting for 64% of the failures. A majority of the failures were localized in the second floor piers spanning in  $y$ -direction, with significant number of failures as well in the first floor piers spanning in the same direction.

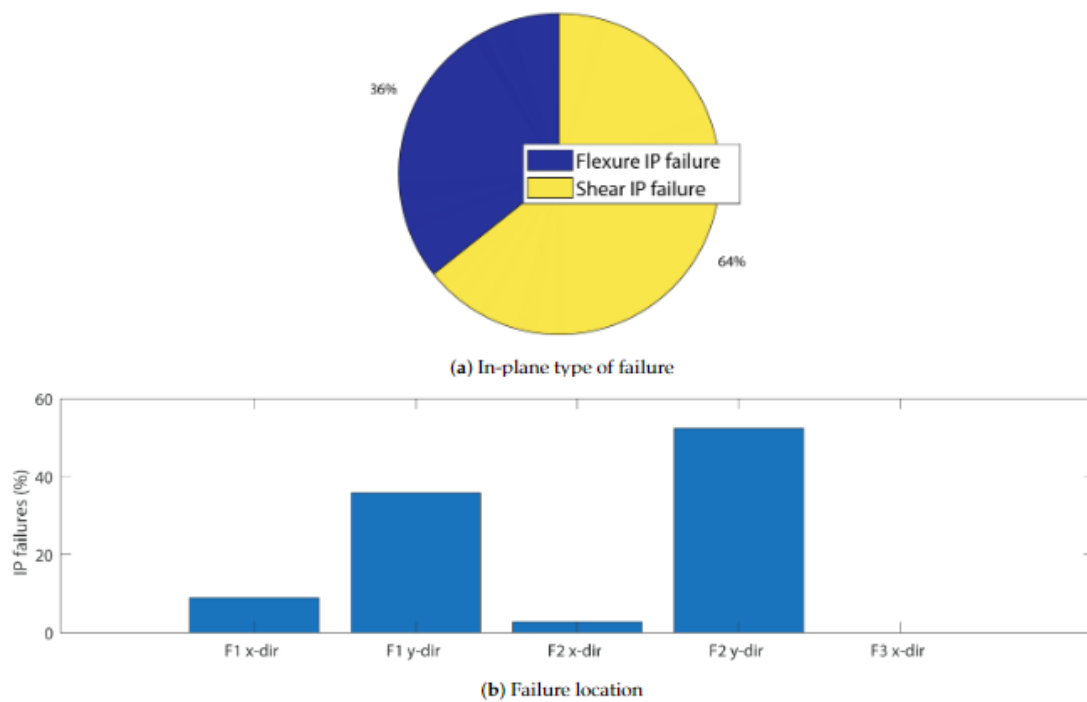


Figure 5.16: Holsteiner Hof model (with out-of-plane disabled and rigid connections) failure statistics: (a) In-plane type of failure. (b) Failure location.

### 5.4.3 Lausanne Malley

The Lausanne Malley building was modelled as described in Section 5.2.2. The walls were modelled using macroelements, the floors were modelled using orthotropic membrane elements, and the wall-to-wall and floor-to-wall connections were modelled using zero-length elements and non-linear material models.

#### Seismic Response Parameters

Figure 5.17 shows the IDA curves for each of the 400 sets of analyses. In this figure, the chosen output variable can be seen to evolve with the PGA increment, which is plotted together with the mean curve and 16th and 84th percentile curves. A similar scatter pattern was observed in both directions.

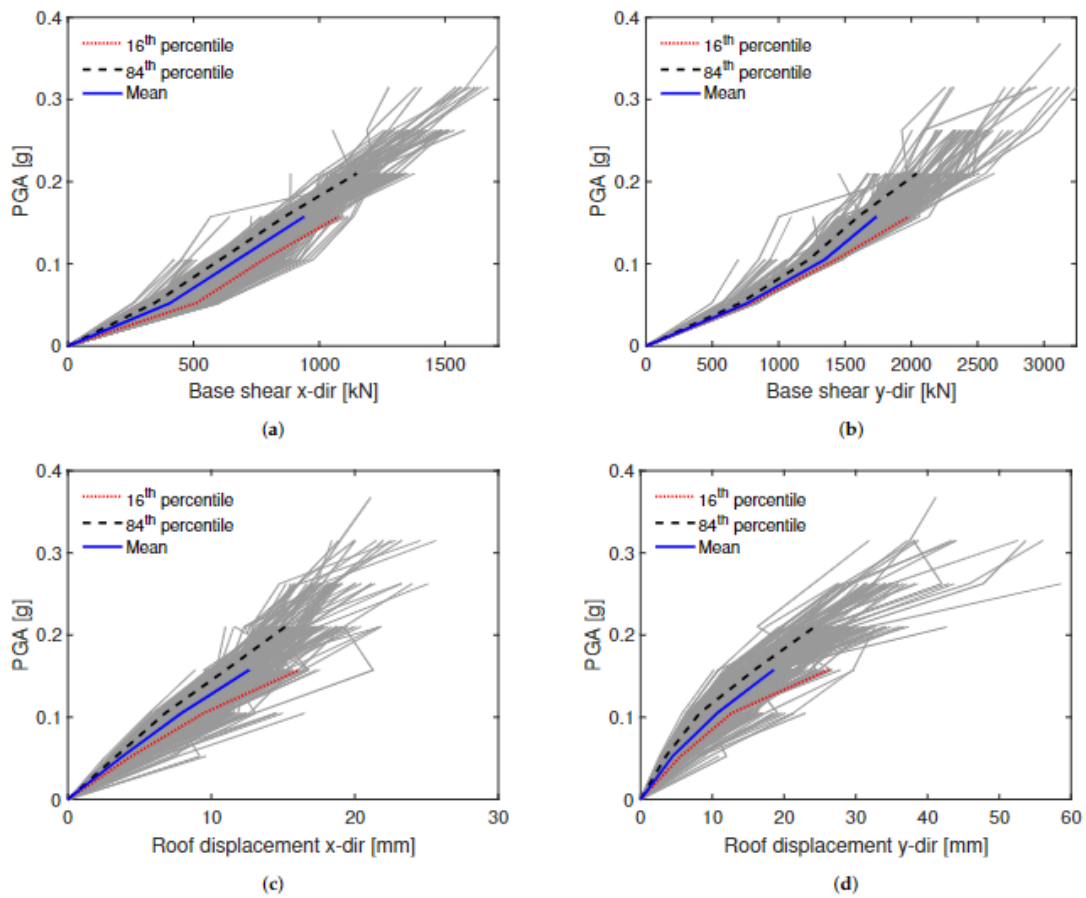


Figure 5.17: Lausanne Malley model IDA curves for maximum values of seismic demand parameters: (a) Total base shear in x-direction. (b) Total base shear in y-direction. (c) Average roof displacement in x-direction. (d) Average roof displacement in y-direction.

Figure 5.18 shows the correlation between the seismic demand parameters and the input parameters for the PGA of 0.105 g, chosen to provide sufficiently large seismic demand parameters without triggering too many failures. For clarity, only the Spearman rank correlation values for those parameters with a p-value less than 5% are displayed. Again, the strongest negative correlation was between the roof displacements and modulus of elasticity, shear modulus, and compressive strength, followed by Rayleigh critical damping ratio and cohesion. Modulus of elasticity, shear modulus, compressive strength, floor stiffness and cohesion showed positive correlations with base shear. Unlike in the case of Holsteiner Hof, there was a positive correlation between floor-to-wall friction coefficient and the base shear, and the negative correlation with the roof displacement in the y-direction. The reason for this lies in the fact that for the Lausanne Malley building, even for the low PGA values in some cases, floor-to-wall connection capacity is exceeded as out-of-plane behavior initiates. However, in most of the cases, the floor stiffness is still a more relevant value. Since the PGA was too low to trigger in-plane element failures, in-plane drifts at collapse did not correlate with the

parameters.

### Failure Analysis

Figure 5.17 shows the results of 400 IDAs for the Lausanne Malley model in terms of modal periods, fragility curve and the failure PGA correlations. At the start of each IDA, modal periods were determined to calculate the Rayleigh damping coefficients and evaluate the stiffness of the building. The material parameters  $E_m$ ,  $G_m$  and  $f_{cm}$  correlated positively with the PGA at failure, with the strongest correlation detected for  $E_m$ . It is important to note that these parameters were set as correlated when the LHS sample was prepared. A correlation between the limit drift values was expected for the in-plane failures. Since the Lausanne Malley building was more prone to failing in flexure, flexural drift at collapse more significantly influenced the PGA at failure than the shear drift at collapse. It was also expected that the Rayleigh damping ratio and the failure PGA will be correlated at failure for any failure mode for non-linear dynamic analyses. This is especially true for buildings that tend to fail out-of-plane, because the damping ratio is known to influence the out-of-plane displacement significantly (Vanin et al., 2020b). Here, the floor stiffness correlated with the PGA at failure. However, the floor-to-wall friction coefficient was more significantly correlated with the PGA at failure, as was expected in a building with such a significant percentage of out-of-plane failures in both directions.

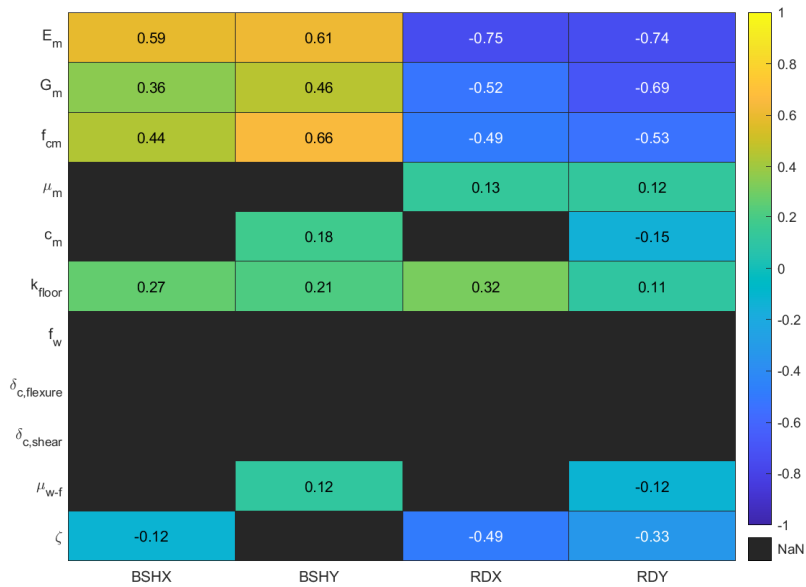


Figure 5.18: Lausanne Malley model Spearman correlation matrix for PGA 0.105 g.

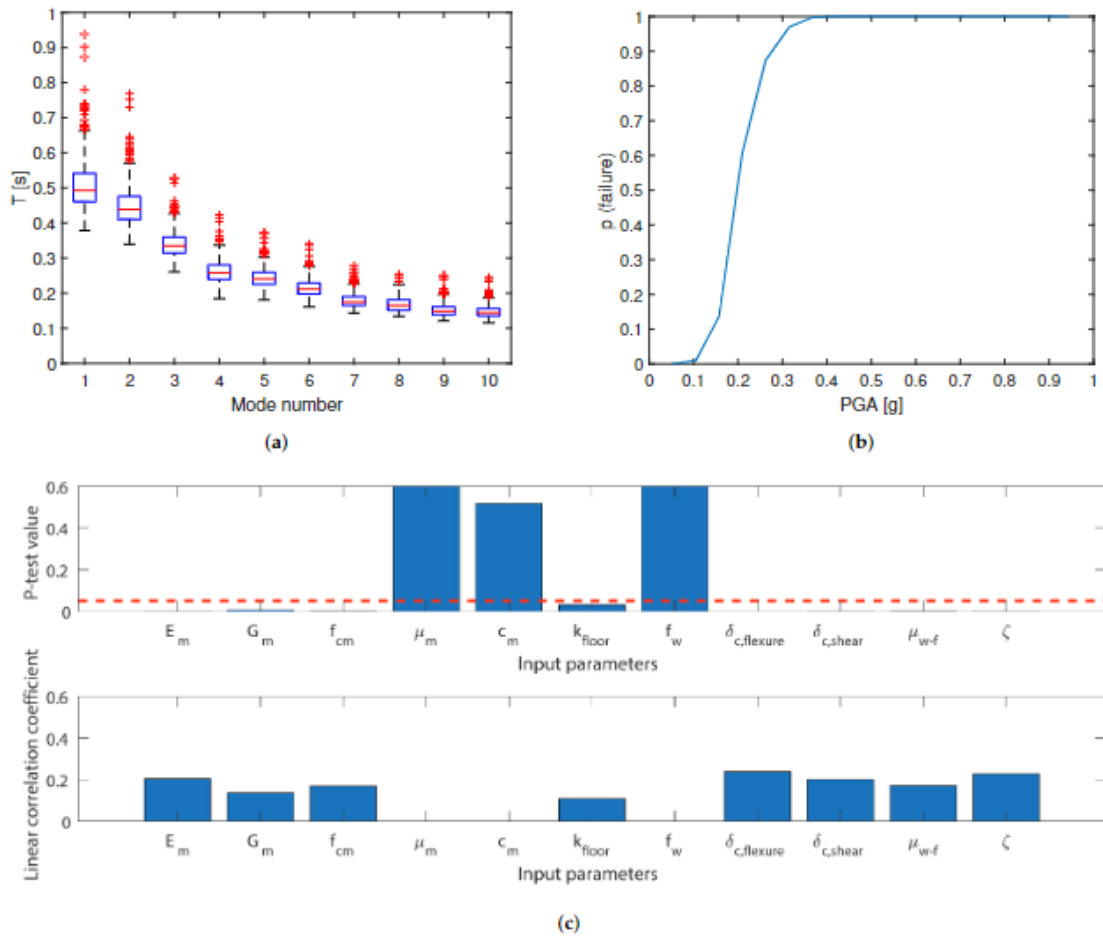


Figure 5.19: Lausanne Malley model (a) Distribution of modal periods. (b) Fragility curve. (c) Correlations between PGA at failure and input parameters.

The part of the building that fails was also influenced by selected material and modelling parameters. The distribution of the types of failure can be seen in Figure 5.20. Out-of-plane is the dominant failure mode, accounting for 92% of the total failures. In-plane failures were again dominated by flexural failures, accounting for 97% of total in-plane failures. This was expected for a tall and slender building, especially for upper floors with rather low axial loads on the piers. A majority of the failures, either in-plane or out-of-plane, were localized in the fifth floor piers. Twice as many in-plane failures occurred in the piers in  $x$ -direction than in the  $y$ -direction, while this difference was smaller for the out-of-plane failure modes. Regardless, in all the other storeys, the failure location was occasionally detected in both directions. This scatter of failures emphasizes the sensitivity of numerical simulations.

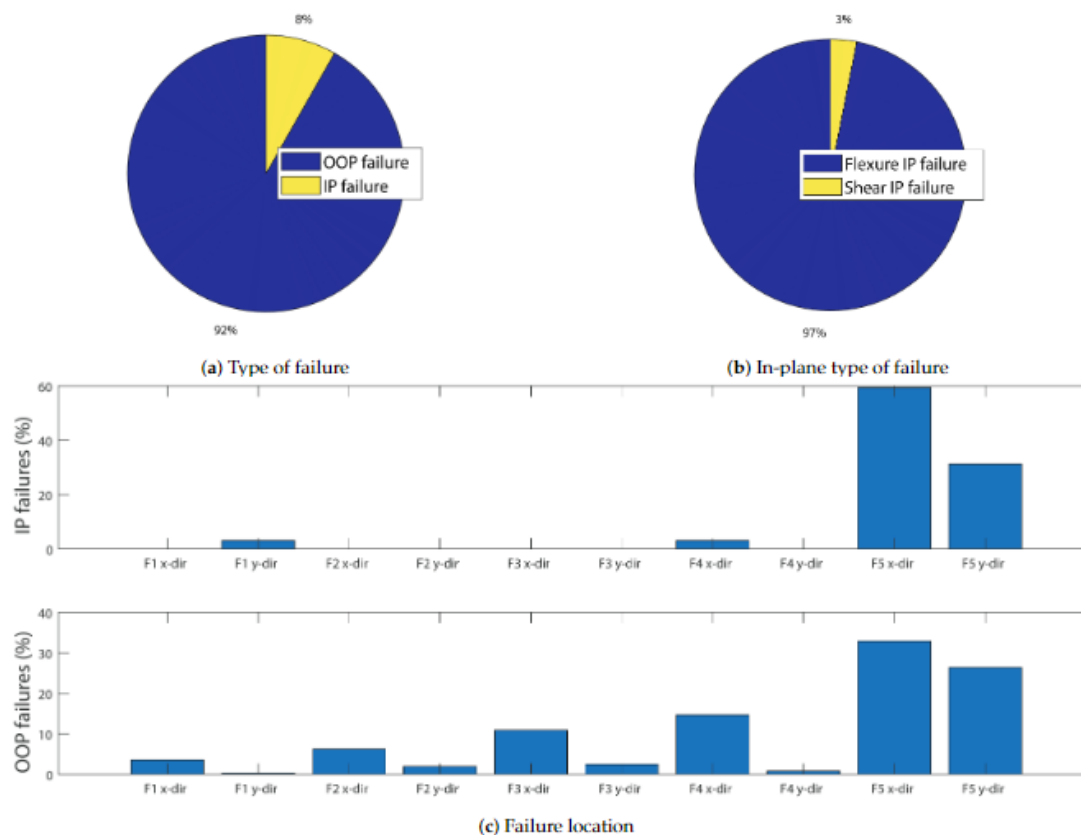


Figure 5.20: Lausanne Malley model failure statistics: (a) Type of failure. (b) In-plane type of failure. (c) Failure location.

#### 5.4.4 Lausanne Malley-Out-of-Plane Disabled and Rigid Connections

Lausanne Malley was again modelled as described in Section 5.2.2. The only difference was that the out-of-plane capability of the macro-element was disabled and connections were modelled as rigid. Therefore, both the seismic response parameters and the failure of the building were governed by the in-plane behaviour.

#### Seismic Response Parameters

For each of the 400 sets of analyses, the IDA curves are plotted in Figure 5.21. The scatter of base shear and roof displacements was similar to the model with out-of-plane enabled.

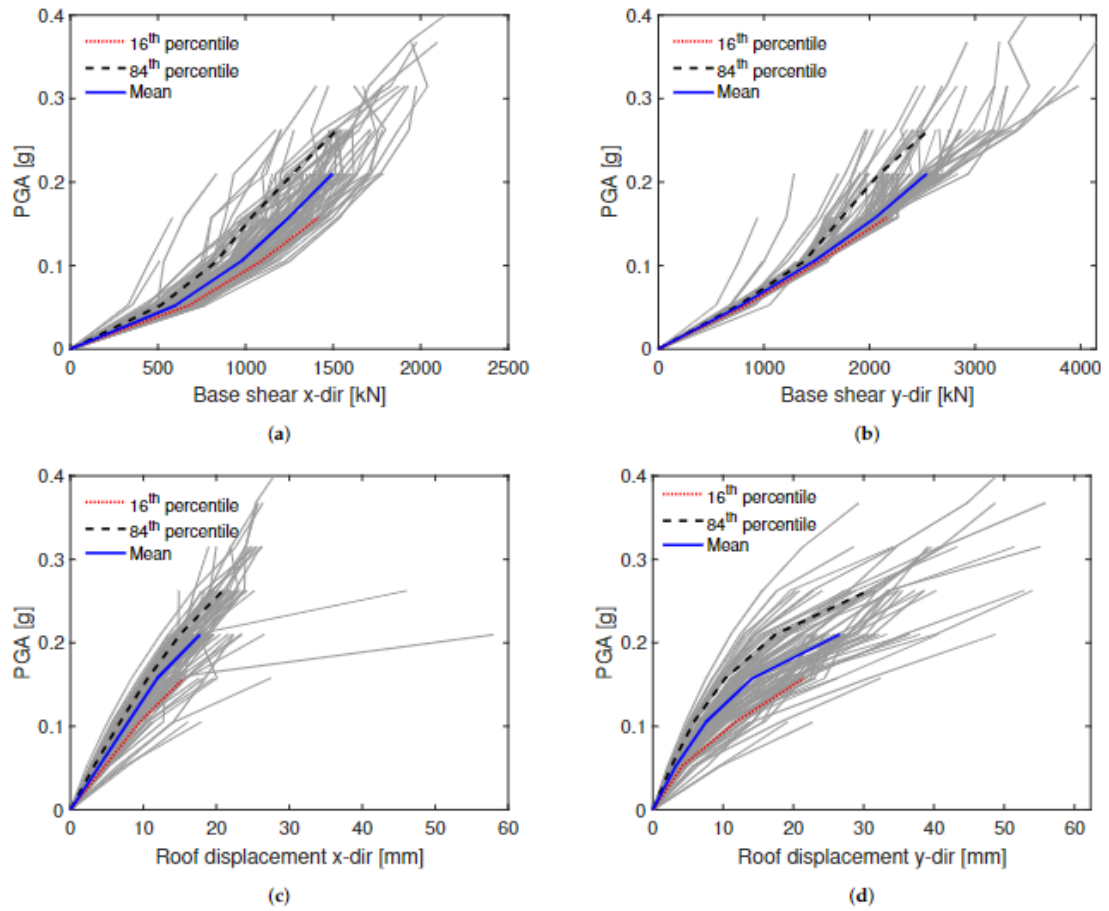


Figure 5.21: Lausanne Malley model (with out-of-plane disabled and rigid connections) IDA curves displaying the maximum values of seismic demand parameters: (a) Total base shear in  $x$ -direction. (b) Total base shear in  $y$ -direction. (c) Average roof displacement in  $x$ -direction. (d) Average roof displacement in  $y$ -direction.

The correlation between the seismic demand parameters and the input parameters for the PGA of 0.105 g is displayed in Figure 5.22. For the selected PGA, the values are very similar to the model with out-of-plane and non-linear connections.

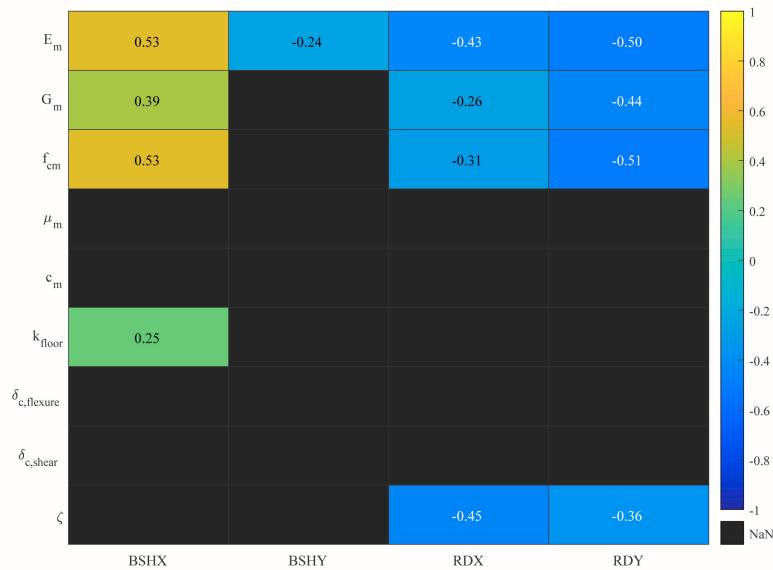


Figure 5.22: Lausanne Malley model (with out-of-plane disabled and rigid connections) Spearman correlation matrix for PGA 0.105 g.

**Failure Analysis**

Figure 5.23 shows the results of 400 IDAs in terms of modal periods, fragility curve and the failure PGA correlations. Significant differences to the model with out-of-plane enabled and non-linear connections were detected. First, in terms of the seismic fragility, and then in the parameters correlated with the PGA at failure. Floor-to-wall friction connection was replaced with the rigid connection, and the floor stiffness was no longer correlated with the PGA at failure. Remaining correlated parameters were the same as in the model with out-of-plane enabled, but with higher correlation coefficients. This was explained by the fact that once the out-of-plane failure mechanisms were disabled, the in-plane mechanisms with which they were associated became predominant.



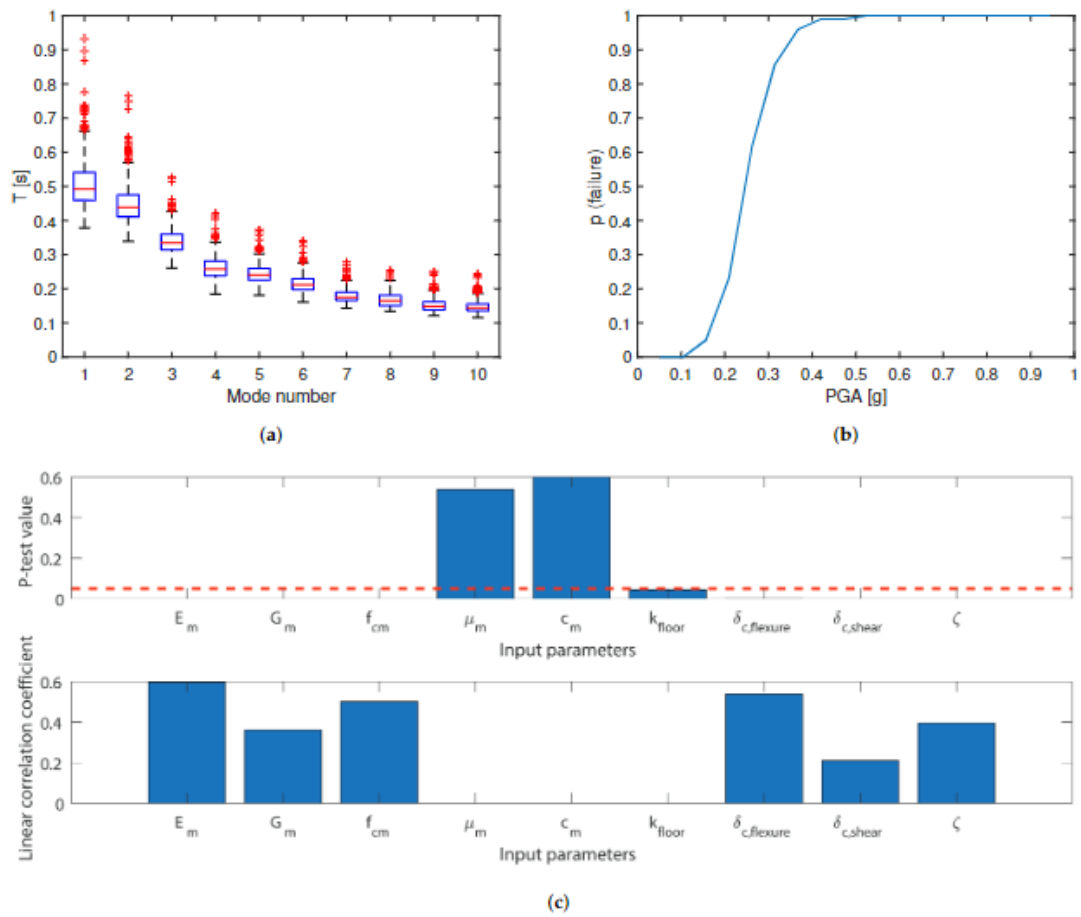


Figure 5.23: Lausanne Malley model with out-of-plane disabled and rigid connections: (a) Distribution of modal periods. (b) Fragility curve. (c) Correlations between PGA at failure and input parameters.

The distribution of the types of failure can be seen in Figure 5.24. In-plane failures were again dominated by flexural failures, accounting for 100% compared to 92% in the model with the out-of-plane enabled and non-linear connections. The scatter decreased, focusing most of the failures in the y-direction of the fifth storey.

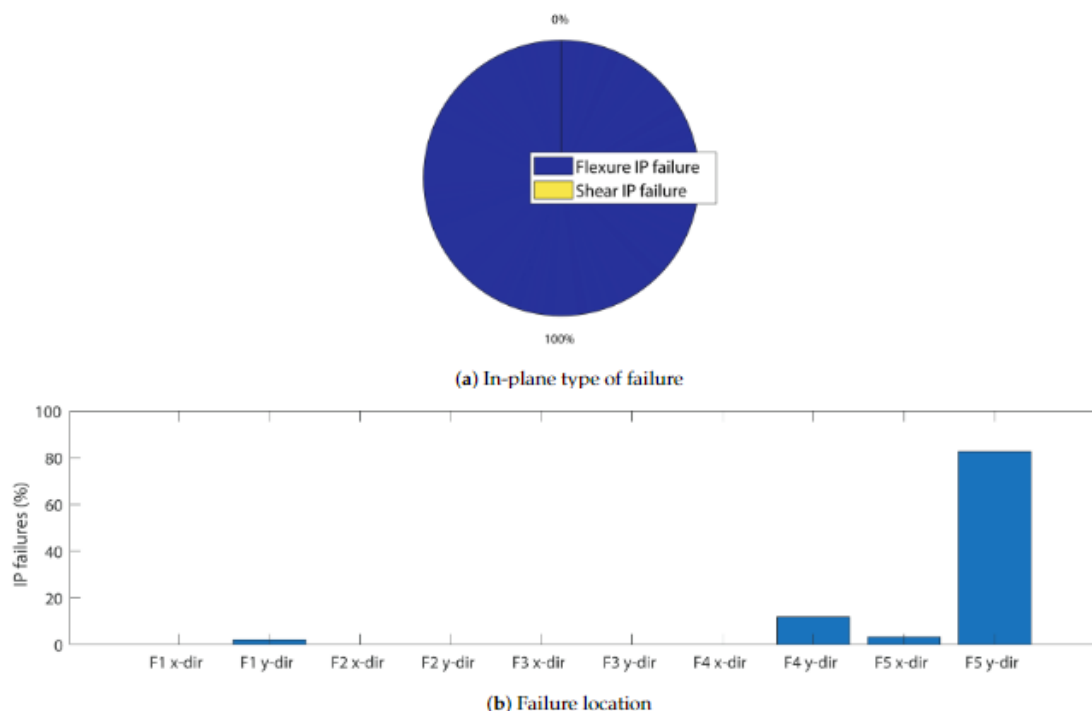


Figure 5.24: Lausanne Malley model (with out-of-plane disabled and rigid connections) failure statistics: **(a)** In-plane type of failure. **(b)** Failure location.

## 5.5 Discussion

This work highlights the importance of considering all sources of material and modelling uncertainty since rather small differences in the material and modelling parameters led to rather different results. Firstly, differences here could produce a different PGA at failure, which was already visible from the fragility curves. Secondly, they could produce different modes and locations of failure; the difficulty in predicting the correct mode of failure was especially evident for the Holsteiner Hof building, where the probability of out-of-plane and in-plane failures were evenly divided. Furthermore, the in-plane failure modes comprised both shear and flexural failures, with 62% of the in-plane failure modes being flexural, and both the flexural and shear drifts at collapse showing a clear correlation with PGA at failure, together with the Rayleigh critical damping ratio, modulus of elasticity, shear modulus and compressive strength.

Although the Holsteiner Hof had a high number of out-of-plane failures, there was no correlation detected between the probability of out-of-plane failures and floor stiffness or floor-to-wall connection effectiveness. This is because the floors of the building span in the  $y$ -direction, whereas Figure 5.12 showed that the majority of out-of-plane failures were located in the second storey walls in the  $y$ -direction. Since these walls fail out-of-plane in the  $x$ -direction

and the timber floor beam span in the opposite direction, the floor-to-wall connection does not influence the out-of-plane failure unless retrofit interventions provide also floor-to-wall connections in this direction.

To link our work with previous studies where EFM were used to compute fragility functions without accounting for out-of-plane failures, the stochastic analyses were repeated with the out-of-plane capability of the macroelement disabled and floor-to-wall and wall-to-wall connections modelled as rigid. The Holsteiner models 84th percentile IDA curves are compared in Figure 5.25. The results in terms of the base shear are almost identical, while the difference in the roof displacements progressed with the PGA increment.

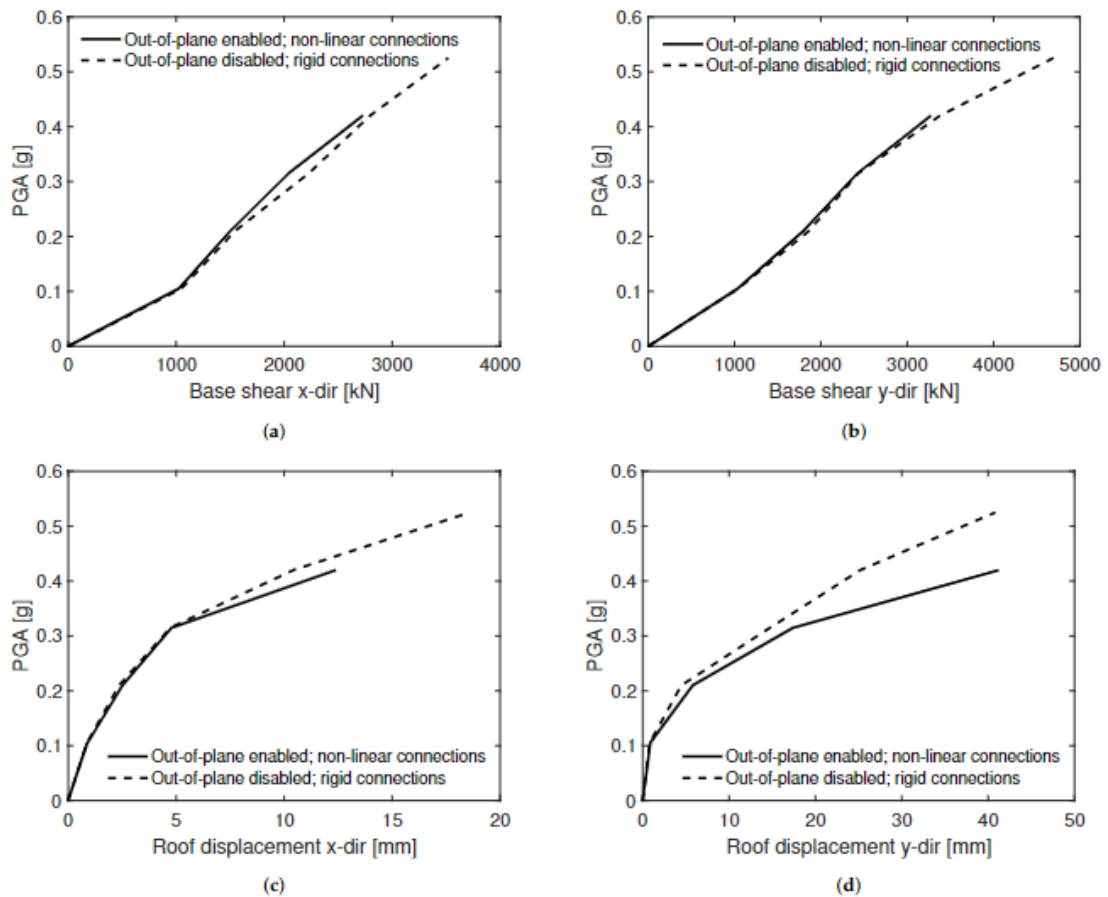


Figure 5.25: Holsteiner Hof comparison of IDA curves for models with: (i) out-of-plane enabled and non-linear connections, and (ii) out-of-plane disabled and rigid connections, displaying the maximum values of seismic demand parameters: **(a)** Total base shear in x-direction. **(b)** Total base shear in y-direction. **(c)** Average roof displacement in x-direction. **(d)** Average roof displacement in y-direction.

Comparison of fragility curves showed that the model with out-of-plane behaviour and non-linear connections was significantly more fragile than the model without out-of-plane be-

haviour and with rigid connections, having higher probability of failure for each PGA level as shown in Figure 5.26. The difference was emphasized for lower PGA levels, where a significant occurrence of the early out-of-plane failure was observed. The difference in failure type and location was significantly influenced by the ability of the macroelement to simulate the out-of-plane behaviour and presence of non-linear connections. Whereas the first model failed in flexure in 62% of the cases, the second failed in shear in 64% of the cases. Although failure was still most common to occur in the second storey, having disabled the out-of-plane behaviour and non-linear connections, the number of failures located in the first storey increased.

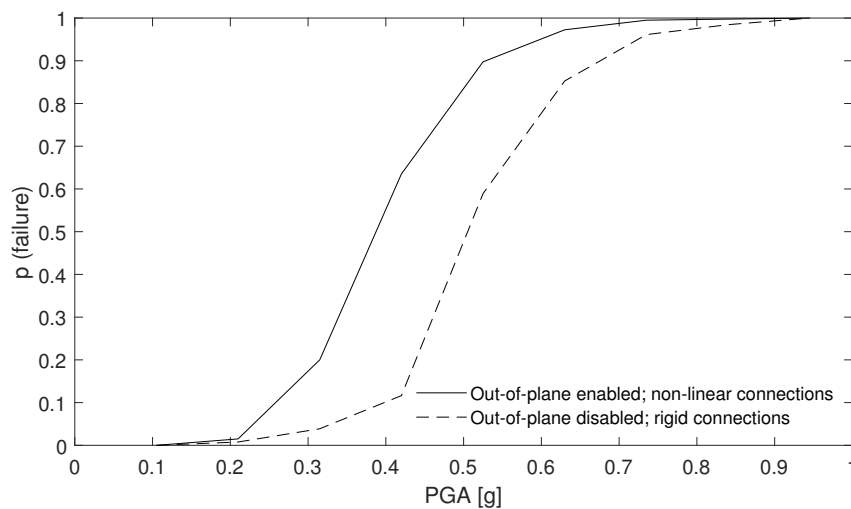


Figure 5.26: Comparison of Holsteiner Hof fragility curves for models with: (i) out-of-plane enabled and non-linear connections, and (ii) out-of-plane disabled and rigid connections.

A different effect of modelling uncertainties was observed in the Lausanne Malley building, which is tall and slender. As such, it failed out-of-plane 92% of the time. A dominant out-of-plane behaviour is shown in Figure 5.20, wherein failures were distributed in both directions and scattered through floors, but nevertheless were mostly concentrated in the fifth storey. This scatter throughout the floors indicates uncertainty on its own, and since out-of-plane was such a significant mode of failure in both directions, this also highlights the importance of floor stiffness and floor-to-wall connections, in particular. This can be seen in Figure 5.19, where a correlation with floor stiffness could be observed along with a stronger correlation with floor-to-wall friction. This result was expected, since only when the floor-to-wall connection capacity was not exceeded, the full stiffness of the floor could have been exploited. This correlation was on the same order of importance as damping ratio, flexure drift at collapse and modulus of elasticity—all values that were expected to significantly correlate with the PGA at failure.

Lausanne Malley models with and without out-of-plane behaviour and non-linear connections also showed differences in performance in terms of the 84th percentile IDA curves, as shown

in Figure 5.27. The differences with the PGA increment were the most significant in the roof displacements in  $y$ -direction.

Comparison of the fragility curves for the Malley Lausanne building showed that the model with out-of-plane behaviour and non-linear connections was significantly more fragile, having higher probability of failure for each PGA level, but especially for the lower PGA as shown in Figure 5.28. The difference was pronounced for lower PGA levels due to a significant occurrence of early out-of-plane failure, whereas the model with only in-plane behaviour started experiencing collapses only for higher PGA levels, when the in-plane capacity was exceeded. Having out-of-plane behaviour and non-linear connections disabled, the floor-to-wall friction coefficient was no longer used and the floor stiffness did not show a correlation with the PGA at failure. This was different in the case of the model with out-of-plane and non-linear connections, where they were correlated with the PGA at failure, stronger for the case of the floor-to-wall friction. The other parameters that passed the P-test remained the same, but with their correlation coefficients increased as a result of governing failure mechanism becoming predominant. Whereas the model with out-of-plane enabled and non-linear connections failed in flexure in 92% of the cases, the model with out-of-plane disabled and rigid connections failed in flexure in 100% of the cases. However, differences were detected in the failure location. In the model with out-of-plane disabled and rigid connections, failure was less scattered and occurred in the fifth storey in most of the cases.

All analyses were carried out with only one ground motion record (see Section 5.2.5). Some of the findings presented in this study might be record dependent. However, due to the rather broad-band frequency content of the Montenegro Albatros 1979 record, it is expected that the qualitative conclusions are applicable to a wide range of records. Dolsek found that both record-to-record variability (aleatory variability) and epistemic uncertainty influence the IDA curves Dolsek (2009). While the aleatory variability influenced the dispersion in the IDA curves, the epistemic uncertainty affected primarily the collapse capacity Dolsek (2009). Our work focused on the epistemic uncertainties, but in future work, the aleatory and the epistemic uncertainties could be combined using the same methodology to confirm the validity of using a record with a rather broad-band frequency content.

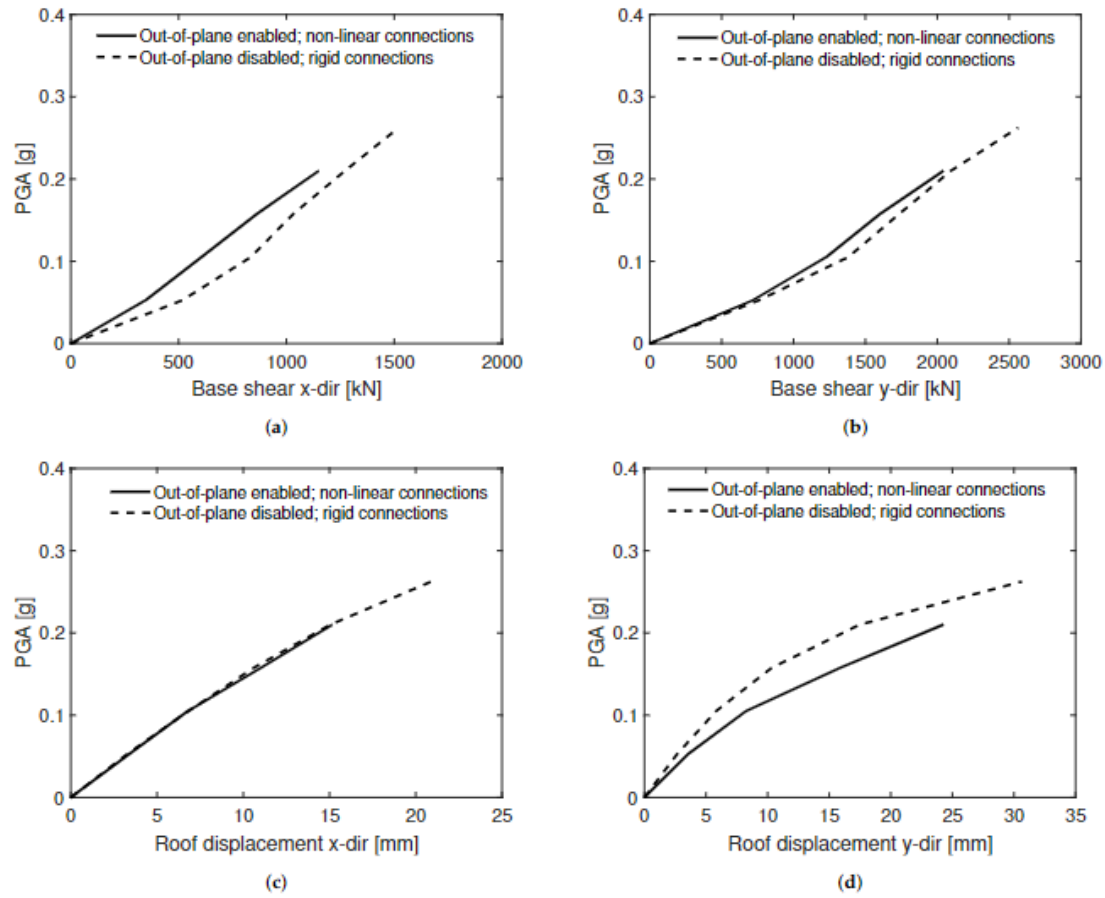


Figure 5.27: Lausanne Malley comparison of IDA curves models with: (i) out-of-plane enabled and non-linear connections, and (ii) out-of-plane disabled and rigid connections, displaying the maximum values of seismic demand parameters: **(a)** Total base shear in x-direction. **(b)** Total base shear in y-direction. **(c)** Average roof displacement in x-direction. **(d)** Average roof displacement in y-direction.

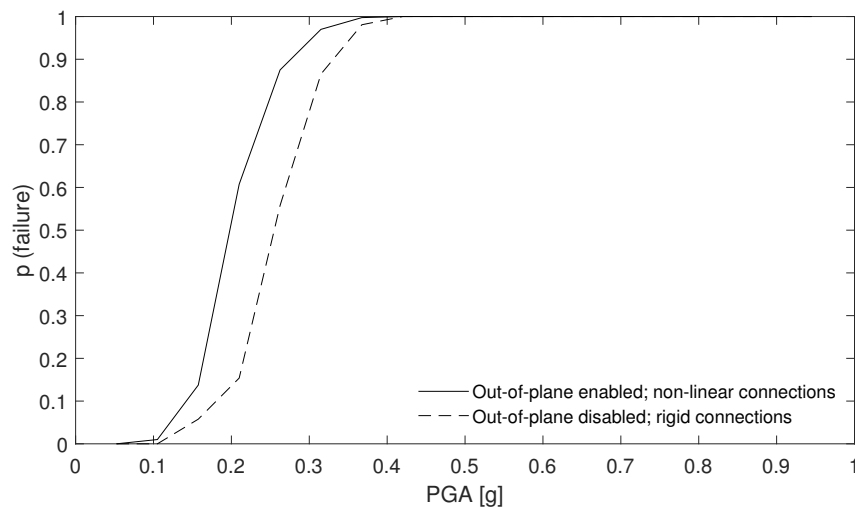


Figure 5.28: Comparison of Lausanne Malley fragility curves for models with: (i) out-of-plane enabled and non-linear connections, and (ii) out-of-plane disabled and rigid connections.

## 5.6 Conclusions

Scientists and practitioners alike often model unreinforced masonry buildings using the equivalent frame model (EFM) approach. This method is affected by numerous epistemic uncertainties, commonly handled by adopting conservative deterministic values. However, any deterministic approach bears the risk that possible damage and collapse mechanisms are overlooked. Therefore, we proposed a methodology to account for epistemic uncertainties and applied it to two masonry buildings representative of their categories: a stiff monumental historical masonry building, and a tall and slender residential masonry building. Each building was modelled twice —first with the out-of-plane capability of the macroelement used for modelling each wall enabled and with non-linear wall-to-wall and floor-to-wall connections, and then with the out-of-plane capability disabled and rigid connections. We used Latin Hypercube Sampling to create 400 sets of 11 material and modelling parameters, distributed according to normal and lognormal distributions, to account for epistemic uncertainties. Then for each model and each set of parameters, we carried out an IDA in OpenSEES using a newly developed macroelement that can couple in-plane and out-of-plane responses until the building failed or collapsed. Failure mode and location were analysed according to a set of criteria considering the loss of equilibrium due to out-of-plane failure of some element(s) or the progressive loss of lateral force capacity due to in-plane failure of walls. The response of each modelling approach was evaluated in terms of the seismic response parameters—base shear and roof displacement, correlations of seismic response parameters with input parameters, seismic fragility curves, correlations of failure PGA with input parameters, and statistical distributions of failure modes and locations.

The factors that clearly impact the failure PGA for each building typology were the mate-

rial parameters (modulus of elasticity, shear modulus, compressive strength) and the EFM modelling parameters (limit drift values, Rayleigh damping ratio). The floor stiffness and floor-to-wall friction coefficient also impacted the failure PGA if the model developed a dominant out-of-plane failure mode. The floor stiffness was second in importance to the floor-to-wall friction coefficient. A similar effect was observed by Vanin et al. (2020b). The importance of the floor stiffness is lower than the force capacity of the floor-to-wall connection if the latter is exceeded because the stiffness of the floor cannot be exploited. On the other hand, for PGA levels farther from failure, the floor-to-wall connection force capacity is not exceeded and the seismic response parameters correlate with the floor stiffness. Hence, the floor stiffness has only a large influence on the results, if the connection between floors and walls is effective enough to fully exploit the contribution of floors. In unstrengthened building configurations this force capacity is typically governed by friction forces between floor beams and wall and is therefore rather small. While this finding is intuitive, it is often overlooked because the floor-to-wall connection is modelled as perfectly rigid. The effect of the floor-to-wall friction coefficient highlights therefore the importance of modelling the nonlinearity of the connections in historical masonry explicitly.

For both the Holsteiner Hof and Lausanne Malley buildings, disabling out-of-plane behaviour and making connections rigid produced significant differences in the seismic fragility, failure modes and locations. The difference in the seismic fragility was even pronounced for lower PGA levels, which for certain sets of material and modelling parameters, could already produce significant out-of-plane behaviour. The models with out-of-plane and non-linear connections disabled, started experiencing failures only for higher PGA levels, when the in-plane capacity would be reached. Therefore, we deduce that modelling the unreinforced masonry buildings with wooden floors without correctly modelling the out-of-plane behaviour leads to incorrect predictions of the seismic fragility, as well as on the mode and the location of the failure. This becomes especially relevant when the analysis is performed to design retrofitting interventions to prevent the detected failure modes.

As a result, we conclude that after the out-of-plane behaviour and non-linear connections are correctly modelled, the appropriate choice of material and modelling parameters, including those of non-linear connections, can impact the seismic demand parameters such as base shear and roof displacements, and the PGA at failure. Failure mode and location are, however, more sensitive to the material and modelling parameters than the seismic demand parameters. Our results highlight the importance of firstly correctly modelling out-of-plane behaviour and non-linear connections, and then performing a probabilistic analysis to account for uncertainties. Although choosing conservative deterministic parameters aims at a conservative approximation of the PGA at failure, there is a risk of overlooking damage mechanisms and their location. This can again be especially problematic if the goal of the analysis is to retrofit the building to prevent certain mechanisms. Further studies should focus on gaining deeper insights into accurately modelling non-linear connections for correctly simulating the global behaviour. Special attention should be paid to extend the modelling of the connections to account for the interaction between units of unreinforced masonry aggregates.



## 6 Numerical Simulation of Unreinforced Masonry Buildings with Timber Diaphragms

This chapter is a post-print version of the paper: Tomić I, Vanin, F, Božulić, I, Beyer K (2021) Numerical Simulation of Unreinforced Masonry Buildings with Timber Diaphragms. Submitted to the journal of Buildings.

The formatting and numbering of equations, tables and figures have been adapted to this document. The contributions of the first author are: generating numerical models, running analyses, interpreting results, visualization and writing.

### Abstract

Though flexible diaphragms play a role in the seismic behaviour of unreinforced masonry buildings, the effect of the connections between floors and walls is rarely discussed or explicitly modelled when simulating the response of such buildings. These flexible diaphragms are most commonly timber floors made of planks and beams, which are supported on recesses in the masonry walls and can slide when the friction resistance is reached. Using equivalent frame models, we capture the effects of both the diaphragm stiffness and the finite strength of wall-to-diaphragm connections on the seismic behaviour of unreinforced masonry buildings. To do this, we use a newly developed macro-element able to simulate both in-plane and out-of-plane behaviour of the masonry walls and non-linear springs to simulate wall-to-wall and wall-to-diaphragm connections. As an unretrofitted case study, we model a building on a shake table, which developed large in-plane and out-of-plane displacements. We then simulate three retrofit interventions: Retrofitted diaphragms, connections, and diaphragms and connections. We show that strengthening the diaphragm alone is ineffective when the friction capacity of the wall-to-diaphragm connection is exceeded. This also means that modelling an unstrengthened wall-to-diaphragm connection as having infinite stiffness and strength leads to unrealistic box-type behaviour. This is particularly important if the equivalent

frame model should capture both global in-plane and local out-of-plane failure modes.

## 6.1 Introduction

Historical unreinforced masonry buildings have proven to be particularly susceptible to earthquakes (Tomazevic, 1999; D'Ayala and Speranza, 2003; Andrea Penna et al., 2014b; Carocci, 2012; Da Porto et al., 2013). To establish effective seismic risk management strategies and design appropriate retrofitting schemes, simulation tools are required that can reproduce the behaviour of historical unreinforced masonry buildings in their unstrengthened and strengthened configurations.

Different modelling techniques have been adopted to simulate the seismic behaviour of unreinforced masonry buildings, which differ regarding both the level of detail at which the building is modelled and the computational costs of the simulations (e.g. P. B. Lourenço (2002) and Roca et al. (2010)). While more detailed techniques, such as the ones used in Bui and Limam (2012), Pulatsu et al. (2020), Matthew J DeJong et al. (2009), Zhang et al. (2017), and Lourenco and Silva (2020), simulate masonry behaviour at a micro-scale, the computational cost limits at present still either the size of the model analysed or the number of simulations. For the simulations in this paper, we chose to use the equivalent frame model approach, which we consider a good compromise between level of detail and computational cost if a large number of analyses are performed (Bracchi et al., 2015). It is also a modelling approach that is widely used in engineering practice, making our findings highly applicable Quagliarini et al. (2017). In equivalent frame models, building facades are idealised as frames consisting of vertical pier elements, horizontal spandrel elements, and nodes (Parisi and Augenti, 2013; Bracchi et al., 2015). This frame idealisation is applicable to buildings with a relatively regular opening layout, such as the layout of many residential masonry buildings (Siano et al., 2017; Siano et al., 2018; Berti et al., 2017).

In equivalent frame models, the response of individual piers and spandrels is captured through macro-elements, which phenomenologically reproduce the force-displacement response of the piers and spandrels. A number of such macro-element models have been proposed for unreinforced masonry elements (Magenes and Fontana, 1998; Kappos et al., 2002; Roca et al., 2005; Pasticier et al., 2008; Belmouden and Lestuzzi, 2009; Rizzano and Sabatino, 2010; Calì et al., 2012; Lagomarsino et al., 2013; Parisi and Augenti, 2013; Andrea Penna et al., 2014a; Addessi et al., 2014; Raka et al., 2015; Peruch et al., 2019; Yousefi and Soltani, 2019; Grande et al., 2013); a recent review is included in Quagliarini et al. (2017). The simplicity of this modelling approach allows multiple static and dynamic analyses to be performed in a short time, and a large number of performed analyses can address aleatory and epistemic uncertainties (Tondelli et al., 2012; Rota et al., 2014; Bracchi et al., 2015; De Falco et al., 2017; Tomić et al., 2021). However, because all but the most recent macro-elements for unreinforced masonry elements (Vanin et al., 2020a) capture only the in-plane and not the out-of-plane response, equivalent frame model analyses were restricted to the global response.

Timber floors and their wall-to-diaphragm connections affect the global response of unreinforced masonry buildings and the formation of local out-of-plane failure modes (Tomazevic, 1999; D'Ayala and Speranza, 2003; Lagomarsino and Serena Cattari, 2015). Solarino et al. (2019) reviewed wall-to-diaphragm connections common in unreinforced masonry buildings as well as classical and innovative strengthening solutions. The effect of timber floors and their wall-to-diaphragm connections has been investigated experimentally by several research groups through large-scale shake table tests on masonry buildings (Miha Tomažević et al., 1991b; D. Benedetti et al., 1998; Dolce et al., 2008; Mauro Dolce et al., 2009; Bothara et al., 2010; Mazzon et al., 2010; Magenes et al., 2010; Guido Magenes et al., 2014; Senaldi et al., 2014; Costa et al., 2013; Vintzileou et al., 2015; Pitilakis et al., 2018; Mouzakis et al., 2018; Kallioras et al., 2018; Guerrini et al., 2019). Other studies numerically investigated the effect of diaphragm stiffness on the global nonlinear seismic response of unreinforced masonry buildings by modelling the diaphragms as elastic membranes and using equal DOF (Degree of Freedom) constraints for the wall-to-diaphragm connection (Kim and White, 2004; Betti et al., 2014; Nakamura et al., 2017b; Nakamura et al., 2017a; Gattesco et al., 2007; Scotta et al., 2016; Scotta et al., 2017). Recent works by Mirra (2017) and Trutalli et al. (2017) proposed modelling timber floors by an assemblage of elastic truss elements and nonlinear springs, which are assigned as a uniaxial material using *Pinching4* of OpenSEES (McKenna et al., 2000) that represents a 'pinched' load-deformation response and degrades under cyclic loading. The necessary parameters for obtaining an accurate pinching cycle were then calibrated against experimental results.

The effect of the quality of the wall-to-diaphragm connection on the seismic response of vernacular masonry buildings was addressed by Ortega et al. through an investigation of the influence of several floor parameters, including the diaphragm stiffness, the beam stiffness and the wall-to-diaphragm and wall-to-beam connections (Ortega et al., 2018). The masonry was modelled using solid 3D elements and an isotropic total strain rotating crack model. Because this method is computationally expensive, pushover analyses rather than time-history analyses were carried out. The wall-to-beam connections were modelled by imposing equal DOF conditions in combination with different embedment lengths for the beams, and the wall-to-diaphragm connections were modelled either with equal DOF conditions or without any connection. The friction connection was therefore idealised as either infinitely strong or non-existent. The results showed that if a proper connection was lacking, a stiffened diaphragm did not have the expected benefits. First equivalent frame models that used the macro-element by Vanin et al. (2020a) showed that this new formulation can capture out-of-plane mechanisms of single walls and parts of buildings that involve one-way bending of single elements (Vanin et al., 2020b). Common post-earthquake, out-of-plane damage patterns, such as those shown in Figure 6.1 illustrate the necessity of correctly modelling this phenomenon.

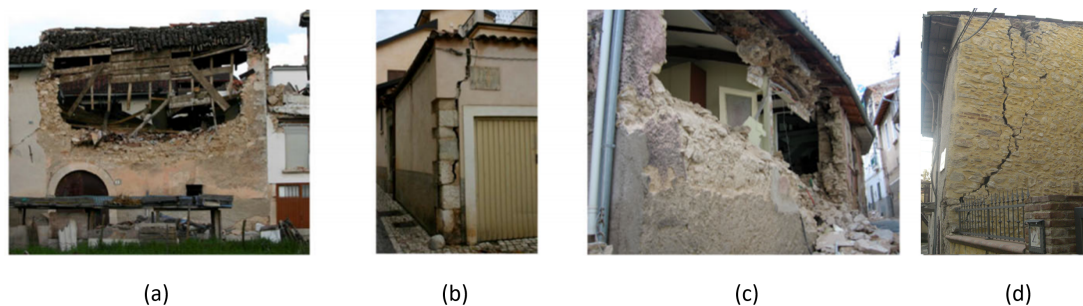


Figure 6.1: Examples of out-of-plane damage patterns from L'Aquila 2009 earthquake: **(a)** Out-of-plane mechanism in long walls. **(b)** Global overturning of external walls. **(c)** Overturning due to the lack of anchorage between walls and horizontal diaphragms. **(d)** Corner out-of-plane mechanism Ortega et al. (2018). (Sources: Dr. Javier Ortega, Prof. Hugo Rodrigues)

The objectives of this paper are to show that the latest equivalent frame modelling approach can be used for studying the effects of diaphragm stiffness and wall-to-diaphragm connections and to highlight the importance of explicitly modelling the wall-to-diaphragm connection. More specifically, we make the following two contributions:

- Equivalent frame model for Building 1 of the Pavia test series on stone masonry buildings (Magenes et al., 2010; Guido Magenes et al., 2014): This test series comprised uni-directional shake-table tests on three stone masonry buildings. Building 1 had a weak diaphragm and wall-to-diaphragm connections that relied only on friction between beams and walls. It developed significant nonlinear in-plane deformations but eventually succumbed to out-of-plane failure. Building 1 has not yet been modelled by an equivalent frame approach, so we close this gap by developing an equivalent frame model for Building 1 and validating it against the experimental results. Buildings 2 and 3 had strengthened diaphragms and wall-to-diaphragm connections. They did not develop any out-of-plane mechanisms and their in-plane response was modelled successfully by Andrea Penna et al. (2016) using Tremuri (Lagomarsino et al., 2013) and the macro-element by Andrea Penna et al. (2014a).
- Interplay between diaphragm stiffness and unstrengthened wall-to-diaphragm connections: We model the unstrengthened wall-to-diaphragm connection of Building 1 and analyse various configurations using a nonlinear spring with a force capacity that is limited by Coulomb friction. We confirm the finding by Ortega et al. (2018) that when a proper connection is lacking, a stiffened diaphragm lacks its beneficial effects. By modelling the connection through a friction connection rather than as fully connected (equal DOF) or disconnected, we show that there is a threshold PGA (Peak Ground Acceleration) value for which the wall-to-diaphragm connections start to slide. For higher PGA values, stiffened diaphragms lose their beneficial effect.

In this paper, we first outline our modelling strategy for unreinforced masonry buildings (Sec-

tion 6.2) and establish the equivalent frame model for Building 1 (Section 6.3). We compare the results of the analyses to the experimental results. We then simulate three simple strengthening interventions that highlight the interplay of diaphragm stiffness and wall-to-diaphragm connection strength (Section 6.4). Based on these simulations, we formulate recommendations for modelling timber slabs in unreinforced masonry buildings in the final section (Section 6.5). Finally, we conclude as much as these case studies permit on the effect of the retrofit techniques on the seismic response of unreinforced masonry buildings and formulate future research needs regarding the modelling of timber slabs in equivalent frame models.

## **6.2 Equivalent Frame Models for Unreinforced Masonry Buildings with Timber Slabs**

Here, we describe the equivalent frame model that we adopted for simulating the seismic behaviour of stone masonry building with timber floors. As our goal is to investigate the role of the timber diaphragm and wall-to-diaphragm connection on the seismic response of unreinforced masonry buildings, we discuss modelling assumptions with regard to these two points in particular detail.

### **6.2.1 A Macro-Element for Modelling the in-Plane and out-of-Plane Response of Unreinforced Masonry Piers and Spandrels**

In this study, we use the newly developed macro-element by Vanin et al. (2020a), which is implemented in OpenSEES (McKenna et al., 2000). It is the first macro-element for equivalent frame models that can capture the in-plane and out-of-plane behaviour of piers and spandrels by modelling each as a three-node element in three-dimensional space (Figure 6.2). The element is formulated as a system of two panels, deformable only in shear, rotating around three end sections and where flexural deformations are lumped. The exact equilibrium is ensured at all sections in the deformed configuration using an approximated  $P-\Delta$  formulation. The in-plane response of this macro-element is based on the formulation by Andrea Penna et al. (2014a).

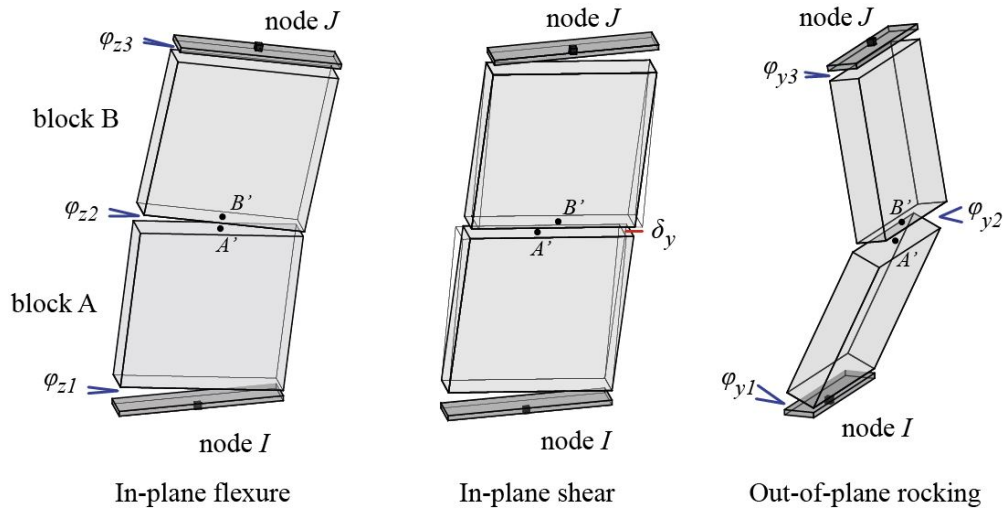


Figure 6.2: Macro-element by Vanin et al. (2020a): deformation modes.

With this approach, the in-plane flexural and shear failures and the out-of-plane overturning of the panel can be modelled (Vanin et al., 2020a). The shear model depends explicitly on the axial load applied to the section. The shear strength of the panel is defined by a Mohr-Coulomb failure criterion imposed by a damage-plasticity model describing residual displacements, stiffness degradation, and post-peak strength degradation. The flexural response, both in-plane and out-of-plane, depends directly on the applied section model. In the following, an analytical section model is used, assuming a material without tensile strength and with limited compressive strength with no post-peak degradation. When large lateral displacements are attained, in-plane failure of the panel is imposed.

### 6.2.2 Modelling Assumptions for Masonry Walls and Wall-to-Wall Connections

The strength of the wall-to-wall connection depends on the material properties and the level of interlocking in the corners, which also depends on the skills of the builders and modifications of the structure in its lifetime. We model masonry wall-to-wall connections in the equivalent frame model using a 1D material model that is linear elastic in compression with no crushing and with finite tensile strength with exponential softening (Vanin et al., 2020a), shown in Figure 6.3. The strength of the connections is calculated according to POLIMI (2010).

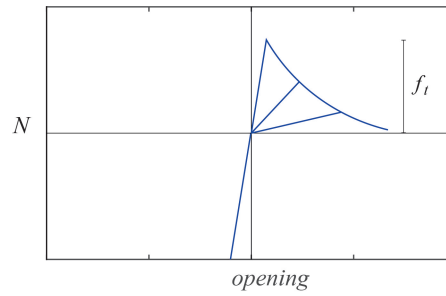


Figure 6.3: Equivalent frame model of wall-to-wall interface Vanin et al. (2020b)

### 6.2.3 Modelling Assumptions for Timber Floors

In equivalent frame models, floors are usually modelled by elastic membrane elements with perfect connections between the floors and walls (Vanin et al., 2020b; Andrea Penna et al., 2014a; Andrea Penna et al., 2016; Quagliarini et al., 2017; Senaldi et al., 2014; Lagomarsino et al., 2013). Such simplified assumptions are justified if the main goal is to describe the force redistribution and the floor-provided coupling of the response between different façades. However, if out-of-plane failure modes that span more than one floor are to be captured, the nonlinear in-plane response of the floor needs to be modelled. Since, in general, little distributed damage is observed on timber floors in post-earthquake surveys, concentrating the non-linearity in the connection between floors and walls is a reasonable approach (Vanin et al., 2020b). The floor diaphragm is therefore modelled as linear elastic orthotropic membrane with a larger axial stiffness in the direction of the beams and a lower axial stiffness in the direction orthogonal to the beams (Brignola et al., 2008; Brignola et al., 2012). To do this, estimates of timber floor properties are needed to describe the in-plane axial stiffness in both directions as well as the shear stiffness.

The diaphragm axial stiffness in the strong and weak direction of the timber floor is based on the timber stiffness both parallel and perpendicular to the grain. The diaphragm shear stiffness is computed according to the approach by Brignola et al. (2008) and Brignola et al. (2012). This shear stiffness, which is given in Equation (6.1), accounts for the (i) rigid rotation of the planks due to the slip of nails; (ii) flexural deformation of timber planks; and (iii) shear deformation of timber planks.

$$G_{eq} = \chi / A(l / (k_{ser} s_n^2) + \chi / (GA) + l^2 / (12EI))^{-1}, \quad (6.1)$$

where  $\chi$  is the shear correction factor (normally 5/6 for the rectangular cross-section),  $A$  is the area of a single plank section,  $l$  is the distance between the nail pairs on the opposite sides of a plank,  $k_{ser}$  is the nail stiffness per shear plane per fastener provided by codes EC 1995-1-1-2004 (2004),  $s_n$  is the nails spacing,  $G$  is the shear modulus of timber planks,  $E$  is the flexural modulus parallel to the grains of timber planks, and  $I$  is the moment of inertia of the plank section. The nail stiffness is calculated according to EC 1995-1-1-2004 (2004) using the

equation:

$$k_{ser} = \rho_m^{1.5} d^{0.8} / 30, \quad (6.2)$$

where  $\rho_m$  is the nail density in kg/m<sup>3</sup> and  $d$  is the nail diameter in mm. The value of  $k_{ser}$  is then in N/mm EC 1995-1-1-2004 (2004).

To model the increase in floor stiffness when an additional layer of timber planks is added as retrofit measure, the thickness and the equivalent shear stiffness are increased. The thickness of the retrofitted diaphragm corresponds to the thickness of the original planks plus the thickness of the new planks. The nails that are needed to fix the additional planks on the original planks increase the shear stiffness. Therefore, for the retrofitted configuration, we rewrite the equation as:

$$G_{eq} = \chi / A (l / (4k_{ser}s_n^2) + \chi / (GA) + l^2 / (12EI))^{-1}. \quad (6.3)$$

#### 6.2.4 Modelling Assumptions for Wall-to-Diaphragm Connections

As outlined in the introduction, we model the limited force capacity of this connection explicitly for the unstrengthened wall-to-diaphragm connection, meaning when the force transfer from the floor to the wall relies on a Coulomb friction mechanism (Almeida et al., 2020). The values for the friction coefficient were derived from a series of friction tests between both timber and timber and timber and mortar (Almeida et al., 2020). As shown in Figure 6.4, we model this connection by a nonlinear spring, coupling axial and shear force. The model allows for loading in the positive direction through sliding (beam pulled off the support) and in the negative direction through pounding (beam pounding against the wall).

Wall-to-diaphragm connections are typically reinforced by anchoring the floor beam to the wall (Solarino et al., 2019), which can make a rather stiff wall-to-diaphragm connection (Moreira et al., 2012; Ciocci et al., 2021). For the purpose of this study, these retrofitted connections are therefore assumed as infinitely stiff and strong and are modelled with the EqualDOF command in OpenSEES, which constructs a multi-point constraint between nodes (Vanin et al., 2020b). In the future, additional simulations with a limited anchor capacity could be envisaged. First strength models for the anchor capacity in stone masonry and numerical simulations of the anchors were put forward by several groups (Moreira et al., 2012; Muñoz et al., 2018; Contrafatto and Cosenza, 2014).



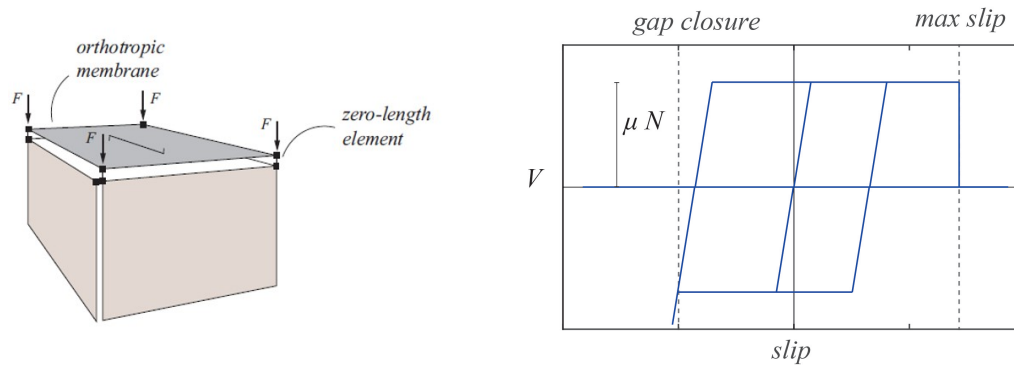


Figure 6.4: Equivalent frame model of wall-to-diaphragm connection Vanin et al. (2020b).

### 6.2.5 Damping Model for Dynamic Analyses

Here, we conduct nonlinear time-history simulations using the equivalent frame model. Vanin and Katrin Beyer (2021) showed that the overdamping that occurs with the classical Rayleigh damping model becomes especially relevant for out-of-plane behaviour. To avoid both the overdamping attributed to initial-stiffness proportional damping and the numerical problems stemming from tangential-stiffness proportional damping, we used the newly developed secant-stiffness proportional damping model in this study (Vanin and Katrin Beyer, 2021). The secant-stiffness proportional damping model defines a correction term for the initial stiffness-matrix proportional damping in the classical Rayleigh damping matrix, thus approximating the secant-stiffness proportional damping model. This correction term is updated at each converged analysis step. The use of secant-stiffness proportional damping simulates out-of-plane rocking with acceptable accuracy when compared to the experimental data and classical rocking formulations, such as those of Housner (1963), and experimental evidence (Vanin and Katrin Beyer, 2021).

### 6.3 Case-Study Building

The case-study building is Building 1 of an experimental campaign by Guido Magenes et al. (2014) comprising a full-scale unretrofitted stone masonry building (Pavia Building 1) and two retrofitted configurations of the same building (Pavia Building 2 and 3) (Magenes et al., 2010; Guido Magenes et al., 2014; Senaldi et al., 2014). The building was tested on the shake table at the EUCENTRE, Pavia, Italy. As outlined in the introduction, the two retrofitted configurations have already been successfully modelled by Andrea Penna et al. (2016). In this paper, we model Building 1, which developed significant in-plane deformations and then an out-of-plane failure mode. We directly base this model on the equivalent frame models of Buildings 2 and 3 by Penna et al., modified so the new equivalent frame model can capture the out-of-plane response developed by Building 1. In the following, we describe the unretrofitted building as well as the obtained experimental and numerical input data and the seismic record.

#### 6.3.1 Experimental Campaign

The Pavia Building 1 (Magenes et al., 2010), shown in Figure 6.5, is representative of an existing stone masonry building without any aseismic detailing. The building was 5.8 m long and 4.4 m wide. It had two storeys and a roof; the total height from the base to the top of the gable was 6.0 m. The walls were 32-cm-thick double-leaf stone masonry, without throughstones except in the corners and in the vicinity of openings. Two leaves of undressed stones were simply built adjacent to each other with smaller stones and mortar filling the irregular gaps. The four facades had different opening layouts such that some rotation in the building was expected. It is therefore a suitable case study of the effects of the floor diaphragms and wall-to-diaphragm connections on the seismic response.

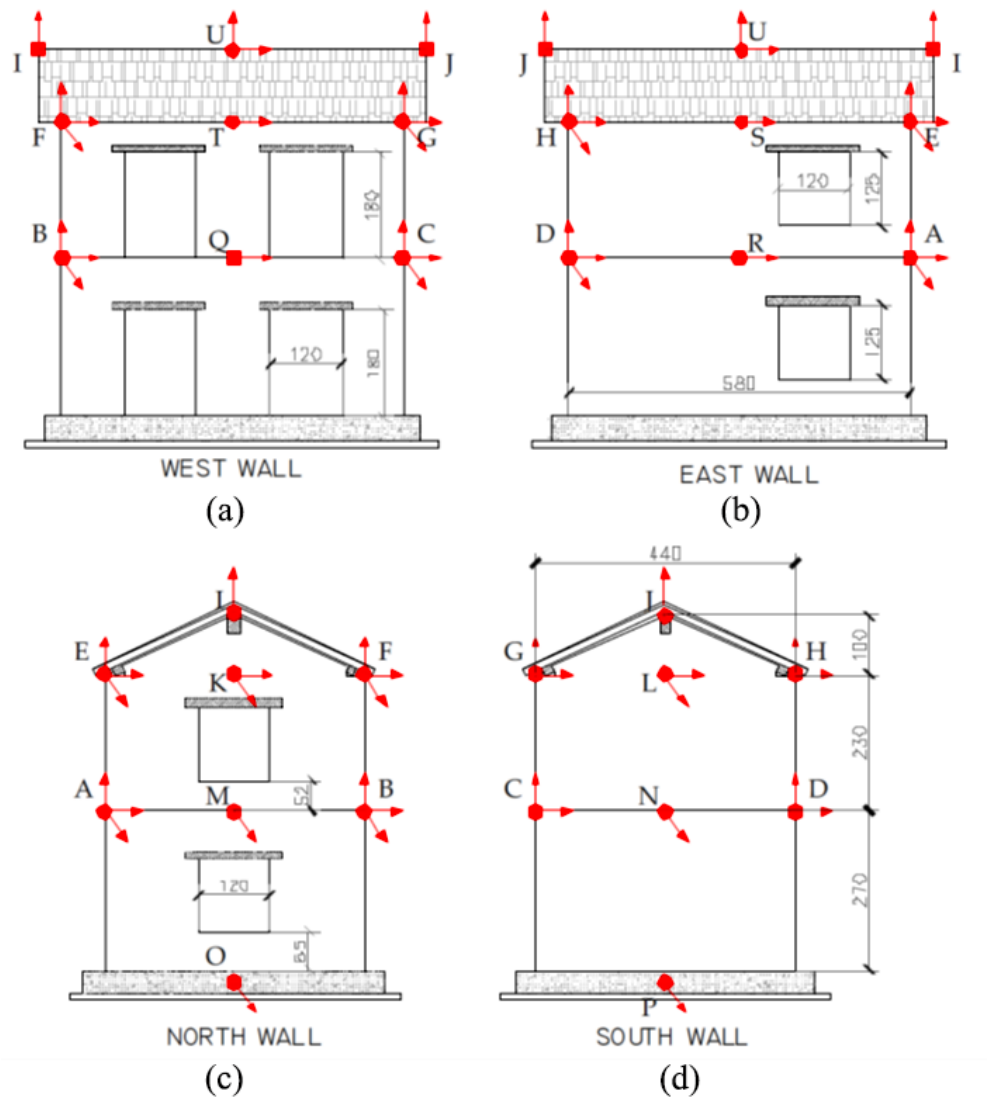


Figure 6.5: Drawings of Pavia Building 1 with the positions of accelerometers: (a) West wall. (b) East wall. (c) North wall. (d) South wall Magenes et al. (2010).

The floor was composed of timber beams that were 12 cm wide and 16 cm thick with planks that were 30 mm thick simply nailed on top of the beam (Magenes et al., 2010). The roof was composed of a 20 cm  $\times$  32 cm ridge beam, two 32 cm  $\times$  12 cm spreader beams and 8 cm  $\times$  12 cm purlins. The 30-mm-thick roof planks were again simply nailed on top of the purlins. The details of the masonry walls, floors and connections are shown in Figure 6.6. Additional masses were evenly distributed onto the floors, for a total amount of 3.2 tons.

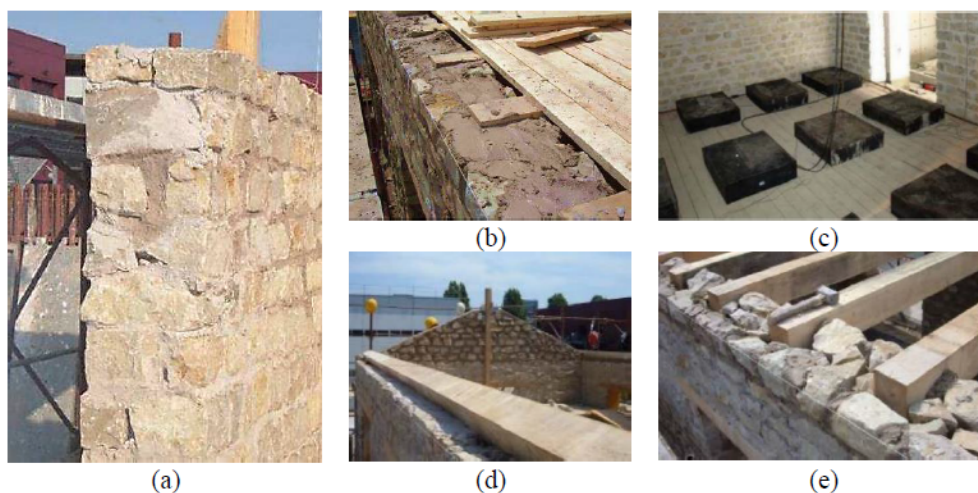


Figure 6.6: Building 1 details: (a) masonry wall. (b,c) timber floor. (d,e) timber roof Magenes et al. (2010), Guido Magenes et al. (2014), Senaldi et al. (2014), and Andrea Penna et al. (2016).

### 6.3.2 Numerical Model

All three buildings had the same overall geometry, differing only with regard to the floor and roof details. The previous model of Buildings 2 and 3 (Andrea Penna et al., 2016) included a sensitivity study regarding the discretisation of the equivalent frame model. We built here on their work and use the “MOD” discretisation, which they concluded to be the most appropriate for capturing the force capacity and damage mechanism observed during testing. In the “MOD” discretisation, the height of the piers was equal to the height of the adjacent openings.

Our material parameters for masonry in the numerical model are based on those used in the equivalent frame models for Buildings 2 and 3 (Andrea Penna et al., 2016), which were analysed using the software Tremuri (Lagomarsino et al., 2013) with the macro-element by Andrea Penna et al. (2014a). As outlined in Section 6.2, we used the macro-element by Vanin et al. (2020a), which builds the in-plane response on the macro-element by Andrea Penna et al. (2014a). For this reason, the macro-element parameters were based on the values used in the original modelling of Buildings 2 and 3 (Andrea Penna et al., 2016). The chosen set of material parameters for the macro-element simulating masonry piers and spandrels is shown in Table 6.1. For each model, the modal properties were calculated first and then the Rayleigh damping model parameters were computed such that the damping ratios at the first and sixth mode corresponded to the damping ratio of this model. We built upon the existing models by using the ability of the macro-element (Vanin et al., 2020a) to explicitly model the out-of-plane behaviour. As shown in Tomić et al. (2021), when the out-of-plane behaviour is accounted for, the influence of non-linear connections can be highlighted. Therefore, unlike the Tremuri model where the floors were assumed to be perfectly connected to the walls and the stiffness was calibrated accordingly, here we explicitly model the non-linear connections to base the

Table 6.1: Pavia Building 1: Material parameters assumed for masonry elements (Andrea Penna et al., 2016).

$E$ (MPa)	$G$ (MPa)	$\rho$ (kg/m) <sup>3</sup>	$f_c$ (MPa)	$\tau$ (MPa)	$\mu$
1900	300	2200	4.50	0.175	0.20

stiffness of the floor diaphragm on material properties and mechanical formulation. The OpenSEES Building 1 model is shown in Figure 6.7.

Floors and roofs were modelled as orthotropic membranes, with the parameters calibrated according to Brignola et al. (2012) and Brignola et al. (2008). The floor-wall connection was modelled using a frictional interface calibrated according to the experimental tests performed by Almeida et al. (2020). The floor parameters and floor-wall connection parameters are summarised in Table 6.2.  $E_1$  and  $E_2$  represent the membrane axial moduli in the strong and weak direction, respectively, and  $G$  represents the shear modulus of the membrane. The first row contains stiffness values that estimate the timber properties of Building 1. For evaluating the influence of the retrofitting strategies on the building response, a diaphragm is first modelled considering a retrofit of an additional layer of planks and nails. Then, the retrofitted floor-wall connection is modelled followed by the seismic performance of the building for both retrofitting techniques applied simultaneously.

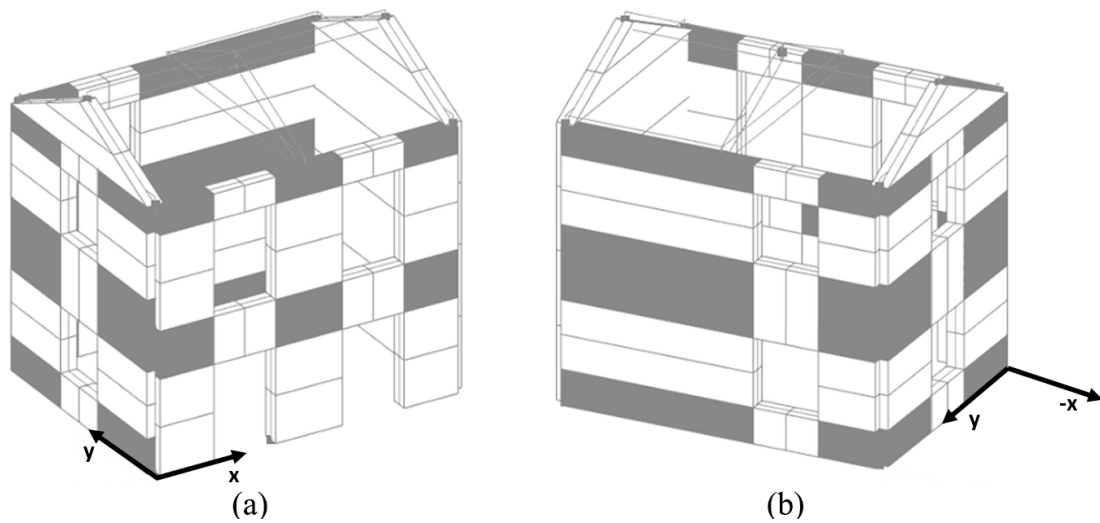


Figure 6.7: OpenSEES model of Pavia Building 1.: (a) View from the northwest corner. (b) View from the northeast corner.

Table 6.2: Pavia Building 1: Material parameters of diaphragms and the wall-to-diaphragm connections.

	$E_1$ (GPa)	$E_2$ (GPa)	$G$ (MPa)	$t$ (m)	$\mu_{w-to-d}$
Unretrofitted	10	0.5	10.3	0.03	1.0
Diaphragms retrofitted	10	0.5	19.6	0.06	1.0
Wall-to-diaphragm connections retrofitted	10	0.5	10.3	0.03	fixed
Diaphragms and connections retrofitted	10	0.5	19.6	0.06	fixed

Table 6.3: Building 1: Summary of shake-table runs Magenes et al. (2010).

Test Run	Nominal PGA (g)	Actual PGA (g)
1	0.05	0.07
2	0.10	0.14
3	0.20	0.31
4	0.30	0.50
5	0.40	0.63

### 6.3.3 Seismic Excitation

In the experimental campaign, Building 1 was subjected to the east-west component of the seismic record of the Montenegro 1979 earthquake at the Albatros station (Magenes et al., 2010). The record was scaled to nominal PGAs (Peak Ground Accelerations) between 0.05–0.40 g, and Building 1 was subjected to five runs of increasing intensities (Table 6.3). The actual applied PGAs were between 0.07–0.63 g. The numerical simulations used the actual applied ground motion as recorded during the test. To capture the damage evolution, we performed one long analysis that comprised all five runs. In between runs, we included zero ground acceleration records to again reach near zero building vibrations at the start of the next run.

For the second part of the analyses where we studied the interplay of diaphragm- and connection-strengthening interventions, incremental dynamic analyses (IDAs) were performed. The applied ground motions comprised both horizontal components of the Montenegro 1979 earthquake at the Albatros station, with the east-west component applied in the x-direction and the north-south component in the y-direction. For these analyses, we used the record as downloaded from Engineering Strong Motion Database (Luzi et al., 2016). The acceleration records and the response spectra are shown in Figures 6.9 and 6.10, respectively. More details on the IDAs are given in Section 6.4.2.

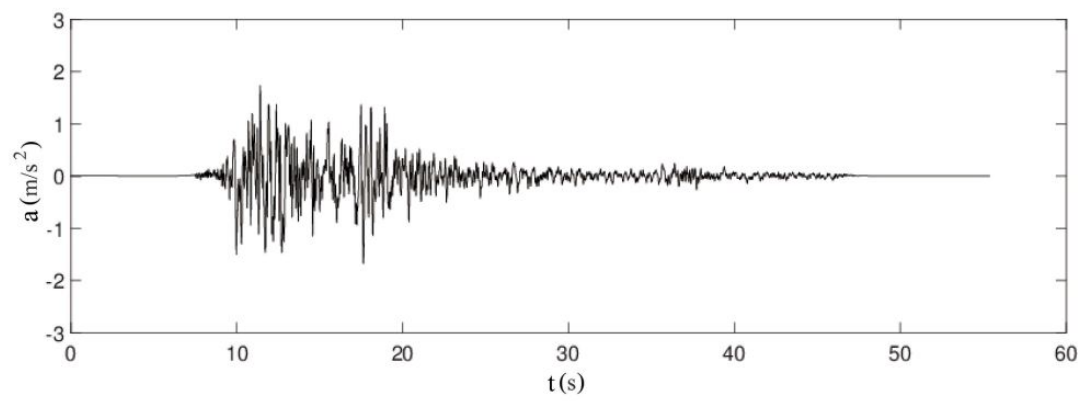
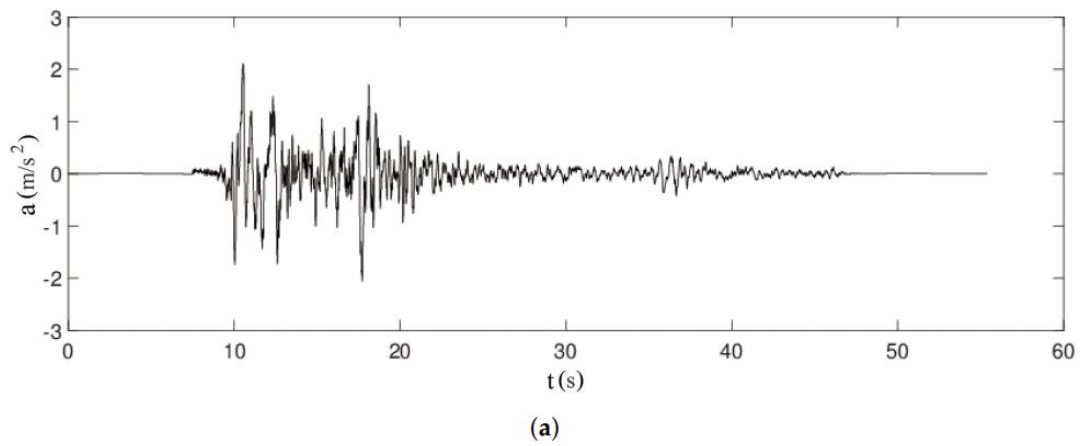


Figure 6.8:

Figure 6.9: Processed acceleration time-histories of the Montenegro 1979 earthquake at the Albatros station: (a) east-west direction. (b) north-south direction Luzi et al. (2016).

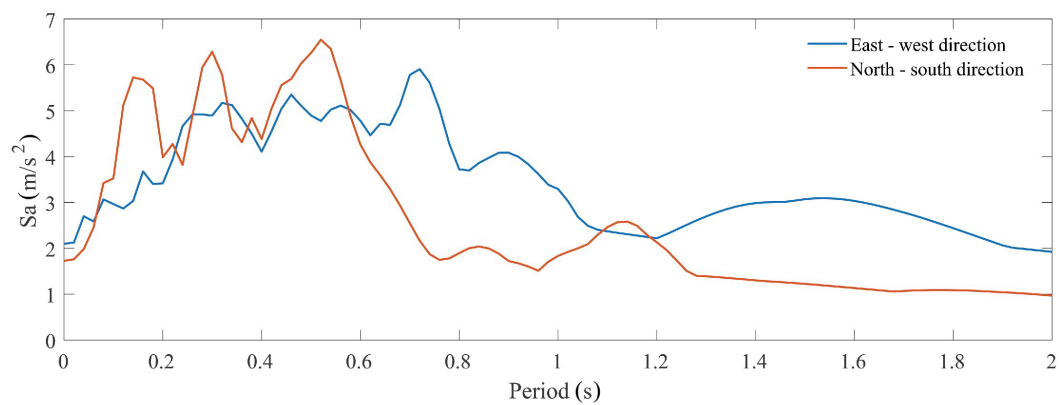


Figure 6.10: Acceleration response spectra of the Montenegro 1979 earthquake at the Albatros station for 5% damping ratio Luzi et al. (2016) .

## 6.4 Numerical Results for the Case-Study Building

We started by validating the numerical model of the unretrofitted building against the experimental data from the uni-directional shake table-test with regard to displacement demands and damage mechanisms. We analysed the four configurations of the case study building, the original unretrofitted and three retrofitted configurations, with regard to the differences in floor diaphragm and wall-to-diaphragm connections. These analyses were performed using the bi-directional seismic excitation of the Montenegro 1979 record. The run time for running a single model IDA analysis, consisting of 12 dynamic analyses, was about 1 hour on an Intel Pentium i7 with 16 GB of RAM and a Nvidia Quadro P2000.

### 6.4.1 Model Validation

For each of the five runs, the experimental data set contained accelerations recorded at 22 positions on the building and its foundation. To derive the displacements, we double-integrated the signals and applied a band-pass filter before each integration. Because it was difficult to choose the single best set of corner frequencies for the band-pass filter, we chose several sets that all produced results that are in agreement with the video recording of the test EUCENTRE (2009a). The corner frequencies of the band-pass filter were judged reasonable if the maximum relative x-displacement between accelerometers F and T (Figure 6.5) was between 4–10 cm, which was the maximum sliding displacement estimated from the video of the test EUCENTRE (2009a). Based on this check, we chose two sets of corner frequencies (wide band: 0.5–450 Hz, narrow band: 1–40 Hz) and assume that the so-obtained displacements are the bounds of likely displacements. The numerical prediction was compared to the experimental results in terms of the average displacement of three measurements: (i) the 2nd storey, (ii) the stiff (east) facade of the 2nd storey, and (iii) the soft (west) facade of the 2nd storey. All displacements are in the x-direction.

The only model parameter that was calibrated was the damping ratio. To do this, we tested damping ratios between 1 and 5%, and the best fit was obtained for a damping ratio of 2.5%. As outlined in Section 6.2, we chose a secant-stiffness proportional damping model. Figure 6.11 compares the maximum displacement values per run. The predicted maximum values of the average displacement of the 2nd storey ( $\Delta_{max}$ ) lay within the bounds of the derived experimental values for almost all levels of excitation; the match is therefore very good. The model tended to underestimate the displacements of the stiff facade ( $\Delta_{max, stiff}$ ), while the displacements of the soft facade ( $\Delta_{max, soft}$ ) were well predicted, except for the last run, for which the model overestimated the displacement demand.



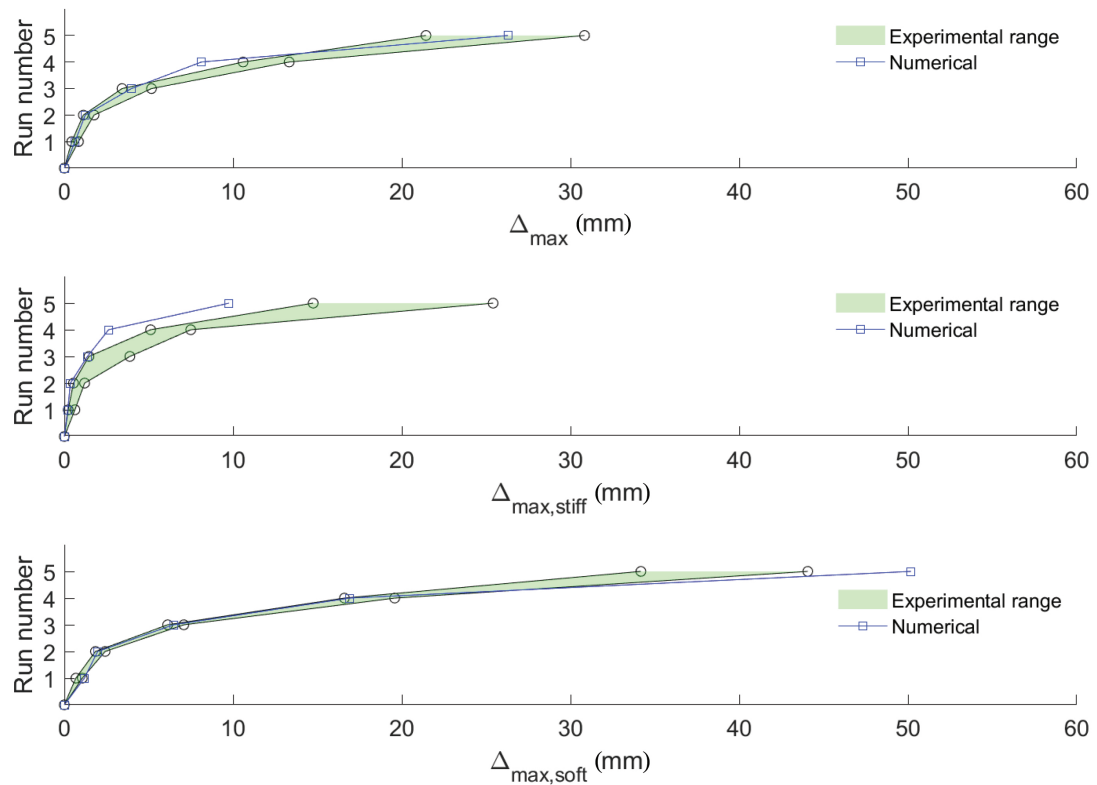


Figure 6.11: Comparison of experimental and numerical maximum displacements at each run.

The out-of-plane displacements of the gables were not measured during the test, but they can be observed via recorded videos EUCENTRE (2009a), EUCENTRE (2009b), and EUCENTRE (2009c) and the mechanism that developed during the final run (nominal PGA of 0.4 g) is sketched in Guido Magenes et al. (2014): (i) The north facade containing the opening developed an out-of-plane mechanism that involved the 2nd storey and gable wall of the facade as well as the adjacent pier and spandrel of the 2nd storey of the west facade. This part of the building rotated around the bottom of the 2nd storey (line A-B in Figure 6.5); (ii) The out-of-plane mechanism of the south facade involved only the gable wall, i.e., the gable rotated around its base (line G-H in Figure 6.5). The numerical model replicated the dominant out-of-plane behaviour of both out-of-plane facades, as shown in Figure 6.12.

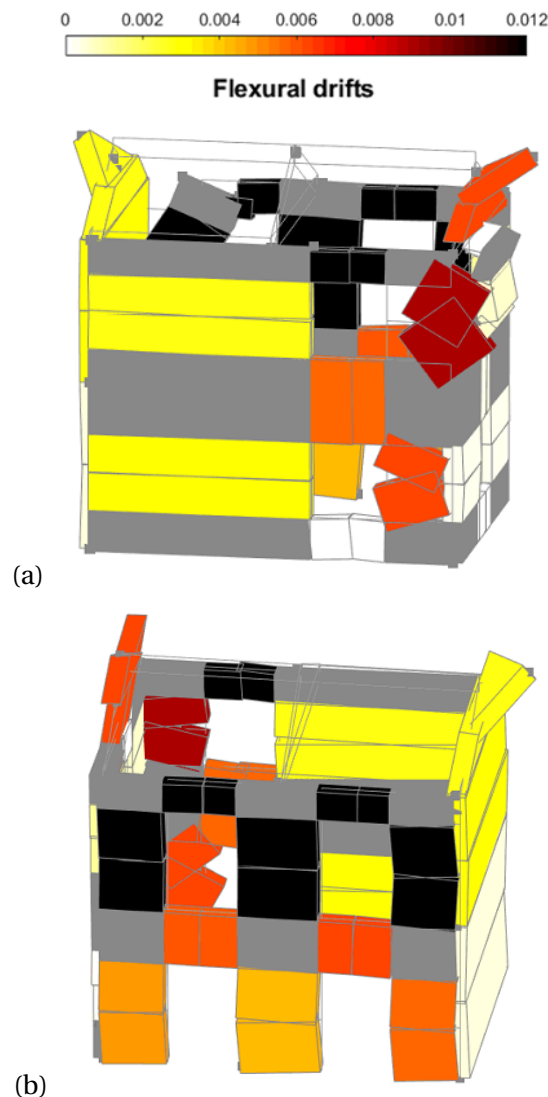


Figure 6.12: Out-of-plane behaviour (magnification factor  $\times 10$ ): **(a)** North facade-out-of-plane displacement involving the 2nd storey piers and the gable. **(b)** South facade-out-of-plane displacement involving only the gable.

#### 6.4.2 Modelling Retrofitting Interventions

Once the model of the unretrofitted configuration was validated, it was used to model the following unretrofitted and three retrofitted scenarios:

- Unretrofitted (diaphragm and wall-to-diaphragm connection unretrofitted): This corresponds to the configuration of Building 1.
- Diaphragm retrofitted: The diaphragm stiffness was increased to reflect the effect of an additional layer of planks (Table 6.2).

- Wall-to-diaphragm connections retrofitted: The wall-to-diaphragm connections were modelled as infinitely stiff and strong using equal DOF constraints.
- Diaphragm and wall-to-diaphragm connections retrofitted: The two individual retrofitting conditions were combined.

Each of the models was subjected to an IDA (Incremental Dynamic Analysis) using the two horizontal components of the Montenegro 1979 record Luzi et al. (2016) (see Section 6.3), with the east-west component in the x-direction and the north-south component in the y-direction. The record was scaled—for the east-west direction, the starting PGA of 0.0525 g was increased in increments of 0.0525 g until a PGA of 0.63 g was reached (the effective PGA applied in the final run of the shake table test [Table 6.3]). For the north-south direction, the starting PGA of 0.043 g was increased in increments of 0.043 g until a PGA of 0.516 g was reached. Figure 6.13 shows the IDA curves for the x- and y-direction. The IDA curves are plotted as PGA vs. the absolute maximum value of the mean 2nd storey displacement.

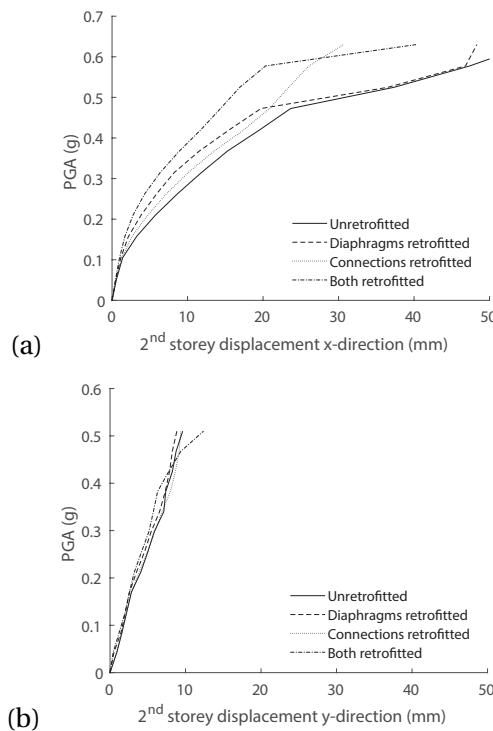


Figure 6.13: IDA curves for the four configurations in terms of PGA vs. the absolute maximum values of average 2nd storey displacement: (a) in the x-direction (b) in the y-direction.

The IDA curves for the x-direction show that for PGA values below a threshold value (here 0.4725 g), retrofitting the diaphragm reduced the displacements, as the sliding displacements of the diaphragm-wall connections were still small. Therefore, the increased shear stiffness of the retrofitted diaphragm proves effective. However, when the PGA rose above the threshold

value, the capacity of the wall-to-diaphragm connection became the weak link, and significant sliding displacements occurred between the floor and wall. Then, in the two models with unretrofitted wall-to-diaphragm connections, sliding occurred at those connections, which drastically increased the mean 2nd storey displacement to produce a kink in the PGA-displacement curve. This means that the force transferred by the diaphragm is limited by the wall-to-diaphragm connections, and therefore, the beneficial effect of retrofitting the diaphragm is reduced. In fact, for PGAs larger than 0.45 g, the mean 2nd storey displacement of the original unretrofitted configuration and the configuration with only the diaphragm retrofitted were almost equal. Conversely, models with retrofitted connections make use of the full stiffness of the diaphragm.

The difference in the y-direction was significantly lower. This was partly due to the lack of significant out-of-plane behaviour in the y-direction for any of the modelling approaches in comparison with the out-of-plane displacements of the gables in the x-direction. The reduced impact of the shear stiffness on the redistribution of the loads between the in-plane walls also lowered the overall difference in the y-direction.

The effect of the retrofitting solutions was also visible when observing the deformed shapes, which are shown in Figure 6.14 for a PGA of 0.58 g. The unretrofitted and diaphragm-only retrofitted models showed a significant out-of-plane displacement of the gable walls. The in-plane deformation of the soft facade (west facade) was slightly lower for the diaphragm retrofitted model than for the unretrofitted model, but a larger effect was prevented by the limited force capacity of the wall-to-diaphragm connections. Otherwise, the two models with retrofitted connections did not show any significant out-of-plane displacements, which are successfully prevented by the rigid connections. The rigid connections fully exploit the beneficial effect of the increased shear stiffness of the retrofitted diaphragm, leading to lower displacements and drifts when compared to the model with only the connections retrofitted.

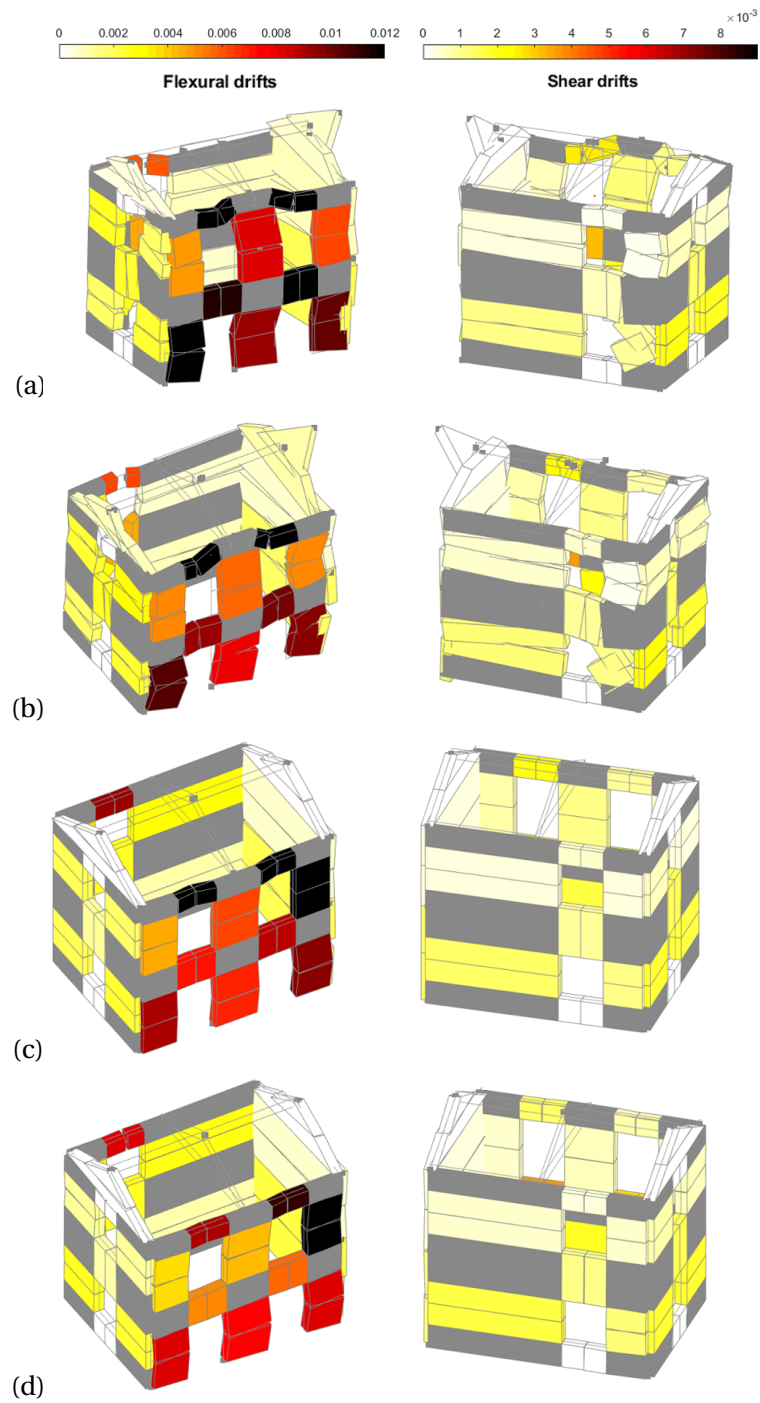


Figure 6.14: Deformed shapes and maximum element drifts in flexure and shear (magnification factor  $\times 10$ ): (a) Unretrofitted. (b) Diaphragms retrofitted. (c) Connections retrofitted. (d) Both retrofitted.

### 6.4.3 Force Demand on the Wall-to-Diaphragm Connections

The analyses showed that retrofitting wall-to-diaphragm connections significantly impacts the behaviour of the case-study building, shifting the failure mode from out-of-plane to in-plane. However, to ensure the behaviour as predicted by the model, the necessary pre-condition is that the wall-to-diaphragm connection must be reinforced by anchors able to sustain the force demand. The EqualDOF command, which was initially used to model the wall-to-diaphragm connections retrofitted by anchors (Section 6.2), did not provide the force transmitted by this connection. Therefore, to measure this force demand in another set of analyses, this connection was also modelled using very stiff elastic elements. The impact on the results was negligible, and the maximum tensile force demands on the wall-to-diaphragm connections for the example of PGA of 0.63 g are given in Table 6.4.

Table 6.4: Maximum tensile force demands on the anchors of the first storey, second storey, and gable of the model with connections retrofitted for the PGA of 0.63 g.

Position	Unit	Maximum Tensile Force
First floor	(kN/m)	20.58
Second floor	(kN/m)	7.56
Gable	(kN)	37.09

For the first storey, the largest tensile force demand of 20.58 kN/m was recorded for the anchors. This value was obtained by dividing the sum of the recorded tensile forces in the anchors with the length of the facade to obtain a value more practical for the design of the retrofitting intervention. For the second storey, the largest tensile force demand anchoring the roof to the wall was 7.56 kN/m. For the gable, the largest tensile force demand of 37.09 kN was recorded and reported here as a concentrated force, as a single anchor pair is assumed to anchor the ridge beam to the gable wall.

Ciocchi et al. (2021) tested the pull-out capacity of injection anchors in masonry of a similar typology to the case-study building. The anchor configurations each consisted of two horizontal anchors that failed at the cone. The test showed a direct relationship between the pull-out capacity and the overburden stress. For a very low overburden stress, such as the one acting on the roof-wall connection, the mean capacity of such a pair of anchors was approximately 30 kN; meaning that even for a very low overburden stress, the tested anchor design would achieve the assumed behaviour in the case-study building with a reasonable number of anchors per meter. Due to the possible high local concentration of force in the anchor pair, special attention should be paid to the anchorage of the ridge beam into the gable wall.

## 6.5 Conclusions

In this paper, we validated an equivalent frame model for unreinforced masonry buildings with unstrengthened timber floors and diaphragm-wall connections. This equivalent frame model completes the suite of models covering the full range of diaphragm and connection details found in unstrengthened and strengthened configurations of historical stone masonry buildings. Building configurations with strengthened floor diaphragms and wall-to-diaphragm connections had already been successfully modelled and validated by Penna et al. (2016). Modelling the unstrengthened configuration required three modifications: First, the new macro-element by Vanin et al. (2020a) captured in-plane and out-of-plane failure modes of piers and spandrels. Second, the wall-to-wall and wall-to-diaphragm connections were modelled with infinite stiffness but limited strength using nonlinear springs. Third, a new secant-damping model prevented the overdamping of rocking motions that is frequently observed for initial-stiffness proportional damping Vanin and Katrin Beyer (2021). These changes allowed us to capture next-to-inelastic, in-plane deformations and large, nonlinear, out-of-plane displacements. The modelling approach was validated against the results of the Pavia Building 1 shake test Magenes et al. (2010).

In a second step, we investigated the influence of strengthening interventions on the global behaviour and local failure modes of the building under earthquake loading. The following modelling assumptions were made with regard to diaphragms and diaphragm-wall connections in their unstrengthened and strengthened configuration:

- In its unstrengthened configuration, the diaphragm consists of timber beams and a single layer of planks nailed to the timber beams. The diaphragm is modelled as an orthotropic elastic membrane. The properties of this membrane are determined according to Brignola et al. (2008).
- The diaphragm is retrofitted by adding a layer of planks at a right angle to the first layer of planks. The increase in stiffness of the diaphragm is again calculated using the formulae provided in Brignola et al. (2008), with a slight modification to account for the deformation of the additional set of nails (Equation (6.3)).
- The wall-to-diaphragm connection in its unstrengthened configuration transfers loads only via friction. Representative friction coefficients were determined by Almeida et al. (2020). In finite element models of configurations with unstrengthened wall-to-diaphragm connections, the connection was modelled as rigid until the friction force was attained and sliding occurred.
- It was assumed that the wall-to-diaphragm connection was retrofitted by injection anchors that are relatively stiff until the peak force is attained. For this reason, they were modelled as infinitely rigid with infinite force capacity. Using the force capacities attained, it was computed how many anchors would be necessary to transfer the

forces between the diaphragm and wall, which were recorded for the numerical model. Reasonable numbers were attained.

The effect of the two retrofit interventions (strengthening of floor diaphragms and of wall-to-diaphragm connections) was investigated by simulating virtual retrofit measures for Pavia Building 1. For this case-study building, strengthening the diaphragm alone only had an effect up to a threshold value of the PGA, where the capacity of the frictional wall-to-diaphragm connection was exceeded. For larger PGA levels, the seismic response of the building could only be improved if the wall-to-diaphragm connections were strengthened. Retrofitted wall-to-diaphragm connections increased the capacity because the failure mode changed from out-of-plane to in-plane. When the wall-to-diaphragm connections were retrofitted, also retrofitting the diaphragm improved the PGA values beyond the threshold value because this prevented sliding of the wall-to-diaphragm connections. Here, retrofitting the diaphragm led to smaller average peak displacements in comparison to the model where only the connections, but not the diaphragm, were retrofitted.

These observations lead to two conclusions: (i) When designing a retrofitting intervention, increasing the shear stiffness of a diaphragm can produce a more favourable response for lower PGA levels but will only negligibly affect the limit states closer to collapse when the wall-to-diaphragm connection becomes the weak link; and (ii) When modelling unreinforced masonry buildings using the equivalent frame approach, it is necessary to explicitly model the wall-to-diaphragm connection, as simplification to a perfect connection might lead to an unrealistic box-type behaviour. This is particularly important if the equivalent frame model should capture both global in-plane as well as local out-of-plane failure modes.

In addition to further validations of this modelling approach against large-scale experimental results, future work should address the nonlinear response of retrofitted wall-to-diaphragm connections and the non-linear response of diaphragms.

## 6.6 Data availability

The OpenSEES models used for producing the results presented in this paper as well as the data with results of the calibration procedure and IDAs are shared openly through the repository DOI: 10.5281/zenodo.4659149.

## 6.7 Acknowledgments

We would like to express our gratitude to Ilaria Senaldi (EUCENTRE, Pavia, Italy) and Andrea Penna (University of Pavia, Italy) for providing the data of the experimental campaign as well as the equivalent frame models of Building 2 and 3.



## 7 Conclusions and future work

### 7.1 Conclusions

Past earthquakes have shown over and over again that historical unreinforced masonry buildings are vulnerable to seismic loading. To evaluate their seismic performance and to design retrofit interventions, researchers resort to models of various complexity. Independent on the modelling approach, the often limited knowledge available for historical structures requires that uncertainties are considered in the evaluation process. Uncertainties stem from the nature of the masonry as a heterogeneous material, connections between structural elements, and various structural details whose properties are ambiguous in existing buildings, where detailed inspection is often not possible. Another reason is the lack of experimental data, due to the cost and complexity of performing large-scale experimental campaigns.

There have been numerous shake-table experimental campaigns on unreinforced masonry buildings, but only one on unreinforced masonry aggregates prior to this work (Senaldi et al., 2019a; Guerrini et al., 2019). The lack of experimental data understandably led to the use of simplifying modelling assumptions with units of an aggregate usually modelled as separate or fully connected, by researchers and practitioners alike. Even if this approach can be conservative in terms of predicted PGA for reaching a certain limit state, it can mislead in the prediction of damage mechanisms and their location.

The recent development of a macroelement able to simulate both the in-plane and out-of-plane behaviour by Vanin et al. (2020a) opened the possibility to assess all key failure modes with the equivalent frame approach. However, at the same time, it opened new research questions, the most pressing being the modelling of nonlinear connections between structural elements. Their influence might have been secondary in the case of in-plane analyses, but with the out-of-plane included, modelling them as rigid introduces an unrealistic box behaviour, which is not something observed in the post-earthquake assessments or experimental campaigns.

This PhD dissertation aims at filling these gaps by:

- Shake-table testing of an unreinforced masonry aggregate at a large scale.
- Organizing and processing the results of a blind prediction competition to address uncertainties related to modelling masonry aggregates across different modelling approaches.
- Developing a new 3D material model for simulating the interaction between units of an aggregate in terms of separation, pounding and shear.
- Analyzing material and modelling uncertainties for dynamic analyses of unreinforced masonry buildings, and their influence on fragility, mode of failure, and location of damage.
- Understanding the influence that retrofitting flexible timber diaphragms and floor-to-wall connections exerts on the seismic behaviour, as well as the consequences of modelling such connections as rigid.

In the following, an overview of conclusions per chapter is reported.

#### **7.1.1 Shake table testing of a half-scale stone masonry aggregate**

- A shake-table test on a masonry aggregate was carried out, second in the literature and first to: (i) apply bidirectional loading, (ii) test an aggregate without interlocking stones, and (iii) detect significant interaction at the interface. All the raw data, functions used for post-processing, and processed data were made publicly available - allowing practitioners and researchers alike to benefit from the new data set to verify and calibrate their models.
- A significant interaction was detected both in the longitudinal and transversal directions. In the longitudinal directions units experienced both pounding and separation. The friction force influenced relative displacement between the units in the transversal direction at the interface - an interaction that was commonly ignored due to the lack of experimental data. After the new findings, we aim to change this practice.
- The principal damage mechanism observed - a soft storey mechanism at the second storey of the higher unit - was influenced by the interaction between the units, again justifying the need for accurate modelling of interaction at the interface. This highlights the flaws of modelling the units of an aggregate as separate or fully connected. Even if modelling units as separate or fully connected can lead to a conservative prediction of PGA for attaining a limit state, it can wrongly predict a damage mechanism. This finding is the first that contradicts the general practice of practitioners and engineers alike when modelling masonry aggregates.

### **7.1.2 Shake table testing of a stone masonry building aggregate: Overview of blind prediction study**

- This was among the only very few (to our knowledge three) blind prediction competitions on the seismic behaviour of unreinforced masonry buildings and (i) the first to address a building developing in-plane and out-of-plane failure modes, (ii) the first that applied bi-directional shaking as input, and (iii) the first on a masonry aggregate.
- Even if material uncertainties were eliminated by providing all the participants with material parameters, modelling uncertainties lead to a very large CoV compared even to previous studies: 160%-268% for displacement quantities and 58%-74% for base shears at the significant damage level. This point proves the complexity of modelling masonry aggregates and is the first such study to systematically question the modelling assumptions for this typology.
- It is concerning that the majority of the models underestimated the order of magnitude of displacements. Furthermore, a large scatter within the same modelling approach, or even software coming just from the modelling uncertainty points to the need to further calibrate the models and perform further experimental campaigns, or to embrace the uncertainty by adopting probabilistic approaches.

### **7.1.3 Uncertainties in modelling the seismic response of historical masonry aggregates: a prediction and postdiction using equivalent frame approach**

- This was the first numerical study to analyze the impact of modelling the units of an aggregate as (i) fully connected, (ii) separated, (iii) connected by 1D nonlinear springs, and (iv) connected by ND-non-linear springs, through nonlinear incremental bidirectional dynamic analyses. The study confirmed the experimental findings about the importance of modelling the interaction at the interface. The study proved that assumptions made with regard to the interaction at the interface influence both the seismic fragility and the type and location of the damage mechanism.
- To simulate and couple longitudinal and transversal interaction at the interface between units, the first 3D nonlinear material model for modelling the interface between the units of an aggregate within an equivalent frame approach was developed and implemented into OpenSEES software. The material model captures separation and pounding in the longitudinal direction, and couples axial force with the shear force to model the shear behaviour at the interface.
- Model calibration and validation proved that calibrating compressive strength and Young's modulus against vertical compression tests leads to the overestimation of those parameters. Instead, when these values are calibrated against the shear-compression tests, better predictions of dynamic behaviour are attained.

#### 7.1.4 Uncertainties in the seismic assessment of historical masonry buildings

- A new methodology to account for epistemic uncertainties was proposed and applied to two masonry buildings. Novelty is that it does not only account for the effect on seismic fragility but as well on the type and location of the damage mechanisms. The study found that including the out-of-plane behaviour of the newly developed macroelement has an important effect on seismic fragility, failure mode and location.
- The introduction of the out-of-plane behaviour in the equivalent frame approach opened a question on the importance of modelling non-linear connections. If the connections are modelled as rigid, the majority of out-of-plane mechanisms are nevertheless prevented. The impact of connection parameters was detected both on the failure PGA and the type and location of failure. Additionally, the study concluded that even if choosing conservative deterministic parameters aims at a conservative approximation of the PGA at failure, there is a realistic possibility of overlooking probable damage mechanisms and their location in the building. This can be problematic if the goal of the analysis is to design a retrofitting intervention.

#### 7.1.5 Unreinforced masonry buildings with timber diaphragms

- The study found that in the case of unreinforced masonry buildings with simply supported timber floors, strengthening the diaphragm alone only had an effect up to a threshold value of the PGA, where the capacity of the frictional wall-to-diaphragm connection was exceeded. For larger PGA levels, the seismic response of the building could only be improved if the wall-to-diaphragm connections were strengthened.
- These observations lead to two conclusions: (i) When designing a retrofitting intervention, increasing the shear stiffness of a diaphragm can produce a favourable response for lower PGA levels but will only slightly affect the limit states closer to collapse when the wall-to-diaphragm connection becomes the weak link; and (ii) When modelling unreinforced masonry buildings using the equivalent frame approach that can capture the out-of-plane behaviour, it is necessary to explicitly model the wall-to-diaphragm connection, as a simplification to a perfect connection can lead to an unrealistic box-type behaviour. This was the first study to directly raise this question which is often ignored when applying an equivalent frame approach. It should be noted, however, that only when the macroelement is able to capture the out-of-plane behaviour, does this question become relevant.

### 7.2 Future work

Based on the present and past work there are several further topics for which I see how they could benefit to more accurately predicting the seismic behaviour of masonry buildings and aggregates:

- Creating a new macroelement for spandrel elements. Such element would incorporate specific properties of spandrel elements such as the interlocking strength at the interlocking with piers, large drift limits, and spandrel-specific peak and residual force (Katrin Beyer, 2012; Katrin Beyer and Dazio, 2012; Katrin Beyer and Mangalathu, 2013).
- Due to a general tendency of models to produce too stiff behaviour, a step forward would be to advance from modelling nodal panels in equivalent frame models as rigid firstly as elastic, and then possibly also incorporating nonlinear behaviour.
- Even if floor-to-wall connections were thoroughly analyzed and accounted for, wall-to-wall connections which as well directly influence the box behaviour and out-of-plane behaviour are not sufficiently studied. In the present literature, there are no clear guidelines featuring mechanical formulation for calculating the strength and stiffness of these connections. Furthermore, in the equivalent frame approach, it is necessary to develop a new 3D material model accounting for frictional force. This step could be achieved by adapting a newly developed material model for simulating unit-to-unit connections in the aggregates.
- The second test on masonry aggregates performed as a part of this thesis is by far not enough to state that we have a satisfying amount of experimental data to fully understand the behaviour of the aggregates. What would be very beneficial for the future would be to test another aggregate, but this time with three units of different properties, or such a configuration that resembles a corner aggregate of a city block. Clearly, the such specimen will be very demanding to design while satisfying shake-table weight limitations. In order to do so it would be necessary to either further lower a scale, and risk difficulties with similitude laws, or to carefully optimize the geometry.
- Finally, having improved the understanding of the seismic behaviour of masonry aggregates, we ought to build upon newly acquired knowledge by designing new retrofitting solutions. By looking at aggregates as a whole, instead unit per unit we could design holistic solutions which could profit the communities due to possibly significantly lower cost of interventions.
- Having looked into the effects of retrofitting timber diaphragms and/or connections, it emerges that another typology which is widespread around Europe and the world are unreinforced masonry buildings with a concrete slab. Sometimes a slab was added in the previous decades as a part of reconstruction or retrofitting efforts. Often a topic of conflict between conservators and engineers, I believe this topic deserves a detailed insight numerically using the equivalent frame approach and newly developed macroelement able to simulate out-of-plane behaviour to understand both the positive and negative impacts of a concrete slab. Ideally, a shake-table test would accompany such analyses.



## Bibliography

- Addessi, Daniela, Alessandro Mastrandrea, and Elio Sacco (2014). “An equilibrated macro-element for nonlinear analysis of masonry structures”. In: *Engineering Structures* 70, pp. 82–93.
- Almeida, João P, Katrin Beyer, Roland Brunner, and Thomas Wenk (2020). “Characterization of mortar–timber and timber–timber cyclic friction in timber floor connections of masonry buildings”. In: *Materials and Structures* 53.3, pp. 1–14.
- AlShawa, Omar, Luigi Sorrentino, and Domenico Liberatore (2017). “Simulation of shake table tests on out-of-plane masonry buildings. Part (II): combined finite-discrete elements”. In: *International Journal of Architectural Heritage* 11.1, pp. 79–93.
- Angiolilli, Michele, Sergio Lagomarsino, Serena Cattari, and Stefania Degli Abbati (2021). “Seismic fragility assessment of existing masonry buildings in aggregate”. In: *Engineering Structures* 247, p. 113218.
- Aşıkoğlu, Abide, Graça Vasconcelos, Paulo B Lourenço, and Bartolomeo Pantò (2020). “Pushover analysis of unreinforced irregular masonry buildings: Lessons from different modeling approaches”. In: *Engineering Structures* 218, p. 110830.
- Atalić, Josip, Mario Uroš, Marta Šavor Novak, Marija Demšić, and Miroslav Nastev (2021). “The Mw5. 4 Zagreb (Croatia) earthquake of March 22, 2020: impacts and response”. In: *Bulletin of Earthquake Engineering* 19.9, pp. 3461–3489.
- Bartoli, Gianni et al. (2017). “Epistemic uncertainties in structural modeling: a blind benchmark for seismic assessment of slender masonry towers”. In: *Journal of Performance of Constructed Facilities* 31.5, p. 04017067.
- Belmouden, Y and P Lestuzzi (2009). “An equivalent frame model for seismic analysis of masonry and reinforced concrete buildings”. In: *Construction and Building Materials* 23.1, pp. 40–53. ISSN: 0950-0618. DOI: <https://doi.org/10.1016/j.conbuildmat.2007.10.023>. URL: <https://www.sciencedirect.com/science/article/pii/S0950061807002796>.
- Benedetti, D, P Carydis, and P Pezzoli (1998). “Shaking table tests on 24 simple masonry buildings”. In: *Earthquake engineering & structural dynamics* 27.1, pp. 67–90.
- Benedetti, D and V Petrini (1984). “On the seismic vulnerability of masonry buildings: an assessment method”. In: *L'industria delle Costruzioni* 149, pp. 66–74.
- Benedetti, D., P. Carydis, and P. Pezzoli (1998). “Shaking table tests on 24 simple masonry buildings”. In: *Earthquake Engineering & Structural Dynamics* 27.1, pp. 67–90.

- Berti, Manuel, Luca Salvatori, Maurizio Orlando, and Paolo Spinelli (2017). "Unreinforced masonry walls with irregular opening layouts: reliability of equivalent-frame modelling for seismic vulnerability assessment". In: *Bulletin of Earthquake Engineering* 15.3, pp. 1213–1239.
- Betti, Michele, Luciano Galano, and Andrea Vignoli (2014). "Comparative analysis on the seismic behaviour of unreinforced masonry buildings with flexible diaphragms". In: *Engineering Structures* 61, pp. 195–208. ISSN: 0141-0296. DOI: <https://doi.org/10.1016/j.engstruct.2013.12.038>. URL: <https://www.sciencedirect.com/science/article/pii/S0141029614000029>.
- (2015). "Time-history seismic analysis of masonry buildings: A comparison between two non-linear modelling approaches". In: *Buildings* 5.2, pp. 597–621.
- Beyer, Katrin (2012). "Peak and residual strengths of brick masonry spandrels". In: *Engineering Structures* 41, pp. 533–547.
- Beyer, Katrin and Alessandro Dazio (2012). "Quasi-static cyclic tests on masonry spandrels". In: *Earthquake Spectra* 28.3, pp. 907–929.
- Beyer, Katrin and Sujith Mangalathu (2013). "Review of strength models for masonry spandrels". In: *Bulletin of Earthquake Engineering* 11.2, pp. 521–542.
- Borri, Antonio and Marco Corradi (2019). "Architectural heritage: A discussion on conservation and safety". In: *Heritage* 2.1, pp. 631–647.
- Bothara, Jitendra K, Rajesh P Dhakal, and John B Mander (2010). "Seismic performance of an unreinforced masonry building: an experimental investigation". In: *Earthquake Engineering & Structural Dynamics* 39.1, pp. 45–68.
- Bracchi, S., M. Rota, A. Penna, and G. Magenes (Nov. 2015). "Consideration of modelling uncertainties in the seismic assessment of masonry buildings by equivalent-frame approach". In: *Bulletin of Earthquake Engineering* 13.11, pp. 3423–3448. ISSN: 1573-1456. DOI: 10.1007/s10518-015-9760-z. URL: <https://doi.org/10.1007/s10518-015-9760-z>.
- Brignola, Anna, Stefano Pampanin, and Stefano Podestà (2012). "Experimental evaluation of the in-plane stiffness of timber diaphragms". In: *Earthquake Spectra* 28.4, pp. 1687–1709.
- Brignola, Anna, Stefano Podesta, and S Pampanin (2008). "In-plane stiffness of wooden floor". In: *New Zealand Society of Earthquake Engineering (NZSEE) Conference, 11-13 Apr 2008*.
- Buckingham, Edgar (1914). "On physically similar systems; illustrations of the use of dimensional equations". In: *Physical review* 4.4, p. 345.
- Bui, Tan Trung and Ali Limam (2012). "Masonry walls under membrane or bending loading cases: experiments and discrete element analysis". In: *Civil-Comp Press*. BHV Topping, Paper-119.
- Calderoni, B, E Angela Cordasco, Antonio Sandoli, Vincenzo Onotri, and Giuseppe Tortoriello (2015). "Problematiche di modellazione strutturale di edifici in muratura esistenti soggetti ad azioni sismiche in relazione all'utilizzo di software commerciali". In: *Convegno ANIDIS "L'Ingegneria Sismica in Italia*, pp. 13–17.
- Caliò, Ivo, Massimo Marletta, and Bartolomeo Pantò (2012). "A new discrete element model for the evaluation of the seismic behaviour of unreinforced masonry buildings". In: *Engineering Structures* 40, pp. 327–338. ISSN: 0141-0296. DOI: <https://doi.org/10.1016/j.engstruct.2012.02.039>. URL: <https://www.sciencedirect.com/science/article/pii/S0141029612001162>.



## BIBLIOGRAPHY

---

- Carocci, Caterina F (2012). "Small centres damaged by 2009 L'Aquila earthquake: on site analyses of historical masonry aggregates". In: *Bulletin of earthquake engineering* 10.1, pp. 45–71.
- Cascini, Lucrezia, Raffaele Gagliardo, and Francesco Portioli (2018). "LiABlock\_3D: a software tool for collapse mechanism analysis of historic masonry structures". In: *International Journal of Architectural Heritage*.
- Cattari, Serena, B Calderoni, Ivo Calì, Guido Camata, Stefano de Miranda, Guido Magenes, Gabriele Milani, and Anna Sabetta (2021). "Nonlinear modeling of the seismic response of masonry structures: critical review and open issues towards engineering practice". In: *Bulletin of Earthquake Engineering*, pp. 1–59.
- Cattari, Serena and Guido Magenes (2022). "Benchmarking the software packages to model and assess the seismic response of unreinforced masonry existing buildings through nonlinear static analyses". In: *Bulletin of Earthquake Engineering* 20.4, pp. 1901–1936.
- Cattari, Serena et al. (2018). "A comparative study on a 2-storey benchmark case study through nonlinear seismic analysis". In: *Proceedings of the 16th European conference on earthquake engineering*, pp. 18–21.
- Cattari, Serena et al. (2019). "Discussion on data recorded by the Italian structural seismic monitoring network on three masonry structures hit by the 2016–2017 Central Italy earthquake". In: *Proc. of COMPDYN*.
- Ciocci, Maria Pia, Serena Van Nimwegen, Arash Askari, Francesco Vanin, Paulo Lourenço, and Katrin Beyer (2021). "Experimental investigation on the behaviour of injection anchors in rubble stone masonry". In: *in preparation*.
- Computers and Inc. Structures (2011). "SAP2000 v14. Integrated software for structural analysis and design". In.
- Contrafatto, L and R Cosenza (2014). "Prediction of the pull-out strength of chemical anchors in natural stone". In: *Frattura ed integrità strutturale* 8.29, pp. 196–208.
- Costa, Alexandre A, António Arêde, Alfredo Campos Costa, Andrea Penna, and António Costa (2013). "Out-of-plane behaviour of a full scale stone masonry façade. Part 2: shaking table tests". In: *Earthquake Engineering & Structural Dynamics* 42.14, pp. 2097–2111.
- Coutinho, Cristiano P, Antonio J Baptista, and Jose Dias Rodrigues (2016). "Reduced scale models based on similitude theory: A review up to 2015". In: *Engineering Structures* 119, pp. 81–94.
- Croci, Giorgio, A Viskovic, A Herzalla, M Erdik, M Akdoğan, Gerardo de Canio, and L Antonelli (2010). "Seismic assessment by numerical analyses and shaking table tests for complex masonry structures: the Hagia Irene case study". In: *Advanced Materials Research*. Vol. 133. Trans Tech Publ, pp. 777–782.
- D'Ayala, D and Elena Speranza (2003). "Definition of collapse mechanisms and seismic vulnerability of historic masonry buildings". In: *Earthquake Spectra* 19.3, pp. 479–509.
- D'Altri, Antonio Maria, Francesco Cannizzaro, Massimo Petracca, and Diego Alejandro Talledo (2022). "Nonlinear modelling of the seismic response of masonry structures: calibration strategies". In: *Bulletin of Earthquake Engineering* 20.4, pp. 1999–2043.

- Da Porto, F, M Munari, A Prota, and C Modena (2013). "M of clustered buildings: Case study of a block in the historic city centre of L'Aquila (Central Italy)". In: *Construction and building materials* 38, pp. 1221–1237.
- Data, STA (2008). "3muri". In: *Seismic calculation of masonry structures according to the Italian Ministerial Decree* 14.01.
- De Falco, Anna, Giulia Guidetti, Matteo Mori, and Giacomo Sevieri (2017). "Model uncertainties in seismic analysis of existing masonry buildings: the Equivalent-Frame Model within the Structural Element Models approach". In: *Proceedings of the XVII Convegno Anidis*. Pisa University Press, pp. 63–73.
- Degli Abbati, Stefania, Paolo Morandi, Serena Cattari, and Enrico Spacone (2022). "On the reliability of the equivalent frame models: the case study of the permanently monitored Pizzoli's town hall". In: *Bulletin of Earthquake Engineering* 20.4, pp. 2187–2217.
- DeJong, Matthew J, Beatrice Belletti, Max AN Hendriks, and Jan G Rots (2009). "Shell elements for sequentially linear analysis: lateral failure of masonry structures". In: *Engineering Structures* 31.7, pp. 1382–1392.
- DIANA, FEA (2017). "Diana User's Manual, Release 10.1". In: *DIANA FEA BV*.
- Dolce, M, FC Ponzo, A Goretti, C Moroni, F Giordano, G De Canio, and R Marnetto (2008). "3d dynamic tests on 2/3 scale masonry buildings retrofitted with different systems". In: *Proceedings of the 14th World Conference on Earthquake Engineering, Beijing, China*. Vol. 1217.
- Dolce, Mauro, Mario Nicoletti, Adriano De Sortis, Sara Marchesini, Daniele Spina, and Francesco Talanas (2017). "Osservatorio sismico delle strutture: the Italian structural seismic monitoring network". In: *Bulletin of Earthquake Engineering* 15.2, pp. 621–641.
- Dolce, Mauro, Felice Carlo Ponzo, M Di Croce, C Moroni, F Giordano, D Nigro, and R Marnetto (2009). "Experimental assessment of the CAM and DIS-CAM systems for the seismic upgrading of monumental masonry buildings". In: *Proceedings of the PROHITECH*. Vol. 9.
- Dolsek, Matjaz (2009). "Incremental dynamic analysis with consideration of modeling uncertainties". In: *Earthquake Engineering & Structural Dynamics* 38.6, pp. 805–825.
- EC 1995-1-1-2004 (2004). *Eurocode 5–Design of timber structures–Part 1-1: General rules and rules for buildings*. Tech. rep. prEN 1995-1-1. Bruxelles, Belgium, pp. 1–123.
- Esposito, Rita, Francesco Messali, Geert JP Ravenshorst, H Roel Schipper, and Jan G Rots (2019). "Seismic assessment of a lab-tested two-storey unreinforced masonry Dutch terraced house". In: *Bulletin of Earthquake Engineering* 17.8, pp. 4601–4623.
- EUCENTRE (2009a). *PROVINO 1 0.40g 20090801 telecamera 01*. <https://youtu.be/SspFD-nHCso?list=PL52352538BE37F38E>. Accessed: 2021-04-02.
- (2009b). *PROVINO 1 0.40g 20090801 telecamera 03*. <https://youtu.be/egYnpB1FlK0?list=PL52352538BE37F38E>. Accessed: 2021-04-02.
- (2009c). *PROVINO 1 0.40g 20090801 Vista Multipla*. <https://youtu.be/7BFuXzrAbG0?list=PL52352538BE37F38E>. Accessed: 2021-04-02.
- European Committee for Standardization Bruxelles, Belgium (2005). "EN 1998-3. Eurocode 8: Design of structures for earthquake resistance - Part 3: Assessment and retrofitting of buildings." In.

## BIBLIOGRAPHY

---

- Faria, Rui, J Oliver, and M Cervera (1998). "A strain-based plastic viscous-damage model for massive concrete structures". In: *International journal of solids and structures* 35.14, pp. 1533–1558.
- Formisano, A, C Castaldo, and FM Mazzolani (2013). "Non-linear analysis of masonry building compounds: a comparison of numerical and theoretical results". In: *Civil-Comp Proceedings* 102.
- Formisano, Antonio (2017). "Theoretical and numerical seismic analysis of masonry building aggregates: case studies in San Pio Delle Camere (L'Aquila, Italy)". In: *Journal of Earthquake Engineering* 21.2, pp. 227–245.
- Formisano, Antonio, Gilda Florio, Raffaele Landolfo, and Federico M Mazzolani (2015). "Numerical calibration of an easy method for seismic behaviour assessment on large scale of masonry building aggregates". In: *Advances in Engineering Software* 80, pp. 116–138.
- Formisano, Antonio and Alfredo Massimilla (2018). "A novel procedure for simplified nonlinear numerical modeling of structural units in masonry aggregates". In: *International Journal of Architectural Heritage* 12.7-8, pp. 1162–1170.
- Fragiadakis, Michalis and Dimitrios Vamvatsikos (2010). "Fast performance uncertainty estimation via pushover and approximate IDA". In: *Earthquake Engineering & Structural Dynamics* 39.6, pp. 683–703.
- Freeman, Sigmund A (1998). "The capacity spectrum method as a tool for seismic design". In: *Proceedings of the 11th European conference on earthquake engineering*. Citeseer, pp. 6–11.
- Gattesco, N, L Macorini, and F Benussi (2007). "Retrofit of wooden floors for the seismic adjustment of historical buildings with high reversible techniques. Seismic Engineering in Italy". In: *Proc. Of the XII National Conference, Pisa*, pp. 10–14.
- Giamundo, V, Vasilis Sarhosis, GP Lignola, Y Sheng, and G Manfredi (2014). "Evaluation of different computational modelling strategies for the analysis of low strength masonry structures". In: *Engineering Structures* 73, pp. 160–169.
- Grande, Ernesto, Maura Imbimbo, and Elio Sacco (2013). "Finite element analysis of masonry panels strengthened with FRPs". In: *Composites Part B: Engineering*. DOI: 10.1016/j.compositesb.2012.09.002.
- Grünthal, Gottfried (1998). *European macroseismic scale 1998*. Tech. rep. European Seismological Commission (ESC).
- Guerrini, Gabriele, Ilaria Senaldi, Francesco Graziotti, Guido Magenes, Katrin Beyer, and Andrea Penna (2019). "Shake-table test of a strengthened stone masonry building aggregate with flexible diaphragms". In: *International Journal of Architectural Heritage* 13.7, pp. 1078–1097.
- Guerrini, Gabriele, Ilaria Senaldi, Simone Scherini, Simone Morganti, and Guido Magenes (2017). "Material characterization for the shaking-table test of the scaled prototype of a stone masonry building aggregate". In: *Material characterization for the shaking-table test of the scaled prototype of a stone masonry building aggregate*, pp. 105–115.
- Heyman, Jacques (1966). "The stone skeleton". In: *International Journal of solids and structures* 2.2, pp. 249–279.

- Housner, George W (1963). "The behavior of inverted pendulum structures during earthquakes". In: *Bulletin of the Seismological Society of America* 53.2, pp. 403–417.
- ICOMOS, Introducing and ICOMOS Mission (1994). "About Icomos". In: *NATIONAL GEOGRAPHIC* 1983.1993.
- Itasca, U (2013). "3DEC—3 Dimensional Distinct Element Code, Ver. 5.2". In: *Itasca Consulting Group Inc., Minneapolis*.
- Jo, Hallquist (2006). "Ls-dyna theory manual". In: *Livermore software technology corporation*.
- Kallioras, Stylianos, Gabriele Guerrini, Umberto Tomassetti, Beatrice Marchesi, Andrea Penna, Francesco Graziotti, and Guido Magenes (2018). "Experimental seismic performance of a full-scale unreinforced clay-masonry building with flexible timber diaphragms". In: *Engineering Structures* 161, pp. 231–249.
- Kappos, Andreas J, Gregory G Penelis, and Christos G Drakopoulos (2002). "Evaluation of simplified models for lateral load analysis of unreinforced masonry buildings". In: *Journal of Structural Engineering* 128.7, pp. 890–897.
- Kim, Sang-Cheol and Donald W White (2004). "Nonlinear analysis of a one-story low-rise masonry building with a flexible diaphragm subjected to seismic excitation". In: *Engineering Structures* 26.14, pp. 2053–2067.
- Krawinkler, H and PD Moncarz (1981). "Theory and application of experimental model analysis in earthquake engineering". In: *NASA STI/Recon Technical Report N 82*, p. 18430.
- Lagomarsino, Sergio, Daniela Camilletti, Serena Cattari, and Salvatore Marino (2018). "Seismic assessment of existing irregular masonry buildings by nonlinear static and dynamic analyses". In: *European Conference on Earthquake Engineering Thessaloniki, Greece*. Springer, pp. 123–151.
- Lagomarsino, Sergio and Serena Cattari (2015). "PERPETUATE guidelines for seismic performance-based assessment of cultural heritage masonry structures". In: *Bulletin of Earthquake Engineering* 13.1, pp. 13–47.
- Lagomarsino, Sergio, Andrea Penna, Alessandro Galasco, and Serena Cattari (2013). "TREMURI program: an equivalent frame model for the nonlinear seismic analysis of masonry buildings". In: *Engineering structures* 56, pp. 1787–1799.
- Lourenco, Paulo B. and Luís C. Silva (2020). "Computational applications in masonry structures: from the meso-scale to the super-large/super-complex". In: *International Journal for Multiscale Computational Engineering* 18.1, pp. 1–30. ISSN: 1543-1649.
- Lourenço, Paulo B (2002). "Computations on historic masonry structures". In: *Progress in Structural Engineering and Materials* 4.3, pp. 301–319.
- (2013). "Computational strategies for masonry structures: multi-scale modeling, dynamics, engineering applications and other challenges". In.
- Lourenço, Paulo José Brandão Barbosa (1997). "Computational strategies for masonry structures." In.
- Luzi, Lucia, R Puglia, E Russo, and WG 5 ORFEUS (2016). "Engineering strong motion database, version 1.0". In: *Istituto Nazionale di Geofisica e Vulcanologia, Observatories & Research Facilities for European Seismology*. doi 10.

## BIBLIOGRAPHY

---

- Magenes, G, GM Calvi, and GR Kingsley (1995). "Seismic Testing of a Full-Scale, Two-Story Masonry Building: Test Procedure and Measured Experimental". In.
- Magenes, G and AD Fontana (1998). "Simplified non-linear seismic analysis of masonry buildings". In: *Proc. Br. Masonry Soc. No. 8*, pp. 190–195.
- Magenes, G, PB Lourenço, and S Cattari (2018). "Special Session 18. Seismic modeling of masonry buildings: present knowledge and open challenges for research and practice". In: *Proceedings of the 16th European Conference on Earthquake Engineering, Thessaloniki, Greece*, pp. 18–21.
- Magenes, G, A Penna, and A Galasco (2010). "A full-scale shaking table test on a two-storey stone masonry building". In: *14th European Conference on Earthquake Engineering*. Vol. 30.
- Magenes, Guido, Andrea Penna, Ilaria Senaldi, Maria Rota, and Alessandro Galasco (2014). "Shaking table test of a strengthened full-scale stone masonry building with flexible diaphragms". In: *International Journal of Architectural Heritage* 8.3, pp. 349–375.
- Maio, Rui, Romeu Vicente, Antonio Formisano, and Humberto Varum (2015). "Seismic vulnerability of building aggregates through hybrid and indirect assessment techniques". In: *Bulletin of Earthquake Engineering* 13.10, pp. 2995–3014.
- Malcata, Madalena, Madalena Ponte, Simone Tiberti, Rita Bento, and Gabriele Milani (2020). "Failure analysis of a Portuguese cultural heritage masterpiece: Bonet building in Sintra". In: *Engineering Failure Analysis* 115, p. 104636.
- Malomo, D and MJ DeJong (2021). "A Macro-Distinct Element Model (M-DEM) for out-of-plane analysis of unreinforced masonry structures". In: *Engineering Structures* 244, p. 112754.
- Mann, W et al. (1982). "Failure of shear-stressed masonry: an enlarged theory, tests and application to shear walls". In.
- Marc, MSC (2008). "Manual Volume A-Theory and User Information". In.
- Marques, Rui and Paulo B Lourenço (2011). "Possibilities and comparison of structural component models for the seismic assessment of modern unreinforced masonry buildings". In: *Computers & Structures* 89.21-22, pp. 2079–2091.
- Mazzon, Nicola, Cano M. Chavez, Maria Rosa Valluzzi, F. Casarin, and Claudio Modena (Oct. 2010). "Shaking Table Tests on Multi-Leaf Stone Masonry Structures: Analysis of Stiffness Decay". In: *Structural Analysis of Historic Constructions*. Vol. 133. Advanced Materials Research. Trans Tech Publications Ltd, pp. 647–652. DOI: 10.4028/www.scientific.net/AMR.133-134.647.
- Mazzoni, Silvia et al. (2018). "2016–2017 Central Italy earthquake sequence: seismic retrofit policy and effectiveness". In: *Earthquake Spectra* 34.4, pp. 1671–1691.
- McKenna, Frank, GL Fenves, MH Scott, and B Jeremic (2000). *Open system for earthquake engineering simulation (OpenSees)*. Tech. rep. University of California, Berkeley, CA. URL: <http://opensees.berkeley.edu>.
- Mendes, Nuno et al. (2017). "Methods and approaches for blind test predictions of out-of-plane behavior of masonry walls: A numerical comparative study". In: *International Journal of Architectural Heritage* 11.1, pp. 59–71.
- Metropolis, Nicholas and Stanislaw Ulam (1949). "The Monte Carlo method". In: *Journal of the American Statistical Association* 44.247, pp. 335–341.

- Michel, Clotaire, Amin Karbassi, and Pierino Lestuzzi (2018). "Evaluation of the seismic retrofitting of an unreinforced masonry building using numerical modeling and ambient vibration measurements". In: *Engineering Structures* 158, pp. 124–135.
- Mirra, Michele (2017). "Analisi parametriche dinamiche non lineari degli effetti dell' irrigidimento di solai in legno in edifici in muratura ordinaria". In.
- Moreira, Susana Maria Trindade (2015). "Seismic retrofit of masonry-to-timber connections in historical constructions". PhD thesis. Universidade do Minho (Portugal).
- Moreira, Susana Maria Trindade, Daniel V Oliveira, Luis F Ramos, Raquel Fernandes, João Guerreiro, and Paulo B Lourenço (2012). "Experimental study on the seismic behavior of masonry wall-to-floor connections". In: *Proceedings of the 15th World Conference on Earthquake Engineering*. Lisbon, Portugal: Sociedade Portuguesa de Engenharia Sismica (SPES).
- Mouzakis, Charalambos, Chrissy-Elpida Adami, Lucia Karapitta, and Elizabeth Vintzileou (2018). "Seismic behaviour of timber-laced stone masonry buildings before and after interventions: shaking table tests on a two-storey masonry model". In: *Bulletin of Earthquake Engineering* 16.2, pp. 803–829.
- Muñoz, Rosana, Paulo B Lourenço, and Susana Moreira (2018). "Experimental results on mechanical behaviour of metal anchors in historic stone masonry". In: *Construction and Building Materials* 163, pp. 643–655.
- Nakamura, Yasuto, Hossein Derakhshan, Michael C Griffith, Guido Magenes, and Abdul H Sheikh (2017a). "Applicability of nonlinear static procedures for low-rise unreinforced masonry buildings with flexible diaphragms". In: *Engineering Structures* 137, pp. 1–18.
- Nakamura, Yasuto, Hossein Derakhshan, Guido Magenes, and Michael C Griffith (2017b). "Influence of diaphragm flexibility on seismic response of unreinforced masonry buildings". In: *Journal of Earthquake Engineering* 21.6, pp. 935–960.
- Ortega, Javier, Graça Vasconcelos, Hugo Rodrigues, and Mariana Correia (Sept. 2018). "Assessment of the influence of horizontal diaphragms on the seismic performance of vernacular buildings". In: *Bulletin of Earthquake Engineering* 16.9, pp. 3871–3904. ISSN: 1573-1456. DOI: 10.1007/s10518-018-0318-8. URL: <https://doi.org/10.1007/s10518-018-0318-8>.
- Parisi, Fulvio and Nicola Augenti (2013). "Seismic capacity of irregular unreinforced masonry walls with openings". In: *Earthquake Engineering & Structural Dynamics* 42.1, pp. 101–121.
- Parisse, Francesco et al. (2021). "Benchmarking the seismic assessment of unreinforced masonry buildings from a blind prediction test". In: *Structures*. Vol. 31. Elsevier, pp. 982–1005.
- Pasticier, Laurent, Claudio Amadio, and Massimo Fragiaco (2008). "Non-linear seismic analysis and vulnerability evaluation of a masonry building by means of the SAP2000 V. 10 code". In: *Earthquake Engineering & Structural Dynamics* 37.3, pp. 467–485.
- Penna, Andrea, Sergio Lagomarsino, and Alessandro Galasco (2014a). "A nonlinear macroelement model for the seismic analysis of masonry buildings". In: *Earthquake Engineering & Structural Dynamics* 43.2, pp. 159–179.
- Penna, Andrea, Paolo Morandi, Maria Rota, Carlo Filippo Manzini, Francesca da Porto, and Guido Magenes (Oct. 2014b). "Performance of masonry buildings during the Emilia 2012

## BIBLIOGRAPHY

---

- earthquake". In: *Bulletin of Earthquake Engineering* 12.5, pp. 2255–2273. ISSN: 1573-1456. DOI: 10.1007/s10518-013-9496-6. URL: <https://doi.org/10.1007/s10518-013-9496-6>.
- Penna, Andrea, Maria Rota, Amaryllis Mouyiannou, and Guido Magenes (2013). "Issues on the use of time-history analysis for the design and assessment of masonry structures". In: *Proc. COMPDYN2013*.
- Penna, Andrea, Ilaria Enrica Senaldi, Alessandro Galasco, and Guido Magenes (2016). "Numerical simulation of shaking table tests on full-scale stone masonry buildings". In: *International Journal of Architectural Heritage* 10.2-3, pp. 146–163.
- Peruch, Matteo, Enrico Spacone, and Guido Camata (2019). "Nonlinear analysis of masonry structures using fiber-section line elements". In: *Earthquake Engineering & Structural Dynamics* 48.12, pp. 1345–1364.
- Pfyl-Lang, Kerstin, Friederike Braune, Pierino Lestuzzi, and Tragverhalten von unbewehrten Mauerwerkswänden (2009). *Erdbebenverhalten von unbewehrtem Mauerwerk—eine SIA Dokumentation*. Tech. rep.
- Pitilakis, Dimitris, Konstantinos Iliou, and Anna Karatzetzou (2018). "Shaking table tests on a stone masonry building: modeling and identification of dynamic properties including soil-foundation-structure interaction". In: *International Journal of Architectural Heritage* 12.6, pp. 1019–1037. DOI: 10.1080/15583058.2018.1431729. URL: <https://doi.org/10.1080/15583058.2018.1431729>.
- POLIMI (2010). *Critical review of methodologies and tools for assessment of failure mechanisms and interventions, Deliverable 3.3, Workpackage 3: Damage based selection of technologies*. Tech. rep. NIKER Project, Italy.
- Pulatsu, Bora, Ece Erdogmus, Paulo B Lourenço, Jose V Lemos, and Kagan Tuncay (2020). "Simulation of the in-plane structural behavior of unreinforced masonry walls and buildings using DEM". In: *Structures*. Vol. 27. Elsevier, pp. 2274–2287.
- Quagliarini, E, G Maracchini, and F Clementi (2017). "Uses and limits of the Equivalent Frame Model on existing unreinforced masonry buildings for assessing their seismic risk: A review". In: *Journal of Building Engineering* 10, pp. 166–182.
- Raka, Eva, Enrico Spacone, Vincenzo Sepe, and Guido Camata (2015). "Advanced frame element for seismic analysis of masonry structures: model formulation and validation". In: *Earthquake Engineering & Structural Dynamics* 44.14, pp. 2489–2506.
- Rathje, Ellen M et al. (2017). "DesignSafe: New cyberinfrastructure for natural hazards engineering". In: *Natural Hazards Review* 18.3, p. 06017001.
- Rizzano, Gianvittorio and Riccardo Sabatino (2010). "An equivalent frame model for the seismic analysis of masonry structures". In: *Proceedings of the 8th Congresso de Sismologia e Engenharia Sismica*.
- Roca, Pere, Miguel Cervera, Giuseppe Gariup, and Luca Pela (2010). "Structural analysis of masonry historical constructions. Classical and advanced approaches". In: *Archives of computational methods in engineering* 17.3, pp. 299–325.
- Roca, Pere, Climent Molins, and Antonio Mari (2005). "Strength capacity of masonry wall structures by the equivalent frame method". In: *Journal of structural engineering* 131.10, pp. 1601–1610.

- Rota, M, A Penna, and G Magenes (2014). "A framework for the seismic assessment of existing masonry buildings accounting for different sources of uncertainty". In: *Earthquake Engineering & Structural Dynamics* 43.7, pp. 1045–1066.
- Ruggieri, Sergio, Chiara Tosto, Giulia Rosati, Giuseppina Uva, and Giuseppe Andrea Ferro (2020). "Seismic Vulnerability Analysis of Masonry Churches in Piemonte after 2003 Valle Scrivia Earthquake: Post-event Screening and Situation 17 Years Later". In: *International Journal of Architectural Heritage* 0.0, pp. 1–29. DOI: 10.1080/15583058.2020.1841366. eprint: <https://doi.org/10.1080/15583058.2020.1841366>. URL: <https://doi.org/10.1080/15583058.2020.1841366>.
- Salonikios, T, C Karakostas, V Lekidis, and A Anthoine (2003). "Comparative inelastic pushover analysis of masonry frames". In: *Engineering Structures* 25.12, pp. 1515–1523.
- Saloustros, Savvas, Luca Pelà, Francesca R Contrafatto, Pere Roca, and Ioannis Petromichelakis (2019). "Analytical derivation of seismic fragility curves for historical masonry structures based on stochastic analysis of uncertain material parameters". In: *International Journal of Architectural Heritage* 13.7, pp. 1142–1164.
- Scotta, Roberto, Davide Trutalli, Luca Marchi, and Luca Pozza (2016). "Effects of in-plane strengthening of timber floors in the seismic response of existing masonry buildings". In: *World Conference on Timber Engineering (WCTE)*, pp. 22–25.
- Scotta, Roberto, Davide Trutalli, Luca Marchi, Luca Pozza, and Michele Mirra (2017). "Seismic response of masonry buildings with alternative techniques for in-plane strengthening of timber floors". In: *XII International Conference on Structural Repair and Rehabilitation (CINPAR)*, pp. 26–29.
- Senaldi, Ilaria, Gabriele Guerrini, Martina Caruso, Francesco Graziotti, Guido Magenes, Katrin Beyer, and Andrea Penna (2019a). "Experimental seismic response of a half-scale stone masonry building aggregate: effects of retrofit strategies". In: *Structural Analysis of Historical Constructions*. Springer, pp. 1372–1381.
- Senaldi, Ilaria, Gabriele Guerrini, Paolo Comini, Francesco Graziotti, Andrea Penna, Katrin Beyer, and Guido Magenes (2020). "Experimental seismic performance of a half-scale stone masonry building aggregate". In: *Bulletin of Earthquake Engineering* 18.2, pp. 609–643.
- Senaldi, Ilaria, Gabriele Guerrini, Simone Scherini, Simone Morganti, Guido Magenes, Katrin Beyer, and Andrea Penna (2018). "Natural stone masonry characterization for the shaking-table test of a scaled building specimen". In: *Proceedings of the 10th international masonry conference, Milan, Italy*, pp. 9–11.
- Senaldi, Ilaria, Gabriele Guerrini, Marco Solenghi, Francesco Graziotti, and Andrea Penna (2019b). "Numerical modelling of the seismic response of a half-scale stone masonry aggregate prototype". In: *Numerical modelling of the seismic response of a half-scale stone masonry aggregate prototype*, pp. 127–135.
- Senaldi, Ilaria, Guido Magenes, and Andrea Penna (2010). "Numerical investigations on the seismic response of masonry building aggregates". In: *Advanced materials research*. Vol. 133. Trans Tech Publ, pp. 715–720.
- Senaldi, Ilaria, Guido Magenes, Andrea Penna, Alessandro Galasco, and Maria Rota (2014). "The effect of stiffened floor and roof diaphragms on the experimental seismic response of a



## BIBLIOGRAPHY

---

- full-scale unreinforced stone masonry building". In: *Journal of earthquake engineering* 18.3, pp. 407–443.
- Siano, Rossella, Pere Roca, Guido Camata, Luca Pelà, Vincenzo Sepe, Enrico Spacone, and Massimo Petracca (2018). "Numerical investigation of non-linear equivalent-frame models for regular masonry walls". In: *Engineering Structures* 173, pp. 512–529.
- Siano, Rossella, Vincenzo Sepe, Guido Camata, Enrico Spacone, Pere Roca, and Luca Pelà (2017). "Analysis of the performance in the linear field of equivalent-frame models for regular and irregular masonry walls". In: *Engineering Structures* 145, pp. 190–210.
- Smith, Michael (2009). "ABAQUS/Standard User's Manual, Version 6.9". In.
- Solarino, Fabio, Daniel V Oliveira, and Linda Giresini (2019). "Wall-to-horizontal diaphragm connections in historical buildings: A state-of-the-art review". In: *Engineering Structures* 199, p. 109559.
- Stavroulaki, Maria E (2019). "Dynamic Behavior of Aggregated Buildings With Different Floor Systems and Their Finite Element Modeling". In: *Frontiers in Built Environment* 5, p. 138.
- Stein, Michael (1987). "Large sample properties of simulations using Latin hypercube sampling". In: *Technometrics* 29.2, pp. 143–151.
- Stojadinović, Zoran, Miloš Kovačević, Dejan Marinković, and Božidar Stojadinović (2022). "Rapid earthquake loss assessment based on machine learning and representative sampling". In: *Earthquake Spectra* 38.1, pp. 152–177.
- Sullivan, Timothy J, Rui Pinho, and Alberto Pavese (2004). "An Introduction to Structural Testing Techniques". In: *Earthquake Engineering Research Report Rose School* 1.
- Tomazevic, Miha (1999). *Earthquake-resistant design of masonry buildings*. Vol. 1. World Scientific.
- Tomažević, M (1978). "The computer program POR". In: *Report ZRMK* 846.
- Tomažević, Miha, Polona Weiss, and Tomaž Velechovsky (1991a). *The influence of rigidity of floors on the seismic behaviour of old stone-masonry buildings*.
- (1991b). "The influence of rigidity of floors on the seismic behaviour of old stone-masonry buildings". In: *European Earthquake Engineering* 3, pp. 28–41.
- Tomić, Igor, A Penna, M DeJong, et al. (2022a). "Shake-table testing of a half-scale stone masonry building". In: *Submitted to Bulletin of Earthquake Engineering*.
- (2022b). "Shake-table testing of a stone masonry building aggregate: Overview of blind prediction study". In: *Submitted to Bulletin of Earthquake Engineering*.
- Tomić, Igor, Francesco Vanin, and Katrin Beyer (2021). "Uncertainties in the seismic assessment of historical masonry buildings". In: *Applied Sciences* 11.5, p. 2280.
- Tondelli, Marco, Maria Rota, Andrea Penna, and Guido Magenes (2012). "Evaluation of uncertainties in the seismic assessment of existing masonry buildings". In: *Journal of Earthquake Engineering* 16.sup1, pp. 36–64.
- Trutalli, Davide, Luca Marchi, Roberto Scotta, and Luca Pozza (2017). "Dynamic simulation of an irregular masonry building with different rehabilitation methods applied to timber floors". In: *Proceedings of the 6th ECCOMAS Thematic Conference (COMPDYN 2017), Rhodes Island, Greece*, pp. 15–17.

- Turnšek, V and F Cacovic (1971). "Some experimental results on the strength of brick masonry walls". In: *Proceedings of the 2nd international brick masonry conference*. British Ceramic Research Association Stoke-on-Trent, UK, pp. 149–156.
- Turnšek Vand Sheppard, Peter (1980). *The shear and flexural resistance of masonry walls*.
- Vamvatsikos, Dimitrios and C Allin Cornell (2002). "Incremental dynamic analysis". In: *Earthquake Engineering & Structural Dynamics* 31.3, pp. 491–514.
- Vamvatsikos, Dimitrios and Michalis Fragiadakis (2010). "Incremental dynamic analysis for estimating seismic performance sensitivity and uncertainty". In: *Earthquake Engineering & Structural Dynamics* 39.2, pp. 141–163.
- Vanin, Francesco and K Beyer (2022). "Equivalent damping ratio for a macroelement modelling the out-of-plane response of masonry walls". In: *In preparation*.
- Vanin, Francesco and Katrin Beyer (2018). "Application of a point estimate method for incorporating the epistemic uncertainty in the seismic assessment of a masonry building". In: *16th European Conference on Earthquake Engineering*.
- (2021). "Equivalent damping ratio for a macroelement modelling the out-of-plane response of masonry walls". In: *In preparation*.
- Vanin, Francesco, Andrea Penna, and Katrin Beyer (2020a). "A three-dimensional macroelement for modelling the in-plane and out-of-plane response of masonry walls". In: *Earthquake Engineering & Structural Dynamics* 49.14, pp. 1365–1387.
- (2020b). "Equivalent-frame modeling of two shaking table tests of masonry buildings accounting for their out-of-plane response". In: *Frontiers in Built Environment* 6, p. 42.
- Vanin, Francesco, João Saraiva Esteves Pacheco de Almeida, and Katrin Beyer (2017a). "Force-based finite element for modelling the cyclic behaviour of unreinforced masonry piers". In: *Proceedings of the 16th World Conference on Earthquake Engineering*. CONF.
- Vanin, Francesco, Dario Zaganelli, Andrea Penna, and Katrin Beyer (2017b). "Estimates for the stiffness, strength and drift capacity of stone masonry walls based on 123 quasi-static cyclic tests reported in the literature". In: *Bulletin of Earthquake Engineering* 15.12, pp. 5435–5479.
- Vasconcelos, Graça (2005). "Experimental investigations on the mechanics of stone masonry: Characterization of granites and behavior of ancient masonry shear walls". In: *In preparation*.
- Vintzileou, Elizabeth, Charalambos Mouzakis, Chrissy-Elpida Adami, and Lucia Karapitta (Oct. 2015). "Seismic behavior of three-leaf stone masonry buildings before and after interventions: Shaking table tests on a two-storey masonry model". In: *Bulletin of Earthquake Engineering* 13.10, pp. 3107–3133. ISSN: 1573-1456. DOI: 10.1007/s10518-015-9746-x. URL: <https://doi.org/10.1007/s10518-015-9746-x>.
- Vořechovský, M and D Novák (2003). "Statistical correlation in stratified sampling". In: *Proc. of 9th Int. Conf. on Applications of Statistics and Probability in Civil Engineering-ICASP*. Vol. 9. Citeseer, pp. 119–124.
- Walter, Rasmus, John Forbes Olesen, and Henrik Stang (2005). "Interface mixed mode model". In: *Proceedings of 11th International Conference on Fracture*, pp. 20–25.
- Wenk, Thomas (2014). "Die neue Norm SIA 269/8 Erhaltung von Tragwerken-Erdbeben". In: *D-A-CH-Mitteilungsblatt-Erdbebeningenieurwesen und Baudynamik* 89, pp. 2–5.

## BIBLIOGRAPHY

---

- Wilding, Bastian Valentin, Michele Godio, and Katrin Beyer (2020). "The ratio of shear to elastic modulus of in-plane loaded masonry". In: *Materials and Structures* 53.2, pp. 1–18.
- Yousefi, Behrooz and Masoud Soltani (2019). "An Equivalent Fiber Frame Model for Nonlinear Analysis of Masonry Structures". In: *International Journal of Architectural Heritage*, pp. 1–25.
- Zhang, Shenghan, Seyedeh Mohadeseh Taheri Mousavi, Nicolas Richart, Jean-François Molinari, and Katrin Beyer (2017). "Micro-mechanical finite element modeling of diagonal compression test for historical stone masonry structure". In: *International Journal of Solids and Structures* 112, pp. 122–132. DOI: 10.1016/j.ijsolstr.2017.02.014. URL: <https://doi.org/10.1016/j.ijsolstr.2017.02.014>.
- Zheng, Da, Fang-zhou Liu, Neng-pan Ju, J David Frost, and Run-qiu Huang (2016). "Cyclic load testing of pre-stressed rock anchors for slope stabilization". In: *Journal of Mountain Science* 13.1, pp. 126–136.
- Zuccaro, G., F.L. Perelli, D. De Gregorio, and Francesco Cacace (2020). "Empirical vulnerability curves for Italian masonry buildings: evolution of vulnerability model from the DPM to curves as a function of acceleration". In: *Bulletin of Earthquake Engineering*. DOI: <https://doi.org/10.1007/s10518-020-00954-5>.

## CURRICULUM VITAE

**Name:** Igor  
**Surname:** Tomić  
**Phone/mobile:** +385911779792  
**Date of birth:** 21<sup>st</sup> March 1992  
**Marital status:** single  
**E-mail:** igtomic@gmail.com



### Education/qualification

1998 - 2006 attended elementary school Bol, grade point average: 5.0  
2006 - 2010 attended Natural Sciences and Mathematical high school in Split, the best high school in Croatia according to state graduation test, graduated with excellent score  
2010 - 2013 Undergraduate studies in Civil Engineering, 1<sup>st</sup> place on the enrolment list, grade point average: 4,07 (5% of the best students)  
2013 Graduated bachelor with thesis "Calculation of the bearing structure of residential building"  
2013 - 2015 Graduate studies at the Faculty of Civil Engineering and Architecture- general track. 1<sup>st</sup> place on the enrolment list, grade point average: 4,37 (5% of the best students)  
2015 Graduated Master with thesis "Recession analysis of Opačac spring (Visual Basic Spreadsheet Macro)"  
2015 - 2016 Postgraduate MSc Advanced Master Study in Structural Analysis of Historical Constructions at Czech Technical University in Prague and Polytechnic University of Catalonia in Barcelona  
2016 Finished Postgraduate MSc study in Barcelona with dissertation "Application of the laser scan technique to support the structural assessment of existing constructions", grade 9.5/10  
2018 - 2022 Doctoral studies at Swiss Federal Institute of Technology in Lausanne (EPFL) on the topic of Experimental and numerical research on unreinforced masonry buildings

### Other activities

2014 - 2015 President of the Student Council of Faculty of Civil Engineering, Architecture and Geodesy  
2014 - 2015 Coordinator of the University Student Council for International Cooperation  
2012 - 2015 Students' rights defender of Faculty of Civil Engineering, Architecture and Geodesy  
2014 Founder of IACES LC Split  
2015 - 2016 Student representative in Senate of University of Split  
2016 - Global Shapers Zagreb Hub Member  
2020 - ICOMOS Croatia Board Member  
2022 - The Explorers Club Member

### Awards and Scholarships:

2010 - 2015 Scholarship of city of Split for especially gifted students  
2015 - 2016 Scholarship of SAHC consortium for attendance of Advanced Master  
2015 - 2016 Scholarship of SPEGRA engineering ltd. for attendance of Advanced Master  
2016 Rector's award for excellence at University of Split for academic year 2014/15  
2016 Dean's award for excellence at Czech Technical University for academic year 2015/16

### Professional education

#### Participation in European projects:

2013 YiA „Educate your mind & train your body“, Struga, Macedonia – Croatian group leader  
2014 TC „Gender equality“, Yerevan, Armenia – Croatian group leader

### Work experience

2011 - 2015 demonstrator in the course Mechanics 1  
2012 - 2014 demonstrator in the course Hydromechanics  
2011 - 2015 work in construction activities - legalization and energy certificates  
2006 - 2013 work in service activities (catering industry, travel agency, survey)  
2013 participated in the series "Game of thrones"  
2014 work in FC "Hajduk Split" department for membership  
2015 - 2017 work in "Spegra inženjering d.o.o.", special construction works  
2018 - Doctoral assistant in the Earthquake Engineering and Structural Dynamics laboratory of Swiss Federal Institute of Technology in Lausanne

#### Other skills and competencies

Knowledge of computer programmes MS Office, Adobe Photoshop, AutoCAD and expert programmes (Scia Engineering, Rockscience packet, ADINA, OpenSEES...)

Programming in HTML, C++, Python program language

Knowledge of Finite element method, basic knowledge of Discrete element method

Work with 3D laser scanner, geometrical analysis and creation of structural models

Driving licence B-category

Completed course of photography

#### Languages spoken

Croatian

English (TOEFL Score 112/120)

Spanish

French

Esperanto (intermediate)

Russian (basics)

Czech (basics)

#### Interests:

To know other cultures and countries – low cost travelled to 60 countries on 6 continents

Computers and programming

Sport